Final Report

A Personal Air Mobility Vehicle as a Maritime Pilot Shuttle (Loodswezen)

by

DSE Group 09

Name	Student number
Y. Bakır	4012178
A. Bayu Putranto	4538811
I. Bukai	4439120
S. de Metz	4340396
N. Gartland Bonet	4464656
H. Ibrahim	4473566
A. Küng Garcia	4556402
C.J.J.M.T. Meire	4214366
C.D.R. Proost	4018508
W. Völker	4303067

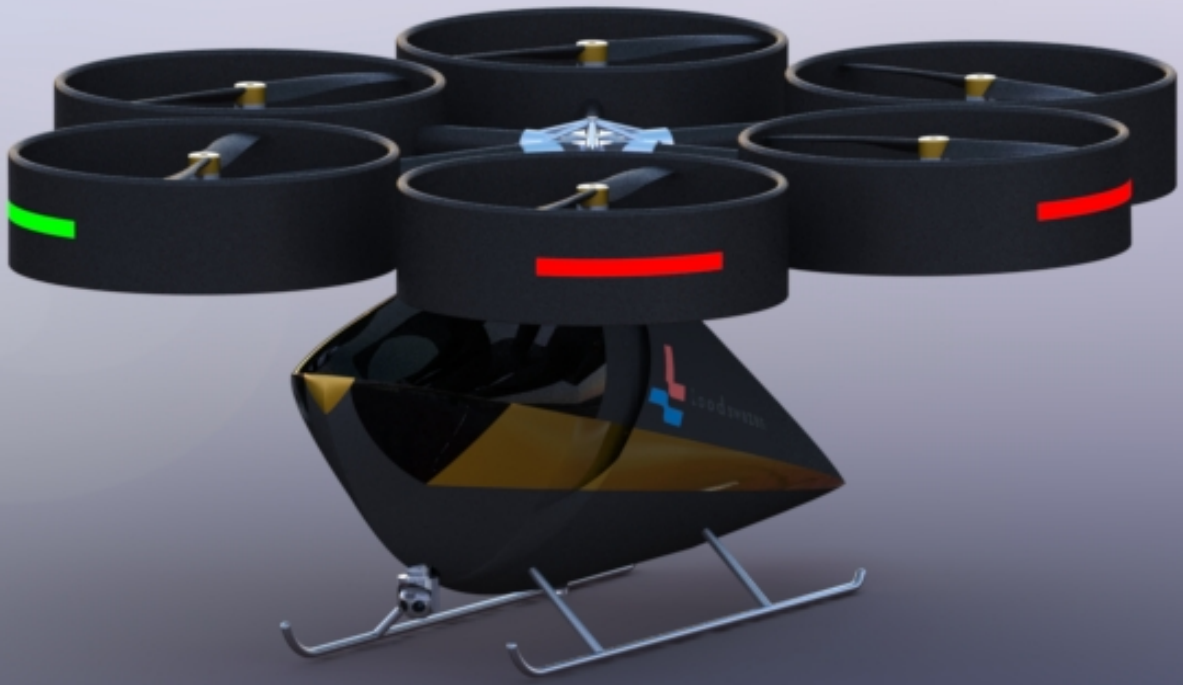

TU Delft

June 24, 2019

Version:1.7

Intentionally left blank

Preface

This final report is the fourth document submitted as a part of the Design Synthesis Exercise (DSE), in which Group 9 expands on the design presented in previous reports in order to realise the final design of the vehicle. The hexacopter design concept was chosen over three other ones to be analysed in detail, and therefore this report will mainly be addressing an audience with a background in Aerospace Engineering.

Group 9 would like to extend their gratitude to project tutors Prof. Fulvio Scarano and Dr. Daniele Ragni for their guidance through the entire design process, as well as Ashwin Candade and Bertrand Mercier for their input in challenging topics. Also a special thank you to Sam Van Elsloo for his valuable advice and remarks during the design process.

Delft, The Netherlands
June 24, 2019

List of Symbols and Abbreviations

Symbols

a	Acceleration $[m/s^2]$
A	Area $[m^2]$
A_R	Aspect Ratio [-]
α	Angle of attack $[rad]$
β	Blade pitch angle [˚]
b	Wing span $[m]$
c	Chord $[m]$
C_d	Airfoil drag coefficient [-]
C_D	Drag coefficient [-]
C_{Do}	Zero drag coefficient [-]
C_l	Airfoil lift coefficient [-]
C_L	Lift coefficient [-]
C_P	Power coefficient [-]
C_r	Rotor root chord [-]
C_T	Thrust coefficient [-]
C_{tail}	Tail volume coefficient [-]
d	Diameter $[m]$
D	Drag $[N]$
δ_{tip}	Rotor-duct tip gap $[m]$
E	Energy $[J]$
e	Oswald efficiency [-]
F	Force $[N]$, tip-loss correction [-]
FoS_{TO}	Factor of safety for take-off [-]
FoS_{F_D}	Factor of safety for drag force [-]
g	Gravity $[N/kg]$
G	Gravitational torque $[Nm]$
γ	Tilting angle $[rad]$
h	Height $[m]$
I_x	Second moment of area $[m^4]$
I_{xx}, I_{yy}, I_{zz}	Mass moment of inertia $[kgm^2]$
J	Advance ratio [-]
J_r	Rotational moment of inertia $[kgm^2]$
K_P	Proportional controler [-]
K_I	Integral controller $[N]$
K_D	Derivative controller $[N]$
L	Lift $[N]$
L_d	Duct diffuser length $[m]$
L_s	Rotor plane separation length $[m]$
l	Length $[m]$
λ	Rotor blade taper ratio [-]
m	Mass $[kg]$
M_E	Effective rotational Mach number [-]
M	Bending moment $[N/m]$
n	Rotation rate $[rps]$
n_p	Number of propellers [-]
N_b	Number of blades per propeller [-]
p	Rotation rate in x $[rad/s]$
P	Power $[W]$
Q	Torque produced by rotor $[Nm]$
q	Rotation rate in y $[rad/s]$
r	Rotation rate in z $[rad/s]$
r_{lip}	Duct inlet lip radius $[m]$
R	Rotor radius $[m]$, distance to mass component $[m]$
ρ	Density $[kg/m^3]$
S	Surface Area $[m^2]$
σ	Stress $[Pa]$, solidity [-]
σ_d	Duct's area expansion ratio [-]
t	Thickness $[m]$
T	Thrust $[N]$
τ	Torque $[Nm]$
ϕ	Velocity angle $[Rad]$, Vehicle's roll angle $[Rad]$
θ	Vehicle's pitch angle $[Rad]$, Blade pitch angle $[Rad]$
θ_d	Duct diffuser angle [°]
Ψ	Yaw angle $[Rad]$
u	vehicle's velocity in x $[m/s]$
U	Total relative velocity $[m/s]$
U_T	Tangential velocity $[m/s]$
U_p	Perpendicular velocity $[m/s]$
v	Volume $[m^3]$
v_i	Rotor-induced velocity $[m/s]$
V	Velocity $[m/s]$
V_c	Vehicle's velocity $[m/s]$
v	vehicle's velocity in y $[m/s]$
V_0	Free stream velocity $[m/s]$
I_O	Mass moment of inertia at the origin $[kgm^2]$
FoS_{neg}	Factor of safety for tail negative lift [-]
ω	Rotation rate of vehicle $[rad/s]$
Ω	Rotation rate of propeller $[rad/s]$
w	vehicle's velocity in z $[m/s]$
W	Weight $[N]$

Subscripts

cr	Cruise
h	Horizontal
tc	Thickness to chord
v	Vertical
x	x-axis
y	y-axis
z	z-axis

Abbreviations

BCU	Battery Control Unit
BMU	Battery Monitoring Unit
CG	Center of Gravity
CDR	Continuous Discharge Rate
DoD	Depth of Discharge
EFS	Emergency Float System
ESC	Electronic Speed Controller
FBD	Free Body Diagram
FM	Figure of Merit

Abbreviations (continued)

FTS	Flight Termination System
ICAO	International Civil Aviation Organization
KD	Kinetic Diagram
L+C	Lift and Cruise
MC	Multicopter
MTOW	Maximum Take-Off Weight
OEW	Operational Empty Weight
PAM	Personal Air Mobility
PCM	Protection Circuit Module
PU	Polyurethane
PMAD	Power Management And Distribution
RDT	Requirement Discovery Tree
RoI	Return on Investment
RPM	Revolutions Per Minute
SEL	Sound Exposure Level
SoC	State of Charge
SoH	State of Health
TA	Teaching Assistant
TLR	Top Level Requirement
TPM	Technical Performance Measurement
TR	Thrust to Weight Ratio
TRL	Technology Readiness Level
VTOL	Vertical Take-off and Landing
WBS	Work Breakdown Structure
WFD	Work Flow Diagram

Summary

For hundreds of years maritime pilots have been contributing to the safe and efficient handling of shipping traffic in all weather conditions. Using today's technology, a new, cheaper, safer and more sustainable way of transporting maritime pilots to incoming ships is possible, which is the subject of this Design Synthesis Exercise (DSE). PAMELA is a Personal Airborne Maritime Electric and Autonomous pilot shuttle designed by ten students within ten weeks.

The vehicle had to be capable of Vertical Take-Off and Landing, which makes a multicopter concept more suitable for our mission. The vehicle has to fit on a 4 x 4 meters surface and be less than 2 meters high. This makes it challenging to fit all the systems/subsystems while keeping an aerodynamic profile, as well as to design the necessary rotor size that could provide the vehicle with sufficient lift. A trade-off is formed to compare between two design concepts; fixed wing and multicopter (with different configurations). This resulted in choosing the hexacopter as the leading concept. This is mainly due to its lower power consumption, its additional redundancy and the availability of commercial off-the-shelf engines on the market.

In order to generate sufficient lift, the hexacopter uses coaxial contra-rotating rotors. For the vehicle to be allowed to fly, it has to comply with the aeroacoustic regulations for noise emissions over harbour areas. For this reason, as well as for the safety of the pilot, the use of ducts for the rotors was chosen.

Furthermore, appropriate battery cells, capable of providing the vehicle with enough power had to be selected, which led to the use of 14 packs of lithium-ion batteries. This resulted in a cruise range of more than 20 kilometres and thus fulfilling the requirement imposed by the customer. For improved stability, the rotors were positioned above the fuselage, adding extra ground clearance. This also allows for easy cabin access, enhancing the comfort of the passenger.

To package the subsystems and host the payload, minimum dimensions for the fuselage were settled. It was then possible to streamline the design of the fuselage by designing the aerodynamic profile, in order to reduce the drag generated during flight. The materials for the structures of the vehicle were chosen to be a combination of an aluminium alloy substructure and composite skin, creating a strong, lightweight, and recyclable composition.

It is estimated that 20 units will be sold between 2024 and 2034. Based on this number the production cost of each unit is €68,149, which meets the economical requirement. Striving for a RoI of 5%, a purchase price of €150,000 is determined.

Contents

1 Introduction

Very large cargo ships are challenged to manoeuvre within harbours, which is why all harbours have maritime pilots specialised in docking these great vessels. The maritime pilots are currently transported with either small boats or helicopters from the harbour to the incoming ships, but ongoing advancements in autonomous multicopter technology allows for an alternative medium of transport, namely a Personal Air Mobility (PAM) vehicle performing as a maritime pilot shuttle. An autonomous aerial vehicle can be faster, safer and more cost-effective for operations in harbour environments. To study the performance of this personal air mobility vehicle, Group 09 was assigned to perform the conceptual design and investigate its complications.

This document is structured as follows; chapter 2 presents the earlier stages of the design process before the final report was written. In chapter 3, the logistics and the operations of the vehicle is discussed. Moreover, chapter 4 sheds light on the main elements of powertrain used for PAMELA. The characteristics of the aerodynamics noise are introduced in chapter 5. Furthermore, chapter 6 analyses the stability & control of the vehicle. In chapter 7, the systems for avionics are selected. Also, the structure analysis and materials selection is done in chapter8. Lastly, the outcome of the design final stage is shown in chapter 9.

2 Project Overview

The industry of personal air mobility vehicles has been getting more attention in the past couple of years. Nowadays, the market is filled with many design concepts that are meant to serve various aspects in life. However, suboptimal efficiency, safety and sustainability pose some of the major challenges to overcome in this sector. The aim of this Design Synthesis Exercise (DSE) is to carry out the design of a personal air mobility vehicle intended to operate in harbour areas. The design is done by a group of 10 students (Group-09) over a timespan of 10 weeks. This chapter briefly introduces all stages the team has gone through to get the design done.

2.1. Project Plan Report

Project planning is a key element in the development process towards realizing the final design. It serves as a guide and reference because it explains how the team plans to carry out the assigned task. In the project planning phase, the team defined the Mission Need Statement and the Project Objective Statement which are "To design an autonomous, electric-powered personal air mobility vehicle capable of transporting a maritime pilot to an incoming ship" and "To transport a maritime pilot from the harbour to an incoming ship" respectively. Also, the Work Breakdown Structure (WBS), Work Flow Diagram (WFD), and Gantt Chart were provided. Furthermore, the team described the organizational aspect of the project and assigned major roles to the members. SWOT (Strength, Weakness, Opportunity & Threat) Analysis and Risk Management were discussed. Lastly, the team examined Reliability, Availability, Maintainability and Safety (RAMS) and incorporated measures in the entirety of the design process.

2.2. Baseline Report

Based on the Mission Need Statement and Project objective Statement (that have been defined in the Project Plan), the Baseline report followed to provide the Functional Flow Diagram (FFD) and the Functional Breakdown Structure (FBS). These two illustrate the operational aspects and the steps taken to achieve the mission. Further, the team did a research on the targeted market to learn about stakeholders, regulations, compliance, and competition so that the final product has the chance to compete and

survive. At this stage also, Requirements Analysis was performed and consequently the following requirements were found to be of substantial importance:

- PAM-SH-CLI-1: The minimum weight of the payload is 100 kg.
- PAM-SH-CLI-2: The indicative maximum vehicle size is 4x4x2 m^3
- PAM-SH-CLI-3: A minimum cruise speed of 100 km/h.
- PAM-SH-CLI-5: An electric power autonomy for 20 km.
- PAM-SH-CLI-11: A maximum level of cabin noise of 60 dBA is allowed.
- PAM-SH-CLI-14: The vehicle propulsive system should still be able to fly with only 50% of the propulsive system actively working.
- PAM-SH-CLI-15: The cost of the final product should not exceed €60,000.

Requirements Analysis is the basis for constructing the Design Option Trees for the vehicle systems and then eliminating those design options that are not either physically feasible, or practical for this design. As an outcome, two main design concepts were chosen to be traded off later on. These are :

- Concept 1: fixed wing with multiple fixed rotors (hybrid winged/copter aircraft).
- Concept 2: contra-rotating multicopter (Tricopter, Quadcopter, Hexacopter).

Lastly, the team adopted a Technical Risk Management approach for both design concepts which includes identification of risks, assessing the probability and impact on the product, coming up with mitigation plans and assessing the post-mitigation impact.

2.3. Midterm Report

The Midterm report builds on its precedents (Project Plan & Baseline) by presenting a preliminary design for the different design concepts. The report includes a total mass budget, take-off analysis, cruise analysis, propulsion group sizing, and initial battery sizing for each concept. This is an important phase of the design process as it provides a sufficient understanding of the the design concepts that allows to perform an educated trade-off.

2.3.1. Fixed Wing Design Concept

For the Fixed wing Design Concept, the final layout can be seen in figure 2.1 and the calculated parameters are listed in tables 2.2 2.1

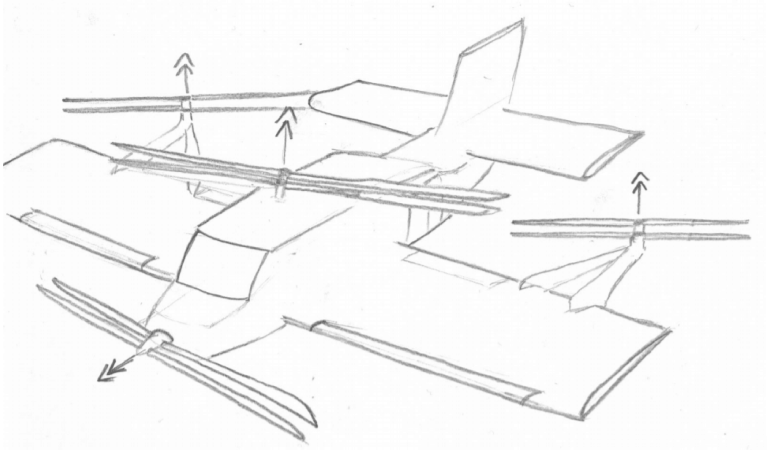

Figure 2.1: Layout of the fixed wing design concept

Parameter	Value	Unit
$n_{p,rotors}$	6	-
$n_{p,propellers}$	2	-
b	3	m
b_{h-tail}	2	m
h_{v-tail}	0.24	m
D_{rotors}	1.53	m
$D_{propellers}$	1.39	m
c	1.42	m
c_{h-tail}	0.85	m
c_{v-tail}	0.85	m
m_{tot}	298.45	kg

Figure 2.2: Specifications of the fixed wing design concept

Table 2.1: Specifications of Fixed Wing Preliminary Design

	Fixed wing concept
P/Cruise [kW]	36
Flight Time [sec]	2211
Battery Capacity [kWH]	22.11
Range at Cruise [km]	61.41

One of the main complications of this design concept is the interaction between the fuselage and rotors/propellers. This has a major influence on the efficiency of the rotors/propellers. Also, the transition from vertical to horizontal flight (and vice versa) is complicated.

2.3.2. Multicopter Design Concept

This design concept comprises of three different configurations; Tricopter, Quadcopter and Hexacopter. All of them have contra-rotating rotor pairs to make the most efficient use of the limited size. Top view of the final layout of the three configurations can be seen in figures 2.3, 2.4 and 2.5. Furthermore, the prime parameters calculated for the different configurations are listed in Table 2.2.

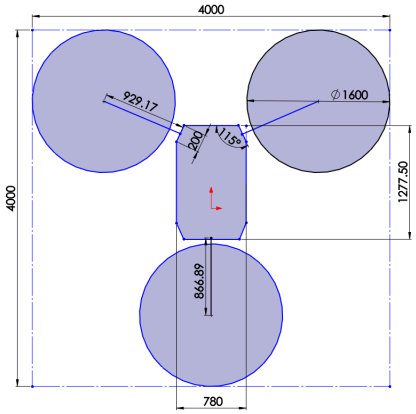

Figure 2.3: Top view of Tricopter Layout

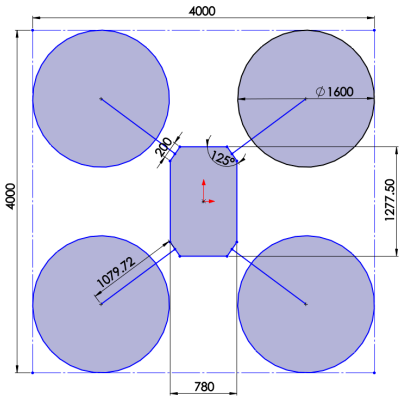

Figure 2.4: Top view of Quadcopter Layout

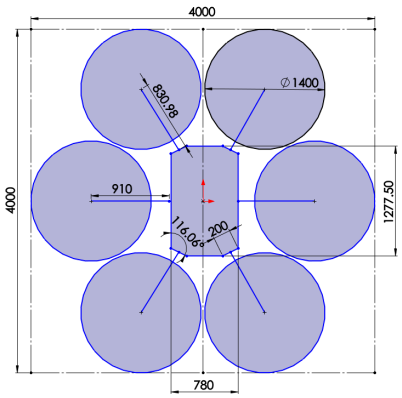

Figure 2.5: Top view of Hexacopter Layout

Table 2.2: Specifications of Multicopters Preliminary Design

	Tricopter	**Quadcopter**	**Hexacopter**
Rotor Diameter [m]	1.6	1.6	1.4
Motor mass [kg]	28	24.5	23
Flight Time [sec]	1349	13.93	13.09
P/Hover [W]	55000	48000	45000
P/Cruise [W]	59000	52000	49000
Arm Length [m]	0.93	1.07	0.83
Battery Capacity [kWH]	22.11	20.13	17.82
Range at Cruise [km]	37.47	38.69	37.36

Once the parameters of the preliminary designs were known for all different concepts, the trade-off was made. A number of design criteria were considered for the trade-off and given a weight in terms of significance. Then, each design concept was graded at each criterion. Consequently, the concept that scores the highest is selected for the final design. The trade-off criteria and their values are listed in table 2.3. Based on the outcome of the trade-off, the Hexacopter had the best values and therefore was chosen for the final design.

Table 2.3: Values of Trade-off Criteria

	Fixed Wing	Tricopter	Quadcopter	Hexacopter
cost [€]	40.9	34.5	32.5	32
Noise [dBA]	73	60	55	56
Redundancy [%]	60	60	8.3	1.6
Stability [$\dot{P}$]	0	19.2	35.5	30.27
Manoeuvrability [$\Delta T\%$]	2.71	2.25	1.93	1.77
Cruise Power [kW]	36	59	52	43

3 Operation Plan

In this chapter, the logistics and operations of the vehicle will be presented. Firstly, the life cycle operation will be explained, followed by an analysis of the mission profile of the vehicle, concluding with a thorough look at the functions of the hexacopter.

3.1. Life Cycle Operations

The life cycle of the product is represented graphically in Figure 3.1. It is divided in 4 phases: design, production, operation and end of life. The DSE team will be concerned with only the first block of the first phase, until the arrival of a conceptual design. This conceptual design must be refined to arrive at a final design of which a prototype can be manufactured, tested and certified.

Once the design has been proven to be successful, the commercial production of the vehicle can commence. A more detailed description of the production and assembly of the hexacopter can be found in section 8.8. The final product is delivered to the costumer, after which operation of the vehicle is possible. The different functions of the vehicle are presented in section 3.4. Finally, at the end of the vehicle's 10 years of useful life, the hexacopter is decommissioned and disassembled, with the discarded parts being sent to the recycling facilities.

3.2. Loodswezen Operations

All ships enter the port of Rotterdam through the Eurogeul (see Figure 3.2) and wait at the Maas Center for the maritime pilot, who will bring the ship through the Maasgeul into the harbour. Thus, Loodswezen must bring maritime pilots from their ports (points L and H) to the ship holding zone (point S).

Currently, various tenders are used for this, which require a crew of two operators and one extra person to help the maritime pilot to embark the incoming ship. Otherwise, Loodswezen also employ larger ships such as the Polaris boat which has various maritime pilots on board. The Polaris class boats are stationed somewhere close to the Maas Center and uses four small speedboats to bring maritime pilots to the ships. These speedboats only require one operator plus one person to help with embarking the ship. However, the operation of the Polaris boat employs many more people.

Loodswezen operates every day 160 ships, of which around 20 have helipads, mainly big oil tanker and large cargo ships. The helicopter itself is only used once a day, so with the current charging time 4 hexacopters could take over the operations of the helicopter and the boats serving ships with helipads.

Of the 19 tenders Loodswezen is using at the moment of writing this report, 7 of them are planned on being decommissioned in the upcoming years. This is the perfect opportunity for the hexacopter to fill the gap left by these boats.

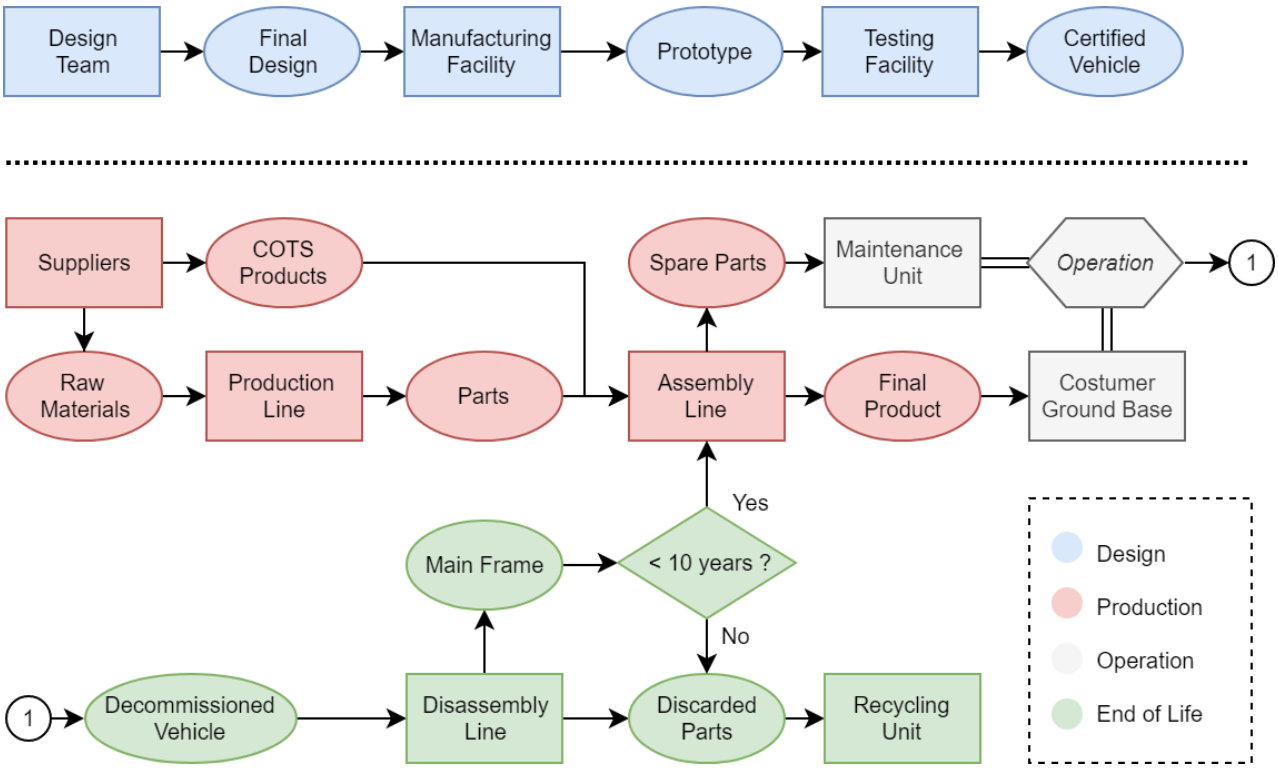

Figure 3.1: Life cycle operations of the vehicle

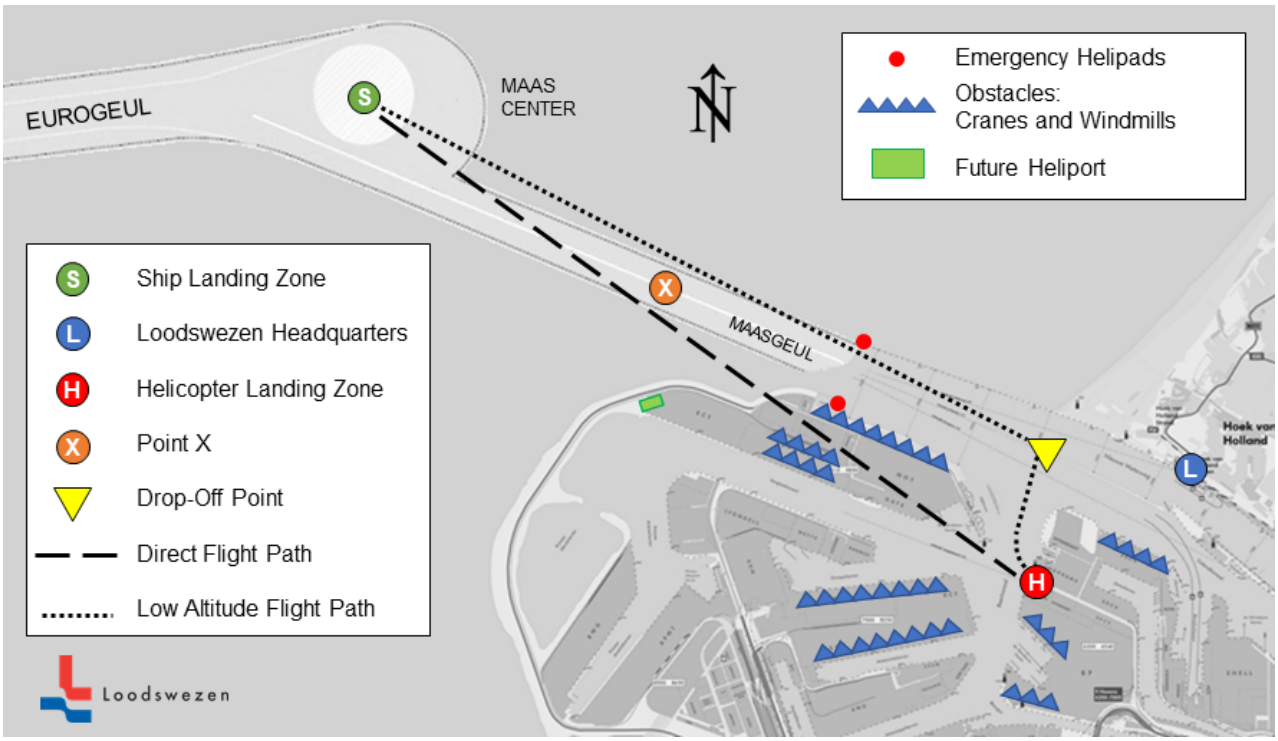

Figure 3.2: Vehicle mission over the port of Rotterdam.

3.3. Mission Profile

The typical mission of the vehicle is represented in Figure 3.3. In case of the port of Rotterdam, the vehicle can cruise in a straight line from point H to point S, point H being the existing helipad for the Loodswezen helicopter and S the helipad on the incoming ship at Maas Center. This direct route would require a higher cruise altitude given that it would be traversing terrain with many high obstacles.

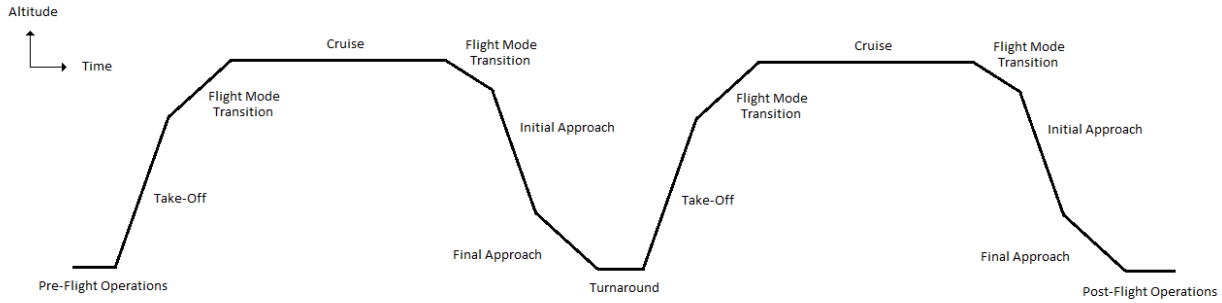

Figure 3.3: Mission profile for a maritime pilot shuttle.

The return trip without the maritime pilot can be done directly from point S to point H, but this would exceed the hexacopter's maximum battery range. Instead, the vehicle stays on the ship until it reaches the Drop-Off Point, at which it will take off and travel a much shorter path to point H. This will allow to save battery power and thus reduce turn-around time as less time is needed for charging. Following this path also allows for a lower cruise altitude as the vehicle flies over the water, by which no energy is used on reaching high altitudes. In addition, not all ships have to wait at Maas Center to wait for a maritime pilot, some ships can come all the way up till point X where the ships will then be boarded by the maritime pilot. After embarking the ship will continue its way to the Drop-Off Point where PAMELA will fly back to the helicopter landing zone. In case of failure, it has been decided that PAMELA will slowly lower itself into the water or onto the ground at the point where 50% of engine failure occurs. In case of landing in the water a safety system has been designed such that PAMELA floats and the vehicle and pilot can wait until it gets recovered by rescue ships.

Oversight of possible mission distances when current Helicopter Landing Zone is used:

1. Mission where PAMELA leaves at point H and lands on the ship in Maas center and then stays on the ship until the ship reaches the drop-off point where it will fly back to point H. The distances that need to be covered by PAMELA will then be equal to:

   - Point H - Maas Center: 20 km.
   - Drop-Off Point - Point H: 3.7 km.

   Thus a total mission distance of **23.7 km.**

2. Mission where PAMELA leaves at point H and embarks the ship at Point X then PAMELA stays on the ship again until the Drop-Off point where it will fly back the to Helicopter Landing Zone. The distances that need to be covered by PAMELA will then be equal to:

   - Point H - Point X: 9.3 km.
   - Drop-Off Point - Point H: 3.7 km.

   Thus a total mission distance of **13 km.**

However, up until now only the initial implementation of the vehicle has been considered using existing infrastructure, namely the helicopter base currently used by Loodswezen. For full implementation with various vehicles, it is recommended to build a ground base with various helipads, charging stations, maintenance units and control tower on the location indicated in Figure 3.2. This is part of the expansion plan of the port of Rotterdam, and has thus available land for construction especially given the heliport would not take a large surface area. The heliport location would allow to nearly half the cruise distance and removes all problems with high obstacles, since the vehicle would only have to fly over the lamps of the road to reach the sea.

Oversight of possible mission distances when future heliport is used:

1. Mission where PAMELA takes off at the new heliport and then flies towards the waiting ships at Maas Center. After the maritime pilot embarks the ship PAMELA will wait on the ship until it has reached Point X where it will fly back to the new helipad. The distances that need to be covered by PAMELA will then be equal to:

   - Future Helipad - Maas Center: 12.35 km.
   - Point X - Future Helipad: 2 km.

   Thus a total mission distance of **14.35 km.**

2. As explained before some ships don't have to wait at Maas Center such that a maritime pilot can be board the ship. For these ships boarding can be done at Point X, at this point it is only needed for the maritime pilot to embark the ship. Therefore, PAMELA can fly straight back to the Helipad after embarking the maritime pilot on the ship. The distances that need to be covered by PAMELA will then be equal to:

   - Future Helipad - Point X: 2 km.
   - Point X - Future Helipad: 2 km. Thus a total mission distance of **4 km.**

Den Helder Proof of Concept

The port of Rotterdam serves many ships every day and thus it would like to be shown a working vehicle before it agrees on implementing it. For this reason Loodswezen has recommended the much smaller port of Den Helder, which has much lower traffic and serves mostly off-shore oil vessels, nearly all of which have helipads. Currently, there is a single tender working at den Helder which costs 8 million a year to operate but is used on average only once a week.

Den Helder proves then to be a great opportunity for a proof of concept with the hexacopter replacing the much more expensive vessel to serve the few ships that need its service. As can be seen in Figure 3.4, Den Helder has an existing helipad which allows to take off with no obstacles and reach the vessels within a very comfortable range.

3.4. Functional Analysis

In this section, the Functional Analysis that was performed in the Baseline Report [9] will be extended on. A complete understanding of the system is provided in a Functional Breakdown Structure (FBS), figure 3.6, and is sequenced in time by a Functional Flow Diagram (FFD), figure 3.5. The Functional Analysis describes what the system will do as functions and sub-function. Each function is described as a limiting requirement for the system.

The FFD is a step-by-step, three-tier diagram, showing the flow and the relations between the functions and sub-functions of the system. It describes the operational life of the system, including operations, support systems, and maintenance and repair processes. The FFD does not show neither the duration, overlap of the processes nor any solutions on how the functions will be performed.

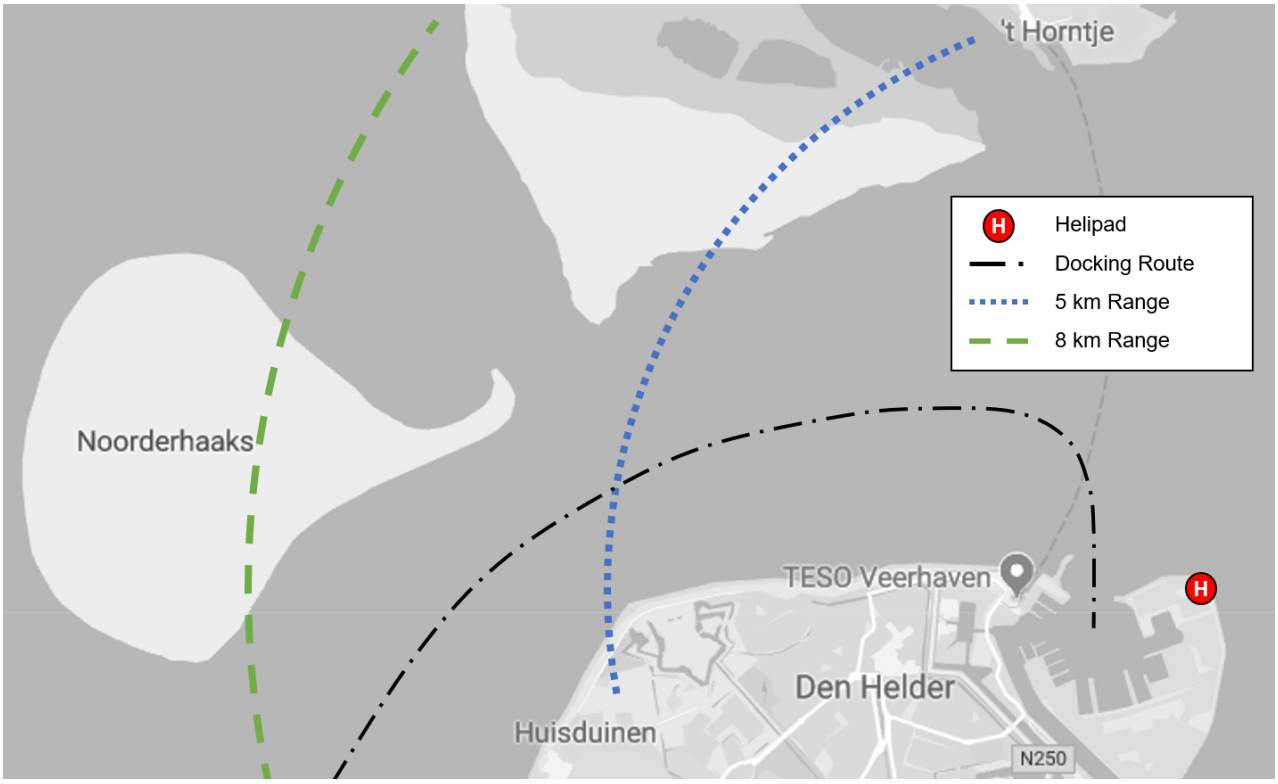

Figure 3.4: Vehicle mission over the port of Den Helder

The first tier is built up out of six blocks, each containing a major function of the system. The second and third tier go into more detail on blocks of the prior tier. All of the first tier functions and some of the second tier sub-functions are broken down into multiple sub-functions, which define the system's functions in more detail. In these tiers OR-statements are used to indicate alternative sub-functions and GO and NO GO-statements are used to mark critical decisions in the process.

Let us walk through the rationale behind the making of the functional flow diagram. The first major (i.e. tier 1) function/phase that has to be done is the pre-flight operations; typical of any aviation mission. A small difference in detail is that the mission starts from the request of the operation centre, which may be some party related to the Port Authority. Once the request for the mission has been received, the vehicle may be started. From here the functionality of all the subsystems are checked, where maintenance is performed when necessary. In case the battery is not sufficiently charged, it will either be replaced or recharged. A decision is then made whether or not the pilot may embark on the vehicle. This decision is relayed to the operation centre to confirm the intention and next actions of the vehicle (i.e. whether or not to take-off).

The second major phase is the vertical take-off; where this commences by starting the engine. Once the engine is ready, the propulsion system performance can be checked. After knowing that nothing is wrong with the propulsion system, the vehicle starts climbing in which it will be gathering relevant data (i.e. of the atmosphere) until reaching the desired altitude eventually. The climb ends officially by preparation for departure, and then the next phase may start.

The third major function is performing cruise. Similar to climb, the cruise requires collecting relevant data (i.e. flight data) that is processed for an eventual navigation. Between the processing and navigation, the flight data shall be communicated to a relevant party (i.e. operation centre) almost at all times; and the control devices take the processed data and will adjust accordingly. The navigation process iterates until the desired location is reached, and the vehicle continues to approach and moves on with vertical landing.

The vertical landing is the fourth major phase. The procedure starts with hovering descent in which

it is analogous to the vertical climb and cruise navigation procedures. The difference is at the final part of descent in which a stable touch down shall be done. This is crucially important since the ship may be very unstable when strong water waves disturbs it (for example in an 8 Beaufort weather condition). The mission of transporting the pilot finishes, thus the system may be shut down. The vehicle then proceeds onto its post-flight operation.

The post-flight operations is the final major phase. It starts with debarking the pilot in which the process shall be easy to avoid any further delay for him to start docking the ship and safe to not cause any injuries. The power can then be resupplied. In this case since it is a necessity for the vehicle to be electrical, the battery shall be either charged or replaced, depending on the design. Next, the flight log is updated for future references and finally the vehicle may prepare for any further mission. Once this is done, the vehicle proceeds with maintenance. A more detailed description of some of the functions can be seen in the FBS.

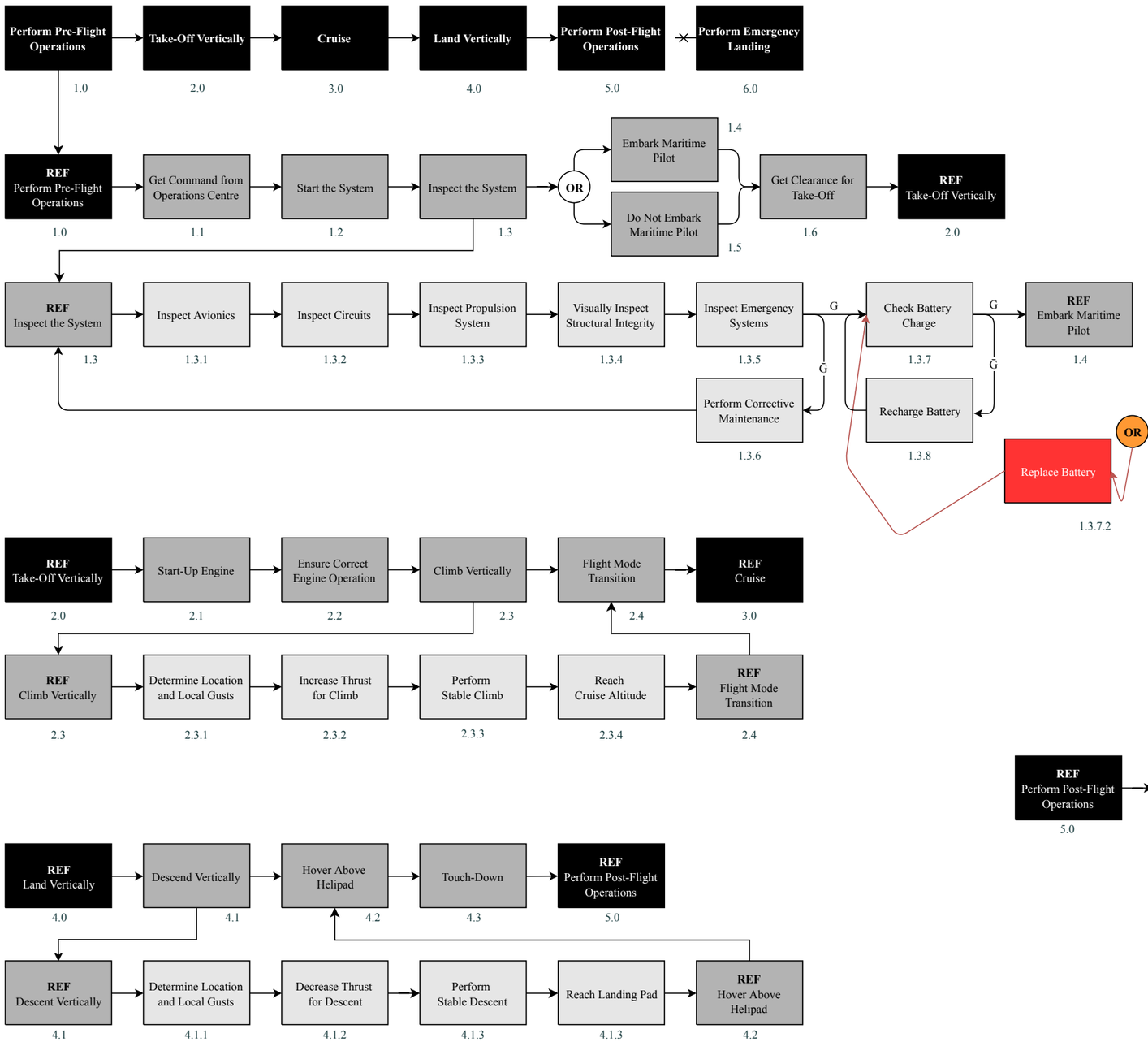

Figure 3.5: Functional Flow Diagram.

- **1.0 Perform Pre-Flight Operations**
  - 1.1 Get Command from Operations Center
    - 1.1.1 Communicate with Ship
    - 1.1.2 Check for Landing Pad Availability
    - 1.1.3 Measure Weather Conditions
    - 1.1.4 Determine Optimal Route
  - 1.2 Start The System
  - 1.3 Inspect the System
    - 1.3.1 Inspect Avionics
      - 1.3.1.1 Inspect Navigation System
      - 1.3.1.2 Inspect Communication System
      - 1.3.1.3 Inspect Autopilot Software
    - 1.3.2 Inspect Circuits
      - 1.3.2.1 Inspect ECTs
      - 1.3.2.2 Inspect Battery
      - 1.3.2.3 Inspect Cabling
    - 1.3.3 Inspect Propulsion System
      - 1.3.3.1 Inspect Propeller Blades
      - 1.3.3.2 Inspect Engine
    - 1.3.4 Visually Inspect Structural Integrity
      - 1.3.4.1 Inspect Rotor Arms
      - 1.3.4.2 Inspect Cockpit
      - 1.3.4.3 Inspect Landing Gear
    - 1.3.5 Inspect Emergency System
    - 1.3.6 Perform Corrective Maintanance
    - 1.3.7 Check Battery Charge
    - 1.3.8 Recharge Battery
  - 1.4 Embark Maritime Pilot
    - 1.4.1 Open Cabin Door
    - 1.4.2 Enter Vehicle
    - 1.4.3 Adjust Seat
    - 1.4.4 Fasten Seatbelt
    - 1.4.5 Close Cabin Door
    - 1.4.6 Put on Headset
    - 1.4.7 Brief Passenger on Mission
  - 1.5 Do not Embark Maritime Pilot
  - 1.6 Get Clearance for Take-Off
- **2.0 Take-Off Vertically**
  - 2.1 Start up Engine
    - 2.1.1 Clear Helipad
    - 2.1.2 Engage Rotors
    - 2.1.3 Reach Operational RPM
  - 2.2 Ensure Correct Engine Operation
    - 2.2.1 Abort Take-Off In Case of Failure
  - 2.3 Climb Vertically
    - 2.3.1 Determine Location & Local Gusts
    - 2.3.2 Increase Thrust for Climb
    - 2.3.3 Perform Stable Climb
    - 2.3.4 Reach Cruise Altitude
  - 2.4 Flight Mode Transition
    - 2.4.1 Increase Thrust for Cruise
    - 2.4.2 Incline Vehicle Forward
- **3.0 Cruise**
  - 3.1 Measure Flight Data
    - 3.1.1 Measure Air Conditions
    - 3.1.2 Measure Velocity
    - 3.1.3 Measure altitude
    - 3.1.4 Measure Location
    - 3.1.5 Measure Attitude and Heading
    - 3.1.6 Measure Wind Gusts
  - 3.2 Process Flight Data
    - 3.2.1 Compute Flight Path Deviation
    - 3.2.2 Compute Required Thurst Control
  - 3.3 Transmit Flight Data to Control Tower
  - 3.4 Adjust Flight Path
    - 3.4.1 Adjust Power Settings
    - 3.4.2 Adjust Thrust Level
    - 3.4.3 Adjust Differential Thrust
    - 3.4.4 Modify Attitude and Heading
    - 3.4.5 Modify Velocity Vector
  - 3.5 Flight Mode Transition
    - 3.5.1 Decrease Thrust for Landing
    - 3.5.2 Set Attitude for Hover
- **4.0 Land Vertically**
  - 4.1 Descend Vertically
    - 4.1.1 Determine Location and Local Gusts
    - 4.1.2 Decrease Thrust for Descent
    - 4.1.3 Perform Stable Descent
    - 4.1.4 Reach Landing Pad
  - 4.2 Hover Above Helipad
    - 4.2.1 Increase Thrust for Touch-Down
    - 4.2.2 Locate Landing Pad
    - 4.2.3 Maneuver against Gusts
    - 4.2.4 Stabilize Vehicle at Zero Attitude
  - 4.3 Touch-Down
    - 4.3.1 Land on Helipad
    - 4.3.1 Secure Vehicle on Helipad
- **5.0 Perform Post-Flight Operations**
  - 5.1 Disembark Maritime Pilot
    - 5.1.1 Take Off Headset
    - 5.1.2 Unfasten Seatbelt
    - 5.1.3 Open Cabin Door
    - 5.1.4 Exit Vehicle
    - 5.1.5 Close Cabin Door
  - 5.2 Perform Turn Around
    - 5.2.1 Receive Command from Control Tower
      - 5.2.1.1 Receive Return Flight Route
      - 5.2.1.2 Receive Clearance for Take-Off
    - 5.2.2 Ensure Empty Helipad
  - 5.3 Shut Down Engines
  - 5.4 Wait For Drop-Off Point
    - 5.4.1 Secure Position on Helipad
    - 5.4.2 Measure Location of Ship
    - 5.4.3 Measure Speed of Ship
  - 5.5 Update Flight Log
    - 5.5.1 Send Flight Data to Data Base
    - 5.5.2 Receive Future Flight Schedule
  - 5.6 Perform Maintenance
    - 5.6.1 Charge Battery
    - 5.6.2 Clean Vehicle
      - 5.6.2.1 Wash Structure with Clean Water
      - 5.6.2.2 Remove Salt From Cabin Joints
      - 5.6.2.2 Remove Salt From Engines
    - 5.6.3 Sheduled Maintenance
      - 5.6.3.1 A-Check after every flight
      - 5.6.3.2 B-Check every night
      - 5.6.3.3 C-Check every Week
      - 5.6.3.4 D-Check every Month
    - 5.6.4 Unsheduled Maintenance
      - 5.6.4.1 Remove Failed Parts
      - 5.6.4.2 Replace with Spare Parts
      - 5.6.4.3 Repair Faulty Elements
- **6.0 Perform Emergency Landing**
  - 6.1 Adjust Power Settings
    - 6.1.1 Increase Working Engine Power
    - 6.1.2 Shut Down Failed Rotors
  - 6.2 Adjust Flight Route
    - 6.2.1 Determine Location at Failure
    - 6.2.2 Find Closest Landing Point
      - 6.2.2.1 Determine Helipad Availability
      - 6.2.2.2 Locate Clear Ground Areas
      - 6.2.2.3 Request Ship Helipads
      - 6.2.2.4 Locate Clear Sea Areas
    - 6.2.3 Transmit New Route to Control Tower
    - 6.2.4 Deploy Extration Team
  - 6.3 Perform Controlled Descent
    - 6.3.1 Adjust Thrust for Descent Rate
    - 6.3.2 Incline Vehicle Forward
    - 6.3.3 Set Heading for Landing Area
    - 6.3.4 Avoid Obstacles
  - 6.4 Crash On Water
    - 6.4.1 Hover Above Waves
    - 6.4.2 Descend Onto The Water
    - 6.4.3 Shut Down Engines
    - 6.4.4 Block Rotors
    - 6.4.5 Deploy Floating Devices
    - 6.4.6 Open Cabin Door
  - 6.5 Land On Ground
    - 6.5.1 Hover Above Landing Point
    - 6.5.2 Descend to Touch-Down
    - 6.5.3 Shut Down Engines
    - 6.5.4 Open Cabin Door
  - 6.6 Extract Maritime Pilot
    - 6.6.1 Send Rescue Boat to Landing Point
    - 6.6.2 Send Rescue Vehicle to Landing Point
    - 6.6.3 Transport Vehicle to Ground Base

Figure 3.6: Functional Breakdown Structure.

3.5. User Requirements

When starting the design process it is imperative to know what requirements PAMELA needs to fulfil. That is why, during the conceptual design stage, all requirements were set up and represented in the baseline report. Most of these requirements are unchanged with respect to the baseline report, however there are also new requirements present. Below, the most updated version of the requirements list is given including definitions, in addition they are subdivided in departments/groups.

General requirements:

- **PAM-SH-CLI-1:** The minimum weight of the payload shall be 100 kg.
- **PAM-SH-CLI-7:** The vehicle shall be operated without a private pilot licence.
- **PAM-SH-CLI-15:** The cost of the final product shall not exceed €60,000.
- **PAM-SH-CLI-21:** The vehicle shall respect emission regulations over harbour areas.
- **PAM-SH-DSE-1:** The conceptual design shall be done within 10 weeks by 10 students.
- **PAM-CON-COST-2:** The development costs of the project shall be €0.
- **PAM-CON-SAF-1:** A contingency plan shall be used throughout the project.

Noise requirements:

- **PAM-SH-CLI-4:** The new vehicle shall respect European (night) noise regulations.
- **PAM-SH-CLI-10:** The vehicle shall respect the aeroacoustic regulations for emissions over harbour areas.
- **PAM-SH-CLI-11:** The vehicle shall have a maximum level of cabin noise of 60 dBA.
- **PAM-SH-CLI-12:** The vehicle shall be allowed to fly overnight.
- **PAM-CON-SUS-4:** The noise levels produced by the vehicle shall be at least 15 dB less than the levels produced by helicopter currently used.

Structural requirements:

- **PAM-SH-CLI-2:** The indicative maximum vehicle size is 4x4x2 m^3.
- **PAM-SH-CLI-6:** The lifetime of the vehicle shall be 10 years.
- **PAM-SH-CLI-18:** The vehicle shall be designed for 1 passenger.
- **PAM-SH-PAS-1:** Commuting in the vehicle shall be safe.
- **PAM-SH-PAS-2:** The cabin shall be comfortable.
- **PAM-SH-PAS-3:** The vehicle shall be easy to access.
- **PAM-TECH-OP-1:** The vehicle shall have a maximum OEW of 201.87 kg.
- **PAM-FUNC-POST-1:** The vehicle shall allow for a safe embarking within 60 seconds after system shutdown.
- **PAM-RISK-4:** The emergency safety system shall be deployable regardless of the working status of any other subsystems.

Propulsion requirements:

- **PAM-SH-CLI-3:** The vehicle shall have a minimum cruise speed of 100 km/h.
- **PAM-SH-CLI-5:** The vehicle shall have an electric power autonomy for 20 km.
- **PAM-SH-CLI-14:** The vehicle shall be able to fly with 50% of the propulsive system actively working.
- **PAM-SH-CLI-19:** The vehicle shall be VTOL capable.
- **PAM-SH-CLI-20:** The vehicle shall be able to commute within 10 km.
- **PAM-SH-CLI-22:** The vehicle shall be conceived for electric propulsion.
- **PAM-TECH-PERF-1:** The vehicle's battery capacity shall have a minimum capacity of 16 kWh with an accuracy of 10%.

- **PAM-TECH-PERF-1.1:** The battery pack shall have a minimum weight of 50 kg.
- **PAM-TECH-PERF-2:** The minimum motor peak power shall be 80 kW with an accuracy of 15%.
- **PAM-TECH-PERF-3:** The minimum range of the vehicle shall be 35 km with an accuracy of 10%.
- **PAM-TECH-PERF-3.1:** The vehicle shall have a minimum flight time of 21 minutes.
- **PAM-RISK-5:** The manufactured rotor shall have precision on dimension of 0.5 mm.

Stability and Manoeuvrability requirements:

- **PAM-SH-CLI-8:** The vehicle shall adopt an autopilot and proximity sensor.
- **PAM-SH-CLI-9:** The vehicle shall be able to operate at 5m distance from people and 3 m distance from any object (also in densely populated areas).
- **PAM-SH-CLI-13:** The vehicle shall fly with a max of 8 Beaufort with or without rain.
- **PAM-SH-INT-1:** The vehicle shall be able to land on a (moving) ship.
- **PAM-SH-INT-2:** The vehicle shall be able to operate within harbour area's.
- **PAM-FUNC-PRE-1:** The vehicle shall be able to receive signals from the operation centre.
- **PAM-FUNC-PRE-2:** The vehicle shall be able to autonomously check the functionality of all the subsystems.
- **PAM-FUNC-TAKEOFF-1:** The vehicle shall measure atmospheric conditions.
- **PAM-FUNC-CRUISE-1:** The vehicle shall be able to send information to the operations centre.
- **PAM-FUNC-CRUISE-2:** The vehicle shall be able to adjust its control devices.
- **PAM-FUNC-LAND-1:** The vehicle shall be able to perform a stable landing.
- **PAM-FUNC-POST-2:** The system shall update the flight log after every mission.
- **PAM-MAN-1** The vehicle must reach a cruise altitude of 100 meters in less than 10 seconds.
- **PAM-MAN-2** The vehicle must be capable of reaching a cruise speed of 100 km/h in less than 1 minute.
- **PAM-MAN-3** The vehicle must be capable of recovering from a horizontal 5° disturbance in less than 2 seconds.
- **PAM-MAN-4** The vehicle must be capable of doing a full 180° turn in less than 6 seconds.

Operational requirements:

- **PAM-SH-CLI-16:** The cost of the final product shall save at least 10% of the Maritime Pilot Operation costs.
- **PAM-SH-EXT-1:** The vehicle shall adhere to the ICAO regulations.
- **PAM-SH-EXT-2:** The vehicle's altitude shall not exceed 500 meters during operations.
- **PAM-CON-COST-1:** The yearly maintenance cost shall be less €100,000/year.
- **PAM-FUNC-POST-3:** The vehicle shall undergo inspection before every mission.

Sustainability requirements:

- **PAM-CON-SUS-2:** The battery supply chain shall be transparent and involve no unsafe work environments.
- **PAM-CON-SUS-1:** The electricity used to recharge the vehicle's battery shall come from a green energy source.
- **PAM-SH-INT-3:** The vehicle shall have a decreased environmental pollution compared to current operations.
- **PAM-SH-CLI-17:** After 10 years the main structure shall be reused for at least other 10 years in other vehicle components (modular). After that the structure should be easily recyclable.
- **PAM-SH-INT-4:** The vehicle shall be able to operate in a safe manner for both the passenger and the vehicle's surroundings.
- **PAM-CON-SUS-3:** The battery shall be recyclable.

3.6. Operating Costs

According to the requirements set by the customer, the operating costs of Loodswezen's operations will be decreased by at least 10%, after replacing their vehicles (partly) by PAMELA. The operating costs of PAMELA have been estimated in the following way. Firstly, the energy cost per hour has been calculated. Using the median price per kWh in the Netherlands of €0.20, and an energy usage of 53 kWh per hour of flight time (cruise), the energy price amounts to 11 £/$hour$ of flight time. Secondly the maintenance costs are added to the energy costs. The maintenance costs consist of battery replacement costs, maintenance employee costs and other parts replacement. The vehicle maintenance is scheduled for half a day a week, plus 1 day a month, where a day is 12 hours. This amounts to 38 inoperative days per year. The cost of a maintenance employee is estimated to be 50 £/$hour$, so this adds up to **€22,800** yearly maintenance employee costs. Assuming 5 cycles a day, and a cycle life of 500 cycles (see subsection 4.8.4), this means that 3.3 batteries are needed per year. A battery costs €9,483, which means that the batteries cost **31,000** £/$year$. Lastly the price of parts other than the batteries that have to be replaced due to unforeseen circumstances (bird strike, etc.), are estimated to be **10,000** £/$year$. The total yearly maintenance costs then add up to **63,800** £/$year$. Taking into account 1 hour of total flight time a day , the total (maintenance and energy) operating cost per hour amounts to **206** £/$hour$. As battery technology improves, the operating cost will go down as the cycle life improves and battery replacement is not necessary as often. Lithium ion battery purchase price is moreover also going down with time, as the technology becomes more common.

The current operating costs of Loodswezen are estimated using figures provided by Loodswezen itself. Loodswezen has calculated an operating cost of **255** £/$hour$ for their tenders, which comprises of fuel and maintenance. This means that the operating cost of PAMELA is 19% lower than that of a tender. Furthermore, the helicopter that Loodswezen uses on average once a day, has an operating cost of €9270 plus 2600 £/$hour$ variable cost. Pamela is therefore 98% cheaper if comparing operation for one hour a day. In practice not all operations not all operations of Loodswezen can be replaced by PAMELA, as not all ships will have an appropriate landing area. Therefore only the operations that do involve ships with a landing area have been taken into account for the calculations in this section. If one looks at the total operating costs of Loodswezen, and if one assumes that only the ships with a helipad can be serviced by PAMELA, the total costs are reduced by 4%. This calculation considers that 20% of ships have a helipad (as estimated by Loodswezen). The outcomes of the operating cost estimation have been tabulated in Table 3.1.

Table 3.1: Operating cost reduction

	Cost reduction
Tender	19%
Helicopter	98%
Total operating costs	4%

The conclusion of this operating cost analysis is that indeed PAMELA's operating cost is far lower than that of a tender and especially than that of a helicopter. The total operating costs reduction is limited by the amount of ships that have a heli pad. However, PAMELA has far less mass than a helicopter and is less than a third of the size (the helicopter used by Loodswezen is 14 m long), which means that a wider range of ships can probably be serviced. The analysis of the ships that enter European harbours is outside of the scope of this project and is therefore left for future consideration. As a last note, the operating cost reduction described in this section does not even include the cost cut as a consequence of the full autonomy of PAMELA. The reduce in paid workers needed is not taken into account here, as Loodswezen's operation cost calculations do not include boat driver salary.

Table 3.2: Product cost

	Cost [€]
Powertrain	34,500
Structure	18,900
Avionics	15,000
Total	**68,400**

3.7. Development Cost

The development cost has been split into four items: the software, the engineers, the prototyping and other. The estimation method for each item is described in this section and the final values are stated.

To estimate the **software development cost** of the flight software for PAMELA, the basic version of the Constructive Cost Model (COCOMO) has been used, developed by the Center for Software Engineering (CSE). The method consists of Equation 3.1.

$$E = a(KLOC)^b \tag{3.1}$$

The values of a and b depend on the complexity of the software. PAMELA's flight software will be relatively complex, will need engineers with specific (control) skills and needs a high reliability. The values of a and b for such a complex software are 3.6 and 1.2 respectively. With an estimated amount of kilo lines of code (KLOC) of 3,000, as for a US military drone software [28], the software development cost amounts to **€47,500**.

The next part of the development cost of the PAMELA project to be approximated is the **engineers' salary**. First the engineering cost of the current team, for the semi-detailed design phase (10 engineers in 10 weeks) is calculated. The average salary of an aerospace engineer is assumed to be 65 £/$hour$ [65]. Therefore the semi-detailed design costs (assuming an 8 hour day) €260,000 in salary. To finish the detailed design, an additional 300% FTEs is assumed to be needed, amounting to a total salary of **€1,040,000**.

The following development cost item to be considered is the **prototyping cost**. The production cost for the prototyping is assumed to be 125% of the estimated product cost, to account for unforeseen design faults. The prototyping cost then adds up to **€165,250**, if two full scale prototypes are built (including the risk that one would get damaged and a new one would have to be built). Prototype design hours are included in the aforementioned engineers' salary estimation.

Lastly the *other* development cost items that cannot be estimated accurately enough at this point, or fall outside of the DSE project scope are bundled, including the logistics costs. 10% is added to the total development cost number to account for these other costs. Finally another 10% is added to account for unforeseen costs and estimation errors, to obtain a total **development cost** number of **€1,516,000**.

3.8. Product cost

The product cost of PAMELA is the cost of producing one unit, including only material cost, off-the-shelf component cost and manufacturing cost. The estimation has been divided into three units: the powertrain (subsection 4.11.2), the structure (section 8.10) and the avionics (section 7.3). All results have been tabulated and summed in Table 3.2.

3.9. Return on Investment

The return on investment (RoI) of the PAMELA project indicates what percentage of the investments, needed to complete the project, will be returned after a certain timespan. The RoI follows from Equation 3.2, where *purchase price* is the market price that a unit is sold for, n is the number of units sold and *product cost* (see also section 3.8) is the cost of a unit (all parts, including manufacturing and assembly). *Development cost* consists the software development, the engineers' salary, the prototyping and other (see also section 3.7).

$$RoI = \frac{purchase\,price\,x\,n - (product\,cost\,x\,n + development\,cost)}{purchase\,price\,x\,n + development\,cost} \tag{3.2}$$

As all cost components for the RoI have been determined, the only two parameters remaining are the purchase price and the number of units sold. Firstly, the number of units sold is covered, which is based on the market in the Netherlands and a period of 10 years. Firstly, the port of Rotterdam is assumed to buy 5 units. 4 units are required to service the daily income of ships with a heli pad, and one is used for backup. This is based on the charging time of 3.5 hours and a daily income of 20 ships that are serviced by PAMELA. Secondly the port of Antwerp is assumed to buy 5 units as well - which is the second largest port of Europe and is also serviced by Loodswezen - if the operations in Rotterdam are successful. Afterwards the sales can be expanded to the other 14 most important seaports in the Netherlands. Assuming 10 of these ports buy one unit as a test model in the first 10 years after the launch of the first PAMELA vehicle, 20 units would be sold in the first 10 years.

Lastly the **purchase price** must be determined. For this, the purchase price of the current Loodswezen vehicles is taken as a reference. A JOL (small launch boat) is their cheapest vehicle, for short distances launched from the pilot ship at sea, and costs €280,000. The vehicle that performs similar operations to these of PAMELA is the tender, which is used to transport a pilot from land to an incoming ship. Its purchase price is €4,100,000. Taking these numbers into account and striving for a RoI of at least 5% in 10 years, a purchase price of **€150,000** is determined. For 20 units sold, this amounts to a RoI of **5.7%**. To relate these numbers, one must realize that this means that 20 PAMELA units are 73% of the purchase price of one tender. Another comparison can be made with the Ehang 184, which costs €200,000 - €300,000.

4 Powertrain

In this section the powertrain subsystem will be explained as detailed as possible for this design stage. What can already be seen is that it will be divided in five main pieces. These pieces being the power sizing method used, the rotor blade analysis, the motor & ESC selection, the battery and the battery management system.

4.1. Power Sizing Method

To start off with, the power sizing method is explained for both the hover at a load factor of 2.1 and the power needed for the speed range needed. In order to do the sizing, a few assumptions were made based on [25].

- Conditions in hover: no forward or vertical speed and axis-symmetrical flow field.
- Momentum theory applies the global balance of mass, momentum and energy.
- The method does not concern itself with flow details around rotor.
- The rotor is modelled as a disk, which adds momentum and energy to the flow.
- Flow is incompressible, steady, inviscid and irrotational.
- Flow is one-dimensional and uniform through the rotor disk.

- There is no swirl in the wake.

In order to comply to the 50% redundancy requirement, helicopter momentum theory for hover is used with a load factor of 2.1 and a MTOW of 360 kg (as in the CLASS I estimate). With this load factor, if half the motors fail, there would be still enough thrust to hover with a slight safety margin (LF = 1.05). Again, the formulas and image 4.1 is based on [25].

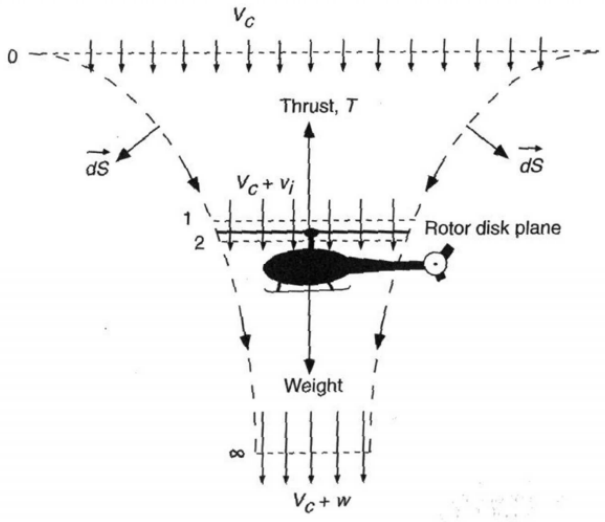

Figure 4.1: Momentum theory in hover [25]

The theory itself is based on the additional momentum given by the rotor to the airflow through the rotor disk area as can be seen in figure 4.1. This is done by adding induced speed to the flow (V_h), over the disk area. With this, a mathematical ideal power to hover can be calculated. However, in order to take real world circumstances into account, a figure of merit (FM) is used. Typically, a the figure of merit lays between 0.8 for optimal rotor designs and 0.6 for less optimal rotor designs [25]. For our contra-rotating propeller design, a FM of 0.7 will be assumed from here on. This is done because 0.8 is not conservative enough in the design stage and because 0.6 would potentially be over-designing (especially combined with the margins on the motor power and load factor).

$$V_h = \sqrt{\frac{T_{prop}}{2A\rho}} \tag{4.1}$$

$$P_{ideal} = T_{prop} V_h \tag{4.2}$$

$$P_{actual} = FM \cdot P_{ideal} \tag{4.3}$$

In equations 4.1,4.2 and 4.3, FM is the figure of merit, which is defined in 4.4. Furthermore, T_{prop} is the thrust given by a single rotor, and is defined as 4.5. Note that this means that the ideal and actual power needed are expressed per motor.

$$FM = \frac{\text{Ideal power required to hover}}{\text{Actual power required to hover}} \tag{4.4}$$

$$T_{prop} = \frac{\text{Class I weight} \cdot \text{load factor}}{\text{number of rotors}} \tag{4.5}$$

To complete this power sizing method section, a method for sizing the hover- and speed power requirements is needed. The formula used to calculate these, is worked out in [52] and can be seen in formula 4.9.

$$V_{horizontal} = \sqrt[4]{1 - 1/\mathrm{TR}^2}\sqrt{\frac{2mg}{\rho C_D A}} \cdot TR \tag{4.6}$$

In this formula, again a few assumptions were made. For the mass, the class I weight estimate (360 kg) will be used. Furthermore, all will be calculated at sea level and as a drag coefficient, the drag for a sphere with Reynolds number 10^6 will be used (0.3 [63]). For the top area (A), 10 m^2 was assumed, based on the expected structural layout of the vehicle including arms and rotors. TR is the thrust ratio, the amount of thrust with zero bank angle divided by the total amount of thrust with bank angle to hover.

4.2. Power Sizing Method Verification & Validation

First off a unit verification is done for equation 4.1 and 4.2. For equation 4.1 this gives the following:

$$m/s = \sqrt{\frac{N}{m^2 \cdot kg/m^3}} = \sqrt{\frac{Nm}{kg}} = \sqrt{\frac{m^2}{s^2}} = m/s \tag{4.7}$$

For equation 4.2 this gives:

$$J/s = \frac{N \cdot m}{s} = J/s \tag{4.8}$$

Doing a unit verification on equation 4.9 gives the following result:

$$m/s = \sqrt{\frac{kg \cdot m/s^2}{kg/m^3 \cdot m^2}} = \sqrt{\frac{m/s^2}{1/m}} = \sqrt{\frac{m^2}{s^2}} = m/s \tag{4.9}$$

In order to validate the power sizing method, data of similar designs is taken and compared to the mathematical results used in the power sizing method. This can be seen in tables 4.1 and 4.2. It should be noted that this validation was already performed in the previous report [10]. To give an impression of the comparable vehicle layouts, they can be seen in figures 4.2 and 4.3.

Figure 4.2: The Volocopter 2X [78].

Figure 4.3: The Ehang 184 [31].

Table 4.1: Validation based on the Volocopter 2X [74].

	D_{prop} **[m]**	$A_{prop}[m^2]$	V_h **[m/s]**	P_{ideal} **[W]**	**FM**	P_{actual} **[W]**	P_{total} **[W]**
Volocopter 2x real	1.8	2.54					39500
Volocopter 2x calc	1.8	2.54	6.27	1538.2	0.8	1922.75	34609
Difference							**-12.4 %**

The values of the above table are based on hover (LF = 1), a class I weight of 360 kg and a FM of 0.8 (assumed for single rotor configurations) for the multicopter concepts. A difference of -12.4% is seen between the calculations and the real Volocopter 2X. This is probably due to a wrong assumption on the figure of merit, which when lowered gives a decrease in percentage difference. For example at a FM of 0.7, the difference becomes 0.13%. Knowing that figure of merit for helicopter designs usually vary between 0.6 and 0.8, the 12% difference is considered small.

Table 4.2: Validation based on the Ehang 184.

	D_{prop} **[m]**	$A_{prop}[m^2]$	V_h **[m/s]**	P_{ideal} **[W]**	**FM**	P_{actual} **[W]**	P_{total} **[W]**
Ehang 184 real	1.6	2.01					152000
Ehang 184 calc	1.6	2.01	13.72	12717	0.7	18168	145343
Difference							**-4.38 %**

Concerning table 4.2, the data is based on the Ehang 184, which also claims to have a 50% redundancy. So for the Ehang also a load factor of 2.1 was assumed. The Ehang has a total motor peak output power of 152 kW. Using our power sizing method with a figure of merit of 0.7 (assumed for counter rotating propellers), a difference of -4.38% is observed. Which again is considered small.

4.3. Rotor Size Revision

In this section, the resizing of the rotors will be discussed. The resizing is done, in order to comply with the size restrictions and in accordance with the structures department. After discussing, it was decided that the rotor size could be reduced from 1.4 meter diameter to 1.3 meter diameter. The implications of this change will be described in this section.

In order to get a good oversight of what the size change imply, figures 4.4 and 4.5 are used. These figures are made using the described sizing methods from section 4.1 and a python script. The changes in total peak power needed and the changes for the power needed for hover and cruise flight, are then clearly listed in table 4.3.

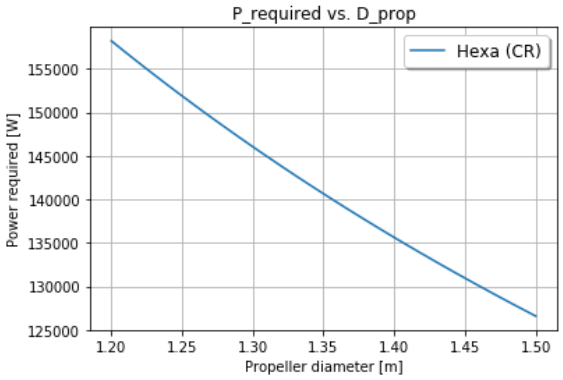

Figure 4.4: Rotor diameter and the total peak power needed for a 360 kg vehicle at load factor 2.1.

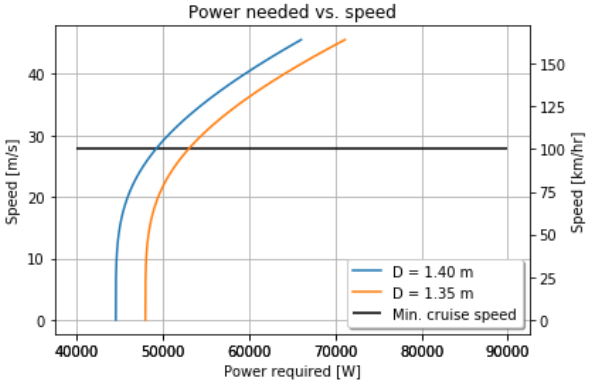

Figure 4.5: Hexacopter power needs for different speeds and different horizontal speeds.

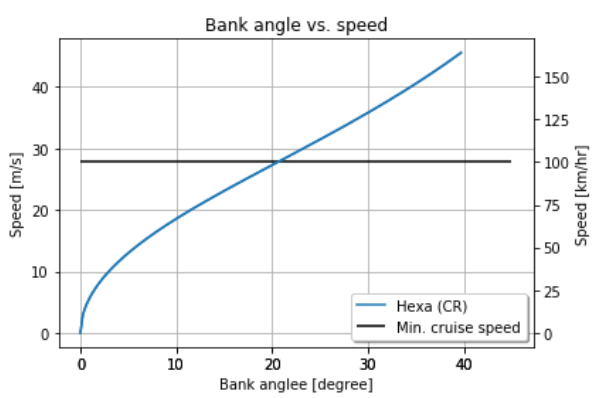

Figure 4.6: Horizontal speed and the matching bank angle.

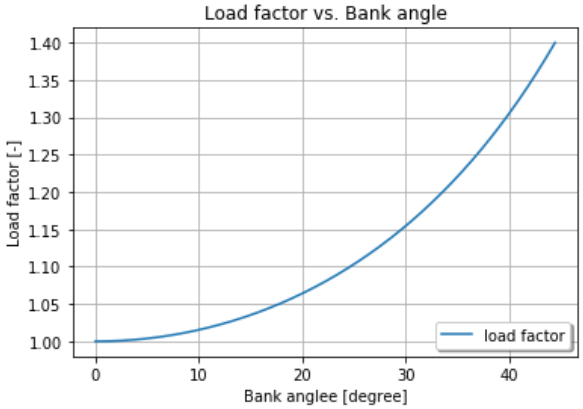

Figure 4.7: The vehicle bank angle and matching load factor.

It should be noted that for the plot involving speed, a few constants were assumed. For the top area, 10 m^2 was assumed and as a drag coefficient for the vehicle, 0.3 was assumed. Furthermore, the figure of merit was set to be 0.7. These values were argued in the previous report.

An overview of the most important changes can be seen in table 4.3.

Table 4.3: New power needs for the hexacopter with a 1.3 meter rotor diameter.

	Hexacopter 1.4 m	**Hexacopter 1.3 m**	**Diff. abs.**	**Diff. %**
P hover [kW]	44.6	48	3.4	7.6
P cruise [kW]	49.4	53.1	3.7	7.5
P peak [kW]	135.6	146.1	10.5	7.7

Since overall more power is needed for all flight modes, the mission endurance will go down. This implies that a larger battery will be needed for the same flight time if the 1.3 meter diameter is compared to the 1.4 meter diameter rotors. The conclusion of this section is, that despite the power needs being bigger, the change is considered still doable because of the relatively small percentage difference (considered within the achievable boundaries, subjectively).

4.4. Sensitivity Analysis

For the power sizing method, described in section 4.3, assumptions were made. These assumptions include the weight (based on the class I weight estimation), the top area effected by drag, the drag coefficient and the figure of merit of the rotor. In this section an analysis is done at the sensitivity of the power sizing method to these assumptions. An overview of the values of these assumptions can be seen in table 4.4.

Table 4.4: Assumed values in power sizing method

	Class I $[kg]$	A_{top} $[m^2]$	C_d [-]	**FM** [-]
Value	360	10	0.3	0.7

4.4.1. Sensitivity to weight changes

The sensitivity on weight changes is analysed by giving different weight inputs to the power sizing method. The influence of a 10 kg and 20 kg heavier and lighter weight than the class I weight estimate of 360 kg, can be seen in figures 4.8 and 4.9. All other parameters are kept the same.

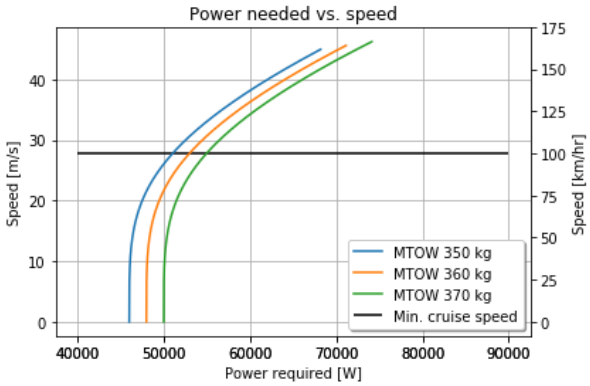

Figure 4.8: Sensitivity to a 10 kg weight change.

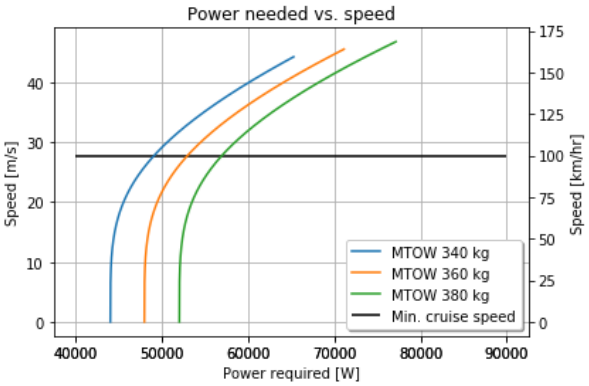

Figure 4.9: Sensitivity to a 20 kg weight change.

What can be seen is that changing weight, has a horizontal shifting effect on the speed vs. power curves. The horizontal shift appears to be linear and about 4 kW overall power needed for each 10 kg of mass difference at the hover condition. Considering that the total power available is 144 kW, 0.4 kW/kg has a medium impact on mission duration. It is advisable therefore to keep the weight under 380 kg.

4.4.2. Sensitivity to the top area effected by drag

The top area effected by drag is currently assumed to be 10 m^2. This is based on the top view of the layout sketch of the hexacopter seen in figure 8.1. The influence of a change in top area of 2 m^2 and 4 m^2 less can be seen in figures 4.10 and 4.11. It should be noted that 10 m^2 was a conservative estimate and this is not expected to increase.

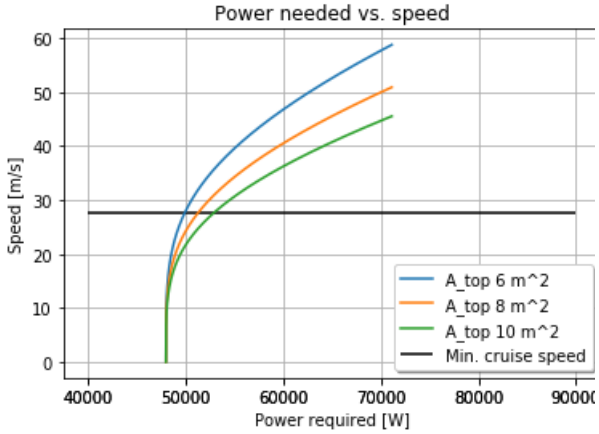

Figure 4.10: Sensitivity to a change in top area effected by drag for 2 m^2 and 4 m^2 less then 10 m^2.

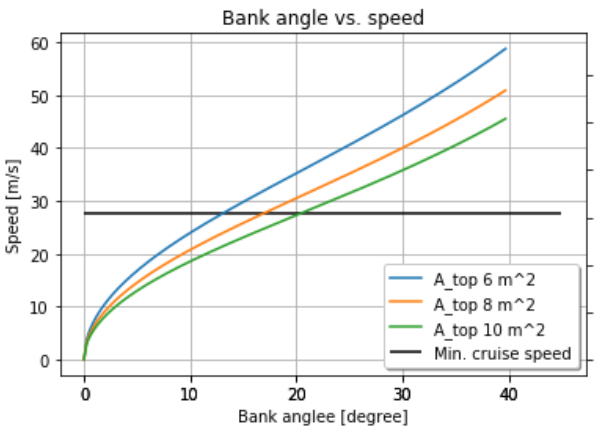

Figure 4.11: Sensitivity to a change in top area effected by drag for 2 m^2 and 4 m^2 less then 10 m^2 for the pitch angle.

The top area, as well as the drag coefficient, determine the maximum achievable speed as well as the power consumption for different speeds. Furthermore, the top area used, effect the bank angle needed to reach certain speeds. At cruise speed a decrease of 4 m^2 of the top area corresponds to approximately 3 kW overall less power needed. This is considered a small impact.

4.4.3. Sensitivity to the drag coefficient

The drag coefficient is currently assumed for a sphere at a Reynolds number of 1,000,000 according to [63]. In figures 4.12 and 4.13, the influence of a 0.05 and 0.1 increase and decrease in the drag coefficient can be seen.

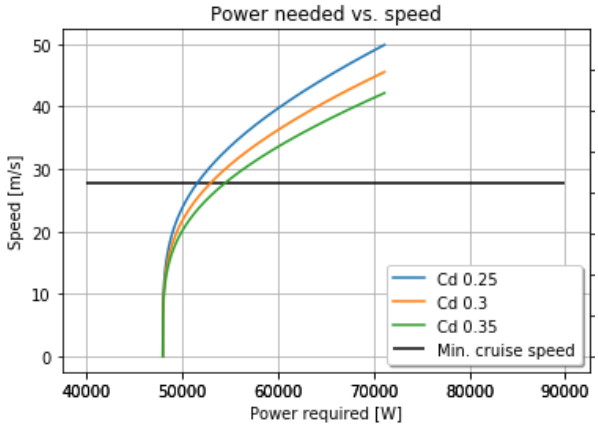

Figure 4.12: Sensitivity to a 0.05 C_d change.

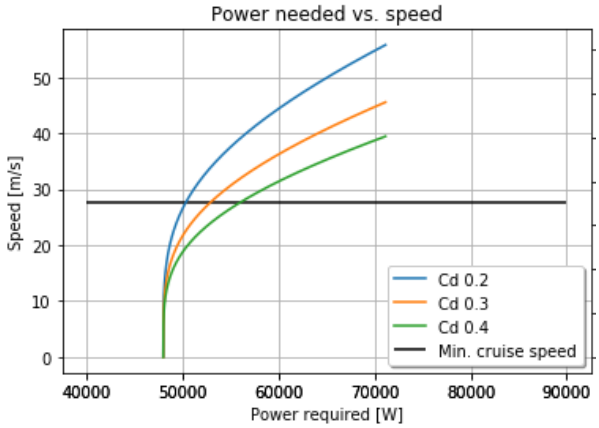

Figure 4.13: Sensitivity to a 0.1 C_d change.

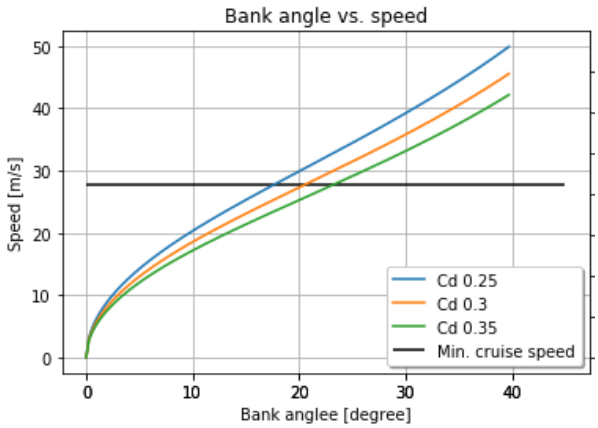

Figure 4.14: Sensitivity to a 0.05 Cd change on pitch angle.

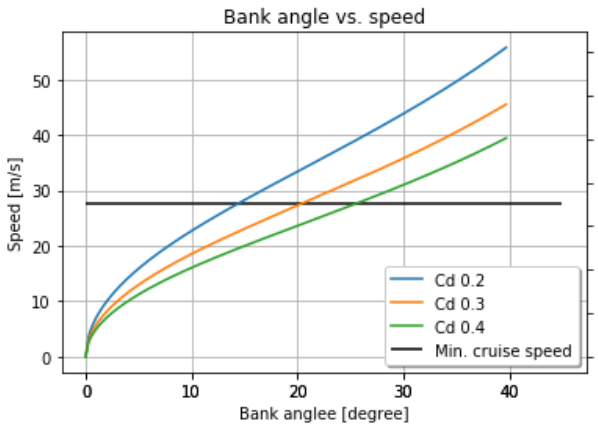

Figure 4.15: Sensitivity to a 0.1 Cd change on pitch angle.

The top area, as well as the drag coefficient, determine the maximum achievable speed as well as the power consumption for different speeds. Furthermore, the drag coefficient used, effect the bank angle needed to reach certain speeds. In figure 4.13, it can be seen that for a change in drag coefficient of 0.1, a change of approximately 4 kW of overall power consumption occurs at cruise speed. Drag coefficient thus, is considered of medium impact to the design.

4.4.4. Sensitivity of the figure of merit used for the rotor

The assumed figure of merit for the rotor design is 0.7. It is expected that this value can only become lower, thus an analysis will be made for a figure of merit 0.1 and 0.2 lower. This analysis can be seen in figure 4.16. According to equation 4.3 in section 4.1, the figure of merit directly impacts the actual power needed. This is also clearly reflected in figure 4.16. A change of 0.1 in the FM, bring an approximate 10 kW change in overall power needed with it. Figure of merit for the rotors, thus is considered of high impact to the design. It is therefore advised to strive to get an as high as possible rotor figure of merit.

4.4.5. Best case vs. worst case

To conclude this section, a best and worst case scenario are made. In the worst case, all values from above that have the worst impact are used (class I weight estimation = 380 kg, A_{top} = 10 m^2, C_d = 0.4 and FM = 0.5). For the best case all values positively impacting the power consumption were used (class I weight estimation= 340 kg, A_{top} = 6 m^2, C_d = 0.2 and FM = 0.7). Additionally, the current expected case is plotted.

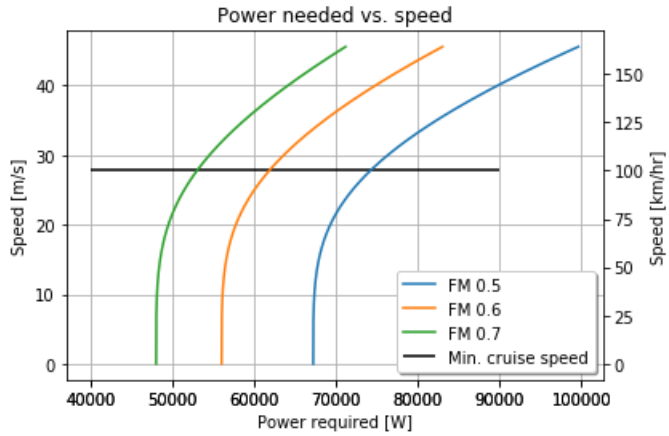

Figure 4.16: Sensitivity to a change in FM by 0.1 and 0.2 less then expected.

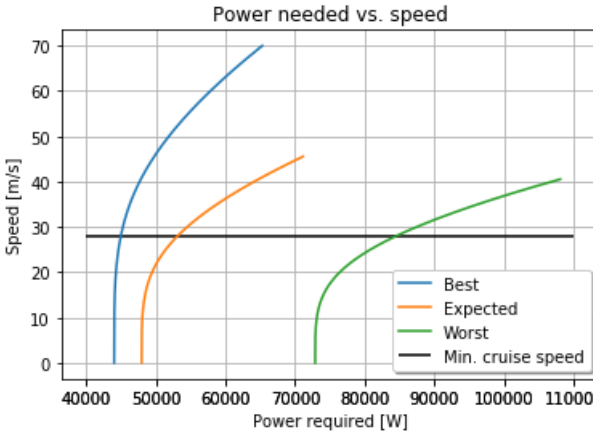

Figure 4.17: An analysis of the worst case scenario vs. the best case scenario with the expected case in the middle.

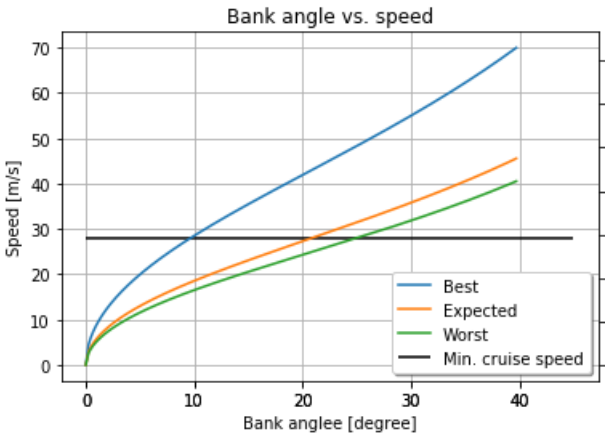

Figure 4.18: An analysis of the worst case scenario vs. the best case scenario with the expected case in the middle for the pitch angle.

It should be noted that there is more "space" to convert to the worst case. This is due to the rotor's figure of merit having the highest impact on the power consumption. However, it is considered very unlikely to end up with a figure of merit below 0.6. Even if this is the case, a rotor redesign might address this issue. Also from figure 4.18, it can be seen that even in the worst case, the overall pitch angle will not increase drastically.

4.5. Rotor Blade Design

As estimated in section 4.1, the thrust to be delivered by each rotor should be 2.1 times the thrust during hover, which leads to 618 N (by equation 4.5). This assumed that for a set of contra-rotating rotors, the thrust produced by one of the rotors is half the total thrust. Furthermore, this calculation was based on conditions during hover. This shall be the starting point for choosing the exact rotor blade geometry. A small note before: if it turns out that the lower rotor produces much lower thrust than the upper rotor, then the RPM of the lower rotor should be increased. This should be achievable since the power estimation took into account a load factor of 2.1, and it is thought that the decrease of thrust by any of the rotors should not reach half the predicted value. Moving on, the discussion in this chapter thus starts with an explanation of the design methodology of the rotor blades. This is accompanied by verification and validation procedures of the method. Once the method is known, the blade geometries are chosen to optimise the performance.

4.5.1. Rotor blade design method

Momentum theory is capable of a preliminary estimation of the rotor sizes, but does not take into account the blade geometry. For this, Blade Element Momentum (BEM) theory shall be used. This method couples blade element theory with momentum theory. The method used can be found in references such as in Ruijgrok ([70]) for aircraft propellers and Cunha lecture series ([23], [24], [25]) and helicopter rotors design. The main idea is the same. The main differences lie in the flight conditions. For example, if the helicopter rotors are designed for hovering conditions, the airspeed upstream of the rotor blades is essentially zero. Other differences are also present such as the definition of C_T and C_P. Therefore it is important to stick with one source for describing the design methodology. Because PAMELA is more similar to a helicopter, the definitions of some variables, as well as the nomenclatures to be used in this report, shall follow those presented in [23], [24] and [25], rather than [70].

First, blade element theory is considered. The blade is divided into a finite number of sections, for which each section has a certain aerodynamic property (which arises from the airfoil of that section). These are illustrated in the following figures:

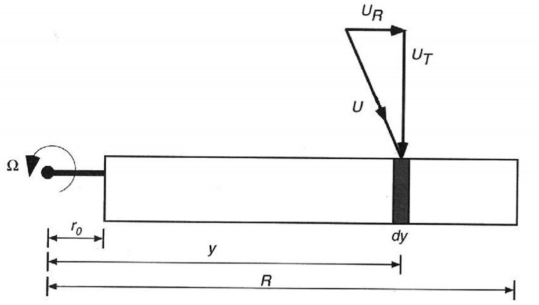

Figure 4.19: Division of the blade along the radial position [24].

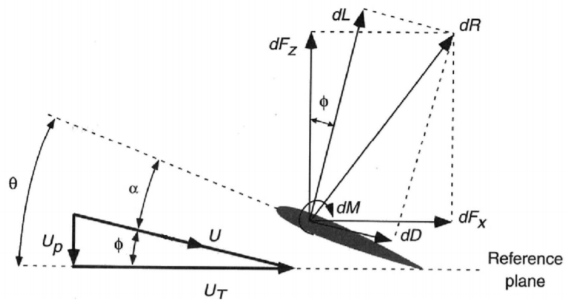

Figure 4.20: Cross-section of a blade section [24].

The total forces generated by one blade is assumed to be equal to the sum of the forces produced by each blade section. For this, an assumption that there is no radial force generated is thus made. Thus, this already puts some question regarding the optimization for rotor design under wind condition. Thus, there will have to be some overestimation of rotor performance to counter-act such conditions. Moving on, it is known that forces acting on airfoils are typically expressed in lift and drag; which, by definition, are forces perpendicular and parallel to the relative airspeed U. For a rotor design, it is more convenient to express the aerodynamic forces to be perpendicular and parallel to the plane of rotation (i.e. the thrust and some torque per unit length). Furthermore, it is more interesting to calculate the power, which is required to rotate the blade i.e. to overcome the torque:

$$P = \Omega Q \tag{4.10}$$

From definitions of lift and drag and the geometry in figure 4.20, for N_b rotor blades, the thrust generated by the blade section, as well as the power required to rotate a blade section, are given by:

$$dT = N_b \frac{1}{2} \rho U^2 c (C_l \cos(\phi) - C_d \sin(\phi)) dy \tag{4.11}$$

$$dP = N_b \frac{1}{2} \rho U^2 c \Omega y (C_l \sin(\phi) + C_d \cos(\phi)) dy \tag{4.12}$$

In addition to this, we look back to figure 4.20 and notice that ϕ is given by:

$$\phi = \arctan(\frac{U_P}{U_T}) \tag{4.13}$$

It is known that the out-of-plane velocity is the sum of the freestream velocity V_c (which depends on the velocity of the vehicle) and some induced velocity v_i, that arises from the necessity of the rotor, to generate thrust (as this is done by accelerating the upstream air). Additionally, the tangential velocity U_T depends on the rotation speed of the rotor Ω and varies linearly along the radial position. Mathematically, these are given by the following expressions:

$$U_P = V_c + v_i \tag{4.14}$$

$$U_T = \Omega y \tag{4.15}$$

Therefore, equation 4.13 can be written as:

$$\phi = \arctan(\frac{V_c + v_i}{\Omega y}) \tag{4.16}$$

and knowing the velocity components, the relative airspeed seen by the airfoil is given by:

$$U = \sqrt{U_P^2 + U_T^2} \tag{4.17}$$

To finalize the design, the blade angle θ is geometrically related to ϕ and the blade section's angle of attack α by:

$$\theta = \alpha + \phi \tag{4.18}$$

To complete the system of equations, v_i is still to be determined. This can be solved by the momentum theory. The exact derivation is not of particular design interest and thus will not be stated here. This can be found in either [70] or [25]. Nevertheless, the result is used for the design. The theory states that half of the total increase velocity occurs at the rotor i.e. the velocity far downstream the rotor is twice of v_i. This result is useful in coming up with another expression of the thrust generated by the disk swept by the rotor blades, or in particular, the blade element. This disk is illustrated in the following figure:

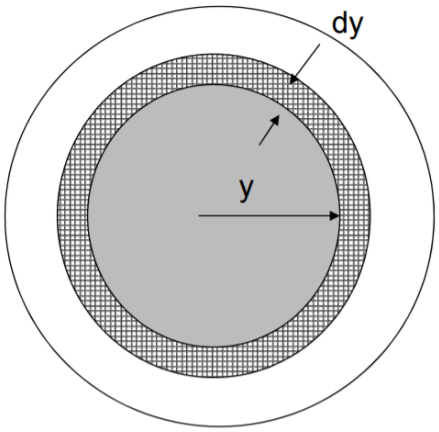

Figure 4.21: Disk annulus [23].

From Newton's second law, the thrust generated is the product of the mass flow with the annulus and the downstream velocity. Therefore, with information regarding geometry (to find the mass flow) as given in figure 4.21, the thrust of a blade section is given by:

$$dT = 4\pi\rho(V_c + v_i)v_i y dy \tag{4.19}$$

To note is that the thrust in equation 4.19 is the thrust generated by *all* blades. Furthermore, for hovering, $V_c = 0$. This is true for all the preceding equations as well. With this, the BEM theory is complete. Before moving on, it is useful to collect the assumptions used in the theory, which will be used in future discussions such as the validity of the design. These are given in the following list:

1. No radial force.
2. Quasi 1D flow.
3. Irrotational flow.
4. Incompressible flow along the slipstream of the propeller.
5. No swirl.
6. Uniform inflow.
7. No tip losses.

Tip-loss correction
As stated in the aforementioned list of assumptions, BEM theory does not account for three dimensional effects and is of a two dimensional nature. This leads to a discrepancy between the calculated data and reality and needs to be corrected for. The three dimensional effects that are not accounted for are related to variations in the wind velocity, blade tip and root vortices, centrifugal forces in the blade's boundary layer and bending of the blades out of the rotor plane.
To correct for these three dimensional effects, the Prandtl tip- and root loss correction factor is used during the BEM analysis. Glauert's approximation of the Prandtl tip- and rootloss function is usually expressed as equation 4.20 [18].

$$F = \frac{2}{\pi}\cos^{-1}\left[exp\left(-\frac{N_b(R-r)}{2r\sin\phi}\right)\right] \tag{4.20}$$

with r being the non-dimensional radial position:

$$r = \frac{y}{R} \tag{4.21}$$

This is a correction to the induced velocity, which is then related to the thrust. Therefore, this correction factor is multiplied into equation 4.11.

Now that the necessary equations have been specified, next is to implement the design. This is discussed in the next section.

4.5.2. Code description and verfication

In essence, the set of equations to be solved are equation 4.11, 4.12, 4.16, 4.17, 4.18 and 4.19. The problem is tackled with a code written in Python. To solve this system of equation, first an initial guess of radial distribution of v_i is made. In conjunction to this, the tangential velocities (U_T) at each section can be calculated by using equation 4.15 with an input RPM. With this, the magnitude as well as the orientation of the air velocity vector (i.e.U and ϕ) is calculated using equation 4.17 and 4.16 respectively. Knowing the required α at each section and ϕ, the sectional blade pitch θ can be calculated. This is one of the outputs of the Python code. The Prandtl's correction factor is calculated after knowing ϕ. Therefore, the thrust at each section can be calculated using equation 4.11 and 4.20. The airfoil, as well as the chord distribution, are set as inputs. Knowing the thrust, the induced velocity can be recalculated using the result of the momentum theory i.e. equation 4.19. If this induced velocity is not sufficiently close to the initially guessed induced velocity, a next iteration is done using the most-recently calculated induced velocity as the next guess. Otherwise, the code has converged, the thrust and power at each section can be finalized. The thrust and power at each section for all blades are summed to get the total thrust and power; which comprise the other outputs of the program. With this, the code is complete. A schematic of the code is given in the following flow chart:

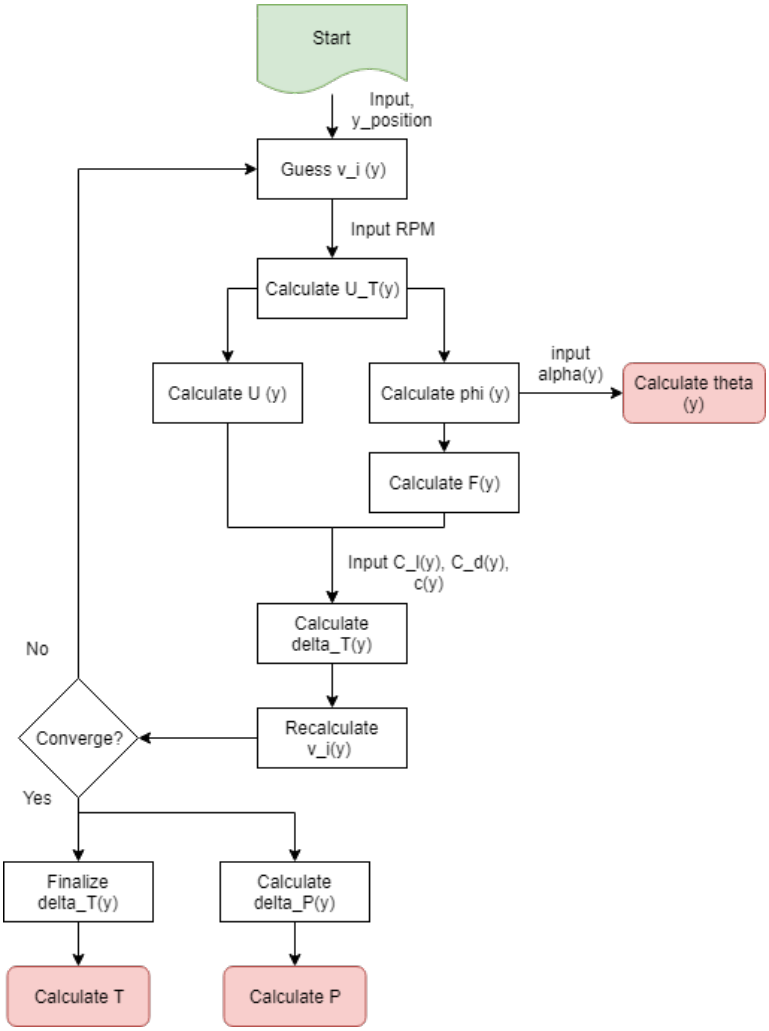

Figure 4.22: Code flowchart of the rotor blade design.

Note: MT stands for momentum theory. The non-geometrical aspect input that was used is the RPM. This input is varied until the designed thrust and power are met. Evidently the RPM to reach these performance parameters are determined.

As per usual, the code would have to be verified before being used. The verification procedure consists of unit tests and system test. The unit tests are simply checking each box of the flowchart, whether or not the equations used are in conformity with those laid out in section 4.5.1. This is done manually.

As for the system test, the flow of the code (i.e. the arrows in the flowchart) is checked. The essence is to set the inputs to zero and see whether or not the outputs are as expected. Changing v_i would not affect anything since theoretically v_i should converge to the correct value. So the verification starts with the flows after the initially guessed v_i. The RPM is set to zero. U_T is therefore observed to be zero, and U is observed to be equal to v_i. Normally setting the RPM to zero sets ϕ to be equal to some multiplies of $\pi/2$. However, Python firstly evaluates the argument in the arctan function, which, when something is divided by zero, gives an error. This is what is observed. In addition, calculating F also gives an error and therefore the parameters downstream the code no longer becomes of interest.

Another input is alpha along the radial length of the blade. Setting alpha to zero equates θ to ϕ. The other inputs are the aerodynamic properties of the airfoil, C_l and C_d. Setting just the C_d to zero increases the value of output thrust and decreases power. This is evident by checking equation 4.11 and 4.12. Setting the C_l to zero actually sets the thrust required to zero; when all iterations are completed. This seems to be because of a consecutive decrease of predictions of v_i, from one iteration to the next. The value of

thrust by BET is so low, such that v_i is under-predicted by MT. Consequently, this leads to zero thrust as convergence is achieved. Finally, setting the chord to zero gives the trivial result of zero thrust and power. With this, the verification is completed.

4.5.3. Method validation

This subsection describes briefly the procedure validation of the method/code. To do this, the thrust calculated by the code is to be compared to experimental results of a certain rotor. For example, such results may be obtained through force balance measurements. Note that to the flow condition should be in static case, because the code written is only compatible with hovering conditions.

Because reliable experimental data is not currently available, only discussions on how some of the assumptions used in the underlying theory shall be described. This would attempt to answer the assumptions used in both blade element and momentum theory. First, consider the incompressible flow assumption. It is thought that this assumption should not create a large error of the simulation, since the maximum Mach number, that the designed blade experiences, is about 0.4 (which is at the tip), which is slightly above 0.3 (which is the typical upper limit that is used to assume incompressible flow). Nevertheless, if such effect were to be seen, it would decrease the thrust since the density (and therefore mass flow) would be lower. Next, consider the irrotational flow assumption. This is perhaps, though not necessarily, more related to the viscous effect of the flow, since inviscid flow may or may not be rotational, but all viscous flows are rotational. The relatively low Reynolds number implies that viscous effect may be more relevant and therefore viscous losses at the rotor need to have extra attention. Finally, the quasi 1D flow needs to be checked. If there are some velocity that is in the rotation plane at the disk, the relative velocity seen by the airfoil would be lower. This would decrease the thrust. This is perhaps in conjunction with the assumption of independent contribution of the blade section to the thrust; since then the relative airspeed "faces" a different section than the airfoil section as described in figure 4.20 and might also produce lower thrust. All in all, the assumptions lead to the overestimation of the generated thrust by the code. Therefore, the validation procedure would primarily look at how much the thrust is overestimated.

4.5.4. Rotor blade geometry

Now that the code implementing the method has been verified and validated, the design of the rotor blade may continue. As discussed before, the geometry of the rotor blades are inherent in the system of equations. The relevant variables are restated below:

$$C_l = C_l(y)$$
$$C_d = C_d(y)$$
$$\theta = \theta(y)$$
$$c = c(y)$$

An analysis of deriving an expression for efficiency (i.e. some available/ideal power versus power consumption) shows that the power required is the least when the airfoil is generating its optimum lift-to-drag ratio. This is true for both aircraft (leading to the so-called propulsive efficiency [70]) and helicopters ([24], leading to the so-called Figure of Merit which, for the multicopter design discussed in section 4.1). This is logical since a high C_l is desirable for producing a higher thrust, and a lower C_d is beneficial to reduce the power necessary to rotate the blade, since the blade generates lower drag. There are two things that can be concluded from this result. Firstly, an airfoil should be selected that has as a high lift-to-drag ratio as possible; ideally at all blade sections. Secondly, choose the twist such that the blade section sees the angle of attack at the optimum lift-to-drag ratio. Concerning the first point, [70] suggested to choose airfoils from the Hamilton Standard series. The aerodynamic properties of these airfoils are compared. These are calculated through XFOIL, and the results of interest for Reynolds number of 10^6 and Mach number of 0.40 (corresponding to the flow condition at the tip) are given in the following table:

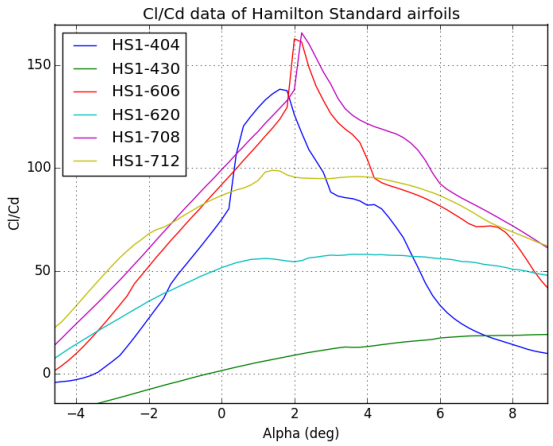

Figure 4.23: Lift-to-drag ratio for Hamilton Standard airfoils at $Re = 10^6$ and $M = 0.40$.

As can be seen, HS1-708 is the best performing airfoil in terms of optimum lift-to-drag ratio and thus is the airfoil that we seek to use. Since the angle of attack at the maximum lift-to-drag ratio is known, this also allows for the specification of the twist distribution (using equation 4.18), given the rotation rate and the blade radius.

At this point, the exact radial variation of the aerodynamic property of HS1-708 needs to be determined. This is because the tangential velocity (U_T) varies along the radius and therefore the Reynolds number, as well as the Mach number, also varies. A number of points along y is therefore chosen. The Reynolds and Mach number at those points are calculated and the airfoil properties are determined; again through XFOIL. Knowing the airfoil properties at these points, a second-degree polynomial interpolation is done through Microsoft Excel. The equations for the interpolation of each variable, as well as the R^2 value, are presented in the following figures.

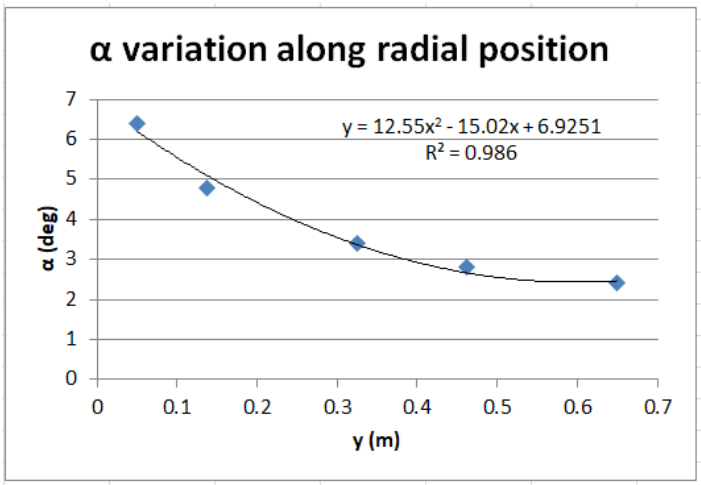

Figure 4.24: Optimum $\alpha(y)$.

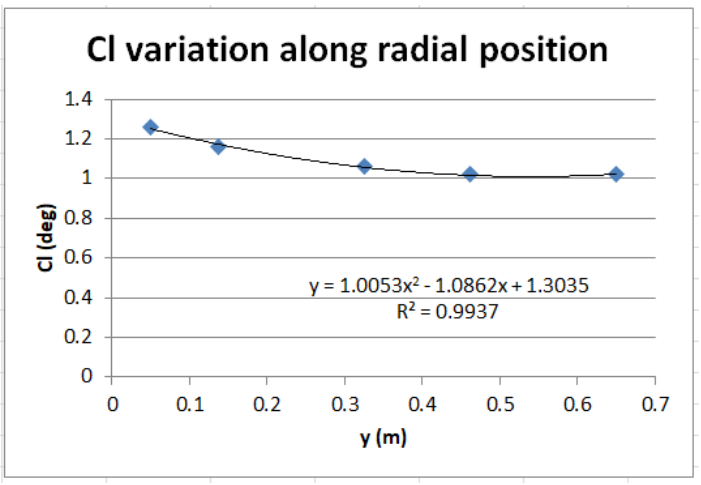

Figure 4.25: Optimum $C_l(y)$.

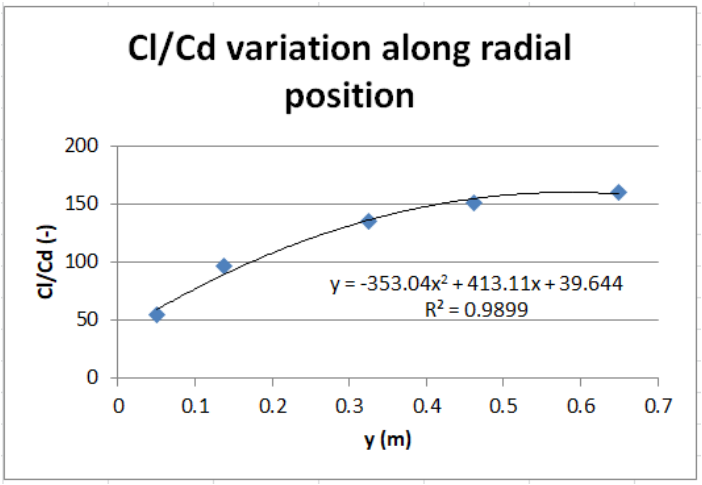

Figure 4.26: Optimum $\frac{C_l}{C_d}(y)$.

Note that the drag coefficient is obtained with the lift coefficient and the lift-to-drag ratio. All-in-all, with the aforementioned information, $C_l(y)$, $C_d(y)$, $\theta(y)$ are thus specified.

The final geometrical definition to be specified is the chord distribution. For this, a so-called rotor solidity (σ) is used:

$$\sigma = \frac{Bladearea}{Rotorarea} \tag{4.22}$$

where typical values range from 0.07 to 0.12 [24]. A high solidity leads to a higher power consumption, since the blade generates a higher drag (higher surface area submerged in the airflow). However, too low solidity might mean that the blade requires a higher amount of RPM in order to generate the required thrust (as can be seen through equation 4.11, 4.15 and 4.17). Furthermore, perhaps it is undesirable to have too low of a solidity since then the load-bearing capability of the blade might be compromised. Hence, an average value of $\sigma = 0.095$ is taken. Next is to finalise the chord distribution.

The method used here, for the chosen given solidity, finds the effect of tapering on the required RPM to rotate the blade. The solution to this is not straight forward since firstly, the thrust generated by rotor mostly comes from the outer part of the blade (see equation 4.11, since U is highest near the tip). However, this part also generates the most drag and therefore creates the biggest increase of required power (equation 4.12). Therefore, this is something to be investigated.

For a tapered blade with a certain taper ratio λ, the solidity is given by:

$$\sigma = \frac{N_b C_r (1+\lambda)}{2\pi R} \tag{4.23}$$

where C_r is the chord length at the root. Solving for C_r would then give:

$$C_r = 2\frac{\sigma\pi R}{N_b(1+\lambda)} \tag{4.24}$$

The value of λ is varied from 0.7 to 1.0, with steps of 0.05. C_r is then calculated using equation 4.24. Knowing C_r and λ specifies the chord distribution. As mentioned before, the other geometrical specifications are known and therefore the BEMT code is used to find the necessary RPM to rotate the blade. The result is given in the following figure:

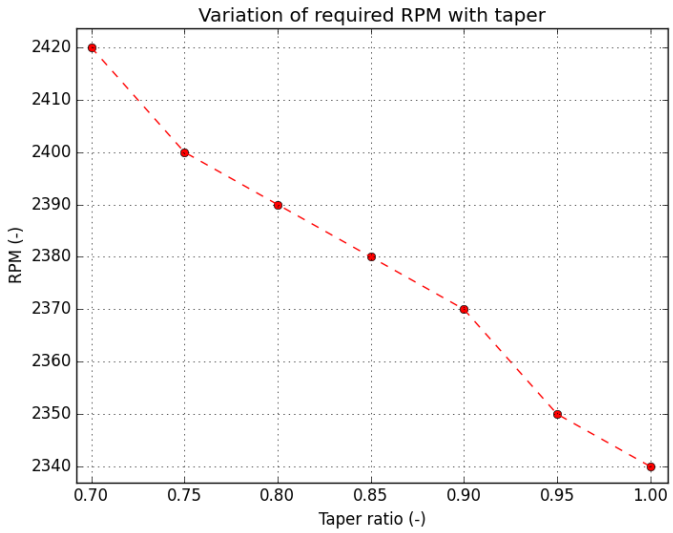

Figure 4.27: Comparison of required RPM with tapering.

It turns out that, with the theory used, a rectangular blade ($\lambda = 1.0$) seems to be the most efficient (requires the least RPM) to rotate. Hence the chord to be chosen is a constant with a value of 0.097 m.

With this, all the necessary inputs for the code have been found. The blade pitch distribution is calculated and given in figure 4.28.

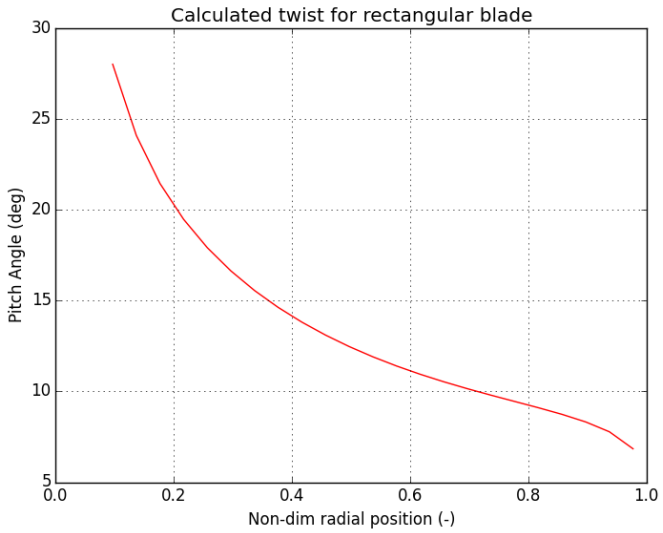

Figure 4.28: Blade pitch distribution of the final blade.

An impression of the blade is made using QBlade v0.963. This is given in figure 4.29 and 4.30.

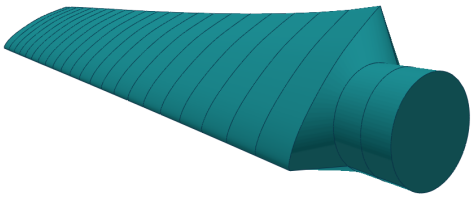

Figure 4.29: Root perspective of the designed rotor blade.

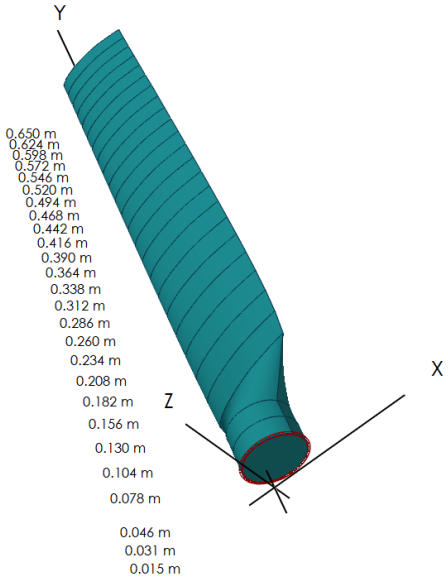

Figure 4.30: Perspective of the designed rotor blade with blade section coordinates.

Finally, it is convenient to define some non-dimensional parameters to specify the rotor blade performance characteristics. These are the thrust and power coefficient, to be defined following the convention in Cunha [25] as:

$$C_T = \frac{T}{\rho\pi\Omega^2 R^4} \tag{4.25}$$

$$C_P = \frac{P}{\rho\pi\Omega^3 R^5} \tag{4.26}$$

Note that C_P is actually equal to the non-dimensional torque coefficient (see [25] for proof). Another parameter that is of interest is the actual Figure of Merit, FM (this parameter was initially estimated in section 4.1 to be 0.7; the general definition given in equation 4.4). For a single rotor in hovering conditions, this is calculated with [25]:

$$FM = \frac{C_T^{3/2}}{\sqrt{2}C_P} \tag{4.27}$$

Data of interest for the designed rotor is given in the following table.

Table 4.5: Designed rotor characteristics.

	Value	**Unit**
C_T	0.0139	-
C_P	0.00148	-
FM	0.78	-
Rotation rate to produce 309 N of thrust	1716	RPM
Power required to produce 309 N of thrust	3.82	kW
Enclosed volume	2.98×10^{-4}	m^3

Note that 309 N of thrust is half the target thrust which was specified at the beginning of section 4.5. This is an initial operational estimate of the thrust during hovering. As can be seen table 4.5, the total power

required (i.e. for 12 rotors) for the thrust would then be 45.9 kW, which is lower than previously estimated (which was given to be 48 kW in table 4.3). The power generation subsystem shall nevertheless adopt to the previously estimated value to be conservative.

As a final reminder, this thrust corresponds to a given mass. At later stages of the design, the mass will most certainly change. The required RPM and power to hover would also then change. Knowing the newly required thrust, these can be calculated easily with equation 4.25 and 4.26. Thus the value of presented in table 4.5 simply serves as an example calculation.

4.6. Motor & ESC Selection

Now that a revision of the rotor diameter has been done and the new power needs are known, a specific motor and ESC selection can be made. First off, the motor can be selected based on table 4.3. After the motor is selected, a fitting ESC can be found for it based on the nominal motor voltage and amperage needed to provide the power.

4.6.1. Motor selection

As has been determined in section 4.7, the peak power needed for a 360 kg hexacopter at a load factor of 2.1 is approximately 146 kW and divided by 12 motors this comes down to 12 kW per engine. The selection of a motor for the hexacopter, based on these values has already been done, as described in the Midterm Report [10]. By looking at off-the-shelf motors that suit PAMELA's needs and have a proven track record, the Hacker Q-150 (see Figure 4.31) - made by the German business Hacker Industrial Solutions - is the obvious choice. This Hacker motor has been developed for the Volocopter, a German tried and tested PAM vehicle for two passengers, with 18 Hacker Q-150 motors and a range of 27 km [77]. No competitors are available, except for some Chinese manufactured units that do not have reliable references, and therefore no detailed comparison has been made.

The Hacker Q-150 is a brushless direct current (BLDC) outrunner motor, where *outrunner* means that the permanent magnets rotate around the stator coils. Outrunner motors inherently produce more torque than their inrunner counterparts, which makes them lighter and therefore the obvious choice for aerospace applications.

The sensitivity of the RPM of the motor due to a certain voltage applied is determined by the Kv value. A Kv of 1 means that the RPM will be 1, when 1 Volt is applied when no load is attached to the motor. Based on this, an optimum Kv value has to be selected to suit our rotor RPM range. The Kv value of the motors can easily be customized by the manufacturer, by adjusting the amount of windings. Unfortunately, contact with the manufacturer has been difficult, and the data sheet and specifications that were promised by the manufacturer have not arrived before the deadline of this final report.

Figure 4.31: Hacker Q-150 motor [40]

4.6.2. ESC selection

With the Hacker Motor GmbH Q-150, comes a recommended ESC. This ESC is the Hacker Motor HST-350 Sensored Motor Controller. This makes the selection of the ESC straightforward and after looking at its

capabilities (capable of powers up to 20 kW [41]), this ESC is chosen.

In this section a brief explanation of its capabilities and system input/outputs is given. These are all based on the HST-350 manual that is provided by Hacker Motor and goes into great detail about its setup [39]. The dimensions of the HST-350 can be seen in figure 4.32.

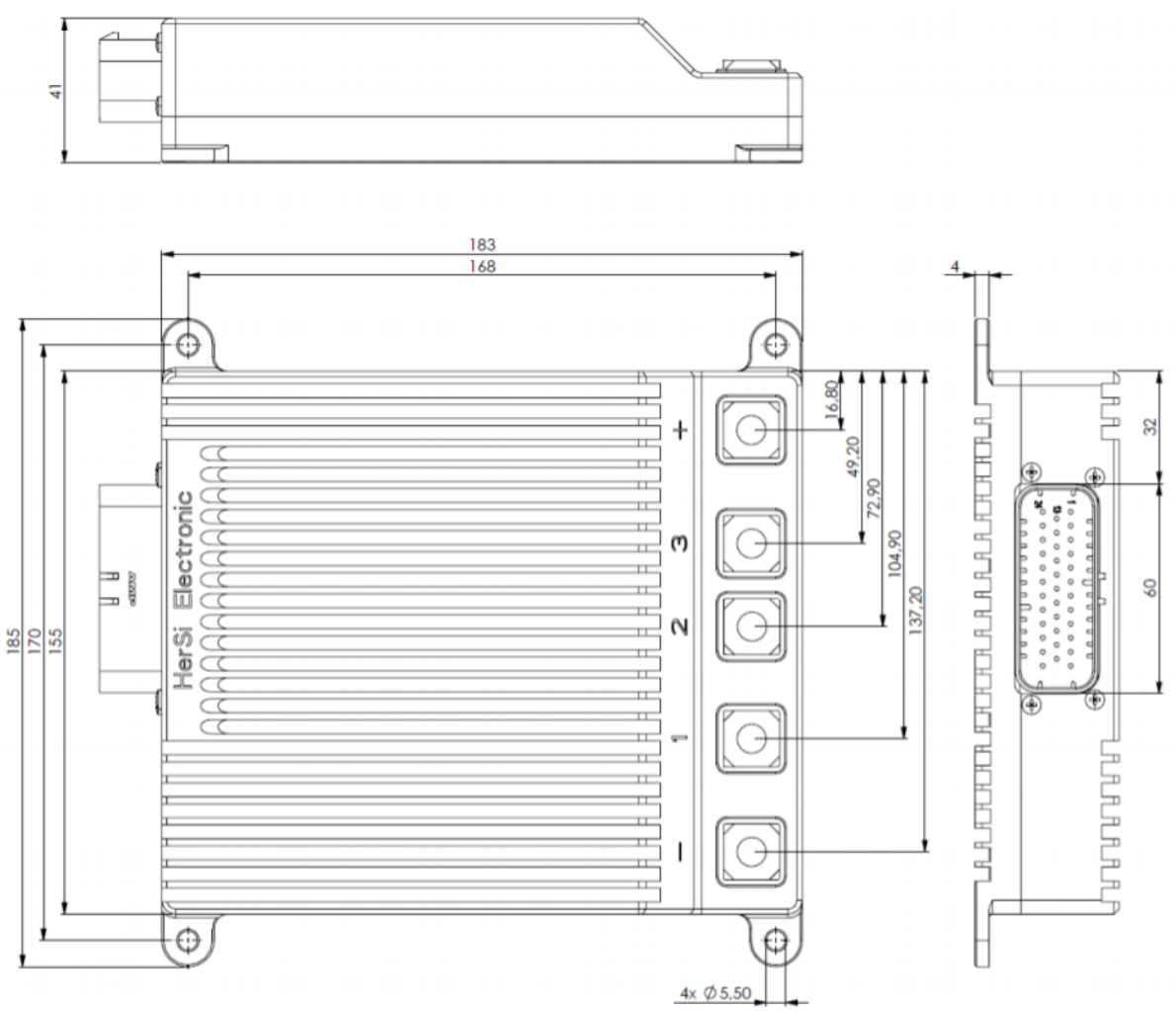

Figure 4.32: Hacker HST-350 dimensions [39]

To begin with the general layout of a HST-350 setup combined with the Q150 ,is given in figure 4.33, taken from [39]. Since the Hacker Motor Q-150 has the HST-350 recommended, in the HST-350 manual, the example setup is made with this motor. Each Q-150 motor needs its own ESC to be controlled, it is not possible to control multiple motors wit a single ESC.

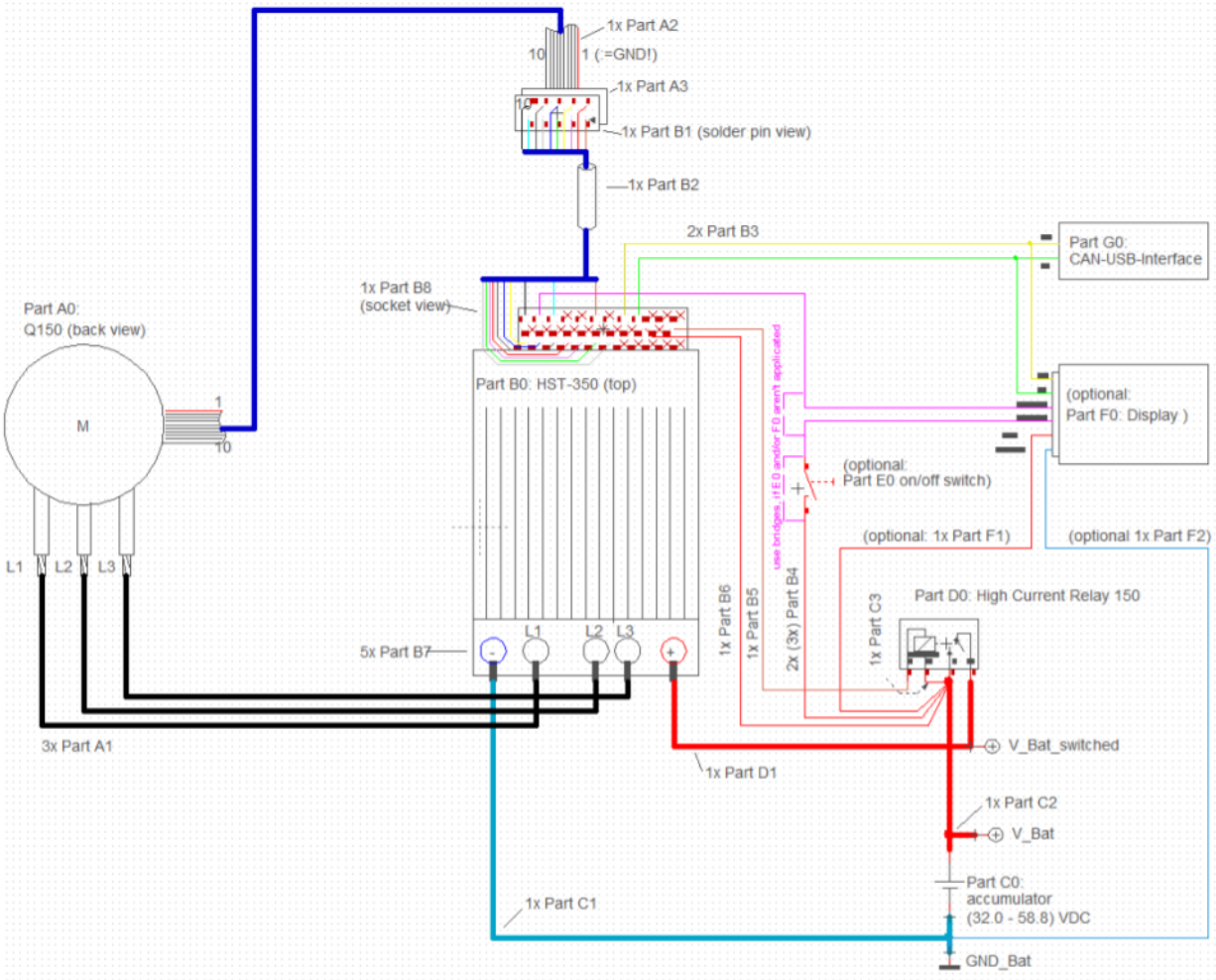

Figure 4.33: Hacker HST-350 layout [39]

At first sight the schematic layout may seem a bit complex, but after a better look a few general observations can be made. To start, cables C1, C2 and D1 connect the battery to the ESC and provide the ESC with an input voltage and amperage which will be discussed further down in this section. Further, since the Q-150 is a three phase BLDC motor, three phase cables (A1) connect to the motor. These cables provide a motor input voltage and amperage, also discussed further down this section. In general, for the cables described up to this point, it can be said that since the amperage is going to be high (in the order 100-200 amps), they are going to be thick and heavy cables. These cables should therefore be as short as possible. The next cables to be discussed are cables A2 and B2, which are 10 pole data cables. These cables carry feedback data from the Q-150 motor. A detailed overlook of this data and its connection ports is given in [39]. The final part relevant to discuss are cables B3 and part G0, which are the CAN data interfaces. CAN or Controller Area Network is a serial communication protocol. In short, CAN allows, depending on the protocol used, between 127 and 253 unique nodes to communicate reliably within the vehicle system. More literature on CAN is readily available online, since it is a widely used protocol that is ISO (The International Organization for Standardization) defined.

The maximum rated power (P_{peak}) of the Hacker Q-150 is 12 kW. This means that this power is provided by the battery and passes through the ESC on to the motor. The ESC is the unit needed to feed this power to the motor, depending on what is required. For this reason, it is very important that the ESC and its wiring is rated for the voltage and amperage used during peak power conditions. If the wiring or ESC cannot handle the amperage used by the motor, they will simply burn through in case of wiring or burn the fuse on the

ESC.

4.6.3. Cable selection

The power requirements placed on the engine in combination with the typical operating voltage (45-60V), makes that the current will be high. The power required to hover for the vehicle, is estimated to be 48 kW. This makes the power to hover during nominal flight conditions (twelve motors operating), approximately 4 kW per motor. However, with the 50 % redundancy requirement, a hover should still be possible with only half the engines operating. Meaning that, in that case, each engine needs to a power output of 8 kW. Combining this power output with the expected motor voltage of 45-60V, this means that an amperage of up to 180 A is possible.

Now that an upper bound of the amperage is know, a high power cable can be chosen. To start choosing a suitable cable, the corresponding area needed for a copper and an aluminium cable are calculated. These calculations are done using a sizing calculator [14]. The results for copper and aluminium can be seen in figures 4.34 and 4.35 respectively. Note that a safety margin of 20 A is taken, so the cables will be sized to handle up to 200 A.

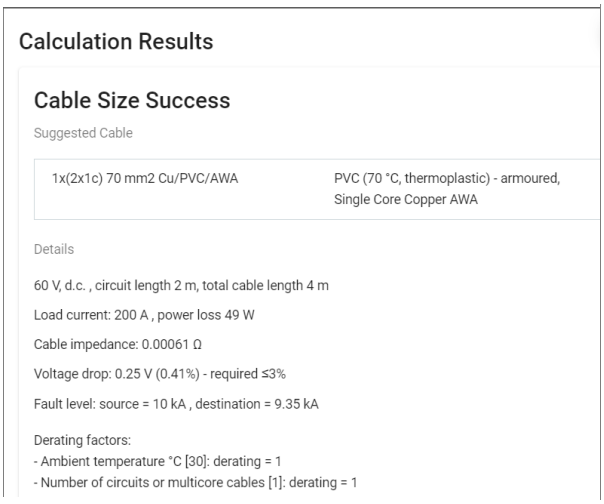

Figure 4.34: Copper cable thickness needed according to [14]

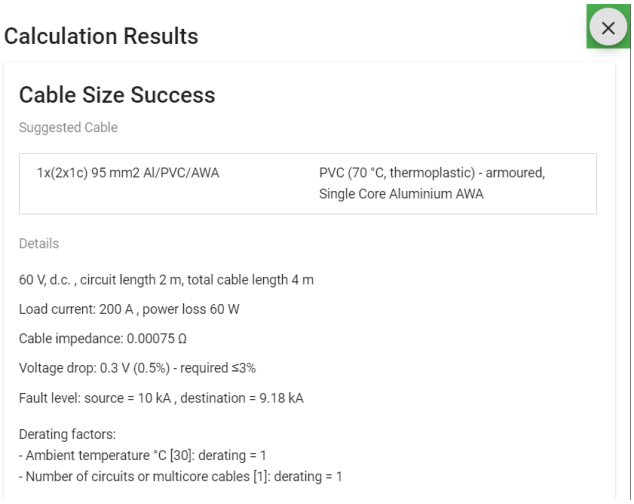

Figure 4.35: Aluminium cable thickness needed according to [14]

The wire thicknesses needed for a copper cable are thus 70 mm^2 and for aluminium; 95 mm^2. The aluminium thickness is larger, as can be expected due to the lower conductivity of aluminium.

Next thing to do, is to get an idea of the total cable length needed in the vehicle. From the ESC to the motor, three of these high current wires run. From the battery to the ESC, two high current wires run. This can be seen in equation 4.28. Note that this is an approximation.

$$(3 * 1.5m + 2 * 0.5m) * 12 = 66m \tag{4.28}$$

Now that the cable thickness and length needed is known, a cable can be chosen. The criteria for cable selection now comes down to weight. The lightest cable will be selected. Looking at commercial websites [45], the copper cable (named High Flex) will weigh 0.780 kg/m and the aluminium cable will weigh 0.444 kg/m. Therefore the Aluminium cable is selected. The total cable weight would then be 29.3 kg.

4.7. Final Power Revision

During the making of this report, more detail about the assumed values mentioned in table 4.4 in the section 4.4. The updated table based on the previously mentioned one, can be seen in table 4.4. This then gives figure 4.36 and table 4.7, where the final power requirements expected for PAMELA are given.

Table 4.6: Assumed values and updated values in power sizing method

	Weight [kg]	**Atop [m^2]**	**Cd [-]**	**FM [-]**
Value	360	10	0.3	0.7
Value	418	10	0.3	0.78 (as from section 4.5)

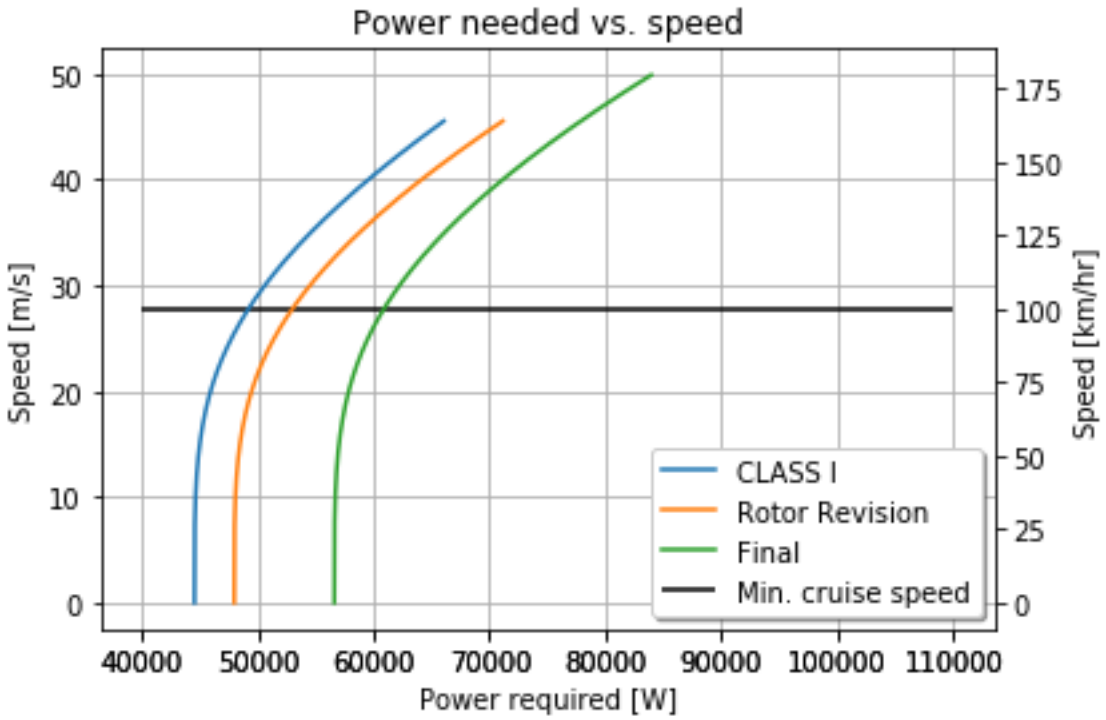

Figure 4.36: Initial and final PAMELA power requirements

Table 4.7: Final power needs for Pamela

	PAMELA initial	**PAMELA new**	**Diff. abs.**	**Diff. %**
P hover [kW]	48	56.6	8.6	17.9
P cruise [kW]	53.1	61.3	8.2	15.4
P peak [kW]	146.1	172.3	26.2	17.9

The final power needs are higher than expected due to an increase in overall weight. This increase was due to unexpected heavy cable weight, the battery being heavier than budgeted and the addition of ducts and a safety system. It can however be expected that in the coming years battery energy density will improve. This means that the battery can be lighter in the future, which can make a big difference.

4.8. Battery Selection & Sizing

Now that the power requirements for PAMELA are known, the sizing of the battery can be done. In this sizing the energy density of the cell as well as its possible power output are of great importance. In general it is possible to find a cell with a high energy density and a low discharge rate and vica versa. However to find a cell with both a high energy density and a high discharge rate is not as easy. In order to come to a good battery cell solution, this section will be structured in an order that aides with the finding of a good battery cell. To start of with, battery chemistry will be explained to get a good insight in its workings. After

this, the basic method for the sizing will be explained. Then, research with respect to battery cell options will be done and a trade of will be made. To conclude, a battery cell will be chosen and different battery packs will be sized.

4.8.1. Chemistry

A lithium ion cell is a rechargeable battery, that just like any other battery consists of one or multiple power generating cells. Regarding the lay-out of the cell, each cell in essence has three components: a positive electrode (Cathode), a negative electrode (Anode) and an electrolyte in between them.[16] The positive electrode is usually made of a chemical compound, namely a metal oxide which in PAMELA's design is lithium nickel cobalt aluminum oxide ($LiNiCoAlO_2$) and the anode consists of a porous carbon. In general all li-ion batteries work the same. When the battery is charged the cathode gives up some of its positively charged lithium ions which are moved throughout the electrolyte to the porous carbon and remain there. During this process the battery stores and takes in energy. During discharge, the anode undergoes oxidation, the ions move back through the electrolyte to the cathode, producing the energy that is used by the battery. In figure 4.37 this process is visualized.

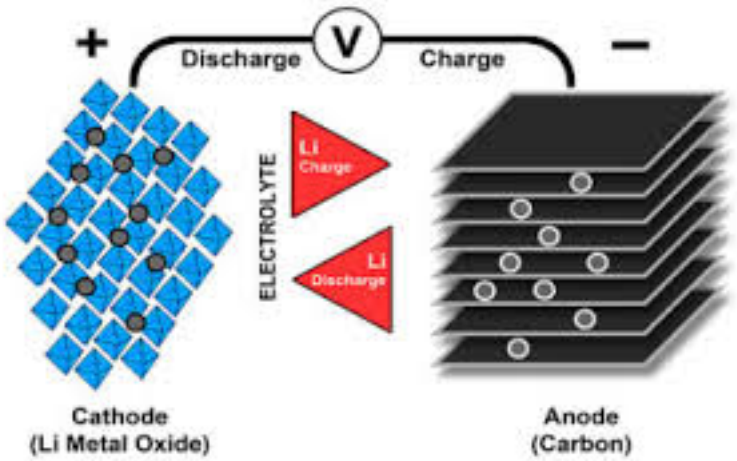

Figure 4.37: Schematic display of li-ion battery chemistry[48]

During both processes, the electrons move in the opposing direction with respect to the lithium ions around the the outer circuit. This is because electrons can't flow through the electrolyte, because to them, the electrolyte is effectively an insulating barrier[48]. The processes of movements of the ions through the electrolyte and the electrons moving around the external circuit are interconnected, if either one of them stops so does the other. Unlike other batteries, Li-ion batteries have battery management systems built in such that aspects as charging, discharging, overcharging and overheating can be regulated, more information about the BMS can be found in section 4.9.

4.8.2. Basic method

In the midterm report[10] a trade-off has been performed between potential battery cells. It was discussed that when producing a battery a lot of aspects needed to be taken into account, as optimal performance in one area may compromise other areas. When producing a battery, for example, one can optimise the specific energy such that the run time is extended, and the current loading is improved by increasing the specific power. This of course means that a trade off has to be made in order to find the optimum configuration.

With respect to the design of battery,the power required by the engines and ESC's is needed to be known. From this, the required voltage, amperage, capacity and kWh will be determined in this section. To create a battery pack that complies with all the requirements, the method of placing battery cells in series

and parallel is used [12]. Thus, for a battery pack to achieve the desired voltage, the cells need to be connected to each other in series, each cell will 'add' its voltage to the total voltage when connected in series with the other cells. The same idea is used for increasing the amperage of the battery pack, only now the cells are connected in parallel with one another instead of a series configuration. The amount of series or parallel connections is always rounded off to the higher value, such that the resulting voltage or amperage is sufficient. Moreover, multiplying the amount of series connections with the amount of parallel connections, we obtain the total amount of cells. By applying this method, a battery pack can be created from single secondary cells. An example of how serial and parallel connections work is given in figure 4.38.

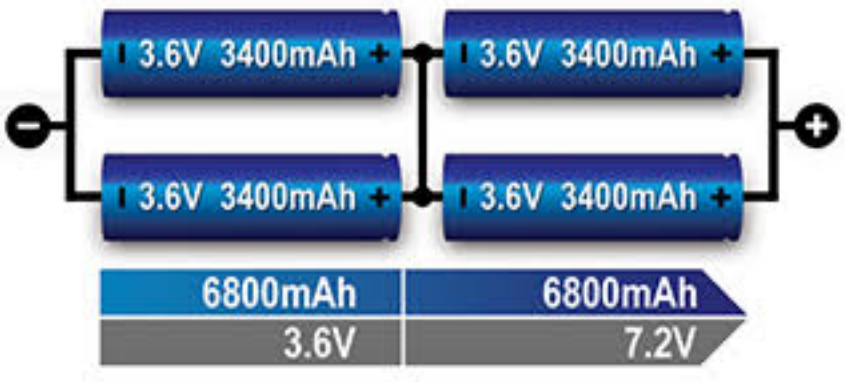

Figure 4.38: Serial and parallel battery configuration[12]

It should also be noted that it is very important that the same battery type is used with the same voltage and capacity and to not mix different kinds and sizes, as a weaker cell causes an imbalance. This is especially important in a series configuration, as a battery pack is just as strong as the weakest cell in the pack. This does not entail that a weak cell would fail immediately, but it does mean that it gets exhausted quicker than the stronger cells, when on a load. When charged, the weaker cells fill up before the strong ones, because there is less capacity to fill and therefore remains in over-charge longer than the stronger cells. When discharged, the opposite happens, the weak cells empty first and get slammed by the stronger ones. Thus it is very important that cells in a battery pack are matched, especially when under heavy loads.[10]

4.8.3. Final battery cell trade-off

In the midterm report it was decided that the ICR18650P is the best battery cell available to design the battery that powers PAMELA. However, the assumption was made that it had the same energy density as the battery cells that Tesla use at the moment. Unfortunately, this assumption was wrong as the manufacturer informed us that the energy density of the specific cell would be 180.7 Wh/kg. Therefore a new search commenced for new battery cells, which resulted in two options the INR21700-40T manufactured by Samsung and the INR2170042P manufactured by Molicell. In table 4.8 both cells are shown with important properties that are used for the trade-off.

Table 4.8: Potential secondary battery cells.[1][72]

Battery Type	Capacity [Ah]	Max. continuous C-rate	Max. Continuous Discharge Current [A]	Nominal voltage [V]	Energy Density [Wh/kg]	Weight per Cell [kg]
INR21700-40T	3.9	11	45	3.6	210	0.07
INR21700P42A	4.2	10	45	3.6	230	0.07

In a glimpse it can already be seen that both cells are almost identical, this is mostly due to the fact that they are the same type, the "21700" type. However, it can also be seen that on some aspects the battery cell of Samsung performs less, for example, the capacity and the energy density are worse than for the INR21700P42A. This means that more battery weight is necessary to produce the same amount of kWh, also the capacity of Samsung's cell is a little bit worse meaning that more cells are needed to have the same run time. While the weight of both cells are equal, thus for the different battery cells to perform the same when assembled into a pack this means that the INR21700-40T is heavier than the INR21700P42A. Therefore, it has been decided that the INR21700P42A cell is used to assemble the battery packs for PAMELA.

4.8.4. Battery estimation

Because a change took place regarding the used battery cell, there will of course be effects present on the ultimate weight and potential kWh production in comparison with the midterm results. With respect to the weight of the battery it is important to elaborate on some design decisions, some mission parameters, and some challenges that need to be faced such that the battery can comply with all of this. Taking all this into account, small changes also have been made with respect to the mission profile. In table 4.9 the parameters relating to the final battery pack used in PAMELA's design are shown, a single battery pack has a 14S7P configuration. Values in this table are for a single battery pack, in the whole design 12 of these battery packs are used values for this are also added in the last two columns of the table.

Table 4.9: Single and total battery pack parameters

Battery Type	**Total capacity [Ah]**	**Maximum used CDR [A]**	**Nominal voltage [V]**	**Weight single pack [kg]**	**kWh single pack[-]**	**Weight 12 packs [kg]**	**Kwh 12 packs [-]**
INR21700P42A	29.4	30	50	6.86	1.58	82.32	18.94

Multiple design decisions, mission parameters and challenges that needed to be faced by the battery and contributed to the final configuration and weight as mentioned before are discussed below:

- **Multiple packs:** The first big change that has occurred with respect to the midterm is the decision to implement 12 single battery packs instead of one big battery pack. This is done to decrease critical failure, for example if 1 of the 12 batteries fail then PAMELA can still continue flight because the required thrust can be delivered by the remaining 11 batteries, which adds redundancy.

- **Speed:** The mission has requirements regarding the speed **PAM-SH-CLI-3:** The vehicle shall have a minimum cruise speed of 100 km/h. This of course requires power, the amount of power that is needed can be seen in table 4.3. Furthermore, take -off and landing approximately require the same amount of power that is needed during cruise flight. Meaning that on average PAMELA needs a total of 58.4 kW to perform take-off, landing and cruise which is divided amongst the 12 motors leading to 4.425 kW per motor. As determined in section 4.6.2, during these manoeuvres 45 volts are used to get the required rpm which means that using $I = \frac{P}{U}$ formula, approximately 108.2 amps are needed to perform the mission. If we relate this to the time in which the battery will be drained, this means PAMELA can fly up to **16 minutes and 19 seconds.**

- **Time:** Another requirement was set with respect to the range: **PAM-SH-CLI-5:** The vehicle shall have an electric power autonomy for 20km. It was determined that landing takes about 20 seconds per landing, and that take-off takes about 20 seconds as well, during a mission, both manoeuvres take place twice, which leads to a time of 80 seconds. Covering the 20 kilometres with a minimum cruise speed of 100 km/s leads up to 12 minutes. Summing up all manoeuvre times this leads to a total mission time of 13 minutes and 20 seconds. Which means that the battery actually has a margin of 3 minutes fly time with respect to this requirement. Moreover, in section 3.3 it was determined that

actually (almost) all potential missions have a range less than 20 kilometres which even leads up to a bigger time margin depending on the particular mission.

- **Range:** If we take a look at the same requirement as in the previous bullet point(PAM-SH-CLI-5) and we take the maximum flight time of 16 minutes and 31 seconds. Then we can determine the maximum possible distance that can be covered by PAMELA. Therefore if we take the 80 seconds it takes PAMELA to perform the take-off and landing twice we have 14 minutes and 59 seconds left to fly at a minimum cruise speed of 100 km/h. This results in a maximum possible distance of 25 km that can be covered by PAMELA. Then if we take a look again at section 3.3 we see that the maximum mission distance in the possible mission profiles is equal to 23.7 km if we use the current helicopter landing zone. Therefore, all mission profiles as they are, can be achieved by PAMELA, although for the 23.7 km, a risk is taken with this possible range. Nevertheless, it should be noted that when a helipad is placed on the suggested position we have a maximum mission distance of 14.35 km which is more than enough with respect to maximum range. In addition, with the new helipad there are even missions that have a maximum distance of 4 km which enable PAMELA to even perform multiple missions on a fully loaded battery.

- **50% redundancy:** Another requirement was set with respect to redundancy: **PAM-SH-CLI-14:** The vehicle shall be able to fly with 50% of the propulsive system actively working. During the design process it was decided that if 50 % of the engines fail PAMELA should be able to fly back to a safe place where it could land. However, the chance of failure of 1 engine is 1/13400[13] which means that the chance of 6 engines failing is equal to $(\frac{1}{13400})^6 = 1.727 * 10^{-25}$. Due to this extremely small chance, it was decided that when the engines fail PAMELA should be able to land in a controlled manner be it on water or land. Because of this PAMELA has a safety mechanism in place that makes sure the vehicle will float when landing on water as can be seen in section 8.6.1. Furthermore this mission profile change leads to a big change in the needed amount of peak power, which in this case will be about the same power that is needed to hover. Which means that the required current for the remaining batteries is now 199 amps for a maximum duration of 3 minutes instead of 240 amps for a maximum duration of 5 minutes during 50% engine failure. Due to this mission profile change, the battery was able to be downsized leading to a weight reduction. Lastly, it should also be noted that when failure of an engine occurs the voltage can be increased such that the continuous current remains the same and the battery drains with the same amount of time.

- **Cooling:** A huge benefit of using the INR21700P42A cell is that PAMELA will not need an active cooling system. As according to contact with the manufacturer and the battery cell's datasheet[1] if we maintain a CDR of maximum 30 amps per cell the temperature rise is not high enough for active cooling to be needed, just passive. In the case of 30 amps, the surface temperature of the pack will reach a maximum temperature of 80°C. A BMS will be put in place that among other situations monitors the temperature of the pack thus cutting of the power of the battery if the battery threatens to go over 75°C (75 degrees taken as margin). Also during normal flight every battery needs to deliver approx 108 amps, which leads up to a CDR of 15.4 amps which is far below the the max CDR of 30 amps. Moreover also in the case of 50% redundancy the remaining batteries should deliver 199 amps which leads to a CDR of 28.5 amps per battery cell thus also still under the max. Therefore, active cooling will not be installed on PAMELA. Nevertheless passive cooling will still be installed, this will be done by creating inlets in the body as can be seen in subsection 8.5.2. While during assembly of the pack, enough space will be designed between the cells such that air can flow in between the cells and packs such that passive cooling is applied.

These were the most major aspects that needed to be taken into account while designing. However there are also disadvantages that come along with the chosen cell, such as:

- **Charge time:** The charge time of the battery packs we use is 3.5 hours as the capacity of 1 pack is equal to 29.4 Ah while the maximum charge rate is 8.4 A.[1]
- **Cycle life:** The capacity of the cells degrades quickly with the amount of cycles performed. After 500 cycles the capacity degrades to 3.5 Ah which means that during regular flight of PAMELA the battery will be drained in 13.61 minutes which corresponds to a distance of 20.4 km. Thus if it is used for missions of which the distance is more than 20.4 km it is suggested to change the old batteries with new ones or use the specific vehicle for missions with a shorter duration and a margin is available. Which will not be the case if the new helipad is installed on the suggested place as then the maximum distance is 14.35 km. Even if the battery retains 70% of its capacity then PAMELA would still be able to cover 16.8 kilometres. Lastly, the batteries should be replaced if the capacity has degraded too much. Thus during maintenance the remaining capacity should constantly be measured to know when to replace the batteries exactly.
- **BMS:** A battery management system needs to be added to monitor the cell status including the voltage, current and temperature such that the battery pack can be used without failure. For example aspects like: LVP- Low voltage protection , OVP-Over voltage protection ,SCP-Short current protection , OTP-Over temperature protection and OCP-Over current protection in the PACK BMS, cut-off voltages, cell balancing etcetera. More information about battery management systems and what they are used for can be found in section 4.9.
- **High discharge rate:** At high discharge rates the cycle life will degrade extra quick. However during normal flight the battery is discharged at a c-rate of 3.35 which is not categorised as a high discharge rate. Nevertheless during 50% redundancy, the c-rate will be 6.1 which is quite high and will definitely affect the cycle life. However, it was already noted that the chance of 6 engines failing is equal to $1.727 * 10^{-25}$ thus an extremely small chance of degradation due to failure of the engines.

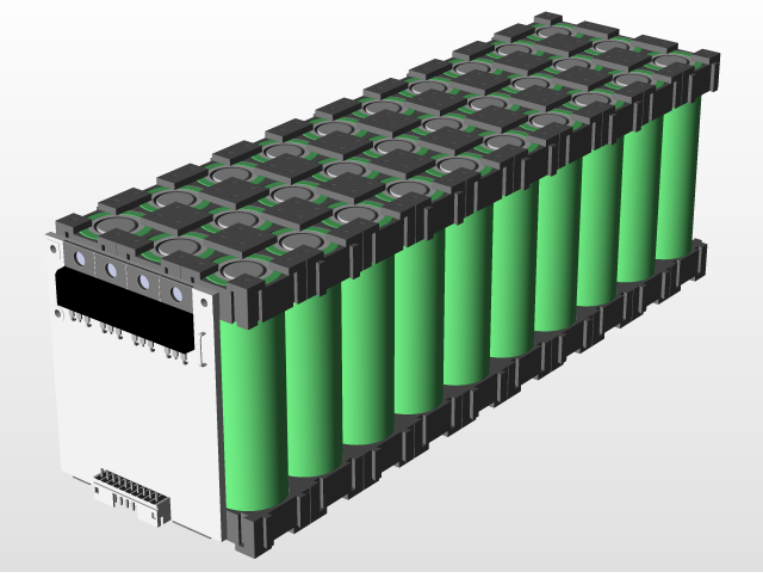

Figure 4.39: Creating space between cells by adding a frame.[37]

Furthermore, the weight calculated in table 4.9 was the net weight of just the battery cells that are in the pack. The weight that will be added during assembly has not yet been taken into account, this will be done by adding a frame (see figure 4.39) such that no contact is made between the cells and also because space is created for passive air cooling. Furthermore, nickel and copper will be added to make the serial and parallel connections between the cells. During the development of the battery system for PAMELA there has been contact with multiple manufacturers which, outside the net weight of the battery, suggested a

battery pack that averaged on 1.2 kg with respect to the packaging weight. Thus adding 1.2 kg per pack for packaging, this results in an approximate total weight of a single battery pack of 8 kg.

Component	Weight[kg]	Cost[€]	Amount[-]	Total weight[kg]	Total costs[€]
Battery pack incl. packaging	8	790	12	96	9480
BMS	0.045	159	12	0.54	1908

Table 4.10: An oversight of the weight and costs corresponding to the batteries and BMS's used to power the engines.

Lastly, it needs to be decided which BMS will be used for the battery packs, it has been decided to use the Tiny BMS s516 from Energus Power Solutions[32]. Which when an external relay and current sensor are used can handle currents up to 750 A, which is amply sufficient. The data sheet contains almost all the data needed except the weight of the BMS itself, therefore an assumption is made with respect to the mass. This assumption is based on the dimensions, this is done by comparing the dimensions of the BMS with other battery management systems of which the weight is known. So the Tiny BMS is compared to the the BMS of LION Smart[53] which has approximately the same dimensions. The BMS of Lion has a weight of 45 grams and this weight will thus be used as weight for the Tiny BMS that is going to be implemented in PAMELA. To conclude, the pricing of the Tiny BMS s516 is equal to €159. An oversight is given in table 4.10 where all prices and weights can be seen of the battery and battery management systems used to power the engines.

4.8.5. Avionics battery

The batteries that power the engines and ensure propulsion have been designed in the previous sections. However, there are still devices on board of PAMELA that need power to to properly function. For example, the avionics that are used for guidance, navigation, communication, autopilot etc. In table 4.11 all remaining systems that need to be powered can be seen with their input voltages, power required and amps that follow from a combination of both. Values for input voltage and power have been taken from chapter 7.

Table 4.11: Avionics components

System	Power [W]	V_{in} [Volts]	Amperage [A]
Picollo II	4	8-20	0.2
TASE400 HD	35	10-30	1.2
LR-D1	1.5	5.2-13	0.1
ULAB-D1	30	10-14	2.1

In table 4.11 the power is the maximum power needed by that specific component during use. The input voltages will be taken with respect to their maximum voltages then we use $I = \frac{P}{U}$ to determine the required amperage for each component. If we take a look at the highest voltage required then this is equal to 30 V and if we take the sum of the required amps then we know what the battery is required to deliver. Therefore, in short, for the remaining subsystems we need a battery that is able to deliver 30 volt and at least 3.6 A. The systems will be connected in parallel, this means that if one system fails this will not have an influence on the functioning of one of the other systems. Consequently, 30 volts will be used throughout the circuit and the amps needed per connection are just taken by the specific system due to the parallel circuit. It should be noted that when components need less than 30 volt, resistors are put in place to ensure each system receives the right amount of voltage. If we take the same method and battery cell as we did for the 12 batteries that power the engines we need a battery with a configuration of 9S1P this equals a net weight of 0.63 kg. Then finally a weight of approx. 0.4 kg is assumed for packaging thus establishing a final weight of 1 kg for the avionics battery.

To ensure redundancy of the avionics systems, two of the 9S1P batteries will be installed in PAMELA. Regarding the discharge time, the rated capacity of the pack is 4.2 Ah meaning that when the battery needs to supply the avionics with 3.6 amps that the battery will be depleted in 70 minutes. This means that the avionics batteries can go 3-4 missions without the need of being charged. After 500 cycles the capacity will decrease to approximately 3.8 Ah[1] if the battery is always drained with 3.6 amps. Meaning that the battery can still power the avionics for more than an hour. Thus, in short, the avionics batteries will probably not need to be replaced for at least the first couple of years, during maintenance the remaining capacity should constantly be measured to know when to replace the batteries exactly. Also in the previous section it was mentioned that only passive cooling was needed if the max CDR was less than 30 A, and with a CDR of 3.6 A the batteries are below that figure thus only passive cooling is needed. Finally, an assumption is made that the avionics battery packs costs are equal to €72 this is determined with respect to the price of the battery pack that powers the engine. As for that, a price was established of €790, when we then take the ratio between the amount of cells of these 2 packs and multiply this with the price we get €72 for the avionics battery pack. To conclude, a Protection Circuit Module with equilibrium function[3] has been chosen to take on the task as battery management system for the avionics batteries.

Component	Weight[kg]	Cost[€]	Amount[-]	Total weight[kg]	Total costs[€]
Battery pack	1	72	2	2	144
PCM	0.039	58	2	0.078	116

Table 4.12: Avionics battery weight and costs.

4.9. Battery Management System

With the irregular operating conditions that the battery of an electric vehicle has to withstand, proper management of the cells and the pack used in PAMELA is crucial to protect the battery and determine its state-of-charge (SoC). Lithium-ion batteries lose a large part of their capacity or fail if they are overcharged, fully discharged, or operated outside of their safe temperature range. A battery management system (BMS) can provide the aforementioned functions and ensure safe operation. The BMS has the following functions, based on the information provided by [82].

- **Cell protection:** Lithium-ion cells are particularly dangerous. They must be operated within their voltage, current and temperature limits. Failure can lead to an explosion or fire. In case of a failure, PAMELA's BMS can isolate the failing part of the battery.
- **Charge control:** Improper charging is a major cause of battery damaging.
- **SoC determination:** The State-of-Charge is analogous to the fuel gauge in a fuel powered aircraft. It is defined as the available capacity as a percentage of the capacity of a new cell. In addition to determining the range, the SoC is used to make sure that PAMELA's battery cells are not overcharged or discharged above their maximum DoD.
- **SoH determination:** The State-of-Health is an indication of the point which has been reached in the life cycle of the battery and a measure of its condition relative to a fresh battery. For PAMELA, it is based on a comparison between the current capacity and the capacity when new, to be able to determine the range of the vehicle.
- **Cell balancing:** Cell imbalances can occur due to manufacturing tolerances, uneven temperature distribution and other minor differences between the operating conditions of cells. PAMELA's battery is made up of all the same cells, which helps to prevent imbalances, but imbalances are nevertheless inevitable. If one cell in a chain has aged more than others and therefore has a lower capacity, it may be overcharged when the pack is charged. The cell would get weaker with every cycle until it

fails. When a single cell would fail, the whole module would have to be replaced, because if a single cell would be replaced, the new, fresh cell would create imbalances as well. To tackle cell imbalances, the BMS of PAMELA will implement a cell balancing scheme, which means that the SoC of each cell is measured and by switching circuits charging, the charge of all cells is equalized.

- **Communications:** To allow for monitoring of the battery condition and modifying of the BMS control parameters, or for diagnostics and test, the BMS communicates via a CAN bus (Controller Area Network bus), which is also used as communication interface in the rest of the powertrain. CAN bus performs well in noisy environments.

To get an idea of how the BMS works together with the other power management systems, see Figure 4.40. In the figure, one can see that the BMS is divided into three units: the battery monitoring unit (BMU), the battery control unit (BCU) and the CAN bus communication network.

The **BMU** consists of a microprocessor, the software of which can be divided into three modules. One of these units is the **battery model**, which models the behaviour of the battery under specific charge and discharge conditions, and after aging. With this model the SoC of the battery can be estimated and the range of the vehicle can be predicted. The output data is communicated with other subsystems through the CAN bus.

Another BMU unit is the **demand module**, or sometimes called the personality module. It contains the logic used for setting and controlling the battery operating limits. It also functions to change the operating mode when safety measures have to be taken, so when for example one or more engines fail. The demand module also processes the battery operating history, which is then used to determine the battery SoH.

The third BMU unit contains the **decision logic**. In the module, the desired battery parameters that come from the demand module are compared to the actual parameters. Using feedback loops, the battery is then driven to its desired operating point, or parts of the battery are isolated in case of failure.

As stated before, the communications in the BMS and of the BMS with other energy management subsystems is done via the CAN bus. More information on this communication interface can be found in chapter 7.

Lastly, the **Battery Control Unit** BCU has the power electronics circuitry of the BMS. Control signals from the BMU are sent to the BCU, which then implements them for the battery charging or to switch power connections to individual cells.
In PAMELA's battery system, each battery module will be managed by a so called slave, and all the slaves are connected to one master. The master is made redundant to ensure redundancy of the whole system. Temperature sensors and connections to measure the voltage are placed on every cell, which are connected to the slave. The slave monitors the cell conditions and implements the cell balancing scheme.

The master calculates the SoC, by taking the data from the slaves and measuring the current. It also performs the communication with other systems.

As a final note, to address safety: PAMELA has a separate battery module for each motor, the failure of a single module, or even half of the modules, is not critical and a safe landing can be realized. For a depiction of the basic hardware components of the powertrain and of how the BMS is integrated, one is referred to Figure 7.1.

4.10. Battery Thermal Management

As mentioned in section 4.9, lithium-ion batteries are very sensitive to low and high temperatures. Operation above their maximum safe temperature can lead to capacity loss, power fade and thermal runaway. Thermal runaway occurs when cell temperature rises and consequently the chemical reaction in the cell is sped up, causing even further heating. Too low temperatures on the other hand lead to higher resistance,

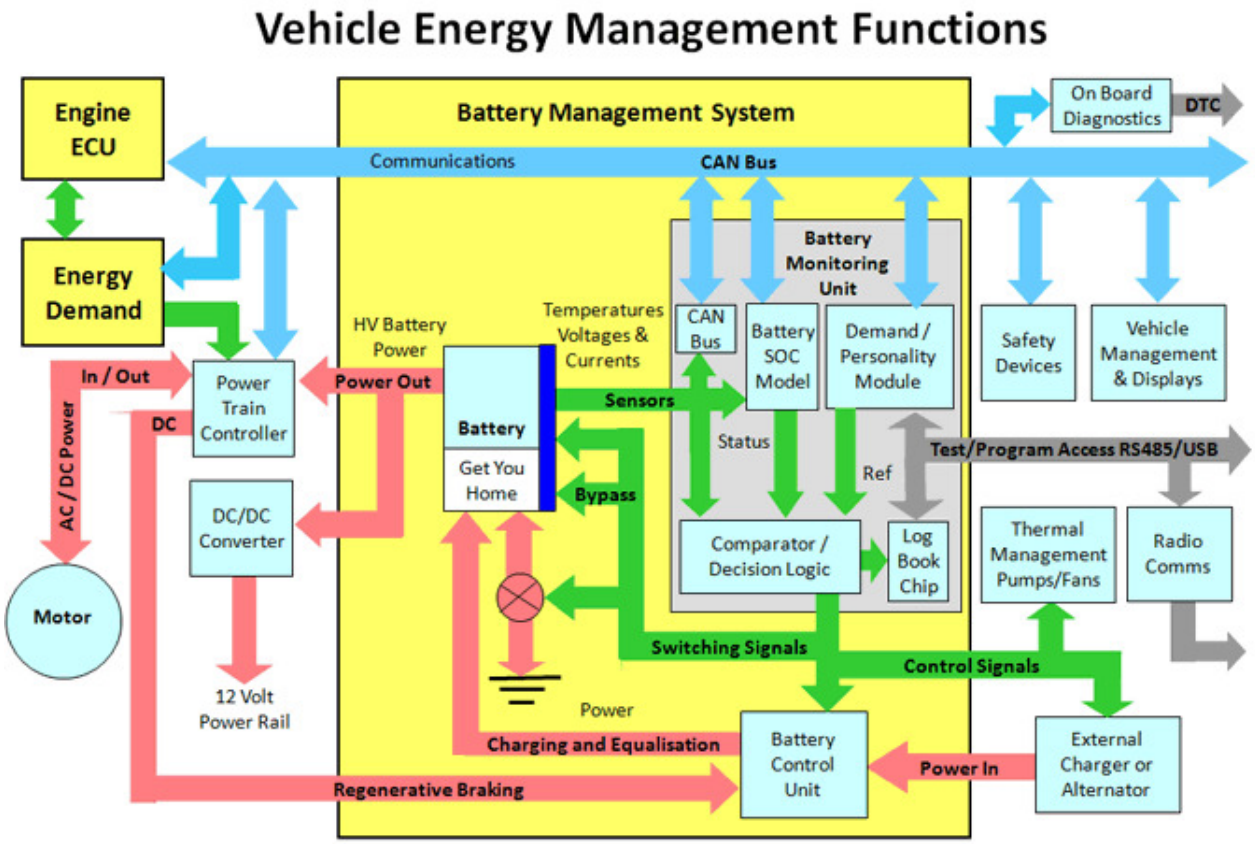

Figure 4.40: Battery Management Implementation [82]

lower efficiency and decreased available capacity [2]. Too cold batteries can also cause lithium plating - which is the deposition of lithium on the anode of the battery [54] - which can even cause failure. Internal heating in lithium cells is mainly caused by so called Joule heating, which is the heating due to the internal resistance of the battery. Other than that, some heat is produced during the chemical reactions when charging and discharging (lithium cells are partly endothermic and partly exothermic during charge and discharge), but this heat is overshadowed by Joule heating. Furthermore, high ambient temperatures can cause excessive heating and low ambient temperatures can cause excessive cooling.

PAMELA's distributed battery setup, with a separate module for each rotor, aids in controlling the battery's temperature, as the increased surface area allows for better convection and conduction. In between all the modules, conductive plates are placed to act as a heat sink. Furthermore, air intakes allow for air to flow past the battery during forward flight to accommodate cooling by convection.

Low temperatures in winter can be a problem for the battery at startup. As the battery is highly distributed, self-heating (Joule heating) might not be enough to raise the battery temperature to a desirable level. Therefore a small heater is incorporated at the battery to heat the battery to above zero temperatures at startup. Afterwards the internal heating will keep the battery warm.

4.11. Updated Weight & Cost Estimation

By adding the weight and the cost of all powertrain subsystems, derived from data provided by the manufacturers or estimated where exact data could not be obtained, the total powertrain cost and weight can be accurately approximated. In this section a summary is given of the powertrain component costs and the

estimation methods. Many component weights were already determined before the Midterm Report, but some have been updated.

4.11.1. Weight

The powertrain weight consists of six components: the rotors, the motors, the ESCs, the cabling, the main battery, the avionics battery the BMSs and the heater. Note that the avionics BMS is included in the avionics battery weight in Table 4.13. The motor, ESC and BMS weight are given by their respective manufacturers. The cable weight estimation has been described in subsection 4.6.3 and the other component weights are approximated as follows.

The **rotors** will be manufactured in-house, thus their weight is approximated by taking into account the volume and the material: a foam core with a carbon fiber skin. The core material is high density polyurethane (PU) foam, which is a typical low cost core material. Its density is 96 kg/m^3 [30]. A carbon fiber cloth can then easily be layed over the foam core, using epoxy as adhesive. The weight of the epoxy is neglected, while the weight of the carbon fiber is assumed to be 600 g/m^2, taking into account two layers of cloth (one with $\pm 45 deg$ and one with $\pm 90 deg$ directed fibers).

From the rotor dimensions determined by the aerodynamics department, an approximate surface area of 0.25 m^2 follows, and a volume of around 2.98×10^{-4} & m^3 (see Table 4.5). The hub of the rotor is assumed to be a 10x10x1.5 cm block made of Al 2024-T4. The weight that follows from these dimensions is given in Table 4.13.

Table 4.13: Powertrain weight

	Weight [kg]	**Amount**	**Sum [kg]**
Rotor	0.6	12	7
Motor	2	12	24
ESC	0.51	12	6
Cabling	29	1	29
Battery	8	12	96
BMS	0.045	12	0.5
Avionics battery	1.04	2	2
Total			**165**

4.11.2. Cost

The cost estimation is done in a similar manner to the weight estimation. The cost of the motors and the ESCs are known from the manufacturers, while the other components' costs are approximated.

The **rotor** cost is determined by using the dimensions stated in subsection 4.11.1, a price of PU foam of 190 £/m^3 [30] and a carbon fiber cost of 24 £/m^2. Moreover, the Al 2024 hub cost is derived from a 5 £/kg price. Lastly, manufacturing cost is based on a manufacturing employee salary of 15 £/$hour$ and a manufacturing time of 30 minutes per blade plus 2 hours for testing. From these numbers a rotor cost of 45 £ is derived.

The **cabling** cost is derived from a cable price of 20 £/m and a total cable length of 60 m. From these numbers a cabling cost of 1,200 £ is derived.

Battery and **BMS** cost have been determined as described in subsection 4.8.4. For the total cost estimation, a battery recycling cost of 350 £ for the complete battery has been added (so included in Table 4.14), based on [11] and taking the lower limit, as Duesenfeld uses highly efficient methods. The avionics battery is treated seperately, and in this case the avionics BMS cost is included in the avionics battery cost. The cost estimation method can be found in subsection 4.8.5.

Table 4.14: Powertrain cost

	Cost [€]	Amount	Sum [€]
Rotor	45	12	540
Motor	1230	12	14,760
ESC	500	12	6,000
Cabling	1,200	1	1,200
Battery	790	12	9,830
BMS	159	12	1,910
Avionics battery	130	2	260
Total			**34,500**

4.12. Sustainability

The recycling of PAMELA's powertrain is divided into two parts: the recycling of the battery and the recycling of the other powertrain components.

4.12.1. Battery

As more electric vehicles are used worldwide, the demand for lithium-ion battery recycling increases. The automotive industry in particular faces the challenge of recycling batteries on a large scale. That industry has proved that with combined efforts, recycling of batteries can be made profitable, as has been done for the lead-acid batteries that are used for starter batteries in almost any car. In the United States even 99% of lead-acid batteries are recycled [38]. However, lead-acid batteries contain a large portion of lead, that can be relatively easily and profitably retrieved to use in a new battery. This is not so much the case for lithium-ion batteries, for which the motivation to recycle them is more because of environmental concerns.Recycling costs must therefore be included in the cost budget for PAMELA, as is done in subsection 4.11.2.

The first step to take in order to realize a sustainable use of the PAMELA's batteries is to reuse them after capacity has faded too much for effcient use in the vehicle. The capacity loss is less of a concern in other uses, such as the storage of solar energy produced from solar panels in the offices of the PAMELA team and other areas in the port of Rotterdam. The stored energy can then be used for lighting in the port at night.

When a battery's SoH has become too low even for lighting purposes, it shall be recycled. The PAMELA team has sourced a business in Germany that specializes in lithium-ion recycling and claims to realize reduced energy consumption and increased recovery of raw materials compared to the competition. The business, *Duesenfeld GmbH*, does so by using combined mechanical and thermodynamical processes instead of the old melting, pyrolysis (decomposition under high temperature) or heating. The method of Duesenfeld uses 70% less energy than traditional smelting furnaces [29].

4.12.2. Other components

The first measure that has been taken to promote the powertrain's sustainability is that components have been sourced at a relatively short distance from the Netherlands, where possible, to prevent an unnecessary carbon footprint from shipping. Therefore, the motors and ESCs come from Germany and the cables come from the Netherlands. The battery cells are a crucial component of the vehicle and the performance of the cells used is rare. Therefore the fact that the cells come from Hong Kong has been accepted. As batteries advance rapidly, a European supplier may be found in the near future.

Then when the powertrain's life has ended, the components must of course be recycled or disposed of properly. To do this in a systematic manner, a list of the materials used most is established and the recyclability is identified, as tabulated in Table 4.15. A material that is not recyclable or extremely costly to recycle

is identified as *poor*. A material that is recyclable, but difficult and relatively costly to do so is *marginal*. The upper range of recyclability is made up of *good* and *excellent*, where excellent means that the recycled material's value is not far off from the original material.

The components where the materials mentioned in Table 4.15 are found, are the following.

Aluminum is found in the wiring, the rotor hubs, and the ESCs.

Carbon fiber is found in the rotors.

PU foam is found in the rotors as well.

PVC is used in the wiring.

Copper is used in the windings of the motors.

Table 4.15: Material recyclability

	Recyclability
Aluminum	Excellent
Carbon Fiber	Marginal
PU foam	Marginal
PVC	Good
Copper	Excellent

4.13. Conclusion

In conclusion, a theoretically functional powertrain subsystem could be designed. Off-the-shelf and proven motors and ESCs will be used, and the battery will be assembled from existing high performance cells. Meeting the requirements on power and range has clearly not been easy with current battery technology, but the vision for the future is bright. Li-ion technology is improving rapidly and even better performing battery chemistries are being developed. Another factor that significantly limits the design is the limited size of the vehicle. Therefore, for future considerations, a thorough ship survey is recommended to be done, to see if a larger vehicle would be realizable.

5 Aeroacoustics

From the start of the project it was clear that the noise characteristics of the vehicle would play a significant role during the design process, since three requirements of the client are noise related. The client demanded that the vehicle will respect European night noise regulations as well as the aeroacoustic regulations for noise emissions over harbor areas. The third requirement is that the vehicle should have a maximum level of cabin noise of 60 dBA. After discussing with the client, the requirement regarding the European night noise regulations is omitted due to its irrelevance with respect to the mission.

Despite that the field of aeroacoustics evolved dramatically in the past decades, a detailed analysis on the noise characteristics of the vehicle is beyond the scope of this project as it involves complex computer operations and detailed aerodynamic analysis. In addition, there are many different sources of aerodynamic noise which makes it unrealistic to design according to all these sources within the given time span of the project. In order to still aim for a quiet design in order to uphold to the noise requirements, a first-class noise estimation has been carried out based on a method from Lowson that can be done using simplified hand calculations which only reduce accuracy by a few percent in contrast to computational methods [60].

This chapter explains how this method influenced the choices made during the design process and further investigates how the noise characteristics of the vehicle can be reduced.

5.1. Rotational Noise

Noise generated by rotors can be separated into a periodic and broad band component. Figure 5.1 shows the different sources of aerodynamic noise. The main focus will be on the analysis of the rotational noise as this is directly involved with the design of the rotors and often has the biggest contribution to the noise characteristics.

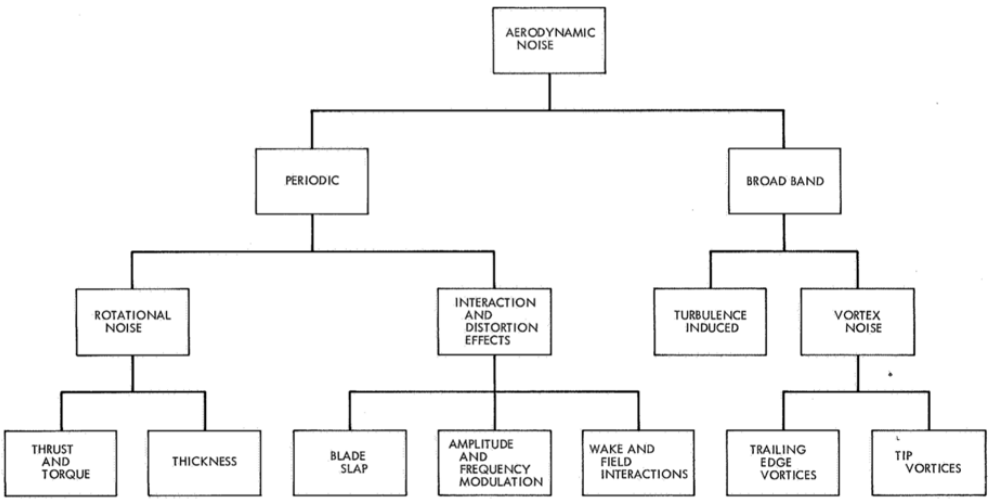

Figure 5.1: Sources of aerodynamic noise [60].

One of the main drivers during the early design of the rotors was to keep the frequency as low as possible in order to benefit from the A-weighted decibel scale. Compared to unweighted decibels, the A-weighted system has lower values for sounds at low frequencies. The reasoning behind this is that the human ear is less sensitive to sounds at low frequency. In figure 5.2 it can be seen that for low frequencies a reduction of 10 to 20 dB can be achieved.

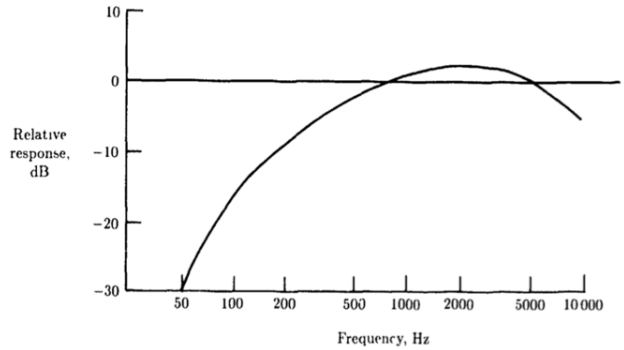

Figure 5.2: Relative response of the A-weighted filter [43].

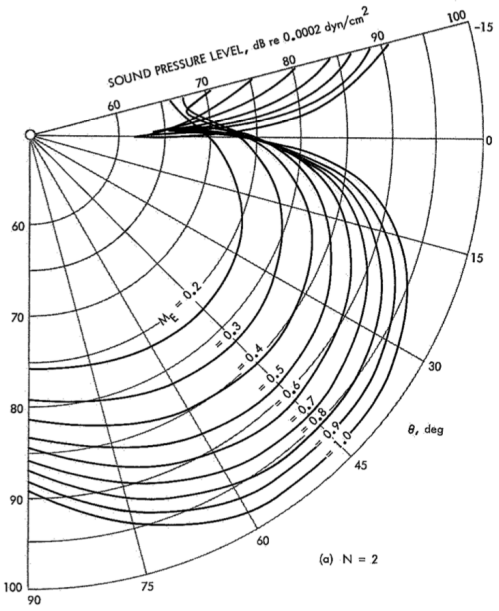

Figure 5.3: Chart from Lowson's method: rotor noise 2^{nd} harmonic sound pressure level as a functions of rotational Mach number and angle from disc plane.

The fundamental frequency is obtained by equation 5.1 as stated in Lowson's method [60].

$$f = \frac{nB}{2\pi(1 - M_F cos(\theta))} \tag{5.1}$$

where M_F is the flight Mach number

$$M_F = \frac{V}{c} \tag{5.2}$$

with V the flight velocity and c the speed of sound in ft/s. θ is the angle between the rotor plane and the observer, i.e the reference point of where the noise is being measured.

$$\theta = tan^{-1}\left[\frac{z}{(x^2+y^2)^{3/2}}\right] i_d \left[\frac{x}{(x^2+y^2)^{3/2}}\right] \tag{5.3}$$

In equation 5.3 x, y, z are the coordinates relative to the vehicle measured in ft and i_d is the rotor disc incidence angle in degrees. Furthermore, n is the rotor angular velocity in rad/s and B is the number of rotor blades. Figure 5.4 gives a graphical overview of how the different parameters are related to each other.

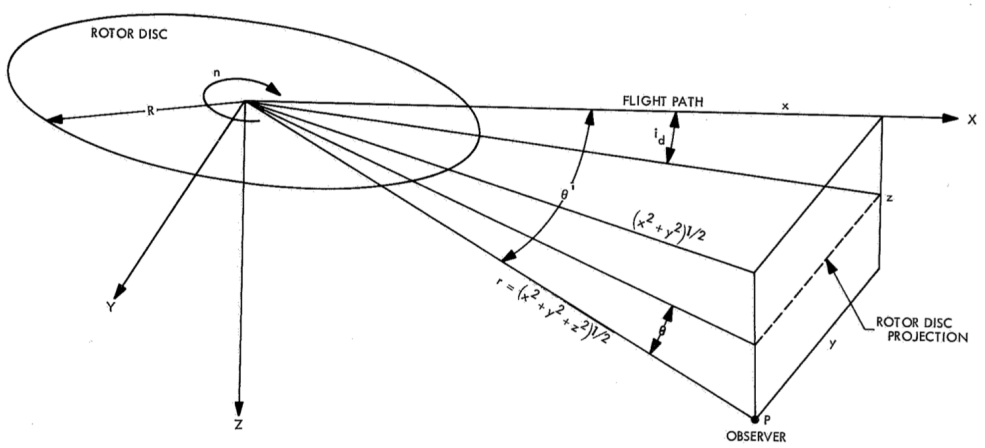

Figure 5.4: Rotor rotational noise axis system [60].

From equation 5.1 it is clear that an increase in rotor blades results in a higher frequency, which is unwanted due to the A-weighted decibel scale. This relation put emphasis to go for the two-bladed rotor configuration during the early design phase. Three or more blades can give the same thrust for lower angular velocities relative to two blades, which is also beneficial for the noise characteristics. However, to aim for a lower frequency the effect of a decrease in angular velocity is insignificant compared to the effect of an increase in blade number.

In section 4.5.4 the angular velocity of the rotor during hovering is estimated to be 1716 RPM which is approximately 180 rad/s. The sound is measured 150 m below the rotorcraft as defined by ICAO [46]. Using equation 5.1 and taking the flight velocity zero results in a frequency of 57 Hz. From figure 5.2 it then shows that a decrease of 28 dB can be achieved[1].

The noise level associated with the rotational noise can be predicted using the chart developed by Lowson in figure 5.3. To use the chart the effective rotational Mach number must be determined first using equation 5.4.

$$M_E = \frac{M}{1 - M_F cos(\theta')} \tag{5.4}$$

$\theta' = cos^{-1}(x/r)$ is the angle in degrees between the flight direction and the line joining the rotor and the field point where $r = (x^2 + y^2 + z^2)^{1/2}$ is the range in ft. M is the rotational Mach number where $M = 0.8nR/c$ with R being the rotor radius in ft. Then for the hovering vehicle at a height of 150 m and a rotor radius of 0.65 m, $M_E = M = 0.27$. Using the chart in figure 5.3 carefully and taking $\theta = 90°$, a sound level of 77 dB is found. This value needs to be corrected for thrust, disc loading, and distance according to equation 5.5:

$$SPL = \left[I_N + 11 + 10log\frac{T}{r^2}\left(\frac{T}{A}\right)\right] \tag{5.5}$$

where I_N is the sound level obtained from the chart, A is the disc area in ft^2 an T is the thrust in lb. Then as indicated in section 4.5.4, a thrust of 309 N is produced per rotor at 1716 RPM. This means that a single rotor has a rotational noise sound level of approximately 59 dB, 150 m below the hovering vehicle. Taking into account that the hexacopter has 12 rotors in total, an addition of $10log(12) \approx 11dB$ is made which results in a total rotational noise of 70 dB. Subtracting the 28 dB as obtained from figure 5.2 gives a final approximation of 42 dBA for the rotational noise of the hovering vehicle.

[1]The relative response is calculated exactly using the equation that produces the graph.

The procedure to estimate the rotational noise of 42 dBA for the hovering vehicle as described in this section acted as the main guidance to design for the noise characteristics of the vehicle. Dutch authorities state that during night a noise limit of 65 dBA holds [80], therefore the vehicle respects the regulations for noise emissions over harbour areas solely based on the rotational noise. A more extensive aeroacoustic analysis needs to be performed, taking into account the many other sources of aerodynamic noise, to come up with a realistic prediction of the noise emissions of the vehicle.

5.2. Interior Noise

The client required that the cabin noise shouldn't exceed a noise level of 60 dBA. This section will briefly describe noise reduction by attenuation during its transmission towards the interior.

The most common method of noise reduction as it travels towards the cabin is by utilising cabin sidewall treatments that lower the sound pressure levels inside of the cockpit to a desired level. It is common to use fiberglass blankets enclosed with thin impervious sheets to protect it from moisture and to give a nice finish to the interior. There are however many different ways to utilise sidewall treatment. In order to benefit from the treatment, a proper understanding of the noise outside of the cabin is needed, otherwise the treatment will mainly contribute to a weight increase of the vehicle without a proper reduction in the noise. For example, figure 5.5 shows that the effect of different types of sidewall treatment depends on the frequency of the noise.

A weak link in interior noise control are the doors and windows of the vehicle. Using multi-pane windows opposed to single-pane will already contribute to an adequate transmission loss, but will increase the vehicle's weight. Because the opening and closing mechanisms of doors, space available for acoustic treatment is limited which increases the chance of acoustic leaks around the door seals.

Although sidewall treatments decrease the noise levels inside the cabin, a better understanding of the noise outside of the cabin is needed in order to choose the right sidewall treatment. At this point it is not possible to give an indication of the interior cabin noise.

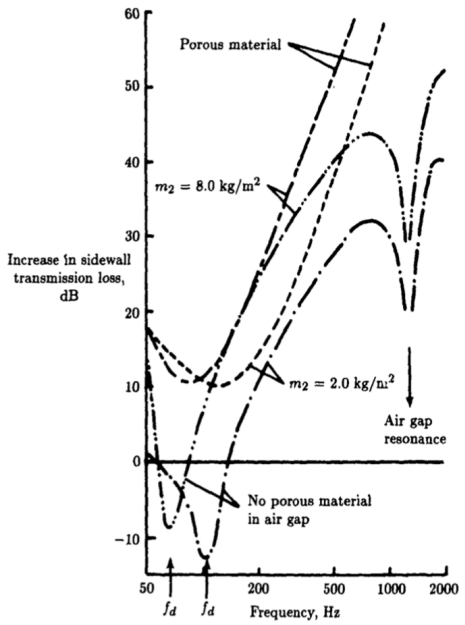

Figure 5.5: Predicted increase in sidewall transmission loss due to addition of a trim panel or fiberglass treatment [43].

5.3. Other Noise Sources

Another way of reducing interior noise is by reducing the noise levels from the source, that is, the rotors. This was the main goal of section 5.1. However, as was mentioned before, there are many other noise sources besides rotational noise. Some of these sources will be analysed in this section in order to understand what measures can be taken to reduce the overall noise and therefore also the noise inside the cabin.

The interaction between the noise fields of the rotors affect the cabin noise characteristics in an important way. When there is a slight difference between the rpm values between the rotors, beating interference between those sources occur. This increases the noise level inside the cockpit in such a way that it is easily detectable and experienced as being annoying [43]. The hexacopter uses differential thrust to manoeuvre, i.e. the rotors operate at different rpm values which will therefore negatively influence the interior noise. The effect of this beating interference can be reduced by controlling the rpm and adjusting the phase in a way that cabin noise is minimised with the use of an electromechanical phasing device [43]. However, the amount of rotors of the hexacopter that can interfere with each other makes this much more difficult.

Another source would be blade-vortex-interaction (BVI), which is noise due to the interaction between rotor-tip vortex and rotor blades. In order to get a better understanding of BVI, an acoustic analysis performed on another electrical VTOL vehicle is analysed. Figure 5.6 shows the BVI of a conceptual single-rotor quadcopter using the simulation tool HELIOS [50]. The simulation shows the aerodynamic interactions between blade-tip vortices and the same rotor, i.e. self-BVI (figure 5.6a). This effect is expected to be lower for the hexacopter as it uses two blades instead of three blades. It is however clear that the use of contra-rotating rotors has a negative effect on the noise characteristics due to the BVI between the two rotors being close to each other.

Figure 5.6 of the quadcopter shows how the interaction between the front rotor wake and the rear blades are avoided due to the vertical separation distance between the rotors, which is positive for the noise characteristics. The rotors of the hexacopter do not have a vertical separation, but it does use ducts which shield the rotors from each other.

The strength of BVI reduces with smaller rotors and lower tip speed which lead to lower BVI noise [50]. The decrease in rotor diameter of the hexacopter as mentioned in 4.3 is expected to reduce the strength of BVI.

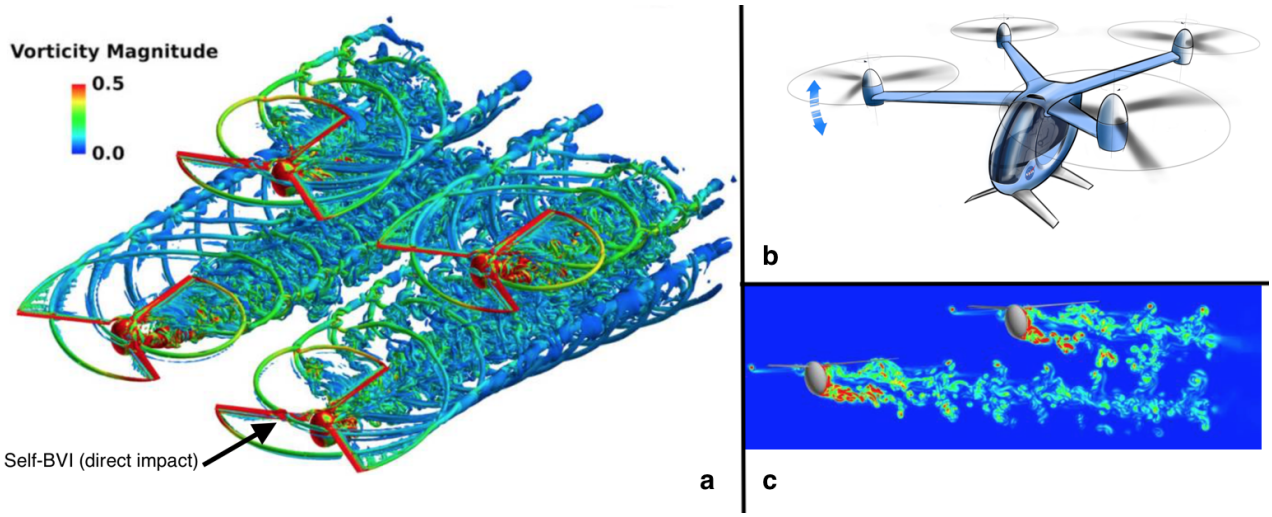

Figure 5.6: Vorticity contour of an iso-surface view (a) and side view (c) of NASA's conceptual quadcopter VTOL design (b) [50].

Lastly the rotor wake-to-fuselage interaction will be mentioned as it is also another source of noise.

Due to the size restrictions as given by the client it was inevitable to keep the vehicle outside the rotor

wake of the two front and two aft rotors without drastically changing the design. This will have negative effects on both the aerodynamics and the aeroacoustics of the vehicle. The team did respond by changing the design of the cockpit which resulted in a less obstructed rotor wake as can be seen in figure 8.30.

5.4. Conclusion

A first class estimation of the rotational noise of the hexacopter aided in the early design of the rotors. To profit from the A-weighted decibel scale, the team aimed for a rotor sound with a low frequency which pushed the design towards a two bladed configuration. As the project advanced, a decrease in rotor radius and angular velocity is achieved which also contributes to a lower noise level. This resulted in a rotor noise level of 42 dBA, experienced 150 m below the hovering hexacopter. This is much lower than the limit of 65 dBA as stated by the Dutch authorities. However, other sources of noise are not taken into account and therefore it is not clear whether the vehicle respects those regulations.

By inspecting other sources of noise it became more clear how contra-rotating rotors have a negative and the use of ducts have a positive effect on the noise characteristics. It also led to an adjustment of the fuselage in order to minimise the rotor wake-to-fuselage interaction (figure 8.30).

This project helped increase the knowledge on aeroacoustics. In the next phase of the project a more detailed analysis will be performed on the noise characteristics using simulations created by available computer programs.

6 Stability & Control Analysis

Multicopters are known for lacking any significant inherent stability, which is why the vehicle's artificial stability and control are crucial for manoeuvres and correct operations. In this chapter a detailed analysis of the vehicle's equations of motion will be presented together with the design of a manoeuvre control system in order to respond appropriately to disturbances.

6.1. Control System Requirements

The Control Subsystem must be capable of adjusting the thrust of every rotor in order to perform the manoeuvres needed for the mission. These manoeuvres must be done in a wide range of operating conditions which have not been covered by the existing requirements. Therefore, the following 5 additional requirements are considered for the control subsystem:

PAM-MAN-1 The vehicle must reach a cruise altitude of 100 meters in less than 10 seconds.
PAM-MAN-2 The vehicle must be capable of reaching a cruise speed of 100 km/h in less than 1 minute.
PAM-MAN-3 The vehicle must be capable of recovering from pitch disturbance of 5° in less than 5 seconds.
PAM-MAN-4 The vehicle must be capable of recovering from roll disturbance of 5° in less than 5 seconds.
PAM-MAN-5 The vehicle must be capable of doing a full 180° horizontal turn in less than 6 seconds.

6.2. Body Definition

Looking at the rotors on an upper and lower plane, the rotational direction of each rotor is shown in figure Figure 6.1. On each plane and pair of rotors, there are as many rotors turning clockwise as there are turning counterclockwise, which creates a zero resultant rotational speed and torque.

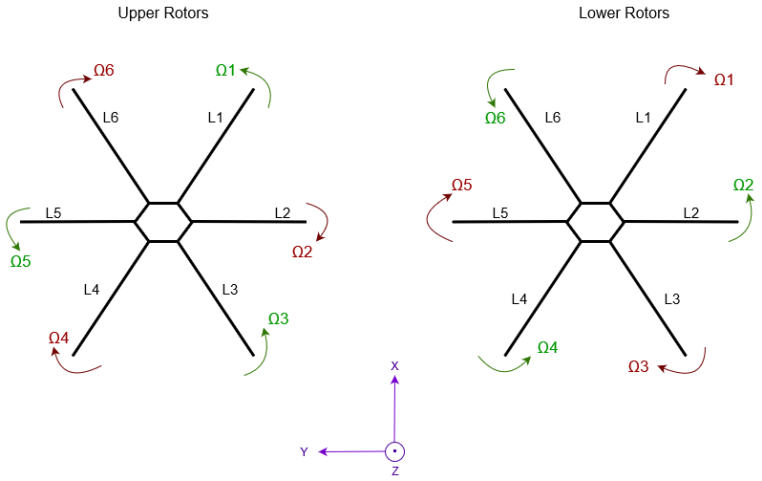

Figure 6.1: Rotors Rotational Direction

The origin of the coordinates systems in the Body Frame is fixed at the C.G. location, which is located in the same location in the xy-plane as the hub, where the vehicle arms are connected. Looking at the vehicle from the front, the y-axis will be pointing to the right, the x-axis will be pointing forwards toward the viewer and the z-axis will be pointing upwards. The hub of the vehicle was found to be located 1.05 meters above the CG location. With the CG location known, the mass moment of inertia could be computed.

To simplify the calculations of the vehicle mass moment of inertia, the propulsion group is assumed to be point masses located at the end of each arm, with the same applying for the cockpit, which is a point mass below the hub. The propulsion group consists of the engine weight, rotor weight, arm weight, and cables weight. The cockpit consists of the cabin structure weight, batteries weight, avionics systems weight, safety systems weight, hub weight, landing gear weight and the weight of all other subsystems in the cockpit.

Now, the mass moment of inertia can be obtained using Equation 6.1 where m_i is the mass of every element in kilograms and R_i is the distance from the C.G. in meters. Table 6.1 shows the calculated mass moment of inertia. As can be seen, the moment of inertia is significantly greater about the z-axis, which might make manoeuvring about that axis challenging.

$$I = \sum m_i R_i^2 \tag{6.1}$$

Table 6.1: Vehicle Mass Moment of Inertia

	Value $[kg.m^2]$
I_{xx}	107.32
I_{yy}	115
I_{zz}	222.32

6.3. Hexacopter Kinematics

The derivation of the equations of motion of the vehicle will be done following the steps taken in [35]. Assuming the hexacopter is a rigid body and symmetric about the x-axis, the EOM can be derived from the well-known Newton-Euler formalism in Equation 6.2, with all values taken with respect to the body reference frame. In this equation, m is the mass $[kg]$, I the inertia tensor $[kgm^2]$, $V = [u \;\; v \;\; w]^T$ is the linear velocity [m/s], $\omega = [p \;\; q \;\; r]^T$ is the angular velocity [rad/s], I_{3x3} is an square identity matrix of size 3, 0_{3x3} is a square zero matrix of size 3. Developing Equation 6.2 leads to Equation 6.3 and Equation 6.4,

which describe the motion of all rigid bodies and thus the forces and moments must be evaluated in order for the equations to be applicable to the hexacopter.

$$\begin{bmatrix} \sum F^B \\ \sum M^B \end{bmatrix} = \begin{bmatrix} mI_{3x3} & 0_{3x3} \\ 0_{3x3} & I \end{bmatrix} \begin{bmatrix} \dot{V}^B \\ \dot{\omega}^B \end{bmatrix} + \begin{bmatrix} \omega^B \times mV^B \\ \omega^B \times I\omega^B \end{bmatrix} \quad \text{where} \quad I = \begin{bmatrix} I_{xx} & 0 & 0 \\ 0 & I_{yy} & 0 \\ 0 & 0 & I_{zz} \end{bmatrix} \tag{6.2}$$

$$\begin{bmatrix} \dot{u} \\ \dot{v} \\ \dot{w} \end{bmatrix} = \begin{bmatrix} rv - qw \\ pw - ru \\ qu - pv \end{bmatrix} + \begin{bmatrix} \frac{1}{m} F_x^B \\ \frac{1}{m} F_y^B \\ \frac{1}{m} F_z^B \end{bmatrix} \tag{6.3}$$

$$\begin{bmatrix} \dot{p} \\ \dot{q} \\ \dot{r} \end{bmatrix} = \begin{bmatrix} \frac{I_{yy} - I_{zz}}{I_{xx}} qr \\ \frac{I_{zz} - I_{xx}}{I_{yy}} pr \\ \frac{I_{xx} - I_{yy}}{I_{zz}} pq \end{bmatrix} + \begin{bmatrix} \frac{1}{I_{xx}} M_x^B \\ \frac{1}{I_{yy}} M_y^B \\ \frac{1}{I_{zz}} M_z^B \end{bmatrix} \tag{6.4}$$

The forces acting on the body include the weight of the vehicle, the thrust of the rotors and the aerodynamic drag as seen in Equation 6.5. The force of gravity always points downward with respect to the Earth Reference Frame, in the negative direction of the z-axis. The thrust force generated by the rotors is on the other hand always pointing upwards in the Body Reference Frame and the drag force will always point in the opposite direction of the velocity vector. All components are represented in Equation 6.6, where g is the gravitational acceleration $[m/s^2]$, ϕ, θ and ψ are the roll, pitch and yaw angles $[rad]$ respectively, T_o is the total thrust generated by the rotors $[N]$, ρ is the air density $[kg/m^3]$, C is the aerodynamic drag constant $[-]$ and S is the reference surface $[m^2]$.

$$F^B = F^B_{gravity} + F^B_{thrust} + F^B_{drag} \tag{6.5}$$

$$\begin{bmatrix} F_x^B \\ F_y^B \\ F_z^B \end{bmatrix} = \begin{bmatrix} mg\sin\theta \\ -mg\cos\theta\sin\phi \\ -mg\cos\theta\cos\phi \end{bmatrix} + \begin{bmatrix} 0 \\ 0 \\ T_o \end{bmatrix} + \begin{bmatrix} -\frac{1}{2}\rho C_x S_x u|u| \\ -\frac{1}{2}\rho C_y S_y v|v| \\ -\frac{1}{2}\rho C_z S_z w|w| \end{bmatrix} \tag{6.6}$$

The moments the hexacopter experiences are dominated by the reaction moments caused by the differential thrust of the rotors, which will be expanded upon in section 6.5. Furthermore, due to the weight distribution of the vehicle, namely the heavy cabin positioned below the rotors, the inclination of the vehicle also causes a moment about the centre of gravity. This will be seen in greater detail in section 6.4. Furthermore, the gyroscopic effect caused by the rotation of the propellers is also taken into account, as seen in Equation 6.7, which is expanded in Equation 6.8.

$$M^B = M^B_{thrust} + M^B_{weight} + M^B_{gyro} \tag{6.7}$$

$$\begin{bmatrix} M_x^B \\ M_y^B \\ M_z^B \end{bmatrix} = \begin{bmatrix} \tau_x \\ \tau_y \\ \tau_z \end{bmatrix} + \begin{bmatrix} G_x \\ G_y \\ 0 \end{bmatrix} + \begin{bmatrix} -J_r q\Omega_r \\ J_r p\Omega_r \\ 0 \end{bmatrix} \tag{6.8}$$

The gyroscopic effect depends on the propeller rotational moment of inertia J_r $[kg \cdot m^2]$ and the sum of rotational speeds $\Omega_r = \sum_{i=0}^{12} \Omega_i$, where Ω_i is the rotational speed of every propeller $[rad/s]$. However, due to the counter-rotation between each pair of rotors, with the two rotating at the same speed but in different directions, the induced torque generated by a single rotor is cancelled out. Changing the speed of each pair individually while maintaining the total thrust results in generating the actuation moments around x-, y-, or z- axis without any gyroscopic disturbance.

6.4. Vehicle Stability

In the midterm report it was found that the vehicle can benefit from some marginal stability by placing the cabin, which groups most of the weight, under the rotors, generating a small corrective torque when the vehicle rolls or pitches, as seen in Figure 6.2. These corrective torques are represented in Equation 6.8 by G_x and G_y, which are computed in Equation 6.9 and Equation 6.10 respectively.

$$G_x = \sum_{i=0}^{6} W_i l_{y,i} \cos\phi - W_{cockpit} z_{cockpit} \sin\phi \tag{6.9}$$

$$G_y = \sum_{i=0}^{6} W_i l_{x,i} \cos\theta - W_{cockpit} z_{cockpit} \sin\theta \tag{6.10}$$

Figure 6.2: Hexacopter roll and pitch stability

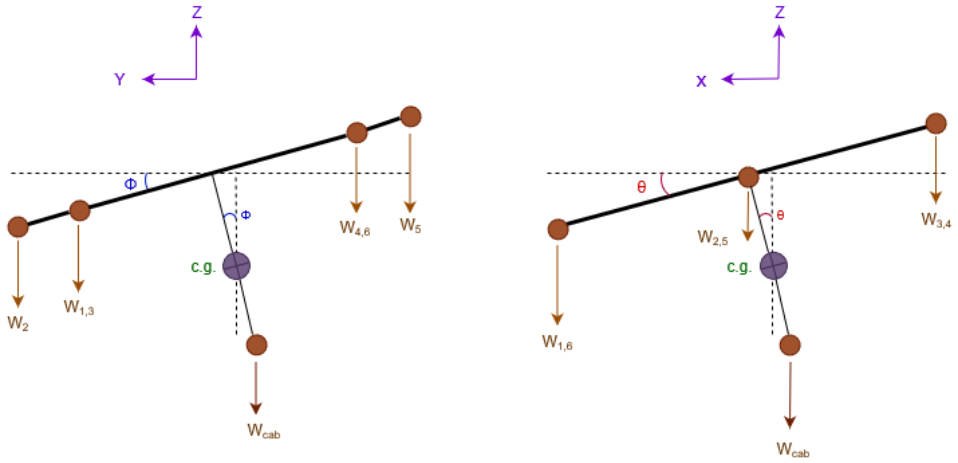

6.5. Rotor Actuators

The hexacopter has 6 arms, each with 2 coaxial counter-rotating rotors. Increasing and decreasing the rotational speed of the rotors allows to increase and decrease the thrust generated on each arm, enabling the control of the vehicle. The relationship between the thrust and the rotational speed of a rotor is given in Equation 6.11, as well as the torque generated by the rotor in Equation 6.12 [35]. In these equations, ρ is the air density, R is the propeller radius, Ω is the rotational speed of the rotor in rad/s and C_T as well as C_Q are constants.

$$T = k_b \Omega^2 \qquad \text{where} \qquad k_b = C_T \rho \pi R^4 \tag{6.11}$$

$$Q = k_d \Omega^2 \qquad \text{where} \qquad k_q = C_Q \rho \pi R^5 \tag{6.12}$$

The control moments of the vehicle are thus achieved by increasing the thrust in specific arms, and the thrust and torque can be controlled with the different speed of the rotors. In Equation 6.13 the relationship between the rotor speed and the total thrust T_o and the torques τ_x, τ_y for the upper rotors is shown, with the relationships being identical for the lower rotors. It can be seen that an increase in speed always increases the thrust, which is why to perform a torque one side increases speed while the other decreases it, in order to keep the overall thrust equal.

In Equation 6.13 the length elements l represent the x or y position of every rotor on the xy-plane. It is clear that increasing thrust in rotors 1,2,3 will cause a negative moment τ_x, whereas the opposite is true for rotors 4,5,6. With regard to the y-axis, rotors 2 and 5 have no effect, whereas rotors 1 and 6 cause negative moment τ_y and rotors 3 and 4 a positive one.

$$\begin{bmatrix} T_o \\ \tau_x \\ \tau_y \end{bmatrix}_{upper} = \begin{bmatrix} k_b & k_b & k_b & k_b & k_b & k_b \\ -k_b l_{y,1} & -k_b l_{y,2} & -k_b l_{y,3} & k_b l_{y,4} & k_b l_{y,5} & k_b l_{y,6} \\ -k_b l_{x,1} & 0 & k_b l_{x,3} & k_b l_{x,4} & 0 & -k_b l_{x,6} \end{bmatrix} \begin{bmatrix} \Omega_1^2 \\ \Omega_2^2 \\ \Omega_3^2 \\ \Omega_4^2 \\ \Omega_5^2 \\ \Omega_6^2 \end{bmatrix}_{upper} \tag{6.13}$$

$$\begin{bmatrix} T_o \\ \tau_x \\ \tau_y \end{bmatrix} = \begin{bmatrix} T_o \\ \tau_x \\ \tau_y \end{bmatrix}_{upper} + \begin{bmatrix} T_o \\ \tau_x \\ \tau_y \end{bmatrix}_{lower} \tag{6.14}$$

The torque caused by the rotational speed of the propellers in Equation 6.12 can also generate an actuator moment τ_z, which depends on the direction of rotation of the propeller, as seen in Equation 6.15, where $\mathbf{\Omega^2}$ represents the rotational speed vector seen in Equation 6.13. This equation is valid for the upper rotors, and in the case of the lower rotors all the signs of the k_d matrix are changed, following Figure 6.1.

$$\begin{bmatrix} \tau_z \end{bmatrix}_{upper} = \begin{bmatrix} -k_d & k_d & -k_d & k_d & -k_d & k_d \end{bmatrix} \begin{bmatrix} \mathbf{\Omega^2} \end{bmatrix}_{upper} \tag{6.15}$$

6.6. State Space Format

The final equations of motion can be expressed as in Equation 6.16 and Equation 6.17. In these equations it is possible to identify a total of 12 states for the system, a position and a velocity state for every degree of freedom, as seen in the state vector **x**. With this state vector it is possible to design a state space model in the form of $\dot{x} = Ax + Bu$ and $y = Cx + Du$.

$$\mathbf{x} = \begin{bmatrix} x & u & y & v & z & w & \phi & p & \theta & q & \psi & r \end{bmatrix}^T$$

$$\begin{bmatrix} \dot{u} \\ \dot{v} \\ \dot{w} \end{bmatrix} = \begin{bmatrix} rv - qw & g\sin\theta & & -\frac{1}{2m}\rho C_x S_x u|u| \\ pw - ru & -g\cos\theta\sin\phi & & -\frac{1}{2m}\rho C_y S_y v|v| \\ qu - pv & -g\cos\theta\cos\phi & \frac{T_o}{m} & -\frac{1}{2m}\rho C_z S_z w|w| \end{bmatrix} \tag{6.16}$$

$$\begin{bmatrix} \dot{p} \\ \dot{q} \\ \dot{r} \end{bmatrix} = \begin{bmatrix} \frac{I_{yy}-I_{zz}}{I_{xx}} qr & \frac{\tau_x}{I_{xx}} & \frac{G_x}{I_{xx}} & \frac{-J_r\Omega_r}{I_{xx}} q \\ \frac{I_{zz}-I_{xx}}{I_{yy}} pr & \frac{\tau_y}{I_{yy}} & \frac{G_y}{I_{yy}} & \frac{J_r\Omega_r}{I_{yy}} p \\ \frac{I_{xx}-I_{yy}}{I_{zz}} pq & \frac{\tau_z}{I_{zz}} & & \end{bmatrix} \tag{6.17}$$

To create the state space system is necessary to also define the required inputs. Technically, the input as defined in Equation 6.13 is the rotational speed Ω of all 12 rotors, a total of 12 input values. Such a large Multiple Input Multiple Output system is very had to tune, and thus following the method of [62], instead only four input values are used, namely the thrust T_o and the three torques τ_x, τ_y and τ_z as seen in Equation 6.18. Once the inputs are known, it is possible to compute the corresponding rotational speeds of the rotors with the inverse matrix of Equation 6.13.

$$\begin{bmatrix} u_o \\ u_x \\ u_y \\ u_z \end{bmatrix} = \begin{bmatrix} T_o \\ \tau_x \\ \tau_y \\ \tau_z \end{bmatrix} \tag{6.18}$$

However, it can be seen that these equations are very nonlinear, and thus to allow the equations to be expressed in state-space format they are linearized using Taylor series expansions. Furthermore, it is very complex to analyse a system with 12 states, and once the aforementioned equations are expressed in state space format it can be seen that the actual matrices are sparse. Thus, in order to simplify the tuning as

described in the following section, the general state space has been decoupled into four separate systems in order to deal with the independent motions of the vehicle.

6.7. PID Controller

In order to tune the response of the vehicle to the different disturbances experienced during the mission, a Proportional Integral Derivative (PID) controller is designed. PID controllers are the most fundamental and most widely used controllers in a wide range of industries, including aerospace. The goal of the PID controller will be to minimize the error between the desired state and the current state, as seen in Figure 6.3.

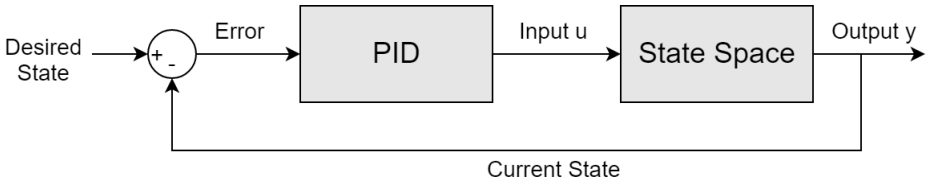

Figure 6.3: PID control loop used to tune the hexacopter

The proportional term of the controller K_P is a direct scaling of the error, and thus a large error will result in a large actuator action to reduce the error. The integral term K_I depends on the accumulated error over time, which allows to reach the desired state faster, but this can also cause a lot of overshoot. To compensate this the derivative term K_D is used, as this term predicts the future error and thus avoid overshoot and increase stability. The output of the PID controller is given in Equation 6.19.

$$u(t) = K_P e(t) + K_I \int_0^t e(s)ds + K_D \frac{d}{dt} e(t) \tag{6.19}$$

The values for K_P, K_I and K_D can be tuned in order to get an appropriate response, i.e. lowering overshoot and reducing delay time or settling time. In the following section, the PID tuning for every input will be presented, based on the decoupling of the equations of motion in the different flight regimes. This tuning will be done using the PID Control Tuner available on MATLAB in order to reach the required behaviour. However, to implement the derivative term K_D in Simulink a filter coefficient term N is used for an approximation as presented in Equation 6.20, where if N is sufficiently large, it will tend to $K_D s$.

$$K_D \frac{Ns}{s+N} \approx K_D s \tag{6.20}$$

6.7.1. Altitude controller

The take-off manoeuvre will require the vehicle to increase the total thrust in order to accelerate at a rate of 0.3 G's, as given by the mission profile in section 3.3. To do this the vehicle will follow a specified trajectory, which for simulation purposes will be represented as a ramp input going from 0 to 100 meters height in 10 seconds. This manoeuvre will be used for the tuning of the altitude controlled, whose characteristics are shown in Table 6.2. As can be seen, a small overshoot of 5 meters exists, but the altitude of 100 meters is reached in less than 10 seconds. The rotors must produce thrust load of 1.3 G's the perform this manoeuvre, which is represented in Figure 6.4.

6.7.2. Pitch controller

For the horizontal manoeuvres, the vehicle will start with a 2 m/s gust that causes a disturbance of 5 degrees, and the vehicle must return to its steady state condition at 0 degrees in less than 5 seconds. For pitch, this is done by creating a moment about the y-axis to return to the steady state condition. The PID controller needed to achieve this is presented in Table 6.3, where it is clear that the 5 second requirement is met. In Figure 6.5 it can be seen how the pitch angle has a small overshoot in order to return to its original

Table 6.2: Gain values and behaviour of the take-off manoeuvre

Altitude Controller Characteristics			
$K_{P,z}$	134.4106	Settling Time	9.91 s
$K_{I,z}$	2.2875	Overshoot	4.86 %
$K_{D,z}$	968.5216	Peak	105 m
N_z	259.4065	Closed Loop	Stable

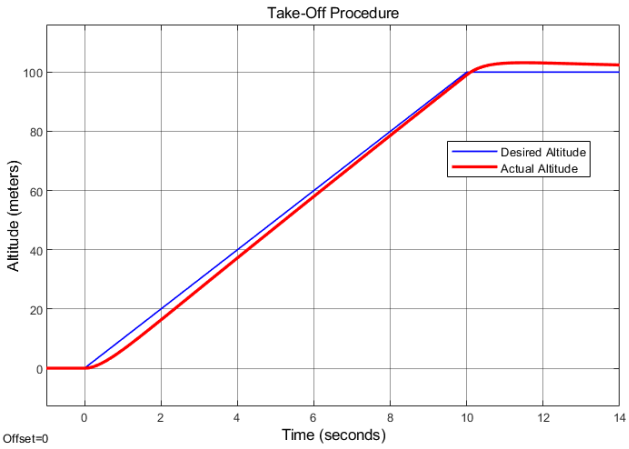

Figure 6.4: Take-Off manoeuvre of the hexacopter

x-location. The thrust setting needed from the engines for this manoeuvre is 1.37 G's, which is within the operating range of the propulsion system.

Table 6.3: Gain values and behaviour of pitch manoeuvres

Pitch Controller Characteristics			
$K_{P,\theta}$	1484.8618	Settling Time	4.91 s
$K_{I,\theta}$	1013.4641	Overshoot	9.16 %
$K_{D,\theta}$	533.7898	Peak	-0.45 °
N_θ	651.8671	Closed Loop	Stable

The pitch controller also allows to establish the speed of the vehicle, since there are no direct actuators controlling the horizontal speed of the hexacopter. Starting from hovering flight, the vehicle must be capable of reaching the cruise speed of 100 km/h by achieving a pitch angle of 18 ° in less than a minute, which can be seen is achieved in Figure 6.6.

6.7.3. Roll controller

The same process has been followed for the roll control as for the pitch control, which both have to fulfil the same requirement. A gust of 2 m/s creates a 5 degree disturbance, and the roll moment must return the vehicle to its equilibrium position in less than 5 seconds. This requirement was however impossible to meet due to the capability of the engines, and thus the manoeuvre is completed in 5.2 seconds, as seen in Table 6.4. The thrust setting needed for this manoeuvre is 1.8 G's, which is very high but within the margins of the propulsion system.

6.7.4. Yaw controller

As seen in Table 6.1, the moment of inertia is greatest about the z-axis, meaning manoeuvres about this axis are more cumbersome. However, the vehicle must be capable of turning around 180° in under 6 sec-

Figure 6.5: Pitch control of the hexacopter against a frontal disturbance

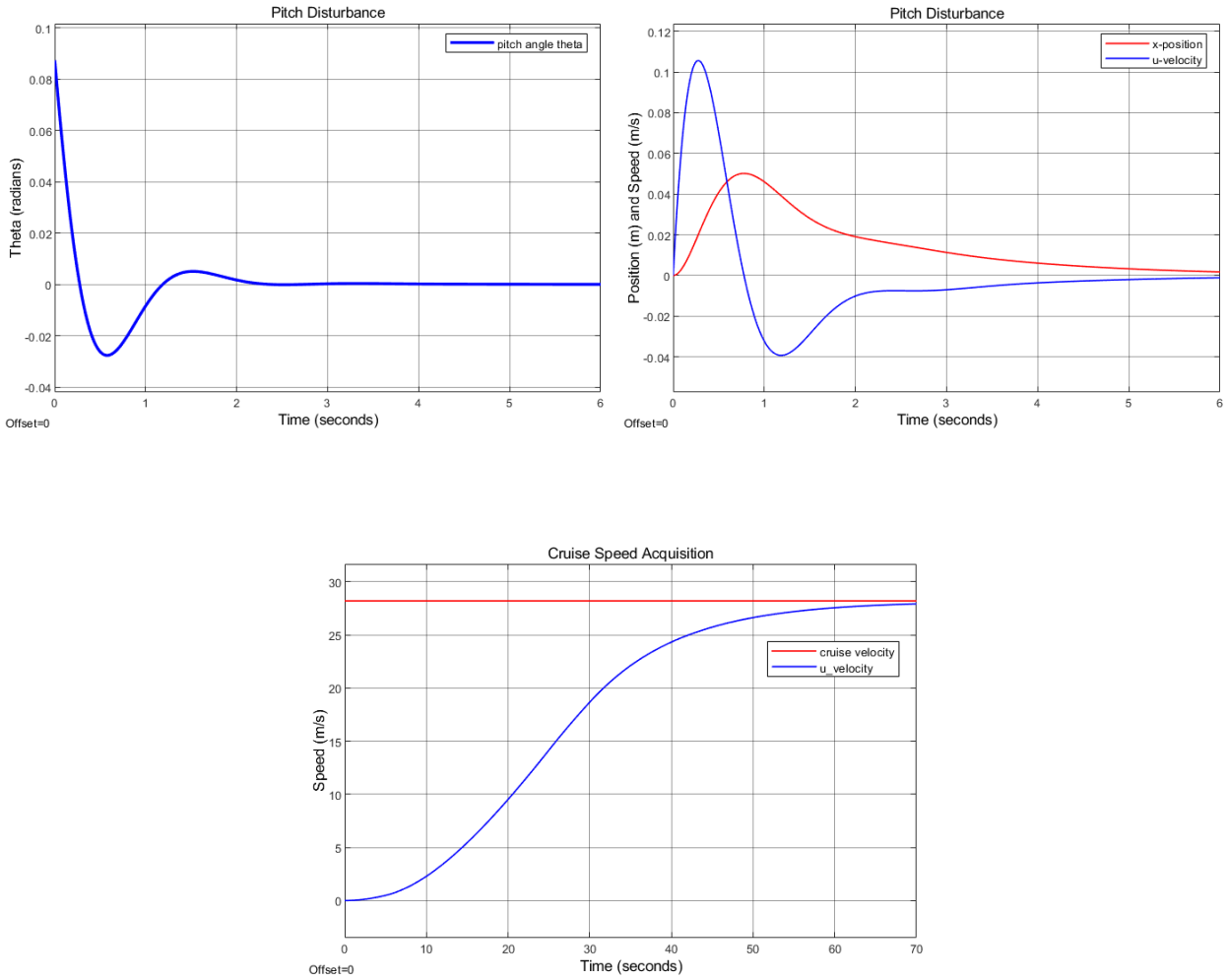

Figure 6.6: Cruise speed acquisition through pitch control

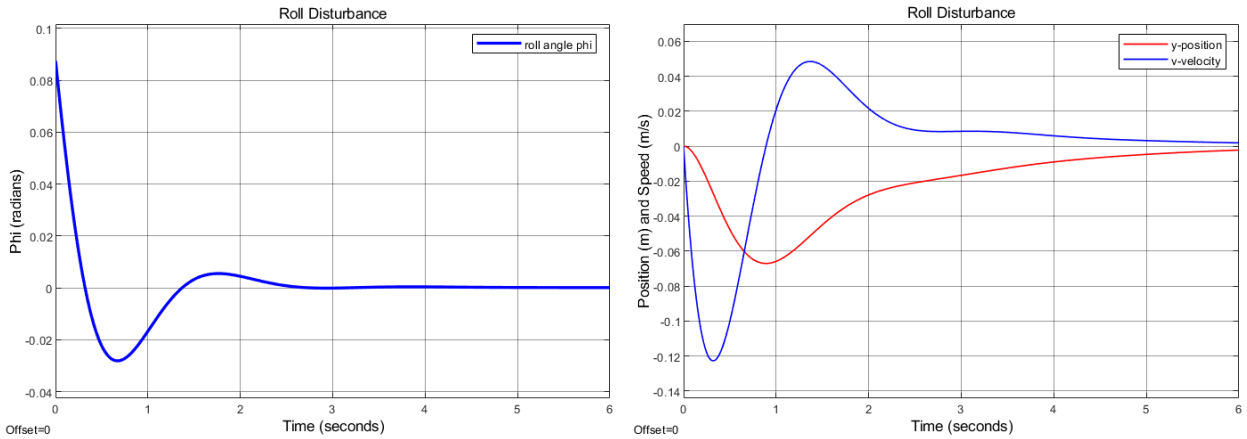

Figure 6.7: Roll control of the hexacopter against a lateral disturbance

Table 6.4: Gain values and behaviour of roll manoeuvres

Roll Controller Characteristics			
$K_{P,\phi}$	1646.0227	Settling Time	5.18 s
$K_{I,\phi}$	1011.1573	Overshoot	11.3 %
$K_{D,\phi}$	664.1660	Peak	0.55 °
N_{ϕ}	555.5639	Closed Loop	Stable

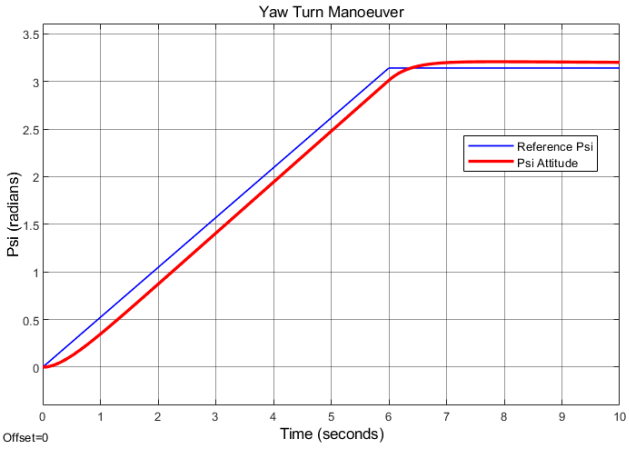

Figure 6.8: Yaw control of the hexacopter for a full turn

onds, which is achieved by changing the speeds of the clockwise and counterclockwise rotating propellers, generating a torque following Equation 6.12. A PID controller can be designed to perform this manoeuvre, as specified in Table 6.5. To perform the manoeuvre, represented in Figure 6.8, the engines must operate at a load factor of 1.95 G's, which was to be expected given the high moment of inertia and the unavailability of direct thrust to control the yaw. Regardless, the requirement can be met, but it is possible that the vehicle can benefit of a lower power consumption and quicker turning if a combination of roll and pitch is used to yaw instead of using differential speeds to control the yaw.

Table 6.5: Gain values and behaviour of yaw manoeuvres

Yaw Controller Characteristics			
$K_{P,\psi}$	42.6631	Settling Time	5.96s
$K_{I,\psi}$	0.673	Overshoot	2.34 %
$K_{D,\psi}$	600.9139	Peak	3.6°
N_{ψ}	309.0159	Closed Loop	Stable

6.8. Verification and Validation

The MATLAB code used to evaluate the motion of the vehicle was verified by a combination of various test, including:

- **Hand Calculations** The moments of inertia computed with the code were compared to the calculations made by hand to ensure consistency and detect any errors in the code. Furthermore, the location of the C.G. was found to be between the cockpit and the hub but closer to the cockpit, as was to be expected from the heavier cockpit.

- **Output Unit Tests** After the construction of the state-space, the outputs of the computations were checked to see whether the correct units are used. This allowed to find various errors regarding the

use of degrees and radians within the code.

- **Zero Thrust Test** When zero thrust is applied, i.e. the input value of u_o is zero, the vehicle is found to decrease in altitude following the gravitational acceleration, as is to be expected.
- **Rotation Speed Test** An increase in the speed of a specific rotor was proven to generate a moment in the correct x- and y-direction. This includes the case for symmetrical pairs of rotors having their speeds increased, which results in the generated moments cancelling each other out.
- **Sign Checks** When a positive change of position or attitude is required, a positive change of force or moment is generated to reach the desired state.
- **Parallel Code** State space calculations where mainly performed in MATLAB, but a parallel code was developed in Python by a different person in order to compare the results of the simulation calculations, which were confirmed to be consistent.
- **Behaviour Test** When simulating flight modes for the controlled, the other state variables behaved in ways that are to be expected, as can be seen in Figure 6.5 and Figure 6.7.

As for validation, the methods used in this chapter have been physically tested by the authors of the papers cited. However, to validate the computations for the hexacopter, a number of tests need to be performed:

- **Single Engine Thrust Test** In order to adjust the k_b value in Equation 6.11 it is necessary to test the COTS purchased engines. The test must validate the relationship between the rotational speed and the thrust generated by the rotor.
- **Single Engine Torque Test** Similar to the previous test, the relationship between the rotational speed and the generated torque of the engine must be validated to adjust the k_d value in Equation 6.12.
- **Rotor Gyroscopic Effect Test** This test must measure the gyroscopic torque generated by turning a rotating propeller in order to implement the results into the equations of model. Such a test would preferably include a counter-rotating propeller such as to have physical evidence that gyroscopic torques are indeed cancelled out.
- **System Flight Test** To validate the real-world efficiency of the controllers, a full flight test must be performed on the vehicle. The measurements taken on this flight test would allow to fine-tune the gains on the four PID controllers. A first small-scale test should be performed on a model to make adjustments before implementing the controllers on the full-scale prototype.

6.9. Sensitivity Analysis

As mentioned at the beginning of this section, the hexacopter has an insignificant amount of inherent stability. The stability is created completely artificially and thus the control system is crucial for the operation of the vehicle. At the current stage of the design, many values have been well-established, but changes are still possible and can affect the efficiency of the control system. In this section the sensibility of the control system to such changes is presented.

Mass Increase During the detailed design of the vehicle, a big increase in weight was observed compared to initial estimations. Such a large increase in the future is unlikely, but still possible. An increase in mass would be detrimental for the control system, as the current selection of engines would have a smaller operations thrust margin, meaning that current manoeuvres might not be possible. If still possible, the settling time would be increased and the requirements will not be met.

Shift in CG An increase in weight can also cause a shift in CG. If this CG shift is towards the cockpit, it will decrease the stability of the vehicle, and again the settling time will increase as the vehicle will take

longer to reach the final value, and a larger overshoot could appear. If the CG shift is towards the hub, this is beneficial for stability and thus the settling time decreases, the overshoot decreases and less thrust is needed to perform manoeuvres.

Increase of Moments of Inertia An increase in mass will very likely increase the moments of inertia, which will increase the resistance of the vehicle against manoeuvring. This will certainly increase the settling time, meaning that the requirements will not be met if the gains are not adjusted. And the possibility exists that even then the engines cannot perform the maneuvre.

Change of Aerodynamic Characteristics The aerodynamic profile has not yet been completely established, as the airflow around the rotors and vehicle is complex and difficult to estimate. In the case of an increase of the drag factors, overshoot will decrease as there is more resistance against movement. Settling time will increase as the larger air resistance will slow down the error reductions in case of disturbances and it will also take longer to reach the reference state, e.g. for the forward speed u.

6.10. Conclusions

The additional requirements set at the beginning of this chapter can be checked for compliance with the set settling times following the design of the PID controllers:

Table 6.6: Settling Time Compliance Matrix for the Control Subsystem

	Req. Value	**Actual Value**	**Comment**
PAM-MAN-1	10 s	9.91 s	✓
PAM-MAN-2	60 s	56.2 s	✓
PAM-MAN-3	5 s	4.91 s	✓
PAM-MAN-4	5 s	5.18 s	Insufficient Thrust
PAM-MAN-5	6 s	5.96 s	✓

These PID controllers have been designed for independent flight modes, but for the development of the vehicle the 4 different flight modes must be integrated between each other in order to optimise the flight profile. This would allow to transition smoothly between take-off and cruise for example, or even allow to merge the two manoeuvres during the mission.

7 Avionics

For navigation, communication and control, the hexacopter has to be equipped with the appropriate avionics, i.e. all the sensors needed that allow for autonomous operation. In this chapter, the avionics systems are selected for the vehicle and discussed in an appropriate level of detail. The avionics that will be included are the following:

- **Flight Control Computer** The FCC is the core of the avionics system, responsible for the full control of the aircraft and the processing of all the sensor data in order to remain on the desired flight envelope. This system is considered as a critical system, thus extra attention is given to its redundancy. However, most of the commercially available flight computers are already designed to be redundant.
- **Navigation System** This system must determine the location of the vehicle with sufficient accuracy in order to successfully cruise and land to the required landing sites.
- **Communication System** The vehicle must establish a digital datalink that creates a data transmission bridge between the vehicle and the ground station, the control tower, or other vehicles.

- **Relevant Sensors** The aircraft relies on this system to measure and transmit all the necessary flight parameters such as airspeed, temperature, pressure, altitude and attitude.

For the hexacopter, four COTS avionics systems will be acquired: an autopilot, a laser altimeter, an airborne radar and a night vision capable imaging system. The autopilot selected is the Piccolo II, developed by Cloud Cap Technology [19]. This system provides a complete integrated avionics solution that includes the flight computer, navigation sensors (GPS), attitude sensors, air pressure sensors and communication systems. As navigation sensors, the Piccolo II combines the use of a GPS receiver and Inertial Measurement Units (IMU). For communications a datalink radio is included, as well as ported air data sensors.

For navigation, the IMU is precise over short distances, but the errors drift over time and must be corrected with another sensor, namely the GPS receiver. However, the GPS system for civilian use has about 4 meters horizontal accuracy and vertical accuracy is even worse [36]. It can be improved with a Ground Based Augmentation System (GBAS) installed on the ground base or control tower which would transmit to the vehicle Differential GPS (DGPS) data. The GBAS would determine the location of the station given by the GPS and compare it to the real location, and thus the difference can be used by the vehicle to determine its real location. Accuracy with DGPS increases to 0.21 meters [56].

Secondly, the TASE-400 HD imaging platform also developed by Cloud Cap Technology will be used. This platform is lightweight and compact in size and can function during day and nighttime operations. Furthermore, it is equipped with an image processing system capable of target tracking, scene steering and electronic image stabilisation [20].

Thirdly, the ULAB-D1 air-to-air radar developed by Ainstein.ai will be used. This radar system enables safe operations and delivers very good detection and tracking capabilities enabled by Digital Beam Forming and on-board real-time processing [7]. The radar will complement the GPS and IMS of the autopilot for positioning.

Lastly, the LR-D1 altimeter developed by Ainstein.ai will be used. This system provides accurate altitude measurement in different operating environments enabling autonomous takeoff and landing even in bad weather conditions. It has an advanced cross-validation technology that continuously monitors multiple data sets for higher accuracy [6].

Figure 7.1 shows the avionics systems used and table 7.1 shows their specifications.

Table 7.1: Avionics Systems Specifications

	Dimensions [mm]	**Weight [kg]**	**Power [W]**	$V_{in}[Volts]$
Picollo II	142.00 x 46.00 x 62.6	0.2	4	8-20
TASE400 HD	ϕ 177.8 & Height 266.7	3.62	35	10-30
LR-D1	140 x 102.5 x 30	0.3	12	12-30
ULAB-D1	260 x 190 x 55.5	3	30	10-14

Figure 7.1: Avionics systems

7.1. Hardware, Electrical and Data Handling Block Diagram

After all the design choices made throughout this report, a hardware, electrical and block diagram can be made. In this diagram, the layout of all functional hardware parts, there electrical and data interconnection will be depicted as precise as currently possible. This block diagram can be seen in figure 7.2.

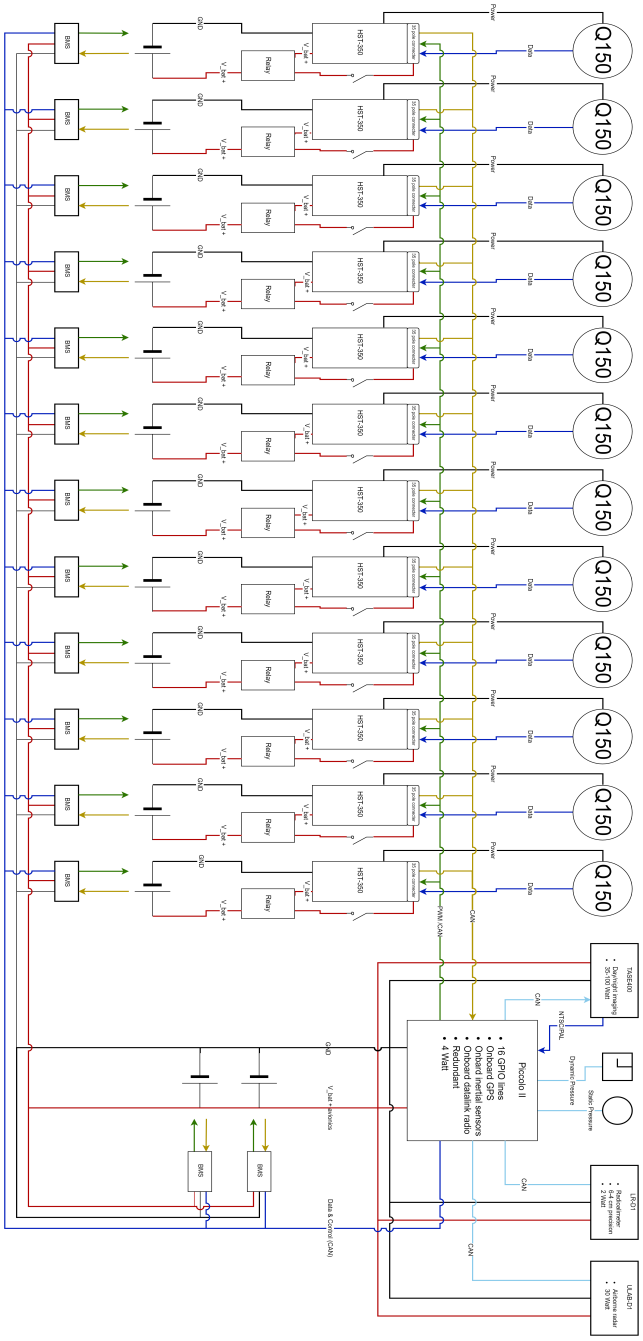

Figure 7.2: Hardware Block Diagram of Avionics Systems

In this block diagram, it can be clearly seen how the Q150 motor is connected to the ESC (for a more specific overview figure 4.33). The motor gives feedback data to the ESC over a 10 pole connector. This data mainly consist of phase timing data by Hall sensors (6 of the 10 poles). Two poles to power the hall sensor, 1 pole to GND of the ESC data unit and a motor temperature sensor [39]. Furthermore the ESC can then be connected to the flight computer (the Cloud Cap Piccolo II) via the CAN data protocol (more

about CAN will be explained further down this section). Then the ESC gets commands back from the flight computer over via CAN and as a separate PWM signal. The PWM signal needed is described in [39] and depicted as a cut-out from this manual in figure 7.3, seen below.

b.) 'pwm control' (voltage control)

- Uses input signals of pwm-input (cp. Table 3-2, not depicted in Fig 2-1)
- Also, the PWM can be adjusted via CAN bus (cp. Table 3-2)
- 'pwm control' represents a typical **voltage control** of a BLDC-engine.

The PWM-Input signal has to meet the following (Servo-PPM)-requirements:

t_d = 1.0 ms up to 2.0 ms	: pulse length (on-time)
f_{per} = 50 Hz up to 495 Hz	: period of the pwm-signal
	0 V: Low-Signal during off-time t_{per} - t_d
	5 V: High-Signal during pulse length t_d

Minimum value:	t_d = 1.0 ms pulse length (-100% = reverse)
Middle setting:	t_d = 1.5 ms pulse width (0% = neutral position, engine off)
Maximum value:	t_d = 2.0 ms pulse length (+ 100% = forward)

Note: In these first two variants, it is possible to operate the controller in conjunction with the display without any CAN control. The display transmits the activation signal via the CAN - Bus. Subsequently, the power can be controlled with a potentiometer (a.) or a PWM signal (b.).

Figure 7.3: PMW ESC control input signal [39]

Furthermore, the Cloud Cap Piccolo II is a very capable flight computer. It has onboard inertial sensors, air data sensors (dynamic and static pressure), GPS sensors, an onboard datalink radio, and an EMI (electromagnetic interference) shielded enclosure. It can communicate with the rest of the systems via its two CAN-bus interfaces and its 16 GPIO (General Purpose Input Output) lines. The GPIO lines will be used to sent the PMW signal over to the ESCs. To add to the Piccolo II 's capabilities, extra sensors are added to the vehicle.

These extra sensors are the Ainstein LR-D1 laser altimeter and the Ainstein ULAB-D1 airborne radar system. These units will be used to aide with precision landings and collision avoidance respectively. These systems also communicate via the CAN protocol to the flight computer.

The Ainstein TASE400 imaging system, will make sure the vehicle will be able to preform day- and night-time missions. It is controlled via a CAN signal from the flight computer. The data received from the TASE400 system will be an image using either NTCS or PAL.

7.1.1. CAN bus data protocol

The CAN data protocol will be the main protocol used in PAMELA. Therefore it is helpful to give a short explanation of what the CAN bus system is. The explanation of the CAN bus system in this section is based on [22].

Every vehicle usually uses multiple electrical control units (ECUs). These ECUs, also called nodes, need to

communicate amongst each other to fulfil various functions. The CAN bus protocol allows these nodes to communicate with each other without the need for complex wiring in between them. To quote [22], there are five critical advantages of using the CAN bus communication:

1. Low cost: ECUs communicate via a single CAN interface, i.e. not direct analogue signal lines, reducing errors, weight, costs.
2. Centralized: The CAN bus system allows for central error diagnosis and configuration across all ECUs.
3. Robust: The system is robust towards failure of subsystems and electromagnetic interference, making it ideal for e.g. vehicles.
4. Efficient: CAN messages are prioritized via IDs so that the highest priority IDs are non-interrupted (key in e.g. vehicles).
5. Flexible: Each ECU contains a chip for receiving all transmitted messages, decide relevance and act accordingly - this allows easy modification and inclusion of additional nodes (e.g. CAN bus data loggers).

Today's CAN systems have a maximum data transfer rate of 1 mb/s, altough with newer versions 8 mb/s by 2020 is exected to be possible. The data messages that are send over the CAN bus network are made up of the sections depicted in figure 7.4, which represents the CAN 2.0B protocol.

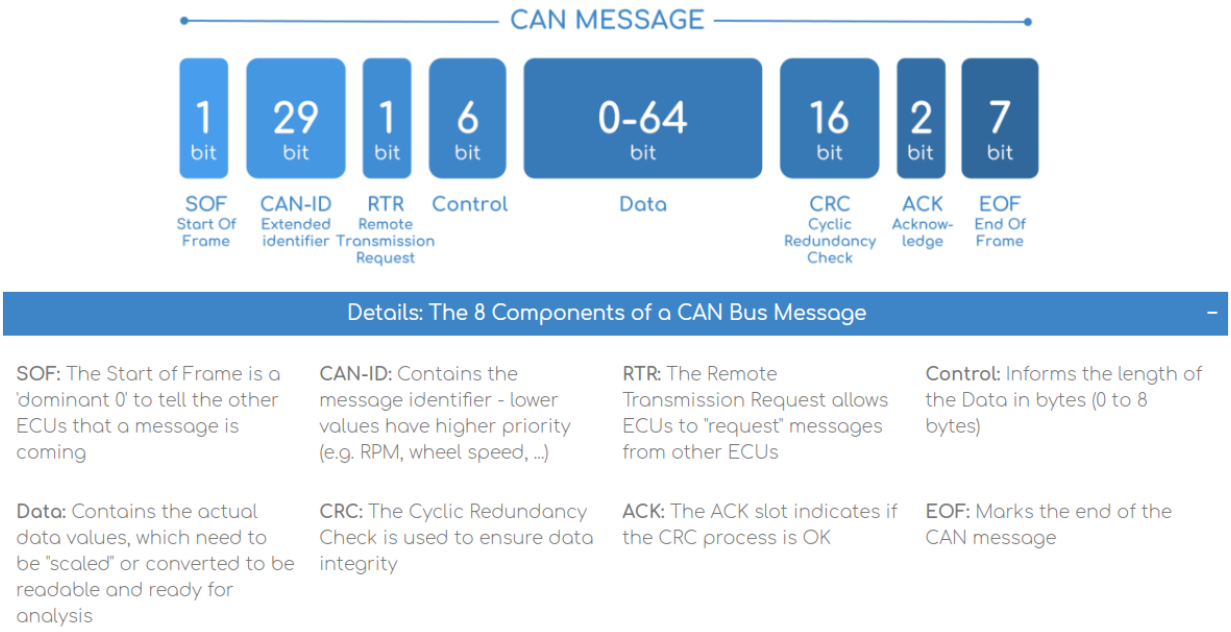

Figure 7.4: A typical CAN message format for CAN 2.0B [22]

With this short description of the CAN bus system, this section is concluded. A lot more literature on the CAN bus data protocol CAN be found online, but is considered outside of the scope of this report.

7.2. Software Flow Diagram

The software flow diagram for this design case explains how the autonomy system of the hexacopter is implemented (see figure 7.5). The system begins with what's called the autonomy driver which consists of an altimeter, imaging system, and IMU. The autonomy driver has the fundamental role of collecting and processing the data observed from the vehicle surrounding environment. This data goes then to the

Scale Estimator which basically runs the Levenberg-Marquardt optimization computing the best estimate of desired parameters. Afterwards, all calculated parameters are sent to the VSLAM unit which in its turn constructs a 3-D map of the outside environment providing the vision. subsequently, the Kalman Filter algorithm gets executed by the Pose Estimator that provides more accurate estimates of the given variables. At this point, the path plan is ready and the controller gives an order to the vehicle to perform the desired movement [68].

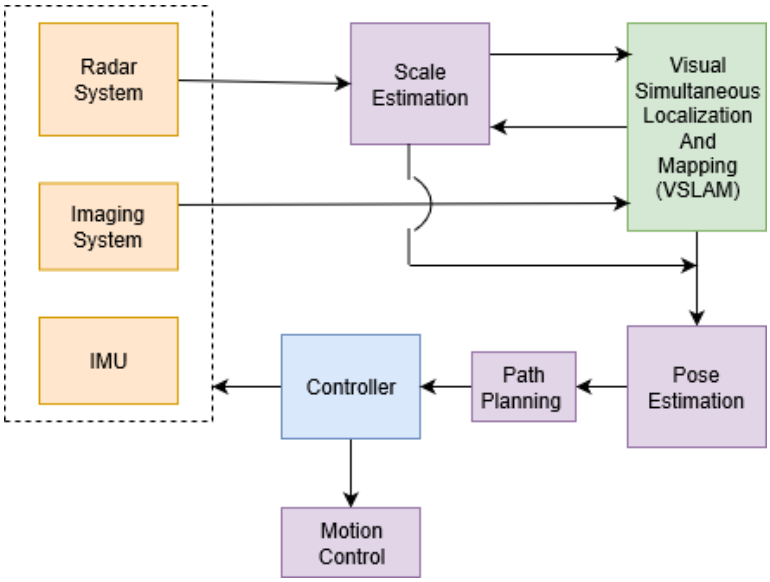

Figure 7.5: Software Flow Diagram

7.3. Cost Estimation

The cost is an important factor to be considered when selecting the avionics systems. Keeping in mind, these systems also have to meet the requirements in order to successfully serve the application scope of the vehicle. Therefore, the system features should not be compromised for the cost.
However, the manufacturers of the chosen avionics systems (CloudCapTech & Aeinstein.ai) have been contacted by the team in order to have an indication about the prices. Unfortunately, this was unsuccessful. Alternatively, doing a research in online helped the team to make an price estimation for each system. In table 7.2, the estimated cost for all systems can be found.

Table 7.2: Avionics Systems Cost

	Cost [€]
Picollo II	7100
TASE400 HD	5000
LR-D1	600
ULAB-D1	2300
Total	15000

8 Structures & Materials

In this chapter, numerous subsystems composing the structures of the vehicle are analyzed, namely: the rotors arms, the hub, the aerodynamic profile, the fuselage, the landing gear, the safety system and other miscellaneous elements. It describes the design methods and process used, including a sensitivity analysis and verification & validation procedure if applied. Furthermore, an explanation on the packaging decision will be presented with a mass and cost breakdowns to summarize the structural elements' characteristics. Finally, an in-depth investigation will be performed on recyclability, sustainability and technical risk assessment on the structures of the vehicle.

8.1. Rotor Placement

To set up the rotors placement, the initial step is to look at the predefined requirements to help constrain the rotor positions and find a favourable configuration. From the customer it is given that 'The indicative maximum vehicle size is 4x4x2 m^3' (**PAM-SH-CLI-2**); from the propulsion department, the rotors' diameters were defined in section 4.3 to be 1.3 meters; from the stability & control department, after analysis done in the Midterm report [10], it was decided to put the rotors above the fuselage for improved stability, increased ground clearance and safety in case of rotor detachment; and from the aerodynamics department, it will be explained further in the chapter that ducts will be included to the rotors for better efficiency, decreased noise and improved safety. With these requirements in mind, it was desired to use the available space as efficiently as possible, leaving 5 centimetres around the rotors for possible ducts and adding a clearance of 2 cm between the ducts as a safety margin. Including all these constraints, the geometry of the copter is determined in figure 8.1 below, drawn on SolidWorks for easy modification and visualization. For now, it is assumed that the rotors arms are meeting in the center for simplicity.

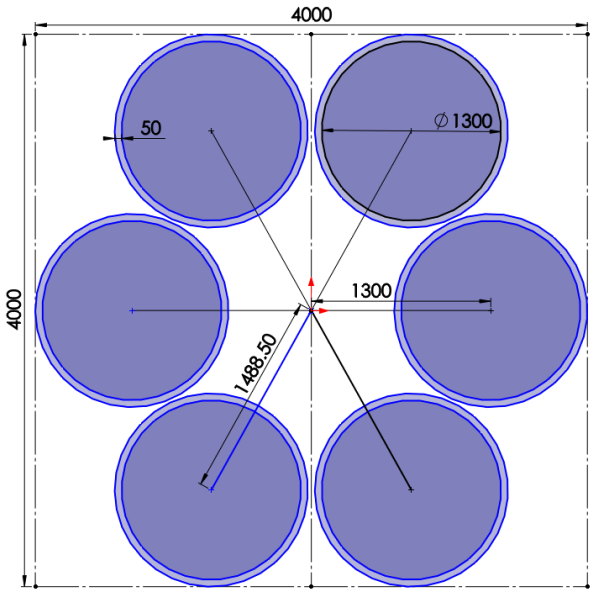

Figure 8.1: Geometry of the vehicle.

8.2. Rotor Arms

After the placement of the rotors is decided upon, the arms are to be designed for. The arms serve as the load carrying structures that transfer the thrust loads from the rotors to the main body of the structure. Each arm will be attached to the chassis of the vehicle using a central connection unit, connecting the motors to the rest of the vehicle through motor mounts. The arm dimensions in terms of length have already

been stipulated as seen in figure 8.1, therefore this section will deal mainly with cross section design and material selection.

8.2.1. Method

Since the arms will be mainly loaded by point and distributed loads along their lengths, it is useful to use bending theory for their stress analysis and to treat them as individual cantilever beams. The forces acting on the beam are shown in 8.2 and 8.3. The first diagram shows the view in the x-y plane and the latter is a view from the top of the vehicle, the z-x plane. In the diagrams, the distributed load w_a represents the weight of the beam, T is the combined thrust of the two motors, W_m is the weight of the motors, p is the wind pressure, and M_n is the torque from the rotation of the motors.

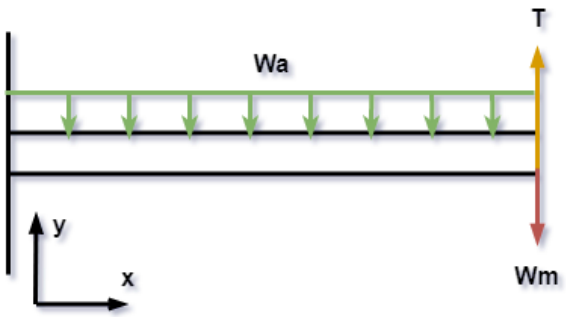

Figure 8.2: FBD of the arm in the x-y plane.

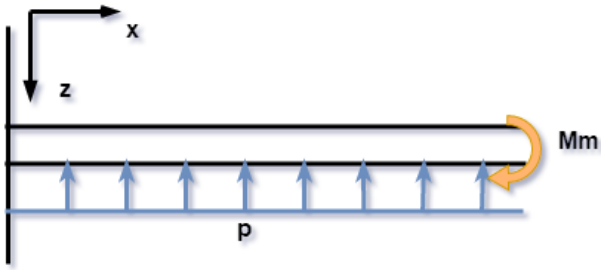

Figure 8.3: FBD of the arm in the x-z plane.

From the figures above, it can be seen that the beam will be subject to both normal stresses, due to bending, and shear stresses. The normal stresses can be calculated, through the use of the following equations;

$$\sigma_x = \frac{M_z I_{yy} - M_y I_{yz}}{I_{zz} I_{yy} - I_{yz}^2} y + \frac{M_y I_{zz} - M_z I_{yz}}{I_{yy} I_{zz} - I_{yz}^2} z \tag{8.1}$$

where

$$M_z = (l-x)(T - W_m) - \frac{1}{2}(l-x)^2 W_a \tag{8.2}$$

and

$$M_y = M_m - \frac{1}{2} p (l-x)^2 (a[l-x] + a[l]) \tag{8.3}$$

In equation 8.3, the expressions of the form $d[n]$ refer to the value of d at n. So for example, $a[l-x]$ refers to the value of a at the location $l-x$, which varies depending at which point on the beam you take the moment around. a represents a cross-section parameter which will be presented later on in figure 8.5

Moreover, the shear stress can be calculated through;

$$q = -\frac{S_z I_{yy}}{I_{yy} I_{zz} - I_{yz}^2} \int_0^s t z ds - \frac{S_y I_{zz}}{I_{zz} - I_{yz}^2} \int_0^s t y ds \tag{8.4}$$

where

$$S_z = p(l-x) \tag{8.5}$$

and

$$S_y = w_a (l-x) - (T - w_m) \tag{8.6}$$

In addition, the deflection of the arms has to be taken into account in the analysis as there are limits for tip deflections, and also this will have vibrational effects on the structure.

The deflections can be calculated by using simplified cantilever beam deflection theory. Since the arms

only experience point loads at the free ends of the beam, distributed loads along their length, and a couple moment at the free end, only three deflection equations are needed, namely;

$$\delta = \frac{Px^2}{6EI}(3l - x) \tag{8.7}$$

for the free-end point loads,

$$\delta = \frac{\omega x^2}{24EI}(x^2 + 6l^2 - 4lx) \tag{8.8}$$

for the distributed loads, and

$$\delta = \frac{Mx^2}{2EI} \tag{8.9}$$

for the couple moment.

These equations are all functions of the beam's length, E-Modulus, moment of inertia, and the x position along the beam. To get the total deflection, the individual deflections due to separate loads are superimposed on each other. This results in two smooth functions describing the deflections along the y and z axes.

As was stated, the deflections can have an effect on the vibrations through the arms due to thrust forces. Depending on the rate at which thrust is applied, the arm will vibrate in one mode or another, which is why it is necessary to find the modes of vibration and natural frequency of the beam. To do this, the beam can be modeled as a vertical spring with a force pushing down on it. For the vibrational analysis in the y direction and neglecting the beam's weight, this force will be $(T - W_m)$, and for the vibration in the z axis, it will be the full force from the pressure. An illustration of this simplification is displayed in figure 8.4.

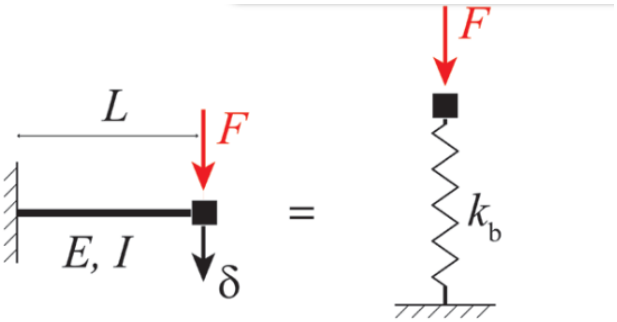

Figure 8.4: Simplification of Cantilever Beam for Analysis.

where the equivalent stiffness, k_b, of the spring is;

$$k_b = \frac{3EI}{L^3} \tag{8.10}$$

so that the deflection equation is;

$$m\ddot{x} + kx = T - W_m \tag{8.11}$$

where m is the mass of the beam. The solution to the above equation is;

$$x = A\sin(\omega_n + \phi) \tag{8.12}$$

and the natural frequency for the first vibrational mode;

$$\omega_n = \sqrt{\frac{mL^3}{3EI}} \tag{8.13}$$

For higher modes, the above equation will be multiplied by a certain constant. It is to be noted that this vibrational analysis is only done for specific thrust levels such as during cruise, hovering, etc. Time variant thrust vibration analyses are too detailed for the level of this project and will not add much more information. The main source of vibration will come from the motors and not the thrust differential.

8.2.2. Cross-section

Now that the equations for stresses and deflections have been established, it is possible to begin with the cross section design. In order to determine the beam's cross section, firstly, three different shapes are chosen. They are all assumed to be thin-walled, although the thickness is left as a variable to be optimized in 8.2.4. These shapes all come from literature and are commonly used as cross sections in beams. Furthermore, since the arms experience stress on two perpendicular axes, and for the sake of manufacturability and computational simplicity, all beams chosen are symmetric. The first option, the oval shape, is chosen in order to represent all possible circular and oval configurations. This is done by setting the major and minor axes' dimensions as variables a and b, which will be explained more in depth in 8.2.4. The next cross section is a "4-chamber box/rectangle", which basically is a combination of two I-beams at 90 degrees where the flanges come together as corners on the tips. Lastly, the final cross-sectional shape is simply two I-beams at 90 degrees without the flanges on the extremes, giving a "cross" shape. The reasoning behind the last two options comes from the fact that the I-beam is the most efficient cross section at bending, with respect to weight, at an axis parallel to its flanges [27]. This is mainly due to the distance of the flanges from the neutral axis, which greatly increase the section's moment of inertia. The "cross" shape was included to compare the effect of the flanges on the stress in each design. These cross-sections are presented in the illustration below.

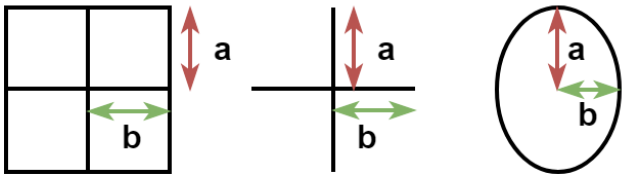

Figure 8.5: Possible cross-sections for the rotors arms design.

The arms will also have to house the cables from the ESCs to the motors and protect them from the harsh coastal environment. However, not all of the options are closed. This is not of primary concern at this stage. If it turns out that the open section is most efficient in carrying the loads, adjustments can be made to enclose the cabling, such as adding a flexible polymer casing around the arms.

8.2.3. Material choice

With the basic cross-sectional shape options laid out, the beam can be given more specific magnitudes in terms of taper, thickness, and dimensions at root and tip. Before that it is done, however, parameters of the material, such as the E-Modulus, yield stress and density have to be identified. This is where the material choice ties into the analysis, as these quantities will differ for different materials.

The materials selection will be limited to three types; Aluminum 7075-T6, Carbon Fiber and Grade 3 Titanium; a high strength titanium that provides excellent corrosion resistance and good weldability [47]. These three material types are commonly used in the aerospace industry for structural applications and all have very high records of performance for similar applications. They are all also lightweight and highly resistant to corrosion, which in the case of this vehicle, is something important to take into account. The properties of these materials are displayed in table 8.1 below.

Table 8.1: Material Properties.

	Aluminum 7075-T6	**Carbon Fiber**	**Grade 3 Titanium**
Yield Stress [MPa]	503	3,500	440
Density $[kg/m^3]$	2810	1750	4500
E-Modulus [GPa]	71.1	288	105
Cost [€ / kg]	3.2	20	17.8

8.2.4. Optimization

To make a decision on the best-fitting material, taper and cross-sectional shape, a program is written on python to calculate the stresses and deflections along the beam's length for varying materials, cross-sections, taper ratios, and thicknesses. In this program, the major and minor axes of the cross section (parameters a and b) at the root, the root thickness, and the rates of decrease of both the thickness and axes from root to tip, are held as variables.

Before the simulation is run, limits are set for the stress and deflection. In order to include a safety margin of at least 2, which is a valid margin in the aerospace industry, the maximum stress on the beam at any point is limited to half the yield stress of the respective material. Also, the deflections are limited to approximately 1 cm at the free ends. The reasoning behind this comes from aircraft structural beam theory [55], to reduce vibrations. Additional constraints are placed on the root and tip diameters based on the total height requirement of 2 m and the 20 cm distance between the two motors at the arm tip.

As was stated, the minor and major axes of each shape decrease from root to tip according to:

$$a = a_0 - d \cdot x \tag{8.14}$$

$$b = b_0 - d \cdot x \tag{8.15}$$

where d is an arbitrary variable that can be altered for optimization. This is also true for the thickness, which can be decreased at a rate d_t.

Parameters such as the cross section area and moment of inertia are calculated at different steps along the beam with corresponding geometric parameters. Through this, the internal stresses and deflections at each step can be calculated. This analysis is done for each material, by altering the E-modulus, density and yield stress.

On the first iteration, arbitrary geometric parameters are set and only the material is altered. This yields values for the beam mass, maximum stress, and max deflections in y and z.

Table 8.2: Aluminum beam properties for different cross-sections.

	Circle	Cross	Square
Mass [kg]	0.91	2.39	7.19
Stress σ **[MPa]**	253.6	787.7	56.8
δ_y **[m]**	0.022	0.028	0.004
δ_z **[m]**	0.014	0.045	0.003
Cost [€]	3.1	7.65	23

Table 8.3: Titanium beam properties for different cross-sections.

	Circle	Cross	Square
Mass [kg]	1.46	3.84	11.52
Stress σ **[MPa]**	253.6	787.7	568.8
δ_y **[m]**	0.015	0.019	0.003
δ_z **[m]**	0.009	0.030	0.002
Cost [€]	26	68.7	205

Table 8.4: Carbon-fiber beam properties for different cross-sections.

	Circle	Cross	Square
Mass [kg]	0.57	1.49	4.48
Stress σ [MPa]	253.6	787.7	56.8
δ_y **[m]**	0.007	0.008	0.001
δ_z **[m]**	0.004	0.014	0.001
Cost [€]	11.4	29.8	89.6

From the information gathered on the tables, many things can be said on both the materials and the cross sections. Firstly, it has become clear that the "square" cross-section, although performs better at carrying the loads and in deflection, will be far too heavy and expensive to manufacture. Therefore, the square cross section will not be further considered.

Secondly, comparing between the "cross" and the oval section, it can be seen that on average, the deflections of the cross are 1.2 times as high as the deflections on the oval. Since none of the maximum stresses for any cross-section material combination reach anywhere close to the yield stress, we can safely disregard the "cross" design on the basis of deflection without placing too much emphasis on the stress. This leaves the oval section as the final cross-section.

With the choice made on the cross section, the material can now be decided upon. Comparing the price of materials for the oval section, it can be seen that the carbon fiber is most expensive. However, it is the lightest of the three, has the lowest maximum strength along the beam, and the lowest deflections, which also comply with the requirements. The final selection is therefore the oval cross section made of carbon fiber.

Now the arms can be optimised by varying the geometric parameters from root to tip to get the optimal stress (half of the yield stress) and weight. Once this has been done in the program, the final beam geometry is set. Figure 8.6 and 8.7 display the geometries of the two arms. It is to be noted that calculations were done for the longer arm, with a length of 1.488 m. The shorter arm will have the same thickness and dimensions as the longer arms for the root and tip cross sections. This means the shorter arms will be over-designed. However, this design choice is made for the sake of consistency, and to cut down costs by having the same sized motor mounts and arm hub connections.

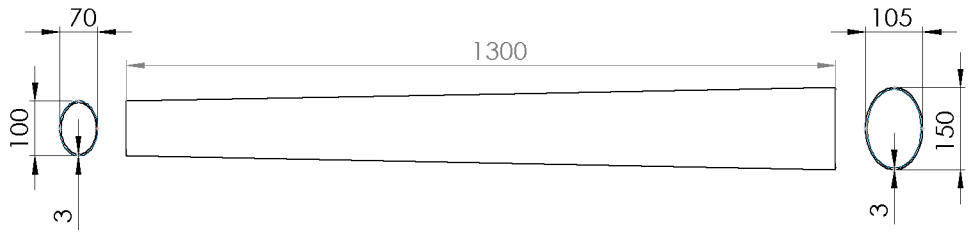

Figure 8.6: Dimensions of shorter arms in millimeters.

Figure 8.7: Dimensions of longer arms in millimeters.

With these dimensions, the natural frequencies of each arm for the first three modes can be found. These are displayed in table 8.5.

Table 8.5: Natural frequencies for the first three modes.

	Mode 1	Mode 2	Mode 3
Frequency Short Arm [Hz]	881.002	5506.262	15442.562
Frequency Long Arm [Hz]	672.446	4202.79	11786.916

These frequencies are very high, but this is to be expected due to the rigidity of the structure. Furthermore, the deflections along the length of the arms are displayed in figures 8.8a and 8.8b below.

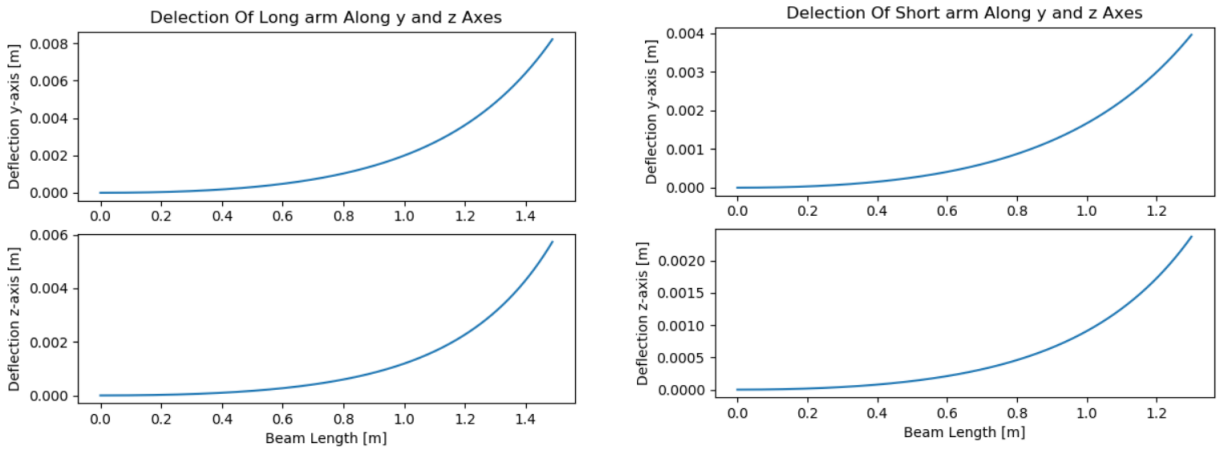

(a) (b)

Figure 8.8: Deflection graphs of both the long and short rotor arms.

8.2.5. Verification & validation

To check the validity and feasibility of the arm designs, it is necessary to check whether the methods used are correct, if any errors were made and whether the results reflect actual systems.

To do this, firstly, the method used will be compared to other sources. Next, the code used will be checked part by part. Calculations made on properties of the beam such as cross section area, moment of inertia and deflections will be compared to other sources, such as online programs. Furthermore, for verification, a FEM analysis will be performed on the arms to test the stresses and deflections on it to make sure they are well within limits. These tests are shown in figure 8.9 and 8.10.

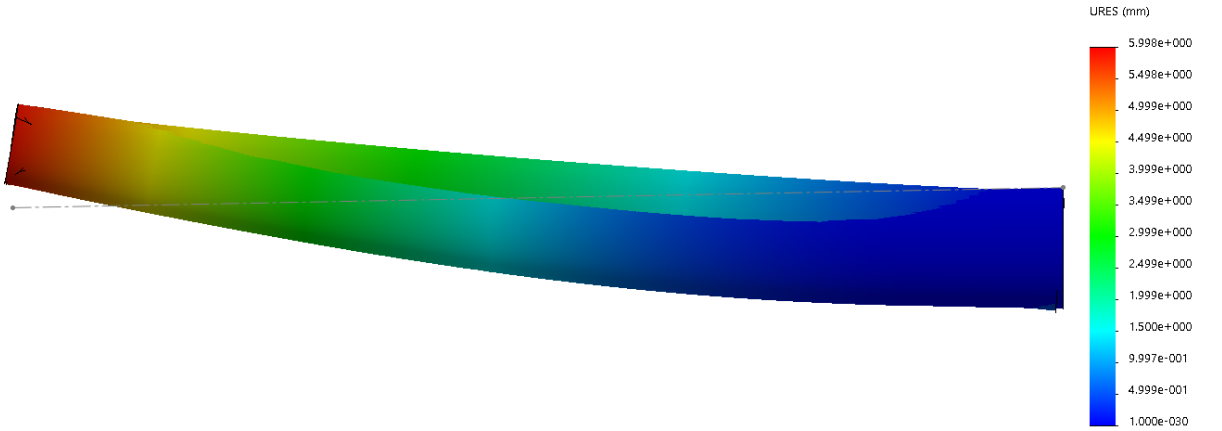

Figure 8.9: Deflection graph of the rotor arm using FEM analysis.

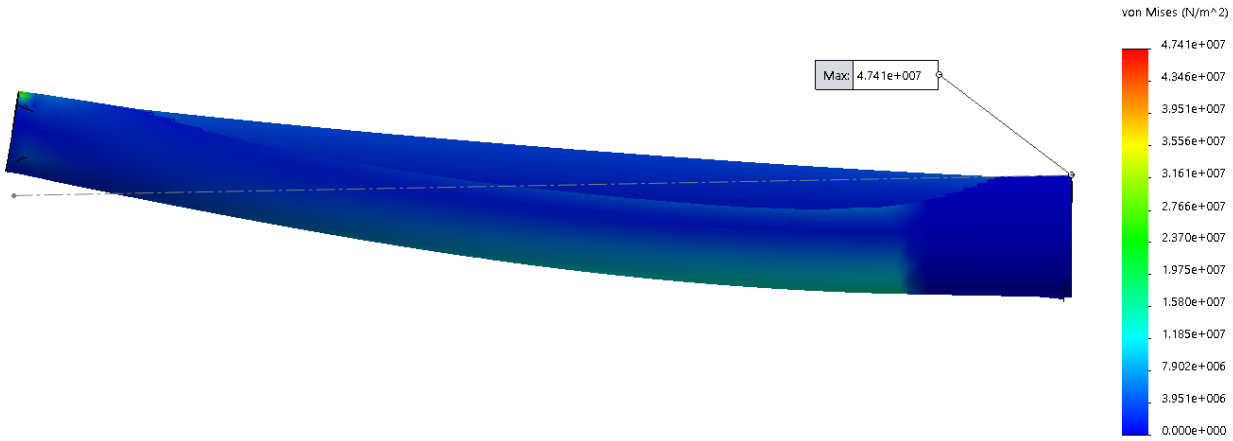

Figure 8.10: Von Mises stress graph of the rotor arm using FEM analysis.

The results from this design were not too far off from the calculated deflections and stresses. Comparing the maximum deflections from the python code and the FEM analysis, shows compatibility between the two methods. The maximum deflection obtained by the FEM is about 20 % greater than the predicted values. This discrepancy, though small, could be attributed to the the presence of non-uniform loads through the cross section that were assumed to be constant in the python program.

8.2.6. Sensitivity analysis

So far, the calculations done for the arms were very conservative and included various factors of safety to assure the resistance of the structure. Even so, since most of the calculations were done on programming software, which has been verified, it is important to see how sensitive the code is and how the outputs change depending on changing inputs. The outputs that will be compared will be the weight and the maximum stress, since these two parameters have the most influence over the design.

Input	**Mass**	Maximum Stress
Thickness + 10%	+ 9.6%	-9.2 %
Major Axis Ellipse + 10%	+ 12.17%	-8.7%
Minor Axis Ellipse + 10%	+ 6.7%	-23.7 %
Length + 10%	+ 7.05%	+33.78 %

Table 8.6: Compliancy table for different paramaters for the arms.

Overall, the mass and maximum stress are very sensitive to altering geometrical parameters, in specific, the length and minor axis ellipse. The length increases the maximum stress by quite a lot because as the length increases, so does the moment at the base of the beam, which in turn increases the stress at that point. This sensitivity analisis shows to a certain extent the relationships between the two outputs and the input parameters, to further optimie the structure.

8.2.7. Future recommendations

At the start of the design of the arms, only three cross sections were considered. Therefore, a more extensive analysis will be performed in order to optimise the arms. Also, with an increase in understanding the different influences acting on the vehicle, the team will search and investigate more suitable materials. A variable thickness will further decrease the weight of the arms, but will increase the manufacturing costs. A more extensive trade-off will tell if it worth using a variable thickness.

8.3. Arm Hub and Connection Points

The arm hub is the structural element where the arms come together and are joined into the main structure. This mechanism is of crucial importance because not only will it have to take up the loads from the arms, but also effectively transfer them throughout the rest of the vehicle structure. Due to the fact that this structure will take the combined stresses of the six arms, it will potentially be the highest loaded structure of the aircraft. A detailed design of the hub is therefore important in order to deal with all the forces that it needs to handle. For the scope of this project, it is unfortunately not possible to go into a detailed design of the hub due to time constraints and insufficient literature on the matter. As the weight of the hub will have a considerable contribution to the structure, an assumption will be made on the structure of the hub to have an estimation. The main idea is to slide the arms inside of six hollow tubes of the hub.

From the initial rotor layout in figure 8.1, the arms are described as vectors that stem out radially from one point at the top of the aircraft. In reality, the arms will be connected into a central piece at the point where they originate. Due to the complexity of this specific structure, a complete stress analysis will not be done. Instead, the part will be designed and reproduced in SolidWorks without performing any important stress calculations.

The hub will most likely be made of metal due to the complexity, stress, and size of it. Based off of the stresses on the arms, a rough estimate can be made with regards to the stresses taken by this structure. From this, a thickness and material can be attributed to the connection holes, namely, 3 mm and aluminum 7075-T6. Furthermore, additional supports were added to the hub to relieve bending stresses. At each connection point, a circular tube originates at the top of the cross section and forms a load path to the arm opposite of it. This way, the bending stresses from one arm are used to relieve those of the arm opposite of it.

The arm material choice was already chosen to be carbon fiber, so in order to transfer the stresses from the composite arm to an aluminum, metal part, three methods are considered: adhesion, welding, and mechanical connection. Mechanical connection methods require holes to be drilled in both materials, which require extra production steps, cost extra time and also weaken the materials. Composite welding has to

be done with special lasers which are expensive and complex. Out of the three, the most obvious choice becomes adhesion.

The adhesive choice is epoxy. Epoxy adhesives are suited for use in structural applications, have high shear strengths, fill up small gaps with little shrinkage and have a good resistance against environmental effects. They are also very resistant to humidity and can dampen shocks.

The final design of the hub is shown in figure 8.11 below.

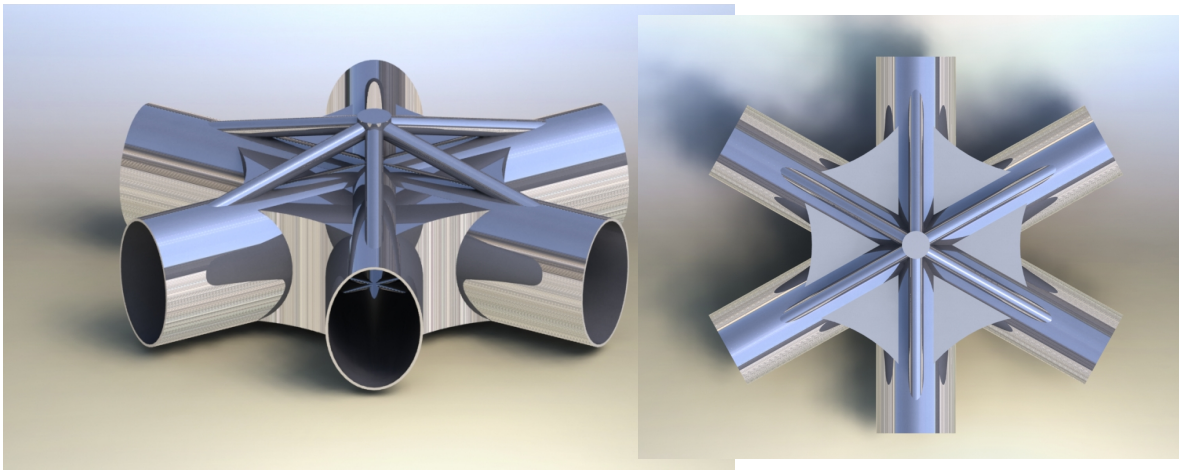

(a) Isometric view of the hub.

(b) Top view of the hub.

Figure 8.11: Visualization of the hub element of the structure.

The hub structure will be attached to the cabin through a quad pod made of metal tubes, and will be placed 40 cm above the cabin for hub and rotor clearance purposes.

8.3.1. Rotor arm reiteration

The design of the hub will have effects on the arm design, therefore it is necessary to revisit and finalize the design of the arms with this in consideration.

The main effects of the hub have to do with the lengths of the arms, since now, in order to fit into the hub housing, the rotors arms will have to be reduced in length. This in turn affects the tip deflections and the stress through the beam. By updating the length in the Python code, new values for these are found. As it can be imagined with the change in length, the stress equations vary and the arms are now over-designed thus can be altered to further reduce their weight. However, since the hub was already designed around the arm dimensions, the root and tip cross sections of the arms will not be altered. The final design of the arms are the same as before, but each arm 15 cm shorter in length.

The new natural frequencies for the first three modes are:

Table 8.7: Natural frequencies of the first three modes for the iterated arms length.

	Mode 1	Mode 2	Mode 3
Frequency Short Arm [Hz]	1219.686	7623.038	21379.156
Frequency Long Arm [Hz]	918.426	5740.166	16098.555

Predictably, these values are higher than the previous frequency calculations due to the fact that the arms decreased in length, therefore their effective stiffness has increased.

The new tip deflections for the iterated arms are then:

Table 8.8: Delfections of the iterated arms length.

	Deflection in y [m]	Deflection in z [m]
Short Arm	0.0021	0.0011
Long Arm	0.0045	0.0028

These values have decreased with respect to the previous iteration.

8.3.2. Future recommendations

Due to clearance issues between the rotors and fuselage, it was not possible to attach the hub directly on top of the fuselage. In the next phase, the team will investigate the possibility of adding a curvature to the arms in order to lower the hub and attach it directly on top of the fuselage. An example of curved arms is seen in figure 8.12. The hub will be redesigned accordingly and a detailed stress analysis will be performed.

Figure 8.12: The Surefly quadcopter with curved rotor arms[1].

8.4. Ducts

The use of ducts is considered in the final design for the following reasons:

- The noise generated by the rotors, directed in all directions within the rotation plane, may be reduced as the duct material absorbs the energy of the sound and the interaction between the rotor wake and the blades is avoided. Unfortunately, the ducts do not have a significant impact on the reduction of noise in the normal direction to the rotation plane of the rotors since it would increase the cabin noise.
- Ducts improve the safety of the vehicle. This is true for both the surrounding (e.g. the duct would act as a shield during rotor failure and detachment from the motor) as well as the rotors themselves (e.g. preventing damage from collision with foreign objects such as birds).
- A well-designed duct may improve the performance of the rotors, explained previously in section 4.5.1 by looking at the assumptions made for the rotor design. One of the sources of thrust losses is the tip losses. If the duct inner wall is close enough to the rotors, this tip losses can be minimized significantly. Furthermore, a diverging cross-sectional area may potentially increase the pressure downstream from the propeller's slipstream, and hence increasing the thrust.

However, there are (potential) downsides to the design of the ducts as well:

- Increase in weight. This is additionally true if we consider the non-aerodynamic elements needed, such as attachment tubes to reduce the vibration of the duct so that it would not hit and damage the rotors during operation and other elements, which adds more material to the vehicle.

[1] https://sureflyaero.com

- The increase in drag at certain flight condition (prominently during high wind speed cases) may outweigh the benefit of increase in thrust or reduction in power. This may also increase complexity in stability performance since the duct is subjected to aerodynamic moments as well.
- It is not entirely clear whether or not the ducts would enhance the performance of the rotors. Martin and Tung [64] found that at low RPM (<4000), which is the RPM range provided by the vehicle's rotors, using ducts actually decreases the total thrust of the vehicle. The paper suggested that this is due to the viscous losses of the duct surpassing the increase in thrust. This seems logical since viscous effects are more prominent at lower Reynolds number (low RPM). Therefore, it adds more risk to the vehicle operation; and optimal design of the duct becomes of high importance.
- The manufacturing of the duct can be relatively complex since the geometry may be complex. Furthermore, the assembly of the ducts to the whole vehicle itself may prove to be relatively difficult, adding risks of imperfect production and increase in costs.

The ducts add significantly to the safety of the vehicle. Therefore, the main purpose of using the duct is not for enhancement of performance; rather for the improved safety. Nevertheless, the reduction in performances mentioned is not completely certain. Thus, an attempt will be made to enhance the rotor's performance (i.e. efficiency) with the duct. However, since it is out of the project's scope, an exact quantitative assessment of the duct with the use of computational methods, such as those described in [57], will not be conducted. Furthermore, it is thought that a quantitative extrapolation of results on the change of performance (of the ducted rotor to the isolated rotor) in past researches would prove to be rather inaccurate. This is because of the different sizes of the ducts to be used as well as the different flow condition that PAMELA will experience. A more qualitative assessment on the geometrical aspects of the duct shall be done.

The design of the duct starts with the findings of Pereira [49]. Even though his paper only considers single rotors and not coaxial ones, we will consider for now the design of ducts for single rotors. The interest is the cross-sectional geometry of the duct, which is given in the following figure 8.13.

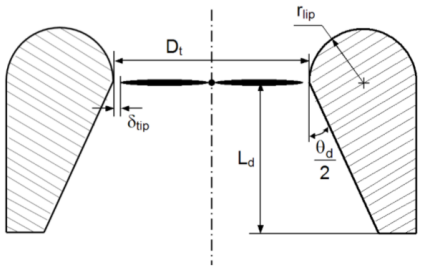

Figure 8.13: Simplified duct cross-section [49].

In addition to the geometrical parameters illustrated in figure 8.13, the diffuser expansion ratio $\sigma_d = \frac{A_{exit}}{A_{throat}}$) should be mentioned. For coaxial rotors, the geometry is presented in figure 8.14.

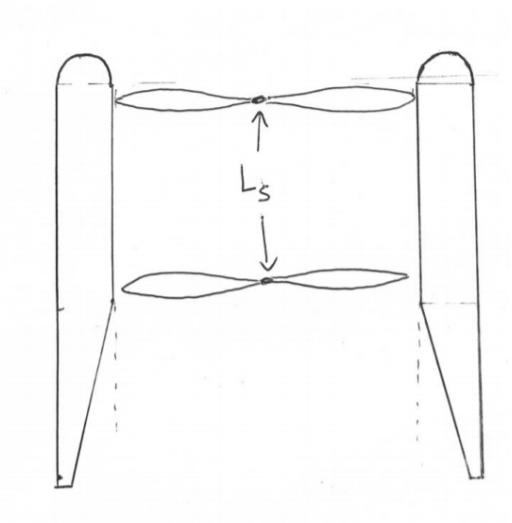

Figure 8.14: Duct template for coaxial rotors.

Note that the geometry is symmetrical. L_s represents the separation length between the rotors rotation plane. This is given to be 200 mm based on the chosen motor dimensions. Furthermore, this value is kept fixed due to the size limitations of the ducts as well as to minimize the additional mass carried on the vehicle.

Now, the choice for the values of the other geometrical aspects will be discussed in the following paragraphs. The discussion is divided into two variable groups, with the first group consisting of the tip gap and the inlet lip radius, and the other group containing the rest parameters, since the grouped variables are closely related to each other. The evolution of the duct design will be represented pictorially in order to facilitate the tracking of parameters.

Tip gap (δ_{tip}) and Inlet lip radius (r_{lip})

As mentioned previously, one of the function of the tip gap is to minimize the reduction in thrust due to tip losses of the rotors. So far from research papers (e.g. [49] or [64]), there aren't any drawbacks presented in reducing the tip gap to simply enhance the output performance of the rotors. However, for reasons mentioned in the disadvantages of using ducts, the smaller the tip gap, the smaller the margin of error. The main deciding factor is thus simply the magnitude of vibration as well as manufacturing imperfections. Nevertheless, [49] managed to test ducted rotors with tip gap as small as 0.1 % of the throat diameter; which is slightly higher than 1.3 mm in the case of PAMELA's rotors. This is thought to be too small of a margin. The smallest duct researched in [64] had tip gap of 1 % of the rotor radius, resulting in 6.5 mm for the vehicle, and still shows considerable enhancement in performance. As a final choice, the tip gap will be a value between 1.3 and 6.5 mm; or more precisely 3mm (representing 0.23 % of the throat diameter).

Because of such a small tip gap, the tip of the rotor blade has to be re-shaped. This is checked by simply plotting a circle with the throat radius (i.e. $x^2 + y^2 = 0.653^2$) to model the duct and using the parametric equations (i.e. $y = 0.65$ and $x = \pm 0.097/2$) for the rotor blade. It turns out that whether the blade is stationary or moving, the blade does not touch the duct. However, the distance between the rectangular vertices of the blade to the duct is considered to be too small, making the error margin very minimal. To reduce this risk, the tip of the blade is rounded which increases the aforementioned distance. This problem is illustrated in figure 8.15 and 8.16. *Note: the size of the gaps have been exaggerated for clarity.*

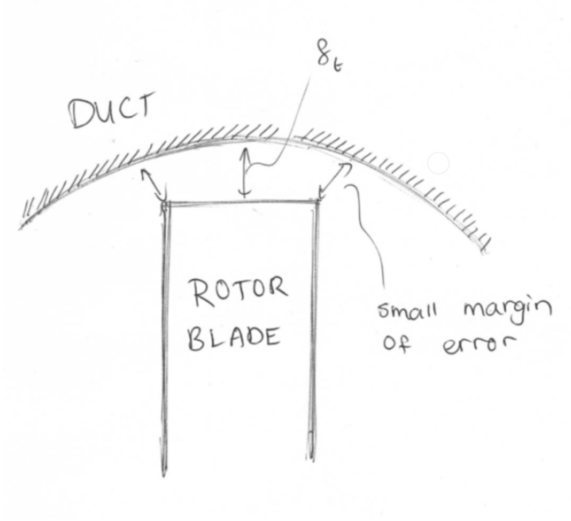

Figure 8.15: Pre-modified blade tip.

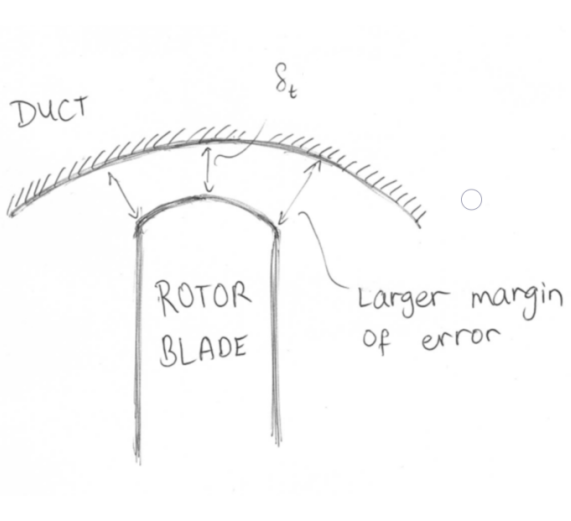

Figure 8.16: Post-modified blade tip.

The size of the inlet plays a role in introducing the flow to the rotors. The circular-shaped inlet causes flow separation. Therefore, in theory, a more circular shaped i.e. higher radius would be beneficial.

Pereira [49] found that generally there is an increase in performance with an increase in lip radius (for example, the findings for the ratio of C_T of a ducted rotor to the open rotor at constant C_P, generally shows a positive trend). However, the range that was tested was for r_{lip} to be between 6.5 to 13 % of the throat diameter. Unfortunately, looking at the available space as seen in figure 8.1, at most, the thickness of the duct (hence twice the lip radius) is limited to 50 mm (leading to r_{lip} = 25 mm, which is 1.9 % of the throat diameter). This limit is even lower considering the necessity of tip gap. Considering this constraint, the ducts of PAMELA shall have r_{lip} of 20 mm which falls short at about 1.53 % of the throat diameter. Nevertheless, this is the value to be used. On the positive side, this small inlet radius should lead to lower viscous losses due to the presence of the ducts, which is prominent at low RPM (<4000 based on [64]). Furthermore, a smaller pitching moment (compared to if the radius were to be larger), during high cross-wind at varying angle of attack would be generated, as was found in [64]. This is beneficial for the stability of the vehicle for flights near 8 Beaufort of wind. The design so far is given in figure 8.17.

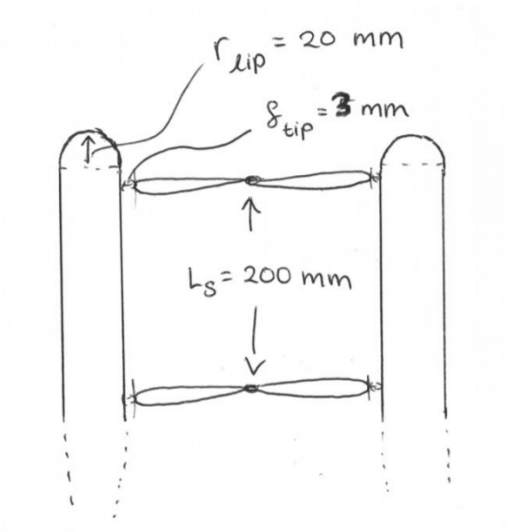

Figure 8.17: Evolution of the ducted rotor with r_{lip}.

Diffuser length (L_d), angle (θ_d) and expansion ratio (σ_d)

It is beneficial to have an increasing duct area (thus the duct acting as a diffuser), to affect the flow region past the propeller. This slows down the velocity downstream the propeller, which consequently increases the pressure as stated in the pro's of adopting ducts to the design. Therefore, in theory, the exit area can be made as large as possible, to mostly benefit from it. However, a peak in changed area can create adverse pressure gradient (similar to an airfoil at high angle of attack); where the flow would start to separate from the wall and thus reduce the size of the rotor's slipstream, consequently reducing the thrust. Therefore, it may be important to have a gradual increase in area. The size of the exit area is directly determined by the expansion ratio. However, it may also be determined by the diffuser length and angle.

Consider the length of the diffuser. The main limitation to L_d is the geometrical constraint. It is limited by the distance from the rotor rotation plane to the fuselage, constrained by the 2 m height requirement, as well as the to-be-designed landing gear/skids. Ideally, because the wall of the ducts are thin; a longer diameter would then lead to a better/more gradual increase in duct area. For a shorter L_d, to achieve the same σ_d, a higher θ_d needs to be applied. However, a large θ_d would cause a large jump in duct area. Taking into account the geometrical constraints, the final chosen parameters are L_d = **185** mm and θ_d = **20**°, which leads to an **expansion ratio of about 1.10**. The final design of the duct is given in figure 8.18.

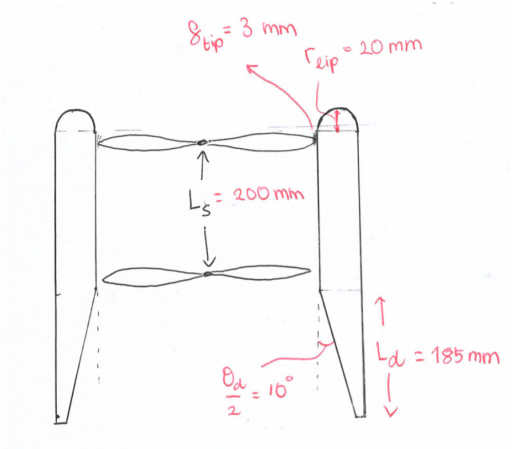

Figure 8.18: Final ducted rotor cross-sectional configuration.

A total of six ducts are used for the 6 sets of contra-rotating rotors. The ducts shall be made with carbon fibre. It is estimated that they should have a thickness of 1 mm. With this in mind, the following properties are derived from the geometry:

Table 8.9: Duct structural specifications.

	Value	**Unit**
Volume of one duct	1.24×10^{-4}	m^3
Estimated material density	1750	kg/m^3
Mass of one duct	2.16	kg
Mass of all ducts	13.0	kg

Finally, because of the relatively thin duct, as well as the small tip gap, the ducts will be connected by some tubular connection in order to minimize the impact of dynamic loading (i.e. amplitude of vibration).

To design this connection, firstly the space between the ducts is considered. Based on the placement of rotors (see figure 8.1) and the thickness of the ducts, the available space between ducts is 3.54 cm for the arms on the side, and 6.41 cm for the arms at the front and back of the vehicle. The connectors will be designed to counteract vibrations in the rotation plane of the rotors, therefore they will be loaded mainly

in compression and tension. The most simple shape that is efficient at counteracting these stresses is a circle, thus the cross section will be circular. This will also be useful in the manufacturing aspect, given that circulars rods are relatively cheap to produce. The material of the connectors, will be carbon fiber due to its high E-modulus and light weight. The diameter of the tubes will be 14 cm to provide enough area for stresses to transfer, without causing too much aerodynamic interference. Due to the relatively low stresses the connectors will be under, the thickness of their cross-sections will be 2 mm. Hence, the total weight of all the connectors will be approximately 409 g. They will be attached to the ducts with epoxy as an adhesive.

8.4.1. Future recommendations

For future project phases concerning the ducts, the main point of interests can be divided into three parts. The first is the quantification aerodynamic performances of the duct-rotor combination. This includes the effects on the generated thrust, as compared to the isolated rotor. An improvement in thrust also means a possibility for saving power. The second is the evaluation of the penalties inherent to the use of ducts. This includes generation of drag and a pitching moment. These would have to be tested for different duct orientations with respect to the relative air velocity. For these first two points of interests, the aerodynamic forces may be obtained by computational methods, preferably since it is relatively easier (less costs and time) to change the geometry when necessary. The last point of interest is the interaction between the ducts and the whole vehicle; what the ducts do for the overall aerodynamic forces. Ideally, these should be obtained through experimentation for a maximization of the accuracy. All-in-all, forces on the vehicle would change and flight performances would need to be re-evaluated for optimization. Changes to the duct geometry will be made if the overall change in vehicle performances turns out to be non-beneficial. Structural effects in these phases will be calculated last.

8.5. Fuselage Design

The fuselage is the main structural body of the vehicle, the backbone for all components. It takes up the totality of all loads, by additionally providing support for the subsystems, protection for the passenger and the inner components and possibilities for a streamlined aerodynamic profile. In this section, the fuselage design will be discussed.

8.5.1. Subsystems packaging

To get an idea on the main dimensions of the fuselage, the first step is to recognize the subsystems that need to be included and confined in the vehicle. By knowing the quantity of subsystems as well as their dimensions, it is then possible to organize the layout of the vehicle in such a way that it fulfill the requirements and permits favourable flight performance. Going through each departments, the vehicle needs to encase the subsystems presented in table 8.10:

Table 8.10: Quantity and dimensions of subsystems encased by the fuselage.

	Subsystem	**Quantity**	**Width [mm]**	**Length [mm]**	**Height [mm]**
Propulsion	Battery pack for propulsion	12	180	350	81
	Battery pack for avionics	2	180	220	81
	ESC	12	183	185	41
Avionics	Autopilot	1	142	62.6	46
	Radar	1	260	190	55.5
Ergonomics	Seat	1	-	-	-

Now, since the vehicle's mission is to carry only one passenger, the first subsystem to be placed on the lay-

out is the chair. For that, baseline dimensions for a standard aircraft business seat were searched, leading to the measures in table 8.12. A business class seat dimensions were chosen as it would add to the pilot's comfort and ergonomics as well as help convince future customers. These dimensions are presented in figure 8.11 to have a better understanding of the parameters. In this case, the seat pitch, seat inclination and armrests are neglected.

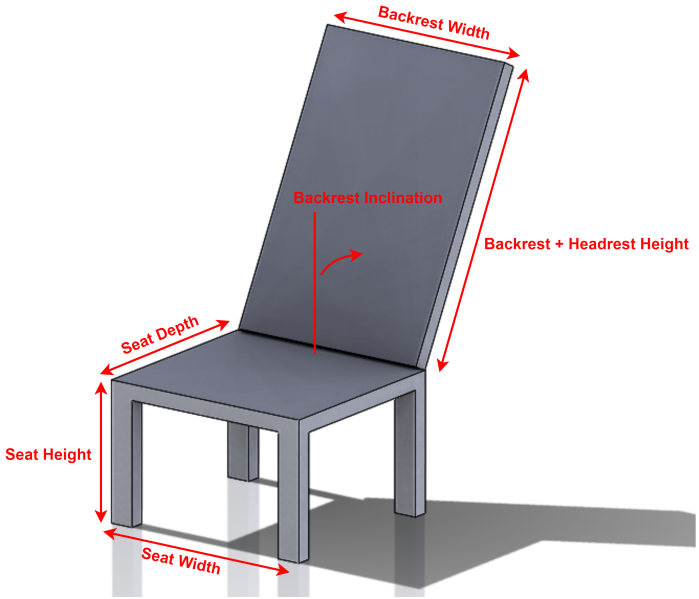

Table 8.11: Overview of the seat design parameters.

Table 8.12: Seat design parameters of an aircraft's business seat [8].

Seat Design Parameters	Values
Seat Height	31.2 [cm]
Seat Width	50.5 [cm]
Seat Depth	55.0 [cm]
Backrest + Headrest Height	75.4 [cm]
Backrest Width	52.0 [cm]
Backrest Inclination	28.0 [°]

As discussed in section 4.3, the vehicle has a maximum tilting angle of approximately 30°. To allow a comfortable and safe flight for the pilot, it is desirable for the pilot's line of view to be parallel to the flight direction vector. Thus, it was taken into account that the chair could rotate to a maximum of 25°, which adds a length margin behind the chair. As for leg space, after analysing normal seating position and standard leg extension measures of dutch team members as the customer is a dutch organization, it was decided that a length of 60 cm (almost the same size as the seat depth) would suffice.

Subsequently, the vehicle will be separated by a wall into two parts: the cabin and the subsystems room, which the latter will contain all the elements defined in table 8.10. These compartments are isolated to allow for specific thermal control and possible safety system (e.g. in case of a fire or electrical breach) for the pilot and the subsystems. With the wall set 2 cm from the maximum chair length including the rotation, it is now manageable to organize the rest of the elements.

It is desired to decrease the cabling mass by reducing the cabling length between the battery packs, the ESCs and the motors. For that, these subsystems were laid out as close as possible to the connection center of the rotor arms, with the ESCs and the battery packs regrouped closely. As for the rest of the subsystems presented in table 8.10, the radar was placed below the battery packs as it needs to rotate and have no horizontal interference from other subsystems, and the autopilot was placed in convenient spot that would not increase the overall structure dimensions excessively.

Now that everything is characterized and laid out, it was time to define the width and height constraints of the vehicle. For the vehicle's width, double the seat's width was set as to account for the arm rest and extra space for miscellaneous elements such as displays or a dashboard. This also avoid the pilot from feeling claustrophobic. As for the vehicle height, a safety factor of 1.25 was added to the chair's height in order to provide space to get in and avoid the passenger's head from colliding with the ceiling, as well as provide extra space below for extra subsystems.

Using the step-by-step thinking process, the first iteration of the packaging of the vehicle can be found

in figures 8.19 and 8.20 below, created using SolidWorks for better visualization. For now, the subsystems were assumed to be boxes for simplicity.

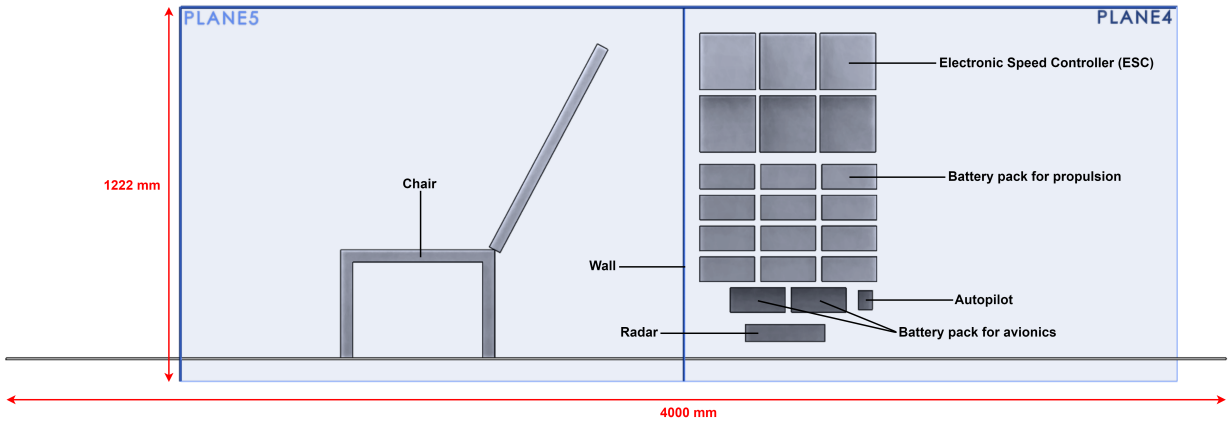

Figure 8.19: Right view of the vehicle's subsystems packaging.

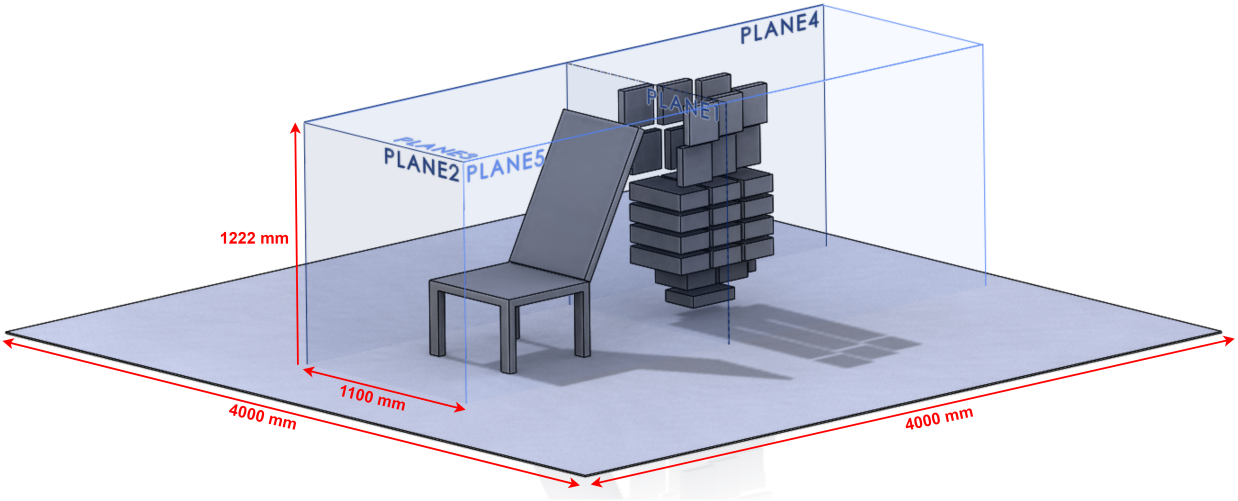

Figure 8.20: Isometric view of the vehicle's subsystems packaging.

By looking at figure 8.20, it can be seen that the ESCs are organized in a certain configuration which is presented in figure 8.21. This is due to the fact that the ESCs, selected in section 4.6.2, contain a radiator that requires direct air flow in order to cool the subsystem. With possible air intakes on the sides of the vehicle's fairing, the ESCs were placed in such as way that each one of them gets direct air flow, they do not hinder each other's cables and they allow for a smoother aerodynamic profile of the fairing.

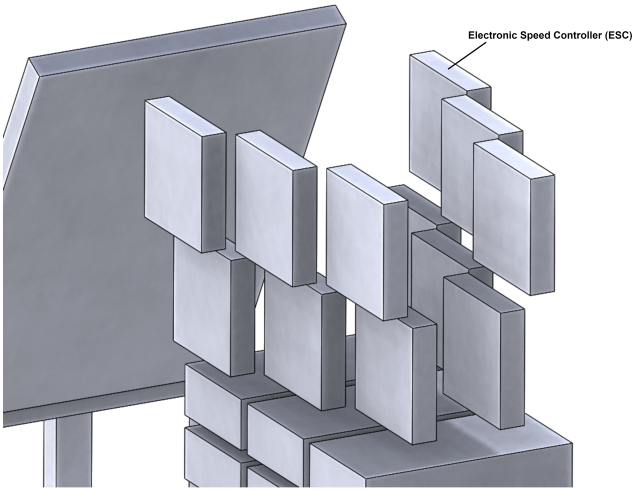

Figure 8.21: ESCs configuration in the vehicle.

Observing figures 8.19 and 8.20, few remarks can be made:

- Even though the subsystems are floating in the figures, they will be directly secured to the structures by the use of "shelves" and rods.
- The figures do not show the cabling management but we will assume that it fits the configuration.
- The chair will include a mechanism (could be hinges on the front legs and hydraulic system on the rear legs) that permits it to orientate itself automatically to a maximum of 25°.
- The length of the vehicle is only constrained by the requirement **PAM-SH-CLI-2** (The indicative maximum vehicle size is 4x4x2 m^3). This allows for the aerodynamic profile to be less constrained on its lengthwise geometry.
- The space behind the chair could be spared and used for fitting subsystems.

By analyzing the first iteration of the packaging, we realize that a large amount of space can be saved to make the fuselage more compact and allow for a smoother aerodynamic profile. Thus, the chair's rotating possibility will be sacrificed and it will be directly fixed at an angle of 21°(as it is the average tilting angle during cruise, see section 4.4). It then leads to a lower mass since a rotating mechanism is not required and to a slight decrease in comfort as the passenger will seat at an angle from the beginning. Additionally, the wall will be oriented as well to be more efficient on the available space. As the chair has been additionally rotated, the height constraint of the vehicle decreases which leads to reorganizing the subsystems in the newly available space. Although, in this iteration, a safety factor of 1.5 was used for the height as the structure of the vehicle and interior elements (e.g. isolation material) also need to be included. Adding all the changes presented above, the newly iterated packaging of the vehicle can be found in figure 8.22. As for the width, it will change to 830 mm since a safety factor of 1.5 was applied as all of these elements described for the height constraint will be taken into consideration as well.

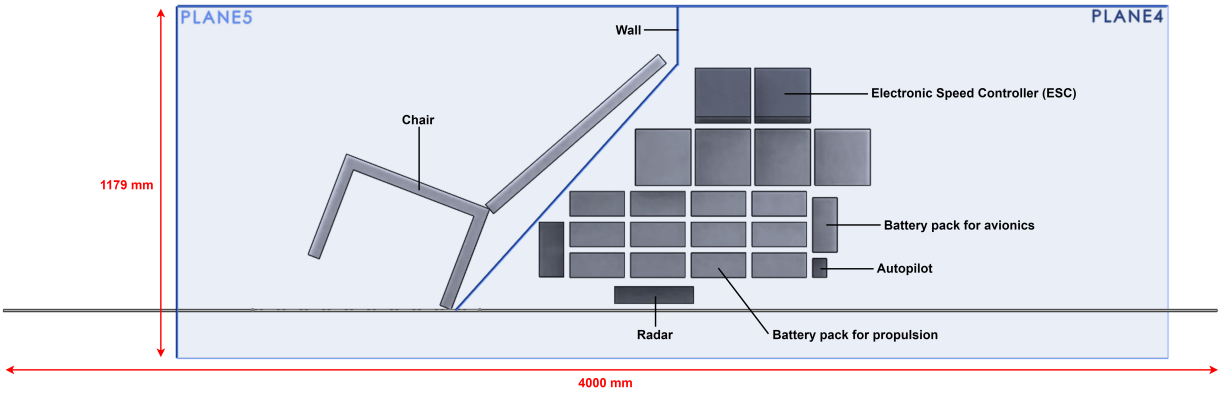

Figure 8.22: Right view of the vehicle's iterated subsystems packaging.

Similarly to the ESC packaging shown in figure 8.21, the subsystems' placements are presented in figure 8.23 below. The advantage of the iterated packing of the vehicle is that due to the subsystem being so compactly placed, the center of gravity will move closer to the center, ideally below the connection point of the rotors arms.

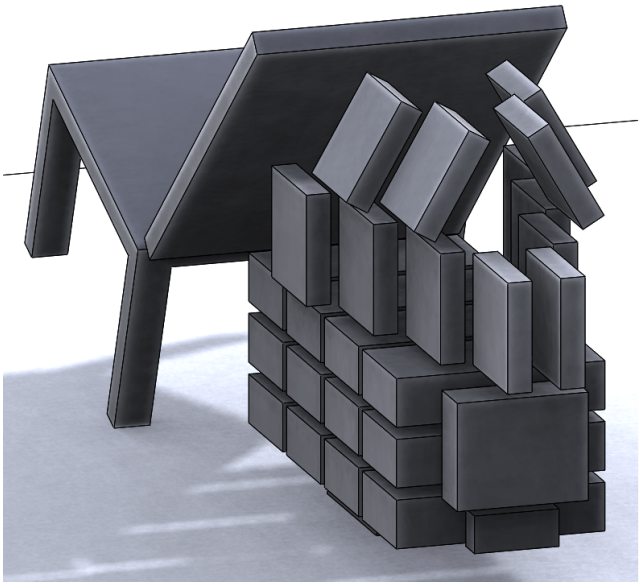

Figure 8.23: Iterated ESCs configuration in the vehicle.

8.5.2. Aerodynamic profile

The design of the aerodynamic profile of the vehicle's fuselage is an iterative process. The aerodynamic profile consists of a thin layer of material on top of the load-bearing frame of the vehicle, giving the vehicle its external shape. This section takes you through all the design stages of the aerodynamic profile, from the first iteration to the final design.

The initial establishment of the fuselage's external lines is primarily dictated by constraints on the fuselage's dimensions, with the lower limits given by the packaging of the vehicle and the upper limits given by requirement **PAM-SH-CLI-2** ('The indicative maximum vehicle size is 4x4x2 m^3.'). The initial configuration of the packaging of the vehicle, discussed in subsection 8.5.1, resulted in a minimum fuselage height of 1.23 m and a width of 1.1 m, as seen in figure 8.20.

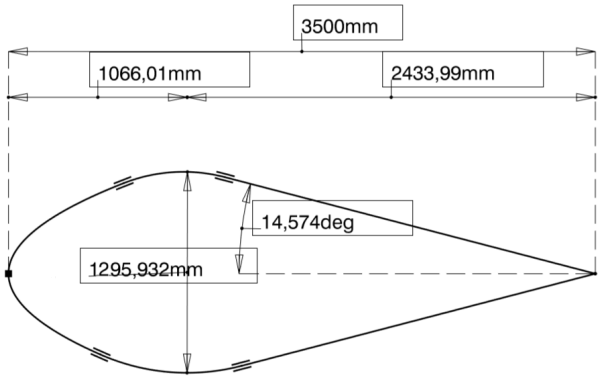

Figure 8.24: Fuselage aerodynamic profile design #1.

Figure 8.24 shows the initial profile of the vehicle's fuselage, which is at this stage comparable to a thick, symmetrical airfoil. The shape of the fuselage has been determined by breaking down the fuselage into three sections: the nose section, the cabin and the afterbody.

For conventional helicopters, the shape of the nose section is usually designed for the visibility of the pilot, where the angle of the canopy highly influences the drag coefficient of the fuselage. This generally results in an elliptical-shaped nose contour with a straight canopy surface area located above. As PAMELA is an autonomous vehicle, it is not required for the pilot to manoeuvre the vehicle by vision and it is therefore not needed to provide a large ground view angle. Thus, the nose section design will not be dominated by the canopy and a more aerodynamically efficient nose section profile, similar to the leading edge of a NACA 0020 airfoil, is chosen. The first two digits of the four-digit NACA airfoil represent a symmetric nose profile due to the absence camber and the last two digits, the airfoil thickness, are dictated by the minimum cabin width of 1.1 m.

For the cabin section, it is desirable to have a circular cross-sectional shape. In [15], the variation in fuselage drag with cross-sectional cabin shape is illustrated, showing the drag of circular, rectangular and typical helicopter cabin shapes for different fuselage angles of attack. It can be observed that a rectangular cabin section compared to a circular cabin results in a drag four times greater at 5° angle of attack. A complication for a circular cabin is the implementation of doors and windows into the design, which would have to blend in the cabin surface smoothly and require more complex opening mechanisms and production and assembling methods.

The afterbody contributes the most to the fuselage drag of a conventional helicopter. By tapering the afterbody, flow separation can be avoided and the adverse pressure gradient can be reduced, resulting in a lower pressure drag. The drag of the fuselage is related to the contraction ratio of the afterbody lines, calculated by the length of the afterbody divided by the fuselage diameter. A contraction ratio between 2.0 and 2.5 is the optimal value for a minimum amount of pressure drag and skin friction drag [15]. For the initial profile of the fuselage's afterbody, the contraction ratio has a value of approximately 2.1.

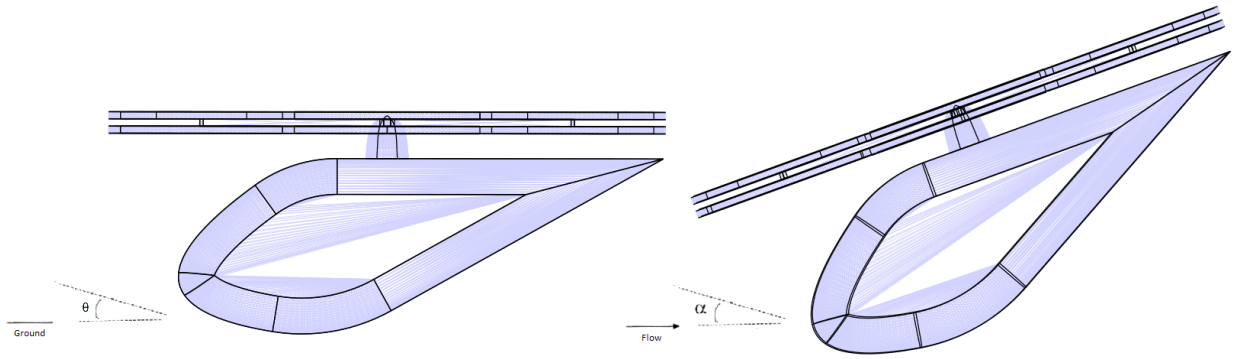

Figure 8.25: Fuselage profile #1 in a ground and cruise reference frame respectively.

Figure 8.25 shows the the vehicle's fuselage in a ground reference frame, which also applies for vertical take-off and landing, and a cruise reference frame for which the vehicle is pitched approximately 20° forward, as elaborated on in section 4.3. It is important to consider both reference frames as during cruise, the aerodynamic characteristics should be optimized, and on the ground the vehicle needs to meet the sizing constraints and allow for a feasible door-mechanism and landing gear connection. In the figure, the expected dimensions at this stage of the rotors, rotor arms and arm hub are added to the fuselage. This allows for translation and rotation of the fuselage relatively to the rotors, changing the angle of attack during cruise and the height of the vehicle while on the ground.

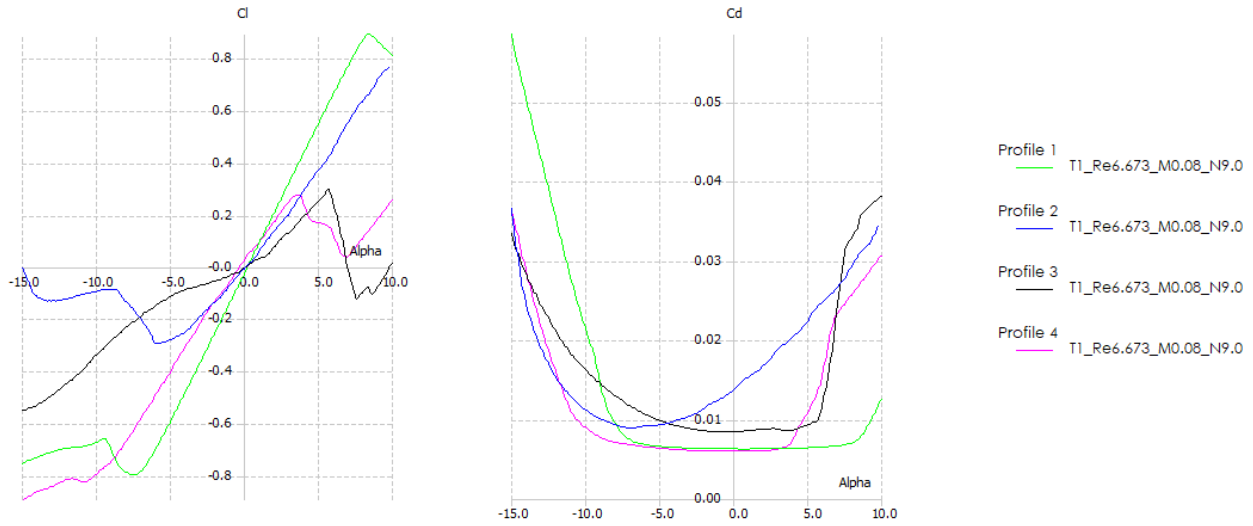

Figure 8.26: Lift and drag coefficients versus angles of attack, for fuselage profiles #1 to #4.

From inspection of figure 8.25, it can be observed that the pitch (θ) of the fuselage with respect to the ground is -15°, resulting in an angle of attack (α) during cruise of approximately -35°. Figure 8.26 shows the lift coefficient (C_l) and the drag coefficient (C_d) versus the angle of attack, created with the software XFOIL for the 4 iterations of the aerodynamic profile. It can be seen that for profile #1, the linear region of the C_l versus α curve is in between -7° and 8°, suggesting stall conditions outside this region and therefore a high amount of flow separation at an angle of attack of -35° during cruise. A negative value of C_l also indicates that the fuselage will produce a down-force, which should be minimized. The C_d versus α shows an increase of drag when the angle of attack decreases below approximately -5°, resulting in a relatively

high drag during cruise.

For the second iteration, the fuselage needs to be pitched up (i.e. the nose needs to go up and the tail needs to go down). A lower tail would also allow for an easier attachment of the landing gear to the vehicle, as longer legs or skids would be required to prevent tail tipping. From visual inspection of figure 8.24, it can also be observed that the overall size of the fuselage is too small, as the minimum fuselage height of 1.23 m is only achieved at the maximum thickness of the profile. This can be improved by extending the cabin section of the fuselage.

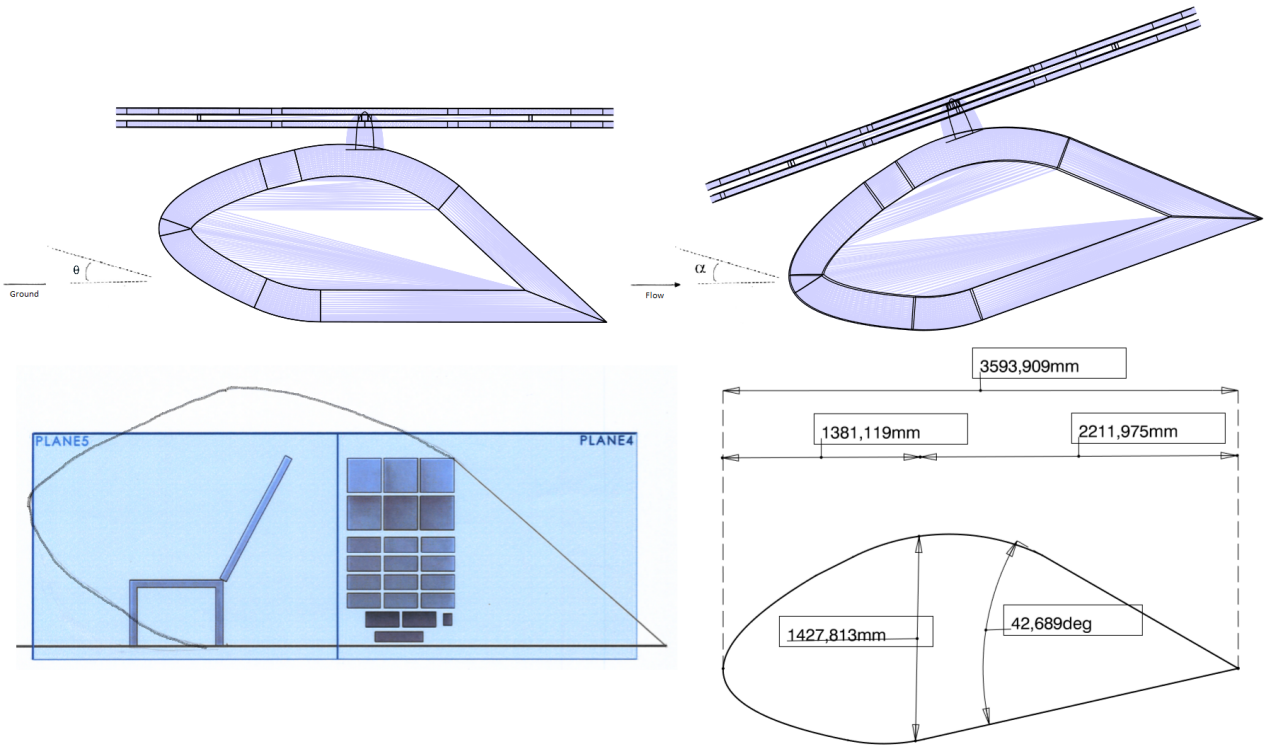

Figure 8.27: Fuselage aerodynamic profile #2.

Figure 8.27 shows the profile of the second iteration of the vehicle's fuselage, together with the vehicle in a ground and cruise reference frame and an indication of the profile with the packaging of the vehicle.

With the nose moved upwards and the tail downwards, the vehicle has a pitch of approximately 13° while on the ground, resulting in an angle of attack of approximately -7° during cruise. In figure 8.26, the linear region of the C_l versus α ends at approximately -6° for profile #2, suggesting stall conditions for angles of attack of -6° and lower. It can be observed that profile #2 creates less down-force, for the same negative values of angle of attack, compared to profile #1. The C_d versus α curve shows an increase of drag for profile #2 compared to profile #1. The minimum amount of drag for profile #2 is at the cruise angle of attack of -7°. For the next iteration of the profile, the fuselage should be pitched up slightly more to decrease the down-force and avoid flow separation.

From figure 8.27, it can be observed that some clearance is needed between the top of the afterbody and the packaging. Due to the decrease of slenderness, the contraction ratio of the vehicle has dropped to a value of approximately 1.6. Also, some extra leg space is required for the pilot. By extending the cabin below the packaging, the contraction ratio would be increased and the extra leg space could be accounted for.

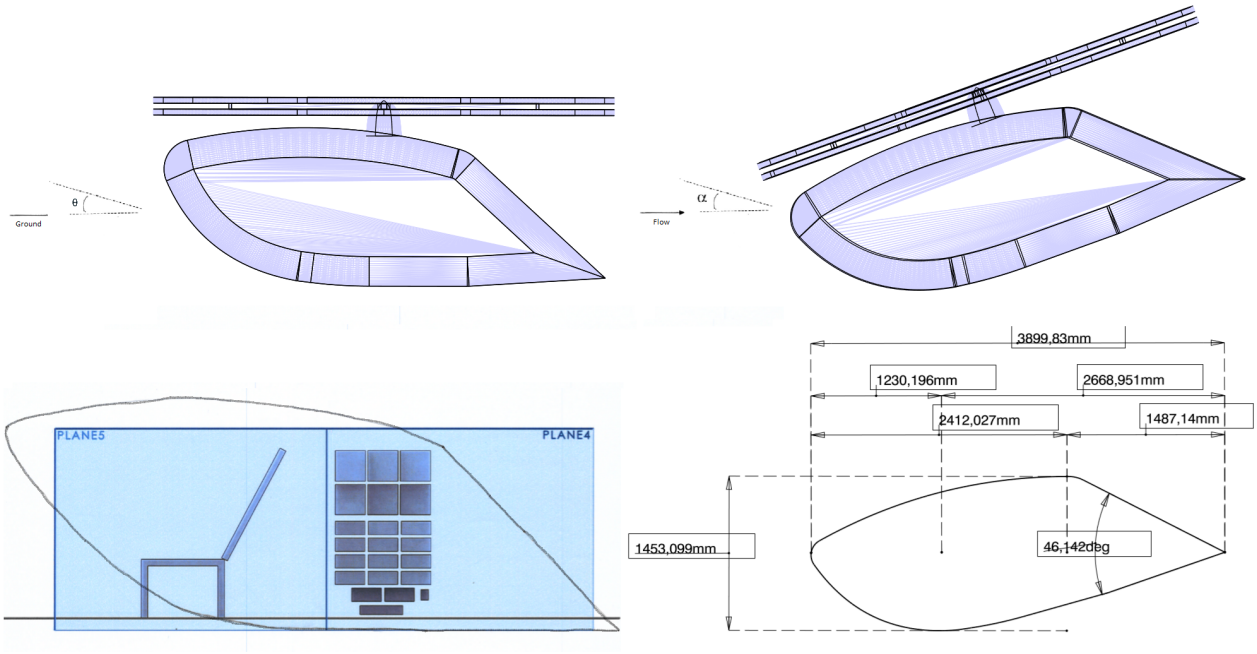

Figure 8.28: Fuselage aerodynamic profile #3.

Figure 8.28 shows the profile of the third iteration of the vehicle's fuselage, together with the vehicle in a ground and cruise reference frame and an indication of the profile with the packaging of the vehicle. It can be observed that the nose has been pulled up again and the cabin length extended, resulting in an increased leg space for the pilot and the addition of a floor below the packaging. The volume below the floor could be used for cabling, storage, miscellaneous subsystems or for the adoption of the landing gear.

The vehicle has a pitch of approximately 16° while on the ground, resulting in an angle of attack of approximately -4° during cruise. In figure 8.26, the linear region of the C_l versus α is hard to determine and is estimated to be between an angle of attack of 0° and 5°. The increase of volume of the fuselage, and therefore decrease of slenderness, has made the calculations of XFOIL inaccurate. This is most probably caused by the methods used by the software (i.e. the calculations of the effective body, which tries to take into account the boundary layer of the fuselage). For a thick fuselage, the boundary layer is calculated to be relatively large and the correction for the viscous effects in the boundary layer become inaccurate in the XFOIL software.

From visual inspection, it can be observed that the vehicle became rather large for one person. However, still more leg space is required for the comfort of the pilot and a corner in the roof of the afterbody, compelled by the packaging, disturbs the aerodynamic characteristics of the profile (i.e. the contraction ratio of the afterbody drops to a value of approximately 1.2). At this point it can be concluded that the vehicle should be decreased in size, also to decrease the amount of interference of the rotor's wake by the fuselage of the vehicle. As the design of external lines of the vehicle is dominated by aerodynamic efficiency and the constraints determined by the packaging, one of these needs to be adjusted to optimize the profile of the vehicle's fuselage. It is chosen to reorganize the packaging of the vehicle as described in subsection 8.5.1.

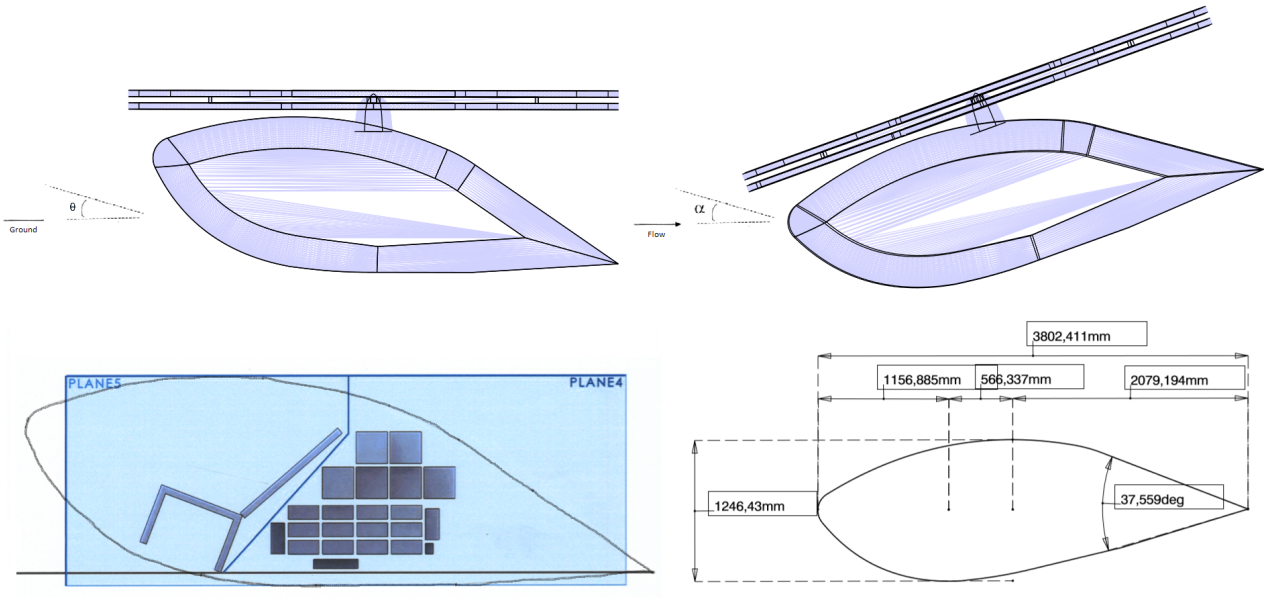

Figure 8.29: Fuselage aerodynamic profile #4.

Figure 8.29 shows the profile of the fourth and final iteration of the vehicle's fuselage, together with the vehicle in a ground and cruise reference frame and an indication of the profile with the packaging of the vehicle. It can be observed that the shape has become more similar to the first iteration of the profile. The fuselage has become more slender, with a smoothed afterbody and a contraction ratio with a value of approximately 2.1.

The vehicle has a pitch of approximately 14° while on the ground, resulting in an angle of attack of approximately -6° during cruise. Figure 8.26 shows a C_l versus α curve with a linear region ranging from approximately -11° to 3.5° angle of attack for profile #4. This gives profile #4 the lowest angle of attack before stall occurs from all four iterations. Additionally, compared to profile #1, profile #4 has a higher C_l value for the same values of negative angle of attack, resulting in a lower generated down-force. The C_d versus α curve of profile #4 shows a wide bucket, with the minimum drag coefficient ranging from approximately -8° to 4° angle of attack. Also for the drag, the fourth and final aerodynamic profile comes out best.

With this final iteration, the constraints determined by the reconfigured packaging have been met and the external lines of the vehicle have been shaped to optimize the aerodynamic characteristics. The fuselage allows for easy adoption of the landing gear due to the floor of the fuselage which is orientated parallel to the ground. With the chair pitched backwards, there is enough leg space available for the pilot and the fuselage allows for a sliding door for the pilot to enter the vehicle.

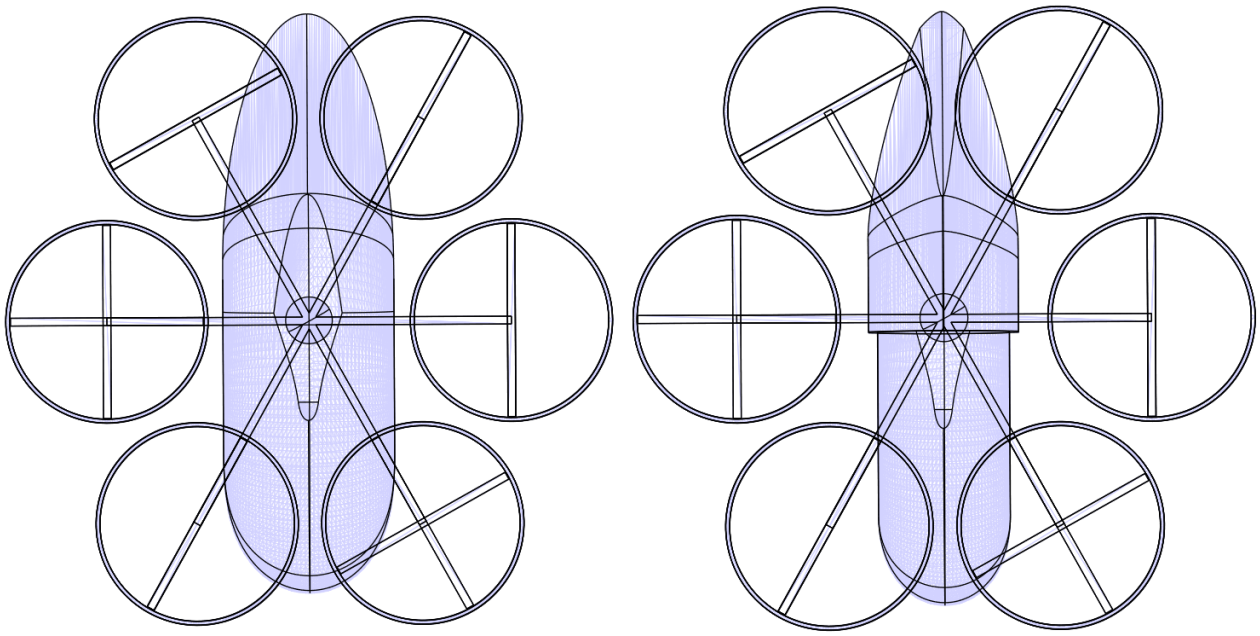

Figure 8.30: The initial (left) and optimised (right) top view of profile 4, respectively.

Figure 8.30 shows the top view of the vehicle at this stage on the left with the fourth aerodynamic profile. It can be observed that there is some overlap of rotor area with the fuselage surface area (i.e. nose section and afterbody). As this decreases the efficiency of the rotors and the performance with respect to the vehicle's aeroacoustics, the rotor-fuselage overlap should be reduced. The first measure that has been taken is a decrease in width of the fuselage, surpassing the constraint determined by the packaging of the vehicle. The minimum width of the packaging was dictated by the cabin, containing a luxurious chair and extra space on the sides with a safety factor on both, see section 8.5.1. The width of the entire fuselage is therefore reduced by 25%, only affecting the extra space and the safety factor, decreasing the width from 1.1 m to 0.83 m.

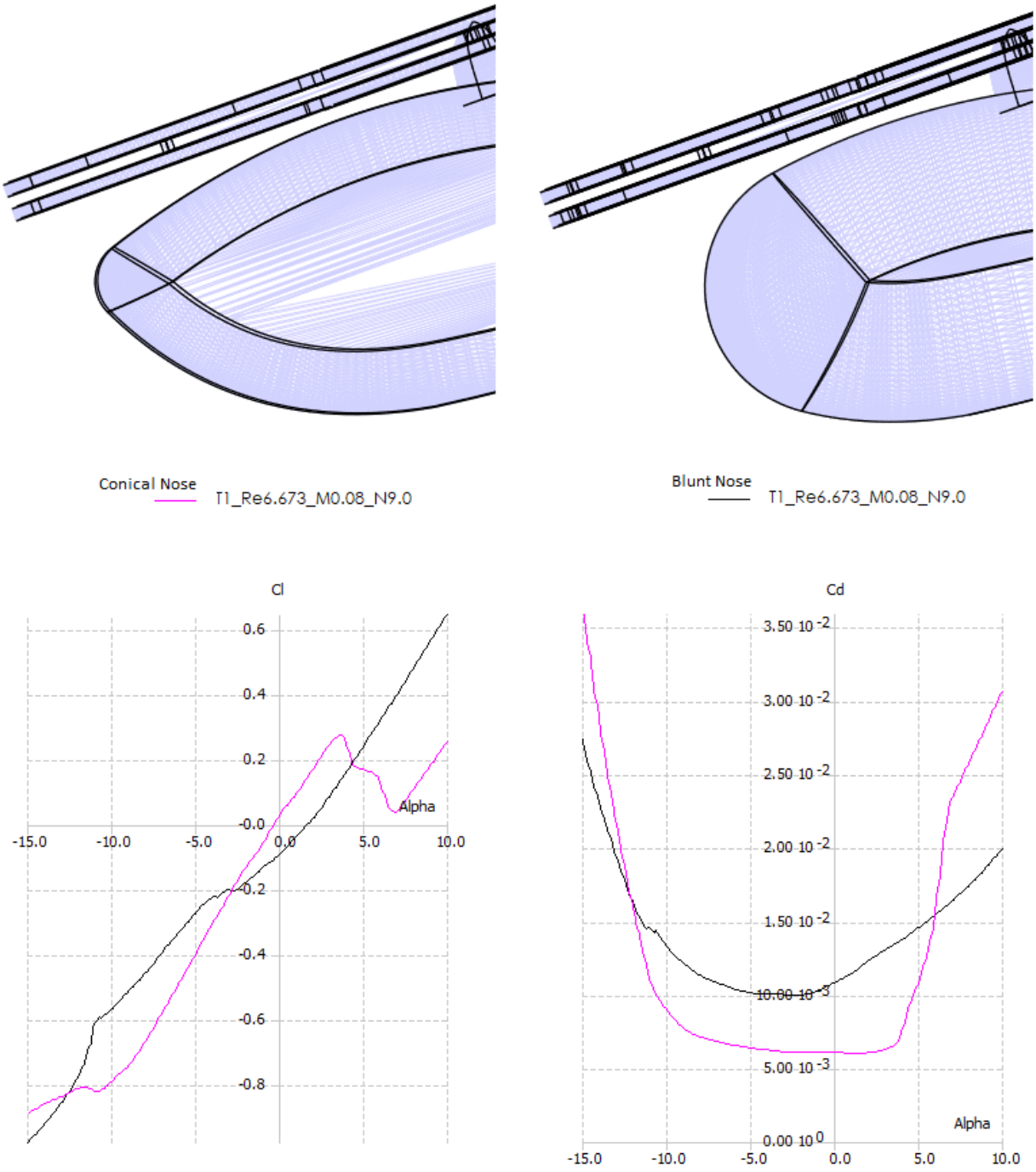

Figure 8.31: Comparison of different nose sections for profile #4.

Figure 8.31 shows an analysis on the nose section of the vehicle. By shortening the nose and making it more blunt, the rotor-fuselage overlap is decreased. However, with the decreased slenderness, the plots generated by XFOIL become inaccurate again. For the blunt nose, the C_l versus α curve is semi-linear, making it uncertain to quantify the stall angles of attack. As the C_d versus α curve seems to show a more valid and typical shape for both profiles, it can be expected that the overall drag generation of the blunt nose is higher than the conical shaped nose. Therefore, it is chosen for the nose section to remain in its former, conical, shape.

The afterbody can be optimized by creating a more conical shape, increasing the aerodynamic properties of the afterbody due to a decreased pressure gradient at the trailing edge of the afterbody. This optimization also decreases the rotor-fuselage overlap. With the width of the fuselage being much smaller than the height, the contraction ratio of the afterbody from a top view perspective exceeds the contraction ratio from the side view and is therefore of a satisfying value.

To finalize the aerodynamic profile of the fuselage, air-intakes need to be added for the cooling of the ESC's and batteries. It was chosen to create a slit on both sides of the cabin, at the location of the internal packaging wall, by increasing the width of the afterbody relative to the cabin. This results in an integration of the air-intakes which blend smoothly into the aerodynamic profile of the fuselage to minimize the increased drag. Figure 8.30 shows the top view of the optimized vehicle on the right, including the more slender body, more conical afterbody and added air-intakes.

To conclude this section, an overview is given of the evolution of the aerodynamic profile design. Table 8.13 shows the angle of attack, lift and drag coefficients, contraction ratio and chord length and height for each profile. It can be observed that during the design process, the profiles got adjusted to meet the preset constraints, resulting in a decreased contraction ratio. We can also see an increase in angle of attack, resulting in a feasible and better lift and drag coefficient. After the internal packaging had been adjusted, the optimal values for most of the parameters were achieved, resulting in the final design. Figure 8.32 shows an isometric view of the final iteration of the aerodynamic profile, with a conceptual impression of the rotors, arms, arm hub and landing gear.

Table 8.13: Evolution of the aerodynamic profile characteristics.

	Profile #1	**Profile #2**	**Profile #3**	**Profile #4**
α_{cr} [°]	-35	-7	-4	-6
$C_{l_{cr}}$ [-]	N/A	-0.3	N/A	-0.4
$C_{d_{cr}}$ [-]	N/A	0.010	0.010	0.006
Contraction ratio [-]	2.1	1.6	1.2	2.1
Chord length [m]	3.5	3.6	3.9	3.8
Maximum height [m]	1.30	1.43	1.45	1.25

Figure 8.32: Isometric view of the final iteration of the aerodynamic profile, with a conceptual impression of the rotors, arms, arm hub and landing gear.

8.5.3. Airframe design

Now that the shape of the fuselage is finalized, a decision needs to be made for its structural design and body. This structure needs to protect the main subsystems, provide support for the fairing, rotor arms and landing skids as well as counteract the static and dynamic loads without undue deflection or distortion, which include:

- The total weight of the operative vehicle.
- Loads from all six arms.
- Tensile and compression forces due to acceleration and deceleration.
- Forces caused by winds up to 8 Beaufort.
- Impact from collisions (e.g. bird impact).

It will be assumed that the total thrust load from the rotors will act as a resultant force on the fuselage at the point where the arms come together. The arms will be attached to the fuselage using a central connection unit which will be explained in more detail in the next section. Looking at other existing multicopters, a trade-off will be performed between using a space frame, a semi-monocoque frame or a monocoque shell to deal with the resultant force. The three configurations will be briefly explained below.

A space frame, shown in figure 8.33a, uses a geometric pattern of welded steel tube trusses to carry all the loads acting on the vehicle. Unlike the monocoque and semi-monocoque frames, the space frame does not rely on body panels for its structural function, therefore the outer shell needs to be designed separately.

For a monocoque frame, presented in figure 8.33b, it is the skin that supports the load by distributing tension and compression forces across the surface. As it doesn't use carrying internal frame, it is also the most efficient option regarding space utilization. Since no truss members are present, the skin must be strong enough to have a rigid structure.

A semi-monocoque frame, visualized in figure 8.33c, is what is mostly used in the design of an aircraft, consisting of a structure made of longerons, stringer, skin bulkheads, and formers to which a skin

is attached. The main advantage of the semi-monocoque frame is that it depends on multiple structural members for strength and rigidity. Because of the stressed skin construction, a semi-monocoque fuselage can withstand damage and still be strong enough.

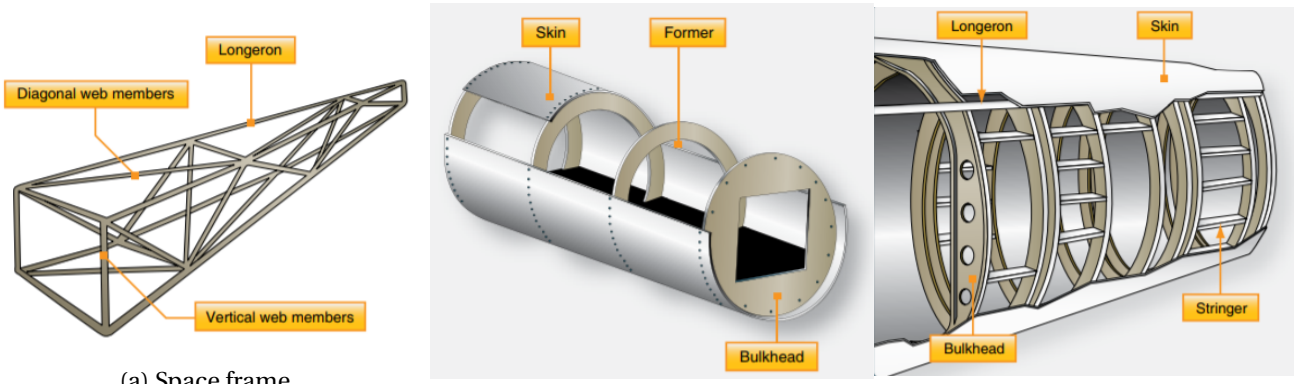

(a) Space frame.

(b) Monocoque frame.

(c) Semi-monocoque frame.

Figure 8.33: Three types of frame configuration for the vehicle [4].

A total overview of the advantages and disadvantages of the three possible frame configurations can be found in table 8.14 below.

Table 8.14: Comparison between the advantages and disadvantages of three different frame configurations.

Configuration	**Advantages**	**Disadvantages**
Space frame	• High stiffness • Great torsional rigidity • Easy structural analysis • Good connection possibilities for rotor arms and landing skids • Cost-effective • Straightforward maintenance • Good recyclability	• Intense manual labor for manufacturing • Time consuming (e.g. cutting, welding) • Can hinder subsystem placement/seat access • Hard to weld if aluminum is used • Harder to create a streamlined fuselage
Semi-Monocoque frame	• Strong and rigid structure • Can withstand damage to the skin • Space efficient • Allows a streamlined fuselage	• Difficult to carry maintenance • High production time
Monocoque frame	• Space efficient • Lighter than other frames • Optimized to fit requirements • Built-in crash protection • Better for aerodynamic purposes • Defines the frame and fairing • Uses less material during manufacturing • Thicker skin is beneficial for lower cabin noise • Better fitting tolerance precision	• Harder and more expensive to design • Uses more complex elements • Low rigidity if metal pressed • Expensive if not mass produced • Harder to recycle • Relies mostly on continuous surface to carry loads • Damage to the outer shell will weaken the integrity on the structure • Difficult to perform repairs

Table 8.14 gives a useful overview on the main differences between the frames. But to make a choice on

the configuration, dominant criteria that influences the design of the vehicle will be looked at to produce a trade-off. The decision of the frame will mainly be based on comparing the cost, space efficiency, survivability in the harsh environment and the mass by additionally looking at reference helicopters to set the benchmark.

The main sources of the cost are the design development, material price and the manufacturing methods. Comparing all three configurations for the cost criterion, the space frame is the most cost-effective of them all. It is produced using standard steel/aluminum tubes found widely on the market, leading to having a decrease in material cost. Although, the manufacturing process (welding) requires intense manual labor from a welder which is more expensive than using an automated machine. On the other hand, the monocoque is the most expensive choice due to its manufacturing methods: requiring special tools, machines and human input for production, the monocoque proves to be more expensive as its features are more complex, necessitating more precise work thus more production time. If the monocoque is made of composite, the need for a mold for the laminating process increases the budget, especially if the vehicle is not mass produced which initially is not. As for the semi-monocoque, the cost is still considerable but requires less big scale machines as its elements are usually separately produced, simplifying additionally the use of different materials compared to the monocoque frame.

Space efficiency is essential for the vehicle as it desired to make the fuselage as small as possible to reduce the weight and drag, as well as avoid interference with the rotors. Fitting all subsystems while not surpassing the dimensions constraints and having an aerodynamic fuselage profile requires good space organization. As the space frame does not follow the streamlined shape of the vehicle to have a more effective load path, the available space it provides is lower than for the monocoque and semi-monocoque frames.

The mission of the vehicle leads to flying in sea environments which can occasionally be harsh due to heavy rain, hail, strong winds, lightnings or even bird strike. As the skin in the monocoque frame is the main load bearing component, the risk of critical harm due to fuselage skin damage is high compared to the other two frames.

The mass is a crucial parameter of the vehicle. The lighter it is, the cheaper it becomes due to having less material, leading to a lower propulsion and power thus smaller subsystems are needed. For the space frame, the skin is not primarily designed to carry loads and is used mainly for protection. Now, since the skin is load bearing for the monocoque and semi-monocoque frames, its combination with the substructure allows to fulfill the same functions as the space frame but in a more optimized and lightweight matter. With more precise manufacturing for the shell frames, it results to having less excess material since for the space frame, it is fully welded by hand which allows production imperfections.

Finally, looking at reference helicopters can help support the decision making on the frame configuration, presented in figure 8.34.

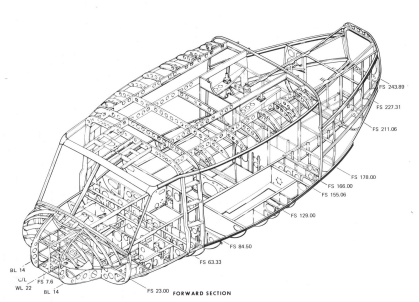

(a) Cutaway of the Bell Model 205A-1[2].

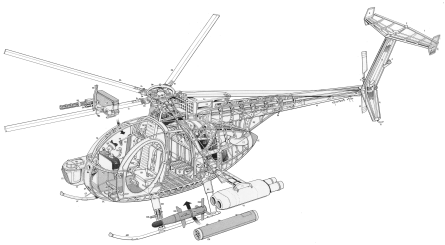

(b) Cutaway of the AH6 'Littlebird'[3].

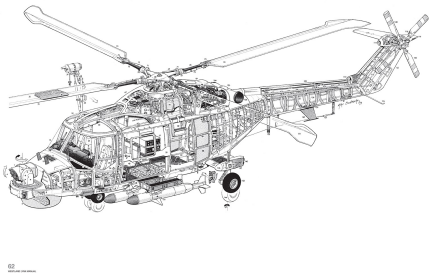

(c) Cutaway of the Lynx HMA Mk.8[4].

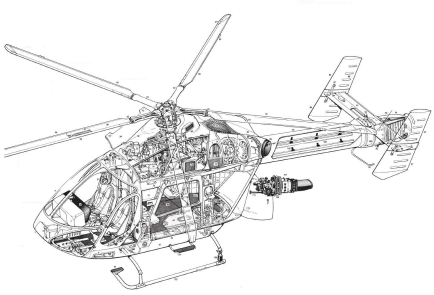

(d) Cutaway of the MD-900 Explorer[5].

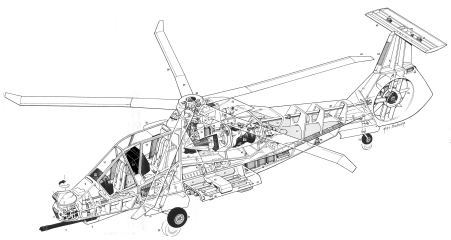

(e) Cutaway of the Boeing RAH-66 Comanche[6].

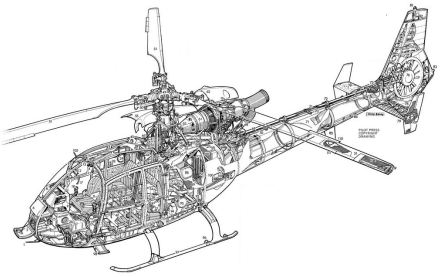

(f) Cutaway of the Westland SA 341 Gazelle[7].

Figure 8.34: Cutaways of different helicopter models.

Even though the hexacopter has few distinctions with standard helicopters, mainly mass and number of rotors, it is still relatable and could be used as inspiration. By observing the cutaways in figure 8.34, we realize that all vehicle use a semi-monocoque frame. The presence of longerons, stringer, skin bulkheads, and formers reduces the load that the skin needs to carry, giving the advantages given both from the monocoque and the space frame.

With all trade-off criteria defined and discussed for each frame configurations, the most suitable choice for the vehicle is the semi-monocoque frame. It is space efficient, lighter than the space frame and provides more protection against the harsh sea environment than the monocoque frame. Even though it results in a more expensive decision, the fact that helicopters available on the market uses the same frame configuration gives better support on the choice made. With this in mind, the production of the hexacopter could use parts that are manufactured for helicopters as it will use similar parts and elements, meaning the production line can already be set-up for the vehicle and the manufacturing cost could potentially be reduced.

To begin with the airframe design, the aerodynamic profile presented in section 8.5.2 will be divided into four main structural sections, shown in figure 8.35.

[2]http://www.huey.co.uk/huey_servicebook.php
[3]https://www.reddit.com/r/ThingsCutInHalfPorn/comments/5it463/ah6_littlebird/
[4]https://twitter.com/haynesmanuals/status/954745703422746631
[5]https://www.reddit.com/r/Helicopters/comments/47ts6w/md900_explorer_cut_away/
[6]https://thelexicans.wordpress.com/2013/09/04/cutaway-thursday-boeing-rah-66-comanche/
[7]https://www.pinterest.com/pin/93942342199553564

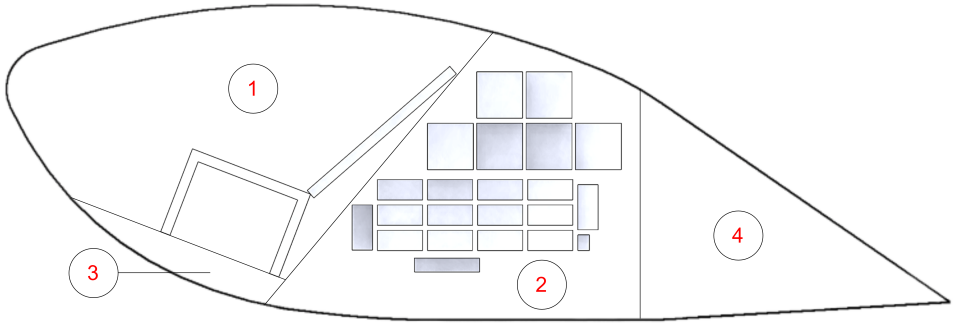

Figure 8.35: Structural division of the vehicle.

Each section has different functions thus different design, with each one of them optimized to be as lightweight as possible. These sections are defined below:

1. This section includes the cabin roof, the nose, the windshield(s) and the doors. This part will not fully carry loads as its main purpose is to protect the payload, allowing easy access to the cabin. It will mainly be composed of a composite skin, which reduces the weight but allows it to be strong enough against object strike and the harsh environment. This part is visualized in figure 8.36 below.

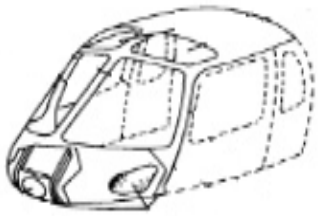

Figure 8.36: Visualization of the cabin section [58].

2. This part will act as the main load carrying structure of the vehicle, the base for all other components to be connected to. As it will attach the rotors arms, the hub and the landing gear as well as support/protect all the subsystems placed inside, it needs to be the most structurally strong and rigid. It will carry most of the loads provided by the propulsion system, creating an optimized load path. It will include the separating wall, or in this case a bulkhead, to allow for specific thermal control and possible safety system for the pilot and the subsystems; formers, stringers and longerons to reinforce the skin and carry some of the bending stress; and beams to connect section 3 to the main structure. This part is visualized in figure 8.37 below.

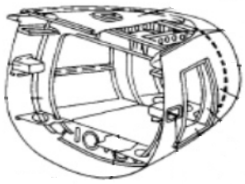

Figure 8.37: Visualization of the base structure section [58].

3. This section will act as the floor of the vehicle, supporting the cabin section as well as carry the weight of the payload while still being connected to the main base structure section. It will mainly be composed of keel beams, topped off with a honeycomb composite panel to reduce the weight. This part is visualized in figure 8.38 below.

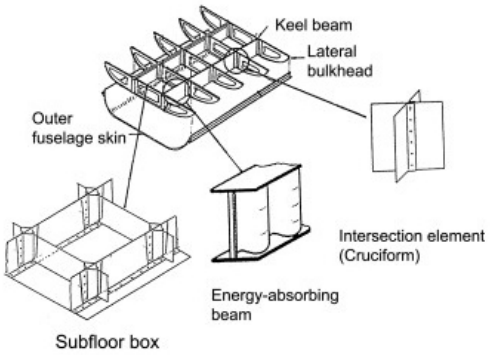

Figure 8.38: Visualization of the floor section [51].

4. Finally, this section is only used for aerodynamic purposes and to close off the structure. It will mainly be made of a composite skin to reduce the weight and will be attached to the base structure section using a bulkhead.
   Note: figures 8.36, 8.37 and 8.38 are based on helicopter design but are still representative for the hexacopter.

In order to precisely design the fuselage, in this case find the number and spacing of the longerons, formers, stringers and bulkheads, two methods are available: the first one is to model the airframe, use Finite Element Method analysis (FEM) and iterate the spacing, quantity and orientation of the elements in the substructure to optimize the design. The second method is done by using specialized program, such as the Common Language For Aircraft Design (CPACS), which "can be used to model all kinds of aircraft configurations ranging from conventional wing and tube design to highly unconventional configurations"[8]. Since the structure design of a vehicle can take months, if not years to finalize, in this report we will take inspiration from existing helicopter structure design and use basic knowledge from structural analysis to determine a preliminary design.

The reference helicopter that will be used for inspiration is the AH6 'Littlebird' shown in figure 8.40c. It was chosen as its fuselage has a similar size and shape without the tail to the hexacopter with a cabin in the front and a structural section in the back. With that in mind, a preliminary structural configuration is presented in figure 8.39 below:

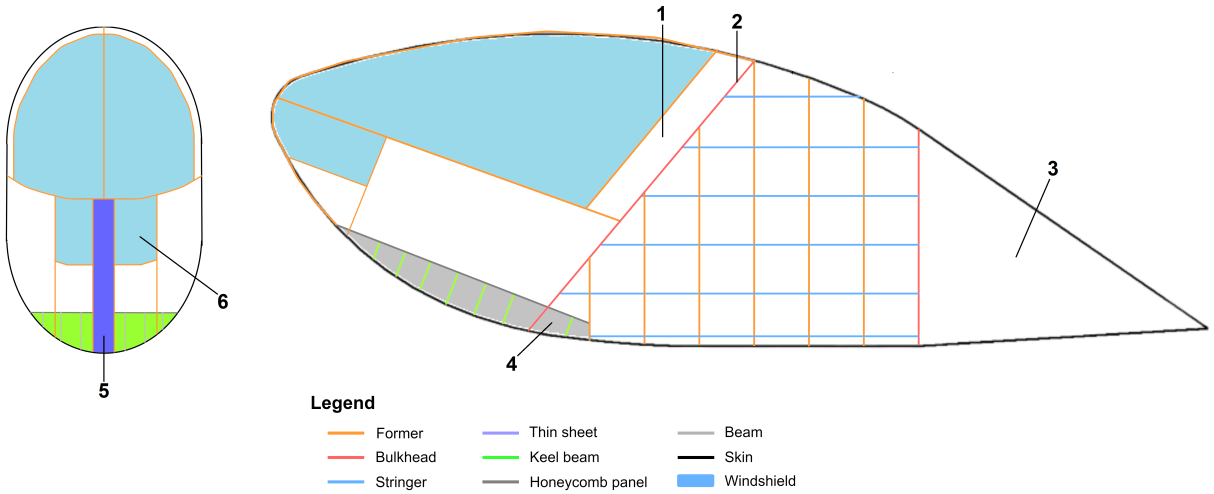

Figure 8.39: Front and side view of the structural configuration of the vehicle.

[8]https://www.cpacs.de/

Analyzing figure 8.39 above, few remarks can be made:

1. The windshields do not go until the bulkhead as some space is necessary for the doors frames and hinges.
2. As discussed before, it is desired to separate the passenger compartment and the subsystem section with a wall. This is done by using a bulkhead.
3. The tail does not have any substructure elements as it does not carry any load. It will be made of a lightweight composite skin, attached to the rest of the structure through a bulkhead. Additionally, a hatch at the bottom can be added in order to simplify the tail removal and easy access to the subsystems.
4. The floor continues through the bulkhead. This is due to the fact that the floor will be connected to the main frame for a better load path and support.
5. A tough sheet will be added between the formers to add support against object impact and strengthen the nose in case of collision. It will also protect the passenger's legs in case of failure (e.g. crash).
6. The windshields will be extended to below the nose of the fuselage, this will be done only at the front of the fuselage, as here the view of the pilot is limited by the ducts of the rotors. During cruise the fuselage will be oriented approximately 6 degrees downwards with respect to the direction of flight, the extended windshield will therefore allow for a ground and frontal view for the pilot.

The arrangement of the substructure elements was defined by understanding where and how the loads are transferred. Here, the spacing between the formers and the stringers was initially decided to be equal, meaning the loads will be carried by these two elements equally which will provide good stiffness to the vehicle. In order to not provide additional bending stresses on the formers, it was decided to orientate them vertically, creating the shortest distance for the loads to be transferred in. As for the formers in the front end of the vehicle, they are used to support the streamlined shape of the aerodynamic profile as well as supply connection points for the doors and windshields. They connect the base structural section and floor, allowing a more effective load and vibration transfer. Concerning the windshields, they were separated in two to allow for two doors option, granting redundancy in case one of the doors fails and give space for a top former to run all along the skin.

Now, a more in depth analysis should be carried to find the most suitable quantity and spacing between the formers, stringers as well as the keel beams. Modelling the structure and realizing FEM analysis is a possibility that could be performed in the future.

8.5.4. Material choice

As it was decided to use a semi-monocoque frame configuration for the vehicle, a material choice is essential for obtaining a strong, lightweight and effective structure. The frame is composed of a substructure, made of longerons, stringers, formers and bulkheads, and an attached stress carrying skin running along the whole vehicle. Starting with the substructure, a variety of materials can be considered, with a comparison carried out in table 8.15 below. Wood will not be taken into account as it is not strong enough and has low resistance towards the harsh sea environment, requiring high maintenance cost and risking requirement **PAM-CON-COST-1** ('The yearly maintenance cost shall be €12,000.').

Table 8.15: Comparison between steel, aluminum and titanium for the substructure.

Material	Advantages	Disadvantages
Steel	• Stiff • Strong • Heat resistant • Cost-effective	• Heaviest • Highly Corrosive
Aluminum	• Lightweight • Flexible • Corrosion resistant	• Strength decreasing with heat (less heat resistant) • Least strong
Titanium	• Strongest • Lighter than steel • High corrosion resistance • Fatigue resistant	• Expensive manufacturing

Four main characteristics are desired for the substructure: lightweight, cost-effective, strong and corrosion resistant, as the vehicle will fly over salty water. Being corrosion resistant will additionally decrease the maintenance cost and increase durability, making a more reliable vehicle. Looking at the material comparison performed in table 8.15 above, the most suitable substructure material would be aluminum. It is the lightest, is strong enough to carry bending stress, has a low price benchmark and corrosion resistant even when untreated. Even though titanium would be a better choice, its cost could put requirement **PAM-SH-CLI-15** ('The cost of the final product shall not exceed €60,000.') at risk as it is 16.7 times more expensive than aluminum [61]. Additionally, the production chain of standard helicopter uses aluminum for the substructure. This could provide a great opportunity to decrease the production cost of PAMELA as it will use the same manufacturing process than vehicles already on the market. Although, elements that require high strength, such as the front and top thin sheets, will be composed of titanium where being lightweight and corrosion resistant is also of high importance.

For the skin material, it will consist of a composite material as it offers multiple advantages over metals: it is lightweight, smooth (for a better streamlined shape) which reduces drag, not affected by corrosion and fatigue resistant which makes it more durable. It will mainly be composed of carbon fiber as it has the best strength to weight ratio, covered by a layer of fiberglass on the inner side to make it electrical resistant and a layer of Kevlar on the outer side to increase its impact and scratch resistance. Now, even though composites are very effective against the harsh sea environment, further measures against lightning strike need to be taken into account. The ruling solution is to spread the large amount of energy delivered by the strike throughout the whole fuselage. As Kevlar is not electrically conductive, fine metal meshes, made generally from aluminum or copper, will be bonded to the skin surfaces [79].

8.5.5. Future recommendations

In the next phase of the project the team wants to investigate a more compact set-up of the subsystems packaging. For example, one of the considerations is to utilise the space inside of the arms for the batteries. This way cable weight can be reduced as the distance from the batteries to the motors will decrease. Another aspect that will be further investigated is the optimization of the centre of gravity by clever placement of the subsystems.

From an aerodynamic point of view, it is recommended by the design team to continue creating improved aerodynamic profiles. As it is an iterative process, the efficiency of the design should increase with every new profile. This way the angle of attack can be optimized by orienting the fuselage with respect to the rotors and landing gear and reshaping the profile, optimizing the lift and drag coefficients of the fuselage. Also, a study must be performed on the relation between the rotor wake and the fuselage. Currently, only the overlap of the fuselage with the rotors is attended to. In the future, besides minimizing this overlap, also the relation between the rotor's wake and the flow direction and velocity near the fuselage

should be elaborated on. It is expected that the aerodynamic characteristics of the fuselage will decrease in efficiency due to the induced velocity of the rotor wake.

Finally, a detailed analysis of the applied loads and stresses will be carried out in order to optimize the design of the semi-monococque frame which will result in a weight reduction of the vehicle.

8.6. Landing Gear

This section explains the design choices made regarding the landing gear of the vehicle. The ability to float plays a dominant role as the vehicle operates mainly over water. Finally the dimensions, weight and cost are determined based on a drop-test from 0.5 m.

8.6.1. Landing gear configuration

From the mission profile of the vehicle, as explained in chapter 3, it is clear that the vehicle only lands and takes of vertically and doesn't require to be able to taxi. This is beneficial for the design of the landing gear, since a design with wheels, which is generally more complex and heavier than other options, can be disregarded. Besides, in order to move the vehicle over short distances, attachment points for wheels can be included on other type of landing gear.

For an improved aerodynamic streamlining of the vehicle, retractable and detachable landing gears were considered. Due to the added complexity, risk and mass of a retractable system, this option was disregarded. The inconvenience of a detachable landing gear with respect to the mission was the reason why this option is also omitted. The vehicle has to land on a different ships every time and therefore it is not realistic to have a specific landing gear set-up ready on those ships to land the vehicle.

Finally, looking at other reference lightweight helicopters, skids are chosen for the design of the landing gear. Normally for helicopters the dimensions of the skids are primarily based on the required minimum roll-over and pitch-over angles. However, the hexacopter is less susceptible to a rolling and pitching tendency during take-offs and landings due to the fact that the control system can easily return to an equilibrium position compared to a helicopter.

Therefore, the dimensions of the landing gear will primarily be based on its ability to safely land and stay afloat on the water in case of emergencies, since the unsteady dynamic surface of water can result in more unsafe conditions instead of a flat landing surface. An added benefit of skids is that there are existing solutions regarding Emergency Float Systems (EFS) (figure 8.40). This played an important role in the design choice, since the vehicle will travel most of its time over water. The main goal in the design of the landing gear is therefore that the vehicle will not capsize when it floats on water.

Another solution to stay afloat on water besides the Emergency pop-out float system is to have fixed-utility floats attached to the skids. Table 8.16 gives an overview of the advantages and disadvantages of both solutions.

(a) Float tubes stowed in low-profile protective covers along the landing gear skids.

(b) Deployment of Emergency Pop-out Float System.

(c) Fixed-utility floats.

Figure 8.40: Float Systems for a Robinson R44 Clipper II.

Table 8.16: Comparison between the advantages and disadvantages of an emergency pop-out float system and fixed-utility floats.

Configuration	Advantages	Disadvantages
Emergency pop-out float system	• Easilly installed on skid type landing gear • Same floatation ability as fixed floats • Less drag during flight • Easy cabin entry and exit	• Compressed gas-filled tank required • Additional maintenance required (e.g refilling deployment bottle, interval leak-down tests) • 23% heavier [21] • Expensive[9]
Fixed-utility floats	• 23% lighter than pop-out system [21] • No additional maintanance required	• Obstructs rotor wake • Produces more drag • Contributes negatively to noise levels • Reduces cruise speed • More difficult to get in and out the vehicle • Harder to fly with winds

The main distinction between the function of the EFS and fixed-utility floats is that the pop-outs are for emergency use only and the fixed-utility floats are for planned use. The mission of the vehicle doesn't involve landing on water and therefore will not take-off when the system analyzes that there is a high chance of not being able to land on a ship. Being able to float is thus in case of emergencies only, but nevertheless an important requirement. Together with the disadvantages that come along with the fixed floats, the vehicle will be installed with an EFS.

For the Robinson helicopter as seen in figure 8.40, the EFS adds an additional 25 kg to the helicopter which has an empty weight of approximately 1200 kg [67][44] and costs approximately €12,000 [76]. The float tubes are stowed in low-profile protective covers along the skids. In case of emergency the autonomous system can deploy the floats, which are inflated within 3 seconds from a compressed helium-filled tank.

No sufficient information could be found with respect to the pricing and weight of an EFS and therefore an estimation is made based on the weight and pricing of the EFS of the Robinson helicopter[76][66]. Considering that the helicopter is up to 3 times higher in weight in comparison to the hexacopter, a weight of 10 kg and a cost of €5000 is assumed for the EFS of the vehicle. The team is trying to contact a manufacturer of EFS to get a more detailed price estimation and expects that the weight and cost will go down.

8.6.2. Skids dimensions

From the previous section it became clear that the hexacopter will have skids for the landing gear. In this section the dimensions, material type, weight and cost will be determined.

[9]No detailed pricing could be found w.r.t. EFS and therefore it is hard to give a proper cost estimation [76].

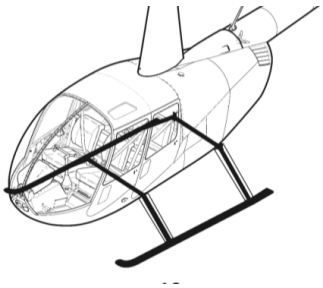

Figure 8.41: Landing gear of a Robinson R44.

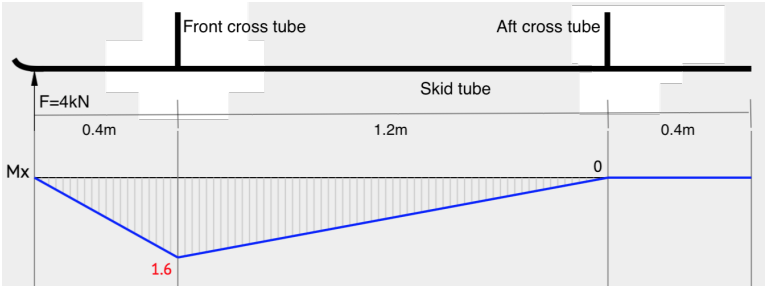

Figure 8.42: Side view of skid landing gear accompanied by the moment diagram due to a point load of 4 kN.

To attach the skid tubes to the vehicle a simple configuration as shown in figure 8.41 will be used. The landing gear therefore consist of two long skid tubes which are attached to two trapezoidal tube configurations, also called the cross tubes. The four 'legs' of the cross tubes will have a length of 424 mm and the bar connecting them will have a length of 300 mm in order to comply with the total height constraints. The angle of the legs will be set to 45 degrees, which will make sure that the skids are further away from the body which is beneficial for the stability of the vehicle when it floats on the water with the deflated EFS. It is better for the stability if the skids are placed even further away from each other, but this will also increase the obstruction of the airflow from the rotors. The length of the skids is chosen to be 2 m in order to have sufficient space for the EFS and for pitching stability when floating on water.

According to the certification specifications for small rotorcraft provided by the European Aviation Safety Agency [33], landing gear with skids must be designed for specified loading cases. The so called 'drop-test' implies that the landing gear must withstand the loads when dropped from a height of approximately 0.5 m. For an estimated total weight of 450 kg the impact force from that height is approximately 4 kN according to equation 8.16:

$$F = \frac{0.5mv^2}{h} \tag{8.16}$$

where $v = \sqrt{2gh}$
By assuming a higher vehicle weight a safety factor is automatically Incorporated. This leads to a maximum internal moment of 1.6 kNm for the skid tubes based on a simple static analysis as shown in figure 8.42. A similar approach for the cross tube results in a lower maximum internal moment, therefore for the sake of simplicity all tubes will be designed in order to withstand the bending stress due to the internal moment of 1.6 kNm. The cross-sections of the tubes will be assumed circular and hollow.

The idea behind the skid configuration as shown in figure 8.41 is that the cross tubes will elastically absorb the energy in case of a hard landing or even yields in an extremely hard landing for the safety of the passenger. A more detailed analysis is necessary in order to design accordingly. However, keeping this in mind the material chosen for the tubes will be aluminum 7075-T6 since the elastic and plastic behaviour of carbon fiber is not suitable for absorbing the loads in case of a hard landing.

Then according to the specifications as stated in table 8.4 and a total tube length of $2 \cdot skidtubes + 2 \cdot crosstubes = 2 \cdot [2m] + 2 \cdot [2 \cdot 0.424 + 0.3] \approx 6.3m$, the tubes will have a diameter of 45 mm and a thickness of 2 mm in order to withstand the yield stress of 503 MPa and to keep the weight as low as 5 kg for the entire landing gear. The material cost for this configuration is only €16. The calculations are based on equation 8.17 (which is a simplified form of equation 8.1 due to the symmetric cross-section and bending in one direction):

$$\sigma_{max} = \frac{M_{max} y_{max}}{I} \tag{8.17}$$

where $I = \frac{\pi d^3 t}{8}$.

8.6.3. Sensitivity analysis

The maximum internal moment of 1.6 kNm is based on the impact force of 4 kN assuming a vehicle weight of 450 kg. This resulted in a total weight of 5 kg for the landing gear. An increase in the maximum internal moment will result in an increase in the tube diameter (when the thickness is unchanged) in order to not exceed the yield stress. An increase of 25% leads to a maximum internal moment of 2 kNm which in turn requires a diameter of 50 mm. This leads to a weight increase of 1 kg (20%) which is acceptable considering the big increase in the moment and doesn't have a considerable impact on the total vehicle weight.

8.6.4. Verification and validation

An unit verification on the used equations gives the following:

$$F = \frac{0.5mv^2}{h} \Rightarrow N = \frac{kg \cdot (m/s)^2}{m} = \frac{kg \cdot m}{s^2} = N \tag{8.18}$$

$$\sigma_{max} = \frac{M_{max} y_{max}}{I} \Rightarrow N/m^2 = \frac{N \cdot m}{m^4} = N/m^2 \tag{8.19}$$

In order to validate the landing gear, the drop test will be performed as stated in the certification specifications for small rotorcraft provided by the European Aviation Safety Agency [33].

8.6.5. Future recommendations

The design of the landing gear is driven by the ability to float in case of an emergency landing on water. This resulted in a skid landing gear configuration with an emergency float system attached. The next step in the design of the landing gear is to analyse the stability of the vehicle when it is floating on water and adjust the landing gear accordingly in order to decrease the chance of capsizing. A trade-off is inevitable as increasing the distance between the skid tubes will increase the stability, it will also produce more drag and increase the vehicle's weight. The weight of the current landing gear can however be decreased as the current design is overdesigned. Therefore the team will optimize the landing gear in the next phase of the project.

8.7. Miscellaneous Subsystems

Insofar, the design of the vehicle has been defined in the main aspects and the necessary subsystems for flight have been presented. However, due to regulations and passenger comfort/safety, additional systems and components are needed in order to operate the vehicle.

Passenger Seat

A trivial aspect that hasn't yet been accounted for is the passenger seat. As discussed in section 8.5.1, an aircraft business class seat was used for the packaging of the subsystem. As the vehicle will tilt most of the time, a seat that keeps the passenger in place is desired. For that, the racing seat shown in figure 8.43 will be used. It has similar dimensions as the one assumed for the packaging and provides a good sense of comfort and aesthetics.

Figure 8.43: Render of the racing seat used in the vehicle's model [71].

Lights

As the vehicle will also perform nighttime flights, it is required to have an approved anti-collision light and navigation light by the lights to be displayed by aircraft regulations (SERA.3215) set by the EASA [34]. For that, the lights need to follow the instructions found in figure 8.44. They will be mounted on the ducts as they are at the extremities of the vehicle, with one additional light mounted on bottom of the fuselage.

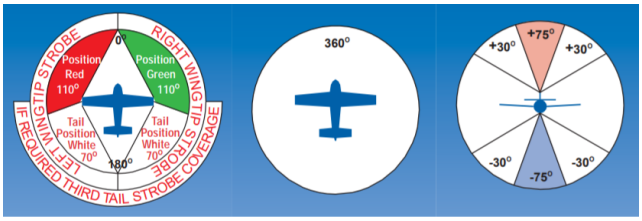

Figure 8.44: Light position requirement on an aircraft [81].

Life jacket

For all flights that involve manoeuvres on water, which is the case for the vehicle, it is required to have "a lifejacket equipped with a whistle and survivor locator light" for the sole passenger (No. 765 - Schedule 6; Part 1) [17]. Even though the requirement comes from UK's authority, it is still representative for the European region. The equipment will be added under the seat, for easy reach for the passenger in need.

8.8. Production Plan

The production plan is a necessary part of the structural design and serves as a guide for the production activities, making sure that the right sequences, activities and techniques are used to deliver the final product in an effective way. It will help meet product demand while "minimizing production time and cost by improving process flow, reducing the waiting time between operations, and optimizing use of plant, equipment and inventory" [Afalah]. For this project, a manufacturing plan will be made for the main structures of the product, which are the only components that will need to be custom made. Afterwards, all the components of the aircraft will come together in a final production plan outlining the entire process of production.

Production Options

There are several options for producing the separate components of the vehicle. Depending on the material, size, complexity and the amount of units to be produced, a certain process will ensue. It is of use to document all the parts involved in the production, and to list the possible manufacturing options. The price of said manufacturing processes also has to be taken into account to make sure the price stays within budget.

Table 8.17: Substructure elements breakdown.

Part	Shape	Material	Amount
Arms	Tubular/Oval Beam	Carbon Fiber	6
Arm Hub	Custom	Aluminum	1
Ducts	Hollow Cilinder	Carbon Fiber	6
Duct connections	Tubular	Carbon Fiber	6
Former	'C'-shape	Aluminum	≈ 13
Bulkhead	Custom	Aluminum	2
Stringers	Hat or 'Z'-shaped	Aluminum	≈ 86
Windshield	Custom	Laminated glass	4
Keel Beam	Custom	Aluminum	7
Beams	'I'-shaped	Aluminum	7
Thin sheet	Custom	Titanium	1
Skin	Custom	Carbon fiber, fiberglass, kevlar and metal mesh	1
Honeycomb Structure	Custom	Carbon fiber and aramid fiber paper core	1
Landing gear	Tubular	Aluminum	1

As can be seen from the table, the main materials used in the rotorcraft are aluminum and carbon fiber, thus the production methods for these two will be treated first.

Firstly, the arms are oval tubes which is a relatively simple shape to manufacture, and made of carbon fiber, so they will be manufactured using the "roll wrapping" method, which is cheaper than the next best option; filament winding. The same will be done for the Duct connectors. For the carbon fiber skin, the lay up method will be used since the radius of curvature in the skin panels is relatively large.

Similar techniques will be used for the metal components. Firstly, the arm hub will be made from plate metal that is cut, formed and welded into the final shape. Similarly, the bulkhead, will also be plate metal that is cut into the desired shape.

The former will be extruded into the desired cross section, then bent to the required radius of curvature. The same process will be used for the stringers. Bending sheet metal in two axes will be used for the metal thin sheet. Lastly, the landing gear bars will be extruded into their cross sectional shape, formed, and welded.

For the Miscellaneous parts such as the windshield, and honeycomb structure, these components will be ordered from outside parties, thus the manufacturing process will not be considered.

After the individual components are manufactured, they will be collected and put together in an assembly line. The assembly will begin with the main structural components and build up to the interior systems and subsystems. The rotors and ducts are placed last to not get in the way of other assembly processes.

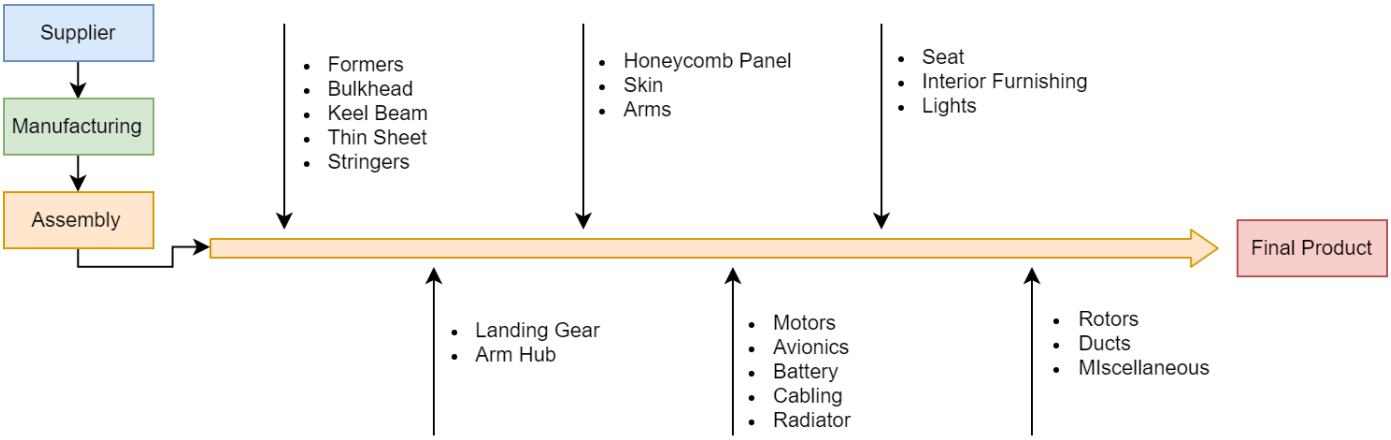

Figure 8.45: The process of the production plan.

8.9. Mass Breakdown

With the design of the structures being settled, it is possible to evaluate its mass by looking at the composing substructures elements, found in table 8.17. Each components has different dimensions, shapes and material, thus to define the overall weight, we will have to analysis each element on its own.

Arms

As seen in section 8.2, the carbon fiber rotors arms have the cross sections presented in figure 8.46 below.

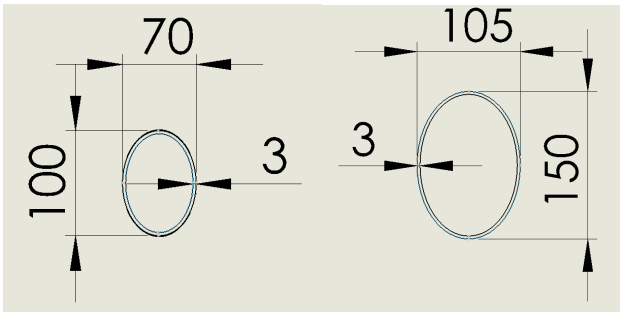

(a) Tip cross-section. (b) Root cross-section.

Figure 8.46: Cross section of the root and tip of the rotor arms.

With the above information taken into account, it is then possible to calculate the mass of the arms, given in table 8.18 below.

Table 8.18: Mass breakdown of the rotors arms.

Quantity	**Length [m]**	**Mass of a unit [kg]**
2	1.15	3.01
4	1.338	3.21
Total mass		19.7

Arm Hub

Explained in section 8.3, the hub was fully designed on SolidWorks to fulfil the function of carrying the rotor arms. It resulted in a design presented in 8.11 made from aerospace grade aluminum 7075-T6. With that in mind, mass evaluation can be done directly on the modelling program, giving a total mass of 11.6 kg.

Ducts and connections

Analyzed in section 8.4, the shape of the ducts is given as well as its dimension. With the element not carrying any loads, it will be manufactured from carbon fiber at a thickness of 1 millimeter. With that in mind, the total duct mass was found to be equal to 13 kg.

As for the duct connection, an extra carbon fiber rod will be added between the motor mount and the duct co-linearly with the rotor arms in order carry half of the duct's weight and to absorb vibrations. It will be a rod of 650 millimetres with a thickness of a millimetre and an outer radius of 50 millimetres, giving a unit mass of 0.354 kg and a total mass for all ducts of 2.12 kg.

Formers

Now, it's a bit more challenging to calculate the total mass of the formers as they different dimensions and orientations. First, we will assume that the former have a 'C'-shape cross-section, taken from a standard aircraft fuselage presented in figure 8.47. Having a thickness of a millimeter, the fuselage of the vehicle will be assumed to be an ellipse to simplify the mass calculation of all formers.

Note that the substructure taken from an aircraft is only used for mass evaluation. For future recommendation, the formers, stringers and bulkhead will have to be designed and optimized specifically for the vehicle. Now, with these assumptions, it was found that the total former length is approximately equal to 39.4 m with a mass of 360 grams per unit meter, giving a total former mass of 14.2 kg.

Figure 8.47: Standard former of an aircraft fuselage found in the hall of the aerospace faculty.

Bulkheads

In the vehicle, there are two bulkheads present. Looking at the structure configuration sketch in figure 8.39, the front one is a bulkhead covering the whole fuselage inner area and the rear one is a simple bulkhead, similar to a former, connecting the base structure and the tail with a width of 100 millimetres. Assuming again that the cross-section of the fuselage is an ellipse, we can then find the total bulkhead volume and thus the mass. Its thickness was taken from the same standard aircraft fuselage as the former, seen in figure 8.48 below, which was found to be 2 millimetres. With all the necessary parameters, he total bulkhead mass was calculated to be 20.74 kg.

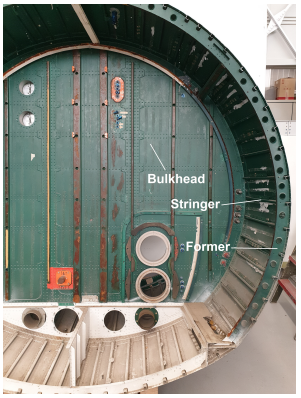

Figure 8.48: Standard substructure of an aircraft fuselage found in the hall of the aerospace faculty.

Stringer

To calculate the total mass of the stringers, we will first assume that they are all of the same length, with their shape presented in figure 8.48. They have a thickness of a millimetre and located in positions shown in the structure configuration sketch in figure 8.39. They thus have a total mass of 1.63 kg.

Windshield

Standard vehicle windshield have a thickness from 5 to 6 millimetres and density of 2.5 g/cm^3 for a double layered laminated safety glass, composed of two glass layer and one polyvinyl butyrate (PVB) interlayer [59]. By assuming that the thickness is uniform all over the windshield, by finding the occupied area, we can then find the total mass which is equal to 26.5 kg.

Keel beams and I-beams

Specifically situated below the passenger, few assumptions will be made: the keel beams and the I-beams have the same unit mass, the keel beams have an average length of 300 millimetres and the I-beams 850 millimetres since the cabin gets more narrow in the front, they will have an average height of 150 mm with a thickness of 2 millimetres. With the quantity of beams presented in table 8.17, we get a total mass of 6.8 kg.

Thin sheet

The single titanium thin sheet used in the nose will be assumed to be of length 600 millimetres, width of 100 millimetres and thickness of 3 millimetres. This gives a mass of 0.8 kg.

Skin

Being one of the main structure element of the vehicle, the skin contributes greatly to the overall mass. Finding the area covered by the element on SolidWorks and assuming a skin thickness of 3 millimetres, we get a total mass of 23.24 kg.

Honeycomb panel

Finally, the only element missing is the honeycomb panel under the seat. This component needs to be bought from specialized company, granting standard dimensions for these panels. Looking at the area that needs to be covered, 4 panels of 305 x 305 millimetres with a thickness of 14 millimetres are required, which have a total mass of 0.852 kg [69].

Total structural mass

Now that the breakdown of each components mass has been defined, adding all the values, including the landing gear and the seat found in sections 8.6.1 and 8.7 respectively, we get a total structural mass of 160.1 kg which is higher than the estimated 90 kg from the Class II weight estimation.

8.10. Cost Breakdown

The overall cost of the materials and production of the structures has to be considered in the design, as one of the main requirements set by the customer pertained to the overall cost. To get an accurate enough estimate, the cost of the materials, labour cost and transportation costs all have to be considered.

To start, the materials used along with their respective price, labour cost and amount used will be presented.

Table 8.19: Material and labour costs for different materials.

Material	Amount Used [kg]	Price [€ per kg]	Labour Price [€]	Total Price [€]
Aluminum 7075-T6	78.21	3.1-4.4	≈ 9,000	9,293
Carbon Fiber	34.8	20	≈ 525	1,221,
Laminated Glass	26.5	-	-	≈ 500
Titanium	0.8	17.8	≈ 150	≈ 164.24
Honeycomb Panel	0.852	-	-	≈ 30

The labour costs of the materials were estimated by taking the hourly wage of professionals in the respective manufacturing fields (i.e. welding), and multiplying that by the estimated time to finish the product. Since most of the components and materials on the aircraft come from China, it is possible to also have the manufacturing done there for the components, and then assembled in the Netherlands. This of course, entails another cost, that of shipping, but that price is relatively low compared to the price of manufacturing in Europe. The cost of shipping a $40' \times 8' \times 8'6"$ container from China to the Port of Rotterdam is roughly €2300, and most of the parts can be fabricated in or nearby port cities, so the transportation 'from the factory to the port wont be considered.

For aluminum, for example, it was assumed that the the components came in their post-manufacturing shape and that a team of 5 welders, each working at an hourly rate of 15 €/h (which is on the upper limit for this type of salary in China) for 8 hours a day would put the structures together in 20 working days. The same logic was used for the other materials, using the respective labor cost, and by estimating the time required for the process. Therefore, the total material cost is €1534 and the cost of production turns out to be €9,675. Adding miscellaneous components such as the lights (€200), the safety systems (€5,050) and the seat (€150), the final structural price comes to a total of €18,909.

8.11. Recyclability

During the requirement analysis of the project, a recyclability requirement was imposed on the structures department: **PAM-SH-CLI-17** ('After 10 years the main structure shall be reused for at least other 10 years in other vehicle components (modular). After that the structure should be easily recyclable.'). In the design of the vehicle, three main material groups are used: metal, polymers and composites. Each one of these groups uses a different process for recyclability, which can differ in time, cost or even availability of the recycling itself.

Starting with metals, their recyclability is quite straight-forward: reheating the material in high temperature furnaces and proceeding with ingot processing which works for both aluminum and titanium. With numerous recycling center present in the country, recycling of the metal parts has no difficulties. Although, the main drawback is the scraping of the metals from the vehicle which include disassembling, cutting and transporting, requiring plenty of man power.

Concerning polymers, in this case the windshields, recycling is possible. Since the windshields are made from laminated glass, as discussed previously, the PVB interlayer must first be separated from the glass layers which can be done by crushing the elements. After that, the glass "cullets", pieces that are collected for recycling purposes, are melted in high temperature. As for the PVB interlayer, it can be used for adhesive application, thus providing no loss during the recycling process of the windshields [75]. This process has been ameliorated in the past decade, facilitating the recycling process by using optical sorting machines to separate the PVB and the glass "cullets", cutting some use of man power and thus cost.

Lastly, concerning composites, the recycling becomes a bit more challenging. As the vehicle will use thermoset composites, meaning the epoxy/resin cannot be reshaped by reheat, special machines and tools are required to separate the fibres from the epoxy/resin and filler parts. This requires specialized companies which are limited in numbers, but since the composite parts are light, transportation can solve the issue.

8.12. Sustainability

In [9], the main goals of sustainability were set, those being;

1. Minimise environmental impact.
2. Promote people's well-being.
3. Positively impact the work environment.
4. Create jobs.

Firstly, the environmental impact was minimised by having a design that opted for smaller dimensions and lower weight thus lowering the amount of material. Next, the production plan will be closely monitored to limit the amount of faulty products made, thereby reducing the energy and resources involved in replacing these faults. Also, the testing of real models will be limited and tests will be run more by using simulations, where physical resources are not used up.

Mostly all of the materials used are recyclable up to a certain extent. The metals call all be melted down and re-purposed using industry standard recycling techniques. The carbon fiber will be recycled using a fluidized bed recycling process which is a process that recovers the carbon fibers from the carbon fiber. For more on the assessment of the recyclability of carbon fiber, please refer to 4.12.

To promote personal well being, the suppliers of the material and the workers will be directly chosen and monitored by the team to ensure that the other parties are not violating any sustainability regulations such as over producing or exploiting workers/ resources.

The structure is designed around the comfort of the passenger and ease of maintainability which will make worker's lives much easier and more comfortable when it comes to fixing or operating the vehicle. Furthermore, the structure will also protect the pilot from the harsh environment.

Jobs will be created for the production, maintenance, and operation of the vehicle. The cost of labour has already been taken into account in the price of production, thus we can be assured that the workers get paid their fair share while still being within budget.

9 Final Design Concept

In this section, the final layout and parameters of the vehicle will be presented. A check is done of the aircraft's characteristics by the means of a compliance matrix. This is followed by a technical risk assesment of the vehicles' subsystems, and a final description of its RAMS characteristics. The chapter concludes with an updated market analysis.

9.1. Vehicle Layout

The vehicle layout can be found in figures 9.1, 9.2 and 9.3 below, presenting renders made on SolidWorks.

Figure 9.1: Isometric view of the final vehicle design.

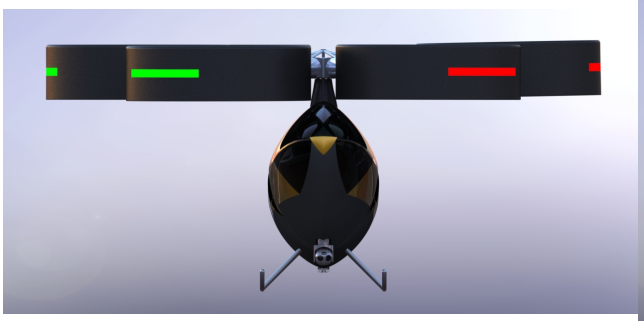

Figure 9.2: Front view of the final vehicle design.

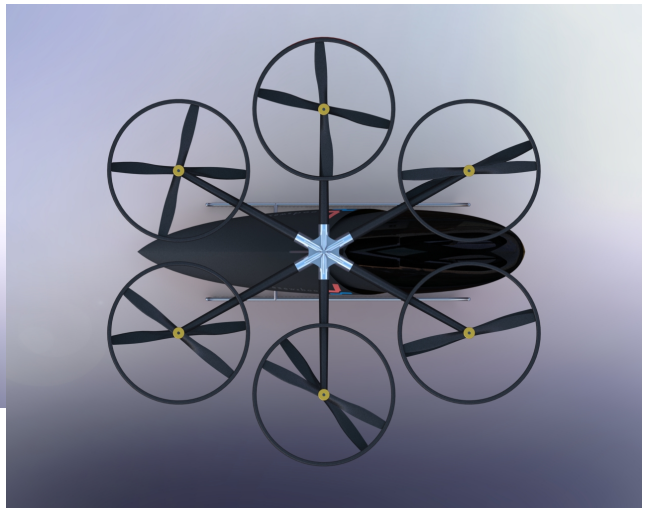

Figure 9.3: Top view of the final vehicle design.

9.2. Final Mass and Cost Breakdown

The final weights and costs for the individual components of the vehicle are shown below, these account for the majority of the subsystems.

Table 9.1: Weight and Cost Breakdown of Components

Type	Mass [kg]	Cost [€]
Propulsion	164.62	34,240
Battery + BMS	98.62	11,740
Motors	24	14,760
Rotors	7	540
Cables	29	1,200
ESC	6	6,000
Structures	160.6	18,909
Cockpit	96.9	-
Arms	19.	-
Ducts	13 -	
Landing Gear	5	16
Floats	10	5,050
Hub	11.6	-
Seat	5	150
Lights	3	200
Passenger	100	
Avionics	7	15,000
Total	432.22	68,149

The prices of some components in the structures were not calculated individually, as the prices were calculated by manufacturing processes and not by individual components.

9.3. Budget Breakdown

Designing a personal air mobility vehicle is a big challenge as this is a field of engineering that has just started to develop in recent years. As a consequence it is very hard to make preliminary weight estimations, nonetheless at the beginning of the design journey weight estimations have been made and budgets

for aspects such as power and range were created. The difficulties lie in the fact that for aircraft's and spacecrafts ready to go weight estimation methods are available which ensure a more accurate representation of the vehicles components. Therefore, to estimate the weight budgets for the personal air mobility vehicle a bit of improvisation is needed to adjust the existing aircraft formulas to move the focus to PAM vehicles. Ultimately the estimates that were determined for PAMELA in the beginning of the project can be seen in table 9.2 just as the contingencies that were established. Lastly in the last row the values of the final design are shown, then it can be deduced if the final values are within the established budgets.

Table 9.2: Oversight off PAMELA's budget breakdown and contingency compliance.

	Mass [kg]	**Bat. [kWh]**	P_{peak} **[kW]**	**Range [km]**	**Size [w x l** m^2 **]**	**Cost [k€]**
Baseline est.	234 (OEW)	16.9	91	31.5	4.3 x 4.2	125
Contingency	max. 257	min. 18.6	min. 100	min. 34.7	max. 4.0 x 4.0	max. 60
Current est.	332 (OEW)	18.94	144	25	4.0 x 4.0	68 149

As can be seen in table 9.2, the OEW is above the contingency by 29.1 %. This is a lot more then anticipated and is due to cable weight, battery weight, cockpit weight and safety float system weight being higher than anticipated. However, due to the higher than expected figure of merit, the effects of these weight increases are partially mitigated. Still more power then expected is needed, meaning a shorter then anticipated flight time. In the coming years, battery energy density is expected to increase by a lot (500 Wh/kg already by 2020), meaning that there is the potential for a battery that is way lighter. At the moment our battery sits at an energy density of 230 Wh/kg.

The higher than expected MTOW means that the overall power required goes up, meaning a shorter flight time. The range therefore dropped from an anticipated 31.5 km to 25 km. This range still meets the mission requirements, but violates the contingencies. Again, the recommendation for a battery with higher energy density would partially mitigate this higher weight. Concerning the design cost, it is expected to be €68,149. This is slightly (€8,149) above the mission requirement. This is considered small, especially as €80,000 was also approved by the clients. Lastly, contingency values such as battery capacity, peak power and size were met.

9.4. Compliance Matrix

To determine whether the requirements represented in section 3.5 have been met in the final design of PAMELA a compliance matrix has been set up. This matrix is shown in table 9.3, when a requirement is met this will be indicated with a tick sign behind the requirement. Requirements that are not yet able to be evaluated at this instant are denoted by 'tbd' and will need to be evaluated in the phase after DSE. When a requirement is not met it will be denoted by an 'X', for the requirements denoted by 'tbd' or 'X' and explanation will be given below the table. In addition, if 'n.a.' (not applicable) is used this is because no section applies to the specific requirement. Furthermore, in the table it is also shown which section relates to which requirement.

Table 9.3: Compliance Matrix.

General Requirements		Section	**Propulsion Requirements cont'd**		Section
PAM-SH-CLI-1	✓	4.3	PAM-TECH-PERF-1.1	✓	4.8.4
PAM-SH-CLI-7	✓	n.a.	PAM-TECH-PERF-2	✓	4.3
PAM-SH-CLI-15	X	3.8	PAM-TECH-PERF-3	**X**	4.8.4
PAM-SH-CLI-21	X	Omitted	PAM-TECH-PERF-3.1	**X**	4.8.4
PAM-SH-DSE-1	✓	n.a.	PAM-RISK-5	✓	4.5.4
PAM-CON-COST-2	X	n.a.	**Stability and Manoeuvrability Requirements**		
PAM-CON-SAF-1	✓	9.3	PAM-SH-CLI-8	✓	7
Noise Requirements			PAM-SH-CLI-9	tbd	6.7.2
PAM-SH-CLI-4	X	5.1	PAM-SH-CLI-13	✓	power ref
PAM-SH-CLI-10	✓	5.1	PAM-SH-INT-1	✓	6
PAM-SH-CLI-11	X	5.2	PAM-SH-INT-2	✓	3
PAM-SH-CLI-12	✓	5.1	PAM-FUNC-PRE-1	✓	7
PAM-CON-SUS-4	tbd		PAM-FUNC-PRE-2	tbd	
Structure Requirements			PAM-FUNC-TAKEOFF-1	✓	7
PAM-SH-CLI-2	✓	8.1	PAM-FUNC-CRUISE-1	✓	7
PAM-SH-CLI-6	tbd	n.a.	PAM-FUNC-CRUISE-2	✓	6
PAM-SH-CLI-18	✓	8.5.1	PAM-FUNC-LAND-1	✓	6
PAM-SH-PAS-1	✓	8.5.3	PAM-FUNC-POST-2	✓	3
PAM-SH-PAS-2	✓	8.5.1	**Operational Requirements**		
PAM-SH-PAS-3	✓	8.5.3	PAM-SH-CLI-16	✓	3.6
PAM-TECH-OP-1	**X**	8.9	PAM-SH-EXT-1	tbd	n.a.
PAM-FUNC-POST-1	✓	8.5.3	PAM-SH-EXT-2	✓	3.3
PAM-RISK-4	✓	8.6.1	PAM-CON-COST-1	X	3
Propulsion Requirements			PAM-FUNC-POST-3	✓	3
PAM-SH-CLI-3	✓	4.3	**Sustainability Requirements**		
PAM-SH-CLI-5	✓	4.8.4	PAM-CON-SUS-2	tbd	n.a.
PAM-SH-CLI-14	✓	4.3	PAM-CON-SUS-1	tbd	n.a.
PAM-SH-CLI-19	✓	4	PAM-SH-INT-3	✓	n.a.
PAM-SH-CLI-20	✓	4.8.4	PAM-SH-CLI-17	tbd	n.a.
PAM-SH-CLI-22	✓	4.8	PAM-SH-INT-4	✓	section 9.6
PAM-TECH-PERF-1	✓	4.8.4	PAM-CON-SUS-3	✓	section 8.11

The general requirement **PAM-SH-CLI-15** is not met, however, it is only exceeded by 2%. Furthermore, **PAM-CON-COST-2** did not make sense, as the engineering costs of the unpaid students should still be accounted for as if they were paid engineers.

For the structure requirements, **PAM-TECH-OP-1:** ('The vehicle shall have a maximum OEW of 201.87 kg.') was not fulfilled as by adding the propulsion and structure mass, found in section 4.11 and 8.9 respectively, the total OEW mass results in 332 kg. As for requirement **PAM-SH-CLI-17** ('After 10 years the main structure shall be reused for at least other 10 years in other vehicle components (modular). After that the structure should be easily recyclable.'), the vehicle is fully recyclable as discussed in section 8.11 but in order to define its lifetime, reference helicopter will have to be looked at. Analyzing how long the vehicle can be used for requires production and testing of the product, which can only be done after the end of the project. This reasoning also refers to requirement **PAM-SH-CLI-6** ('The lifetime of the vehicle shall be 10 years.').

Some of the sustainability requirements can not yet be regarded as being complied with. **PAM-CON-SUS-2** involves detailed information on the supply chain of the battery, while currently the contact with the battery manufacturer is very limited and closer cooperation will have to be established in the future. **PAM-CON-SUS-1** has not yet been determined due to similar reasons. Cooperation with local energy suppliers is something that is saved for a later development stage. Lastly, note that for the fulfilment of **PAM-SH-INT-4**, one is referred to section 9.6.

The requirements **PAM-TECH-PERF-3** and **PAM-TECH-PERF-3.1** are requirements that were actually expectations that followed from the first class weight estimation in the baseline report. A power budget and weight for the battery was established and that is where these values were determined. Therefore, PAMELA does not comply with these requirements. However, it should be noted that the requirements set by the client that were similar to the these were actually accomplished only less hard to achieve. As fulfilling the requirements that followed from the weight estimation would have a big increase in the weight as everything needs to scaled up and will be more expensive. In addition, the weight increase will have negative consequences for example the structure weight and price as well ending up in a negative spiral.

Requirement **PAM-SH-CLI-9** is yet to be determined as more must be known about the integration of the senosr with the control system, but at this moment it does seem that the control system would be able to manoeuvre within those limits. Requirement **PAM-FUNC-PRE-2** cannot be fulfilled for the same reason, at it would require a deeper analysis of the avionics and the software that is not available at this moment.

Requirement **PAM-SH-CLI-11** has been omitted after discussing this with the client. It states that the vehicle should respect European night noise regulations. However, those regulations state that a noise level above 40 dBA during night time is unwanted due to a negative influence on health e.g. sleep disorders, stress, concentration problems and even an increase in heart and vascular diseases. The mission of the hexacopter however takes place in a harbour area and mostly over water, thus not influencing the health of the population in a negative way.

The requirement **PAM-CON-SUS-4** states that the noise levels produced by the vehicle shall be at least 15 dB less than the levels produced by helicopter currently used. As only the rotational noise has been analyzed it was not checked if this requirement was fulfilled. When a more detailed aeroacoustic analysis is performed in the next phase of the project the team will investigate the current noise levels of helicopters that operate in harbour area to check if the hexacopter fulfills this requirement.

9.5. Technical Risk Assessment

Now that the vehicle has been designed, the risk management pertaining to its subsystems shall be performed. Firstly, the risks are identified, then the impacts are assessed through a risk map, next a mitigation plan is created and finally the risk map is updated. The vertical axes of the risk maps represent the probability and the horizontal axes the impacts. The probability scale is elaborated on next (inspired by [26]):

- Feasible in theory - This is the highest probability of the risk to occur. Subsystem risks categorised here are those where no calculations have been done and sources referred are either non-existent or have design conditions that are very far from those of PAMELA.
- Working laboratory model - For risks based on calculations with extreme assumptions and/or where ideas have been brainstormed by external sources, but not yet applied to existing flights.
- Based on non-flight engineering - This is for risks based on preliminary calculations and/or where applications of other sources are available, but the testing condition differs from the application condition.
- Extrapolated from existing flight design - Typically this is for risks based on sufficient calculations to back-up the design and/or exist in other aircraft, but the application to PAMELA may slightly differ.
- Proven flight design - This is the lowest probability of the risk to occur. Either based on detailed calculations and/or the related subsystem is something conventionally used by other aircraft.

As for the impact scale, these are (inspired by [26]):

- Negligible - Almost no reduction in overall performance, no compromise on the safety of the maritime pilot and the surrounding.
- Marginal - Observable reduction of the vehicle's performance but mission completion is still possible. No threat on the safety of the pilot and the surroundings.
- Critical - Clear reduction of the vehicle's performance. Mission completion becomes uncertain. Safety of the pilot and the surroundings is very much threatened.
- Catastrophic - The vehicle is no longer able to maintain flight. Mission completion is not possible; where the best situation for the vehicle is to perform an emergency landing. The life of the pilot is endangered.

The risk management procedure is done for separate categories of subsystems. This will be done in the following subsection. The subsystem divisions are the propulsion-related parts (rotors and ducts), power generationsupplier parts (Battery, ESC and motors), structural-bearing parts (cockpit) and the flight safety and control parts (avionics, flight automation/control system and safety systems).

Unlike the previous reports, the rankings of each risk will be argued more explicitly since more detail regarding the design of each subsystems is available. Note that mitigation is not applied to all risks. Typically only the top two to three shall be mitigated. This is because of the limited resources that are available, and so additional resources should be put only to use for those that are deemed more important. Finally, the mitigation plans do add new requirements, though for post-DSE activities. They are written in boldface and italic to facilitate finding the exact phrase where requirements may come from.

9.5.1. Rotor and duct

The risks pertaining to the rotors and ducts are given in the following list and risk map (figure 9.4).

1. Overestimated rotor performances (i.e. C_T and C_P).
2. Severe aeroelastic-induced vibration of the rotor blades.
3. Rotor performances below expectation during cruise.
4. High noise experienced by surroundings.
5. High noise experienced by the maritime pilot.
6. Ducts have a negative influence on the rotor performances.
7. Duct vibration damages the rotor.
8. Damaged duct caused by a collision with external object.
9. Large aerodynamic drag created by the ducts.

Feasible in theory				
Working laboratory model				
Based on non-flight engineering	4	5, 6, 8, 9		
Extrapolated from existing flight design		1, 3	7	
Proven flight design			2	
	Negligible	Marginal	Critical	Catastrophic

Figure 9.4: Pre-mitigation risk map of rotors and ducts.

Let's briefly discuss the ranking of each risk item. Risk related to generation of thrust/demand for power of the rotors (i.e. risks 1 and 3) have a marginal impact or lower. This can be said with confidence since the rotors were built to be able to provide twice the nominal condition and it is highly unlikely that flights would require generation of thrust to such an extent. As for the probabilities of rotor thrust/power performances, they are ranked to be near the lowest probability scale. This is because when comparing performances of existing rotors (e.g. those in [49]), the calculated C_T and C_P are very much comparable. The aeroelastic problem (risk 2) is highly unlikely to occur when looking at the relatively short length of the rotors, as well as the materials used to built the rotors that are similar to existing ones. Regardless, if it turns out that such problem does occur, then the impact might just be critical to the mission since the rotors are the only subsystem that enable motion.

A closer look at the noise-related problem (risk 4 and 5) would reveal that they do not really affect mission completion. The noise felt by the surrounding is highly damped with the use of the duct. The noise felt by the cabin might be more of a problem since the rotor slipstream coincide with the cockpit of the vehicle. Nevertheless, with some existing noise cancellation systems (e.g. foams, noise cancelling headphones,...), the impact of high generation of cabin noise becomes marginal at most. However the probability of risks occurring is still deemed to be relatively high since an accurate estimation of the noise performance is highly difficult.

Finally, consider the risks related to the duct. Currently in the design, no computational estimation or experimental results are available to assess the impact of the duct on the rotor performances (risk 6). It was thought that simple calculations would be far too inaccurate. However, the shape was comparable to other sources as described in the duct design section and therefore perhaps the probability for this risk can be comparable to "based on non-flight engineering". As for the impact, this is assessed to be marginal for the same reason of impact assessment risks 1 and 3. The planar vibration of ducts (risk 7) are unlikely to damage the rotors because of the rigid connection between them. However at higher life cycle perhaps the vibration becomes more severe as material property becomes more and more deteriorated. An accurate estimation of this is quite difficult since perhaps a detail history of loads experienced by the duct structure is required. However based on some aircraft applications it should be possible to retain sufficient material property. Thus the probability of risk is deemed very low. If the such damages were to happen and go unnoticed, indeed the rotor performance would be compromised and it is possible that the impact would be critical since, as stated before, rotors are the subsystem that enable motion. Next, on the foreign object damage (risk 8). Because the control subsystem is not necessarily designed to detect incoming object, currently it is deemed that the risk to be somewhat possible to occur; especially since the vehicle operates at sea where there may be lots of birds and tall objects. The risk is nevertheless deemed to be marginal since ducts were not primarily designed for thrust generation. Finally, risk 9 was put to be in "non-flight engineering" phase since no calculation was done, but it can be thought that because of the large surface area then the ducts may be a large contributor to drag. As for the impact, this is assessed to be marginal again for the same reason of assessment of risk 1 and 3.

Now the mitigation method for some of the risks are to be discussed. It is quite difficult to see (from figure 9.4) which ones are the most dangerous risks since none are in the dark-red zone and the choice is left to see whether impact or probability is more important. The risk manager has decided that resources should be put to mitigate risk 5, 6 and 9. The common theme between them is the necessity of accurate aerodynamic calculations. The general way to do this is to preferably perform accurate wind-tunnel testings (i.e. simulate in conditions close to the flight conditions of PAMELA) rather than CFD calculations before production of the vehicle. ***The testing should provide accurate data for performances of duct-rotor combination.*** On the benefit of the project team, such testings would also give better understanding of the problems related to risk 1,3 and 4. The If such actions were to be done, risks 1,3,4,5,6 and 9 would have the

lowest possible probability (i.e. comparable to "proven flight design") although the impact on the mission does not change since the way the vehicle operates do not change solely on these mitigation actions. ***However if testing do costs more than expected, then the resources should still be concentrated on mitigating risks 5, 6 and 9***. This is what is to be done, and the post-mitigation risk map for the rotors and ducts are given in figure

Feasible in theory				
Working laboratory model				
Based on non-flight engineering	4	8		
Extrapolated from existing flight design		1, 3	7	
Proven flight design		5, 6, 9	2	
	Negligible	Marginal	Critical	Catastrophic

Figure 9.5: Post-mitigation risk map of rotors and ducts.

9.5.2. ESC, motor and battery

Risks concerning the ESC, motor and battery are given in the following list and risk map (figure 9.6).

1. Connection points ESC burning through due to high amperage and bad contact
2. High current wires burning through due to excessive amperage
3. ESC producing unexpectedly high amount of heat
4. Erroneous cable connection to the ESC
5. Insufficient cooling of a battery
6. Faulty battery cell
7. Overestimating power density of the battery
8. Underestimated packaging weight
9. Higher degradation of performance over charge cycle than expected
10. Motors structurally weakness to handle the required RPM
11. Short circuit

Feasible in theory				
Working laboratory model				
Based on Non-flight engineering	7	4, 6, 8	5	
Extrapolated from existing flight design		10	1	
Proven flight design		2	3, 9	
	Negligible	Marginal	Critical	Catastrophic

Figure 9.6: Pre-mitigation risk map of ESC, motor and battery

First consider the risks related to the ESCs, starting with risk 1. It is thought that since the cables are relatively thick, the amperage would have to be really high to cause the cable to burn. Therefore it is unlikely

to happen; but perhaps since no tests data have been obtained by the project team, the risk manager has chosen to classify this risk to be of the second lowest probability. If ESC were to be burn during flight, the flight performance would most certainly be compromised. However, it is unlikely that all of the ESCs burn through and therefore the vehicle should still be able to perform emergency landing. Thus the impact is assessed to be critical.

Unexpectedly high heat production of ESC (risk 2) is thought to be rather unlikely since the RPM of the rotors is not that high, and thus the risk is put at the lowest probability. Nevertheless, even if it were to happen, the impact would be perhaps lower speed converted to the rotors (and thus the power supplied would need to increase); but since the rotors were capable of generating up to twice the necessary thrust this risk should prove to be marginal. Then the erroneous cable connection (risk 3) is perhaps related to human factor. This should be highly unlikely to happen since pre-flight checks (or even other checks) are performed. The impact is still critical regardless if it were to happen, since this highly disturbs the automated flight commands.

Next are the risks related to battery. All of them are deemed to have probability comparable to "non-flight engineering extrapolation" because of the custom made battery to be used which were built based on supplier data that were communicated to the power department. The impact of risks 4, 6 and 8 are at most marginal; again because the vehicle has been designed such that it can perform twice the nominal loads. Degradation of power-supplying performance due to these risk events should not halve the capacity of the battery. The impact of a faulty battery (risk 5) can be detrimental to the flight. However since there are 14 battery packs (with two of them for avionics), then if up to three batteries are found to be faulty, emergency procedures should still be able to be operated hence the critical (and not catastrophic) impact.

Finally, consider the risks related to the motors beginning with risk 9. Typically of-the-shelf motors should be strong enough to handle the structural loads (torque) of the rotors; especially for such (relatively) low RPM of PAMELA's rotors. Therefore the probability is put at the lowest scale. The impact on the mission is assessed to be critical for reasons similar to risk 1 and 5. Short circuit (risk 10) should be unlikely to happen based experience of other aviation application. The impact is reduced to marginal since a PCM is used.

The risks to be mitigated are risk 1, 5 and 8. They are all mitigated by testings. ***Risk 1 is mitigated by performing sufficient tests in order to gain confidence on the electrical performances of ESC. Risk 5 and 8 also need to be tested, again for the electrical performance, since the battery is custom made***. The post-mitigation risk map is given in figure 9.7.

Feasible in theory				
Working laboratory model				
Based on Non-flight engineering	7	4, 6		
Extrapolated from existing flight design		10		
Proven flight design		2, 8	1, 3, 5, 9	
	Negligible	Marginal	Critical	Catastrophic

Figure 9.7: Post-mitigation risk map of ESC, motor and battery.

9.5.3. Vehicle body parts

The risks related to the rotors and ducts are given in the following list and risk map (figure 9.4).

1. Structural loading higher than the yield stress
2. Inaccurate prediction of natural frequency of arms resulting in resonance
3. Delamination of composite material due to interaction with surrounding particles
4. Corrosion of metal components (hub, motors, landing gear,...)
5. Windshield crack due to foreign object collision
6. Vehicle tilting over due to poor prediction of centre of gravity
7. Fatigue becoming a severe problem of the vehicle
8. Landing gear too weak during touchdown
9. Produced components not to specification
10. Production costs more than expected
11. Damage during assembly
12. Higher production time due to non-compliance to production plan

Feasible in theory				
Working laboratory model				
Based on Non-flight engineering		9, 10,11, 12		
Extrapolated from existing flight design		6	2, 4, 8	1, 3
Proven flight design		5	7	
	Negligible	Marginal	Critical	Catastrophic

Figure 9.8: Pre-mitigation risk map of vehicle body parts.

The risks related to estimated structural property of the vehicle's parts (risks 1, 2, 6 and 8) are all estimated to have probabilities comparable to "extrapolation from flight design" since some calculations, while simplified, have been done. The theories (e.g. beam theories) used are those that can still model the worse case scenarios of real flights with sufficient accuracy. In addition to this, safety factors have been used. The impact of risk 1 is deemed catastrophic since most of the structural parts are built out of composites. In fact once the yield stress is surpassed, the structure breaks and evidently poses the highest threat to the mission. The vibration of rotor arms (risk 2) most definitely endangers the mission; but it is deemed highly unlikely for all of the rotor arms to resonate at the same time. If one or two arms break, the vehicle is still able to manoeuvre to safety hence the risk is deemed critical. Next, risk 6 has the highest impact when the vehicle is in stationary condition but should not pose much problem in flight hence the marginal impact. It is unlikely for the landing gear to break (risk 8) since the maximum landing gear speed is 2.6 m/s. The impact is deemed critical since even though such risks would likely to occur once PAMELA has reached her destination, the safety of the pilot is still very much threatened.

The risks related to the material property used (risks 3, 4, 5, and 7) in general are deemed to have low probability of occurrence (lowest 2 of the scale). This is because of the common use of these materials for aviation. The main difference is simply the material performance near-sea environment, which still needs to be checked through experience. For risks 3 and 4, it is thought that such environments should not compromise too much the probability of material performance degradation. Nevertheless because it is still not 100 % known by the project team how composites and metals would exactly perform near-sea

(for instance how much they would interact with surrounding moisture), risks 3 and 4 are not put at the lowest probability. The impacts of the risks for degradation of composites (risk 3) is catastrophic since most of the structures are made of this material. The degradation of metals (risk 4) are deemed to be more critical-like since small percentage of the body is made out of it. Of course deterioration of material parts are still detrimental to the mission. Damage on the wind shield (risk 5), while creates discomfort for the pilot, should not compromise flight performance hence deemed marginal. Finally, degradation of material due to fatigue (risk 7) typically should not have much impact if systematic checks/maintenance are performed, but material degradation from fatigue can compromise on the load bearing capability of some structural parts during flights hence the impact is critical.

The estimation of the probabilities of risks related to the production of the structural parts (risks 9, 10, 11 and 12) are somewhat difficult. The production plan itself does not add much to the uncertainty. This is mostly due to the human factors that should be taken into consideration. It can be thought that the manufacturers are experts in their job, but nevertheless mistakes can always happen which, of course, adds to the costs and time required. To be on the safe-side, the probability of these risks are then deemed to be half the worse scale. As for the impact, because the design has been somewhat conservatives, it is thought that slight imperfections on produced part should not pose threat to flight performances and therefore given to be marginal.

As can be seen in the risk map, two of the risks pose catastrophic threat on the mission. Therefore the primary use of resources shall be on the mitigation of risks 1 and 3. ***To mitigate risk 1, detail computational method should be performed (e.g. a complete finite element analysis on the structure) to ensure no stress concentrations or just any region of abnormally high stress are present***. Furthermore, conservative/overestimation of loading conditions that can be expected in these detailed calculation should be used. Testing can be done when needed. ***As for risk 3, testings should be done to accurately represent the effect of the environment on delamination***. These mitigation actions should reduce the probability of occurrence to the lowest scale. The post-mitigation risk map is given in figure

Feasible in theory				
Working laboratory model				
Based on Non-flight engineering		9, 10,11, 12		
Extrapolated from existing flight design		6	2, 4, 8	
Proven flight design		5	7	1, 3
	Negligible	Marginal	Critical	Catastrophic

Figure 9.9: Post-mitigation risk map of vehicle body parts.

9.5.4. Avionics, control and safety system

Finally, the risks pertaining to the rotors and ducts are given in the following list and risk map (figure 9.10).

1. Degraded performance of positioning system (Piccolo II's IMU, GPS receiver and GBAS)
2. Degraded performance of imaging system (TASE-400 HD)
3. Degraded performance of the radar system (ULAB-D1)
4. Degraded performance of sensors/altitude determination system (LR-D1)
5. The vehicle experiencing higher disturbance than expected during flight

6. Failure of the vehicle to dodge incoming objects
7. Slower manoeuvre than estimated under normal flight conditions
8. Failure of deployment of float system
9. Damage to the float system
10. Inaccuracy in approximating the vehicle major components to point masses when calculating the C.G. location and mass moment of inertia.
11. Inaccuracy in the input values of the PID controller

Feasible in theory				
Working laboratory model				
Based on Non-flight engineering		5, 6		
Extrapolated from existing flight design	7		11	
Proven flight design			1, 2, 3, 4, 10	8, 9
	Negligible	Marginal	Critical	Catastrophic

Figure 9.10: Pre-mitigation risk map of avionics, control and safety system.

It is clear that the risks of avionics systems (risks 1,2,3 and 4) would be related to the reliability of each system to function properly during flight. Because the systems to be used are taken from the market; it can be thought that they are very reliable. Thus the probability of degradation of performances are very low, in the category "proven flight design". The impact of such risks is assessed to be critical. Indeed mission completion becomes questionable since the manoeuvrability of PAMELA completely relies on the automation system that relies on the data gathered by the avionics system. It is not deemed to be catastrophic since "degradation" does not include "destruction/complete malfunction" of the systems. Theoretically PAMELA should not fly if even one of the avionic system is not functioning (which would be detected during pre-flight checks), and based on the packaging it is thought that destruction of the system should never happen during flight hence such risks are not considered.

The assessment of manoeuvrability of the vehicle was done by giving a displacement or speed input, and see how fast the vehicle would return to equilibrium. It still needs to be verified how much disturbances (such as gust) would affect the vehicle, perhaps through a more elaborate/full scale analysis on the aerodynamics of the vehicle. Because of this uncertainty factor, risk 5 is deemed to be comparable to "non-flight engineering". The impact here should not be critical or higher since disturbances should not damage the vehicle, but may cause discomfort and hence the impact of the risk is marginal. For risk 6, the impact is also deemed to be marginal since under nominal flight condition, moving objects identified so far are birds. Collision with birds should not cause damages based on the material used by the vehicle. Finally it is thought that slower manoeuvres (risk 7) should not happen since the forces that resist motion (e.g. drags) is estimated to be small at low speeds. However, because experimental data is not readily available, the probability is not as low as "proven flight design" but a level higher. The impact of such risks should not endanger the mission completion nor the pilot's life. The problem related to calculation of centre of gravity (risk 10) could, in practice be critical since this might change the input response characteristics of the vehicle. However, this problem is not complex and rather complicated. The method for detailed calculation is straightforward though tedious. With careful calculation, the risk occurring in reality is almost null. For the PID controller (risk 11), similar to the previous risk, it might change the response of the vehicle hence

critical. However, for the next part of the project, it can be thought that more flight conditions would be thought of. The PID controller can be designed with relatively large margin of error for these conditions; which would put the probability of risk as low as "extrapolated from existing flight design".

Finally consider the risks regarding the safety system used (Emergency Floating System). Similar to avionics, since this will be bought from the market, they should in theory have high reliability and therefore the probability of risk occurring is at the lowest scale. The impact, however, is catastrophic since the life of the pilot (which is the highest priority) would be endangered if the vehicle were to drown.

Then, from the risk map in figure 9.10, the risks to be mitigated are risk 5, 6, 8 and 9. ***The mitigation of risks 5 and 6 is done by performing flight tests of the vehicle manoeuvrability before selling the product. This is accompanied by gathering data of the aerodynamic forces during flight for a better modelling of the control system***. This should reduce the risks at least comparable to "extrapolation from existing flight design". The aforementioned mitigation action is unlikely to rank these risks lower since it is thought that vehicle's usage experience (i.e. having many flight hours) would be necessary to fully take into account unexpected conditions. As for mitigation actions of risk 8 and 9, ***the vehicle shall add another emergency safety system*** before production. This may include a hatchet or just control system where when a command is given the rotors would then produce thrust compatible with safe descent immediately. With this the impact of failure of one safety system (i.e. the EFS) would be marginal. The post-mitigation risk map is given in figure 9.11.

Feasible in theory				
Working laboratory model				
Based on Non-flight engineering				
Extrapolated from existing flight design	7	5, 6	11	
Proven flight design		8, 9	1, 2, 3, 4, 10	
	Negligible	Marginal	Critical	Catastrophic

Figure 9.11: Post-mitigation risk map of avionics, control and safety system.

9.6. RAMS Characteristics

A first version of the RAMS characteristics of the product or system is established in the Mid-Term Report. This first version is generally based on similarity with existing products. For the Final Report the RAMS characteristics are refined, reflecting the actual design. They shall at least address a list of safety critical functions, the redundancy philosophy applied, the expected reliability and availability, and, for maintainable systems, an outline of scheduled and non-scheduled maintenance activities.

Reliability

In the case of this project, reliability is the idea of having standards over a certain period of time under certain operating conditions[42]. To asses the reliability of the design, it is important to look back at it under a different lens. The most obvious way to prove that the system is reliable is the fact that we use commercially available products for the avionics system, motors, ESC's and the emergency floating system. These all have to prove their airworthiness, thus we can be assured that they're reliable. This proves the reliability

of the flight control and communication systems.

The second aspect we can use to prove the product's reliability is the material choice. So far, the materials used in the vehicle are all common and widely used in the aviation sector. They have all proven to be suitable materials, given they have high stress resistance, fatigue properties and corrosion resistance. Proof of this can be found in the countless aircraft designs made of these materials. Furthermore, the manufacturing techniques are very common, thus none or very little imperfections in the production can be expected.

Thirdly, it is possible to look at the structures of the aircraft and compare them to those of existing aircraft. All structures used are common in the industry and have been used for decades in similar applications.

Availability

Availability is related to the possibility of the product to be used at nominal standard at any specified time. The variables affecting the availability of PAMELA may be divided into two categories: variables that are intrinsic to the vehicle and those that are extrinsic. First consider the former. One of the characteristic of the vehicle is that the product is autonomous, thus virtually anyone can operate it with little preparation. This means after the first production, the vehicle can be expected to be available for the customer in relatively short amount of time. Another factor inherent to the vehicle is the battery. The charging time is much longer than the flight time, thus actually reducing the availability of the vehicle for consecutive flights. However, the battery charging rate found was the best available in the market, therefore actually this aspect of availability is optimised with respect to real life condition. The last factor of this category to be mentioned here is the frequency of maintenance. Two types of maintenance shall be performed: once per week for half a day for small scale maintenance, and once per month for a day for extensive maintenance.

Aspects of availability that are extrinsic of the vehicle's design shall now be briefly discussed. One of them is the number of product the customer (Loodswezen) shall buy. The more they buy, the higher the availability. The other factor is the how widespread the products are placed; whether they will be concentrated in one harbour or not. The availability in this case varies with area of concern.

Maintainability

Maintainability is the capability of an item to be maintained [42].

With this in mind, it is important to show the accessibility of the vehicle for maintainability. Due to its relatively small size, compared to other aerial vehicles, the multicopter can be inspected visually on all sides and all parts can be reached with, in the worst of cases, a ladder. All parts are simple and put together using common, and also simple, methods. Procedures for maintainability of the vehicle require very little manpower, tools and time, which, of course, have financial benefits.

Safety

Safety is is the freedom from hazards and potential dangers to humans and equipment [42]. This related to the pilot, the vehicle itself, the personnel involved, the environment, and any tools/ surrounding the aircraft comes into contact with.

There's a couple of ways safety has been implement in the design. To start, most of the calculations done for the design have included safety factors to account for any errors or discrepancies that cannot be directly predicted. As an example, the powertrain subsystem has more than enough energy such that power available during operations will never be lower than what is required. Another way safety has been implemented in the design is the fact that there are 12 rotors, which lowers the likelihood of 50% of them failing or a crash. Moreover, the aircraft uses a BMS, meaning that short circuits will have minimal impact. Last,

but not least, an emergency floating system has been included in case all other systems fail and the aircraft has to crash land over a body of water.

9.7. Market Analysis

With the final product established, a strategic analysis is performed with the use of a SWOT matrix (Strength, Weakness, Opportunity and Threat). For the proof of concept in Den Helder, as discussed in section 3.3, a single vehicle will be produced. For what comes next, it is important to have an understanding of the vehicle's position in the market with respect to business competition. Currently, while the demand for PAM vehicles rises, it is an untouched subject in the maritime industry. For now it is assumed that the competition in this field are conventional helicopters and boats. The market SWOT analysis is presented in table 9.4.

Table 9.4: Market SWOT Analysis.

	Helpful	**Harmful**
Internal	- Autonomous - Airmobility - VTOL - Complies to aviation and port regulations - Sustainable	- Complex stability and control - Short-range to mid-range only - Cannot withstand strong winds and storm - Availability (recharge times)
External	- New market - Small competition - Faster than boats - Efficient	- Potential new regulations - Slower than helicopter - Helipad required

10 Design & Development Logic

As stated in the project guide: the D&D logic shows the logical order of activities to be executed in the post-DSE phases of the project. It contains a number of blocks connected by arrows, the blocks contain a description of activities [73]. The post DSE phase finds place after the final report, PAMELA will thus not be developed further. Nevertheless, what should happen in the post DSE phase can still be evaluated and analyzed. Due to the description given in the project description the D&D logic is basically a continuation of the work flow diagrams that were established during the project. Therefore an elementary flow diagram of the 'finalization of the vehicle design' and of the future 'production & marketing' has been made during the midterm report. This has been done such that a clear overview is given of the project and its feasibility, this can all be seen in figure 10.1.

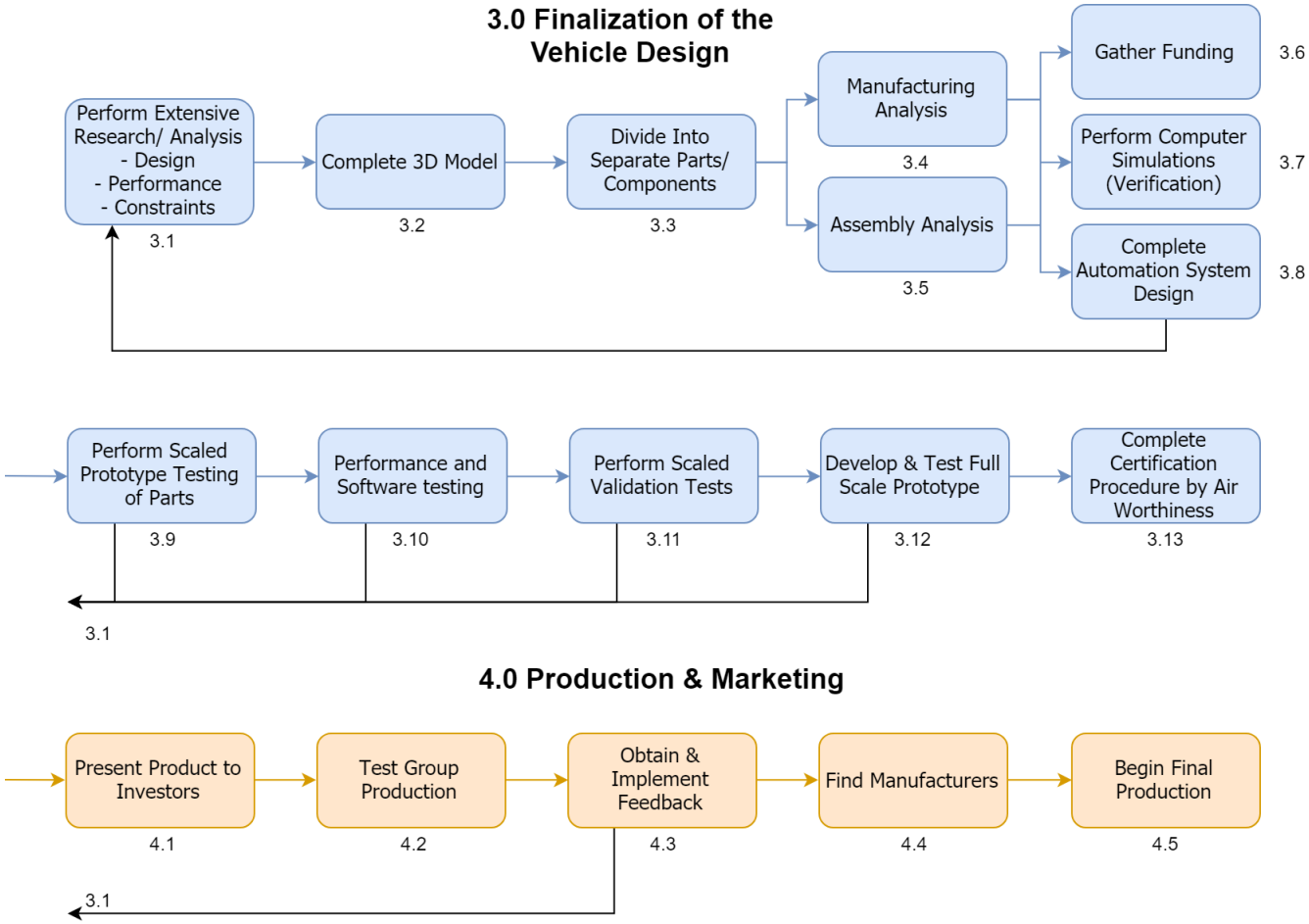

Figure 10.1: Post-DSE design and development process [10].

The 'Finalization of the Vehicle Design' deals with finishing up the technical aspects of the design, by possibly going even deeper into the design and really make sure that every aspect is correct. The 'Production & Marketing' block considers the flow up to the realization of the product. In short, it starts with setting up communication with potential investors to gather more funds for production. Moreover, potential users would be asked to test the product and give feedback such that the product can be improved. If it turns out that during testing or at another stage in the post DSE phase something crucial was overlooked by the design team, the team would have to go back to the drawing board and find the flaw. When every block up till finding manufacturers in figure 10.1 has been accomplished then the production can finally start and the sales of the product be realized.

As the flow diagram gives a great overview of what happens in the post DSE phase, it gives a bad overview of the timeline corresponding to the processes. To try and visualize this, a 'Post DSE Gantt chart' has been made, this can be seen in figure 10.2. The advantages of the Gantt chart with respect to the flow diagram is that a better representation of time is given of the processes that occur after the DSE. In addition, it also gives a more accurate and extensive representation of what happens in the post DSE phases. As here you can see exactly what kind of procedures are executed and the estimated times that go along with that specific task.

	Task Name	Start	Duration
1	**Detailed Subsystem Design**	**Mon 08-07-19**	**255 days**
2	**FEM Analysis**	**Mon 08-07-19**	**135 days**
3	Generate Computer Models of the Structure	Mon 08-07-19	15 days
4	Perform Detailed FEM Analysis On Parts	Mon 29-07-19	30 days
5	Perform Detailed FEM Analysis On Sub-Assemblies	Mon 09-09-19	45 days
6	Perform Detailed FEM Analysis On Final Assembly	Mon 11-11-19	45 days
7	**CFD Analysis**	**Mon 08-07-19**	**135 days**
8	Generate Computer Models of the Vehicle	Mon 08-07-19	15 days
9	Analyze Single Propeller Aerodynamics	Mon 29-07-19	15 days
10	Analyze Counter-Rotating Propeller Interaction	Mon 19-08-19	30 days
11	Analyze Rotor-Arm Interaction	Mon 30-09-19	15 days
12	Analyze Landing Gear Aerodynamics	Mon 30-09-19	15 days
13	Analyze Cabin Aerodynamics	Mon 21-10-19	30 days
14	Analyze Cabin-Arm Interaction	Mon 02-12-19	30 days
15	Apply Findings to Vehicle Design	Mon 13-01-20	45 days
16	Define Improved Vehicle Design	Mon 16-03-20	45 days
17	Generate Technical Drawings	Mon 18-05-20	30 days
18	**Prototyping & Testing**	**Mon 29-06-20**	**435 days**
19	Build Scaled Aerodynamic Model	Mon 29-06-20	30 days
20	Perform Wind Tunnel Tests on Model	Mon 10-08-20	60 days
21	Test Performance of Engines	Mon 29-06-20	30 days
22	Analyze Rotor Noise Performance	Mon 10-08-20	60 days
23	Test Performance of Batteries	Mon 10-08-20	30 days
24	Test Propulsion System Performance	Mon 21-09-20	30 days
25	Apply Findings to Vehicle Design	Mon 02-11-20	45 days
26	Develop Autonomous Flight Software	Mon 04-01-21	105 days
27	Test Avionics in Iron Bird Rig	Mon 31-05-21	30 days
28	Install Avionics in Cabin	Mon 12-07-21	15 days
29	**Prototype Strucuture**	**Mon 04-01-21**	**135 days**
30	Manufacture Arms	Mon 04-01-21	45 days
31	Test Arm Structural Performance	Mon 08-03-21	30 days
32	Manufacture Cabin	Mon 04-01-21	45 days
33	Test Cabin Structural Performance	Mon 08-03-21	30 days
34	Assemble Arms and Cabin	Mon 19-04-21	15 days
35	Test Vehicle Structural Performance	Mon 10-05-21	45 days
36	Attach Rotors to Arms	Mon 12-07-21	15 days
37	Install Batteries in Cabin	Mon 12-07-21	15 days
38	Perform Complete Flight Test	Mon 02-08-21	60 days
39	Implement Test Results to Commercial Design	Mon 25-10-21	90 days
40	Update Autonomous Software for Prototype	Mon 25-10-21	60 days
41	Apply for EASA Certification	Mon 17-01-22	30 days
42	**Commercial Production**	**Mon 28-02-22**	**435 days**
43	Purchase Production Machinery	Mon 28-02-22	60 days
44	Set Up Production Facilities	Mon 23-05-22	90 days
45	Produce Structural Parts	Mon 26-09-22	60 days
46	Perform Quality Checks on Parts	Mon 19-12-22	30 days
47	Order Regular Batches of Battery Cells	Mon 19-12-22	30 days
48	Order Regular Batches of Engines	Mon 19-12-22	30 days
49	Order Regular Batches of Avionics	Mon 19-12-22	30 days
50	Perform Quality Checks on COTS Elements	Mon 30-01-23	30 days
51	Transport Parts to Assembly Line	Mon 13-03-23	15 days
52	Assemble Sybsystems	Mon 03-04-23	45 days
53	Perform Quality Checks on Sub-Assemblies	Mon 05-06-23	30 days
54	Assemble Full Vehicle	Mon 17-07-23	45 days
55	Perform Final Quality Check	Mon 18-09-23	30 days
56	Deliver Vehicle to Costumer	Mon 30-10-23	15 days
57	Set Up Mobile Ground Station	Mon 30-10-23	45 days
58	Set Up Mobile Maintenance Unit	Mon 30-10-23	45 days
59	Set Up Operations	Mon 01-01-24	30 days
60	Launch Vehicle	Mon 12-02-24	1 day

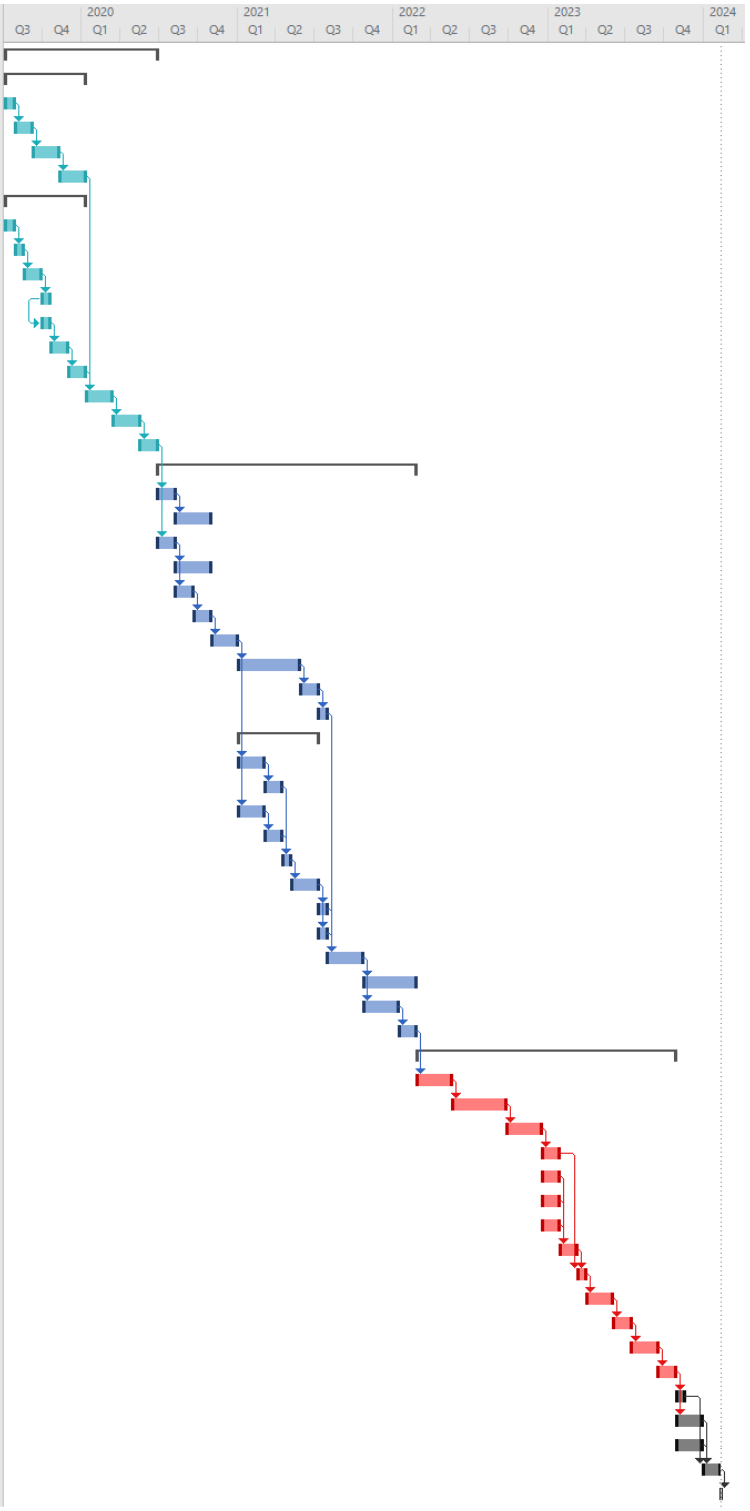

Figure 10.2: Post DSE Gantt chart.

11 Conclusion

As a part of everyday harbour operations, ships need to enter and leave the harbour area which can often be difficult to maneuver, dangerous or congested requiring the aid of a maritime pilot to navigate through. In the port of Rotterdam, this service is provided by the company Loodswezen. Every day, the maritime pilots of Loodswezen assists 160 ships with navigation into and out of the port of Rotterdam. Today, boarding these ships is done by the help of small boats and helicopters. These operations require a great amount of planning and are costly. The goal of PAMELA is to transport a maritime pilot from the harbour to an incoming ship. Implicit in this goal is to do so in a more time and cost efficient manner.

With the improvements in battery energy density, electric motor power density, light weight composite materials, advancement in avionics, and computing technology, the relatively new field of Personal Air Mobility Vehicles (PAMs) has a lot of new functionalities to offer. The need to transport maritime pilots to an incoming ship is the one PAMELA was designed for. In order to achieve a good design for PAMELA, a whole design trade off process was done. From this it was decided to go for a hexacopter configuration. This offered the most efficient solution based on the size constraints. Then, the three main subsystems were worked out. These are powertrain, avionics and structures, accompanied by an aeroacoustic analysis and a control and stability analysis.

From Chapter 4 (Powertrain), it became apparent that for a weight of 432 kg a cruise power of 61.3 kW is needed for the vehicle. With this cruise power required, the rest of the powertrain could be sized. The most important parameters of the powertrain were then found to be a battery weight of 98 kg with a capacity for propulsion of 18.94 kWh, giving a range of 25 km. The total cost of the propulsion system is estimated to be €34,500 and a weight of 165 kg is expected.

In the avionics section, the main take away is a total cost of €15,000 and an expected weight of 7 kg. The avionics are furthermore expected to be capable of providing PAMELA with fully autonomous operations.

The structure and materials chapter is the one that dictates the external lines of the fuselage of PAMELA. The fuselage will also determine the aerodynamic properties, the structural integrity, the sustainability as well as the passengers comfort. It is easy to see the big importance of this subsystem on the overall design. In the structure the main materials used are aluminum and carbon fibre. These materials have in general a good recyclability possibility (especially aluminum). The main take away from this section is that the structure is expected to cost €18,900 and have a weight of 160.6 kg.

Concluding, PAMELA will all together have a design cost of €68,149 and a MTOW of 432 kg with a 100 kg payload. The expected range is 25 km.

Bibliography

[1] E-One Moli Energy Corp. (2019). Approval sheet lithium-ion rechargeable battery. https://www.18650batterystore.com/v/files/INR21700P42A-01-0.2.pdf.

[2] A. Hunt, I., Zhao, Y., Patel, Y., and Offer, G. (2016). Surface cooling causes accelerated degradation compared to tab cooling for lithium-ion pouch cells. *Journal of The Electrochemical Society*, 163:A1846–A1852.

[3] AA Portable Power Corp. (2019). Protection Circuit Module (PCM) with Equilibrium function for 37V Li-Ion Battery Pack at 15A limit. https://www.batteryspace.com/pcmwithequilibriumfunctionfor37vli-ionbatterypackat15alimit.aspx.

[4] Aeronautics Guide (2019). Fixed wing aircraft structures. https://www.aircraftsystemstech.com/p/fixed-wing-aircraft-fuselage-fuselage.html.

[Afalah] Afalah, B. Production planning in 5 steps. http://www.pakistansmetoolkit.com/quick-links/production-planning-in-5-steps/1508321309547-224944a5-f426.

[6] Ainstein.ai. *LR-D1*. https://ainstein.ai/drone-makers-drone-service-providers/lr-d1/.

[7] Ainstein.ai. *ULAB-D1*. https://ainstein.ai/ainstein-drone-products/ulab-d1/.

[8] Aminian, N. O. and Romli, F. I. (2018). Ergonomics assessment of current aircraft passenger seat design against malaysian anthropometry data. *International Journal of Engineering Technology*.

[9] Bakir, Y. and et al. (2019a). Baseline report - a personal air mobility vehicle as maritime pilot shuttle (loodswezen). Technical report, Delft University of Technology.

[10] Bakir, Y. and et al. (2019b). Midterm report - a personal air mobility vehicle as maritime pilot shuttle (loodswezen). Technical report, Delft University of Technology.

[11] Battery University (2019). Battery Recycling as a Business. `https://batteryuniversity.com/learn/article/battery_recycling_as_a_business`.

[12] Battery University Group (BUG) (2019). Bu-302: Series and parallel battery configurations. `https://batteryuniversity.com/learn/article/serial_and_parallel_battery_configurations`.

[13] BNP Media (2015). Reliability estimation of permanent magnet dc motor. https://www.assemblymag.com/articles/94887-reliability-estimation-of-permanent-magnet-dc-motor.

[14] Cable calculator (2019). Ecofriendly recycling of lithium-ion batteries. https://myelectrical.com/tools/cable-sizing-calculator.

[15] Charles N. Keys and Robert Wiesner (1975). Guidelines for reducing helicopter parasite drag. Journal of the American Helicopter Society.

[16] Chris Woodford (2018). Lithium-ion batteries. https://www.explainthatstuff.com/how-lithium-ion-batteries-work.html.

[17] Civil Aviation Authority (2016). The air navigation order. `http://www.legislation.gov.uk/uksi/2016/765/schedule/6/made`.

[18] Clifton-Smith, M. (2009). Wind turbine blade optimisation with tip loss corrections. *Wind engineering*, 33(5):477–496.

[19] CloudCapTech. *Piccolo II*. www.cloudcaptech.com/products/detail/piccolo-ii.

[20] CloudCapTech. *TASE400 HD*. http://www.cloudcaptech.com/products/detail/tase-400-hd.

[21] Corporate Helicopters (2019). Robinson r44 clipper. https://www.corporatehelicopters.com/helicopter-services/helicopter-sales/robinson/r44-clipper/.

[22] CSS Electronics (2019). Can bus explained - a simple intro (2019). https://www.csselectronics.com/screen/page/simple-intro-to-can-bus/language/en.

[23] Cunha, F. (2013a). Blade element momentum theory. `https://fenix.tecnico.ulisboa.pt/downloadFile/845043405440067/9-Blade%20element%20momentum%20theory.pdf`. Lecture Slides.

[24] Cunha, F. (2013b). Blade element theory. `https://fenix.tecnico.ulisboa.pt/downloadFile/845043405440065/7-Blade%20element%20theory.pdf`. Lecture Slides.

[25] Cunha, F. (2013c). Momentum theory. `https://fenix.tecnico.ulisboa.pt/downloadFile/282093452028191/3-Momentum%20Theory%20in%20hover.pdf`. Lecture Slides.

[26] Curran, R. & Verhagen, W. (2019). Lecture 8 - Risk Management & Reliability Engineering.

[27] D Pasini, D. J. S. and Burgess, S. C. (2003). Structural efficiency maps for beams subjected to bending.

[28] Desjardins, J. (2017). How many million lines of code does it take? https://www.visualcapitalist.com/millions-lines-of-code/.

[29] Duesenfeld GmbH (2019). Ecofriendly recycling of lithium-ion batteries. https://www.duesenfeld.com/recycling$_e n.html$.

[30] Easy Composites (2015). 100mm high density polyurethane foam block 30cm x 30cm. https://www.easycomposites.co.uk/!/patterns-moulds-and-tooling/pattern-making/high-density-polyurethane-foam-block.html.

[31] EHANG (2019). Ehang 184 gallery. http://www.ehang.com/ehang184/gallery/.

[32] Energus Power Solutions, Ltd. (2019). Tiny BMS s516 - 150A/750A. https://www.energusps.com/shop/product/tiny-bms-s516-150a-750a-36.

[33] European Aviation Safety Agency (EASA (2007). Certification specifications for small rotorcraft cs-27. https://www.easa.europa.eu/sites/default/files/dfu/CS-27%20Amdt.%201.pdf.

[34] European Aviation Safety Agency (EASA) (2012). Notice of proposed amendment (npa) no 2012-14. https://www.easa.europa.eu/sites/default/files/dfu/NPA%202012-14.pdf.

[35] Fogelberg, J. (2013). Navigation and autonomous control of a hexacopter in indoor environments. Master's thesis, Lund University.

[36] Government, U. S. (2017). https://www.gps.gov/systems/gps/performance/accuracy/.

[37] GrabCad (2017). 10s3p diy li-ion battery pack for e-bike. https://grabcad.com/library/10s3p-diy-li-ion-battery-pack-for-e-bike-1.

[38] Group, S. S. (2014). National recycling rate study. Technical report, Battery Council International.

[39] Hacker Motor GmbH (2016a). Hst-350 brushless controller. https://hacker-industrial-solutions.com/wp-content/downloads/anleitungen/AN-HST350-Application-Note-07072016.pdf.

[40] Hacker Motor GmbH (2016b). Q-150 brushless dc. https://hacker-industrial-solutions.com/elektro-antriebssystem/q-150-brushless-dc-motorenserie/?portfolioCats=53.

[41] Hacker Motor GmbH (2019). Hst-350 brushless controller. https://hacker-industrial-solutions.com/elektro-antriebssystem/hst-350-brushless-dc-controller/.

[42] Hamann, R. J. and van Tooren, M. J. L. (2006). Systems Engineering & Technical Management Techniques.

[43] Harvey H. Hubbard (1991). Aeroacoustics of Flight Vehicles: Theory and Practice. *NASA Reference Publication 1258*, (Technical Report 90-3052).

[44] HELIFLITE (2019). R66 emergency pop-out float system. http://www.heliflite.com.au/accessories/r66-emergency-float-system.

[45] Hokamo BV. (2019). Groothandel in elektriciteitskabel en toebehoren. https://www.hokamo.nl/.

[46] ICAO (2008). Environmental Protection. Volume 5. International Standards and Recommended Practices.

[47] Inc., A. A. S. M. (2015). Titanium technical data sheets. http://www.aerospacemetals.com/titanium-distributor.htmltech.

[48] Isidor Buchmann (2019). Understanding lithium-ion. `https://batteryuniversity.com/learn/archive/understanding_lithium_ion`.

[49] J. L. Pereira (2008). Hover and wind-tunnel testing of shrouded rotors for improved micro air vehicle design. PhD Thesis.

[50] Jia, Z. and Lee, S. (2019). Acoustic analysis of a quadrotor evtol design via high-fidelity simulations. *25th AIAA/CEAS Aeroacoustics Conference*.

[51] Johnson, A., Thomson, R., David, M., and Joosten, M. (2015). Design and testing of crashworthy aerospace composite components. *Polymer Composites in the Aerospace Industry*.

[52] Klaus and Lita (2015). How fast can a quadcopter fly? https://klsin.bpmsg.com/how-fast-can-a-quadcopter-fly/.

[53] LION Smart GmbH (2019). LION Li-BMS Datasheet. https://www.lionsmart.com/wp-content/uploads/2018/11/Datasheet$_L iBMS_E NG.pdf$.

[54] Liu, Q., Du, C., Shen, B., Zuo, P., Cheng, X., Ma, Y., Yin, G., and Gao, Y. (2016). Understanding undesirable anode lithium plating issues in lithium-ion batteries. *RSC Adv.*, 6:88683–88700.

[55] Lizotte*, A. M. and Lokos, W. A. (2005). Deflection-based aircraft structural loads estimation with comparison to flight. page 18. American Institute of Aeronautics and Astronautics.

[56] Luís Sardinha Monteiro, Terry Moore, C. H. (2005). What is the accuracy of dgps? 58:207–225.

[57] M. Rutkowski and W. Kruszi (2013). Design and analysis of ducted fan for multirotor vtol uav. http://sdpg.pg.gda.pl/pij/files/2013/09/02$_2$013$_2$4 – $rutkowski.pdf$.

[58] Malaysian Institute of Aviation Technology (2014). AJD 21603 Rotorcraft system, maintenance and role equipment (Lecture notes). https://www.slideshare.net/partyrocka99/1-week-1-helicopter-structure.

[59] Mallick, P. (2012). Advanced materials for automotive applications: an overview. *Advanced Materials in Automotive Engineering*.

[60] Marte, J. E. and Kurtz, D. W. (1970). A review of aerodynamic noise from propellers, rotors, and lift fans. *National Aeronautics and Space Agency (NASA)*, (Technical Report 32-1462).

[61] MetalMiner (2019). MetalMiner Prices. https://agmetalminer.com/metal-prices/.

[62] Mostafa Moussid, Adil Sayouti, H. M. (2015). Dynamic modeling and control of a hexarotor using linear and nonlinear methods. *International Journal of Applied Information Systems*, 9(5):9–17.

[63] Nancy Hall (2015). Drag of a sphere. https://www.grc.nasa.gov/www/k-12/airplane/dragsphere.html.

[64] P. Martin and C. Tung (2004). Performance and flowfield measurements on a 10-inch ducted rotor vtol uav. https://apps.dtic.mil/dtic/tr/fulltext/u2/a537657.pdf.

[65] Payscale Inc. (2019). Average aerospace engineer salary. `https://www.payscale.com/research/NL/Job=Aerospace_Engineer/Salary`.

[66] Robinson (2019a). Faa certifies floats for r66 turbine. https://robinsonheli.com/news/faa-certifies-floats-for-r66-turbine/.

[67] Robinson (2019b). R44 raven ii clipper ii. https://robinsonheli.com/r44-specifications/.

[68] Robotics@QUT (2015). Vision guided flight. Technical report.

[69] Rockwest Composites (2019). Twill-nomex-sandwich. https://www.rockwestcomposites.com/plates-panels-angles/sandwich-panels/twill-nomex-sandwich.

[70] Ruijgrok, G. J. (2009). *Elements of airplane performance*. Delft Academic Press, Delft, The Netherlands. Second Edition.

[71] Ryn, T. V. (2012). Performance car seat with rails. https://grabcad.com/library/performance-car-seat-with-rails.

[72] SAMSUNG SDI. (2017). Lithium-ion rechargeable cell for power tools. http://thunderheartreviews.blogspot.com/2018/12/samsung-40t-high-drain-21700-li-ion.html.

[73] Scarano, F. and Ragni, D. (2019). Ae3200 project description.

[74] Shamiyeh, M., Rothfeld, R., and Hornung, M. (2018). Performance benchmark of recent personal air vehicle concepts for urban air mobility. http://www.icas.org/ICAS$_A RCHIVE/ICAS$2018/$data/papers/ICAS$2018$_0$794$_p aper.pdf$.

[75] Thompson, P. (2016). Can auto glass be recycled? https://info.glass.com/recycling-auto-glass/.

[76] TJ Helicopters (2019). R44 pop out floats with ground handling wheels. https://www.tjhelicopters.com/product/r44-pop-out-floats-with-ground-handling-wheels/.

[77] Volocopter GmbH (2017a). Our high flier: The volocopter 2x. https://www.volocopter.com/en/product/.

[78] Volocopter GmbH (2017b). Volocopter home page. https://www.volocopter.com/en/.

[79] Waybuilder.net (2018). Types of aircraft construction. https://www.waybuilder.net/free-ed/Resources/15-Transportation/Aviation/AircraftStructure.asp?iNum=3.

[80] Wettenbank Overheid (2018). Activiteitenbesluit Milieubeheer - Geluidshinder. https://wetten.overheid.nl/BWBR0022762/2018-01-01Hoofdstuk2$_A fdeling$2.8.

[81] Whelen (2019). Lighting regulations. https://www.whelen.com/pb/Aviation/System%20Requirements/Anit-Collision%20Systems.pdf.

[82] Woodbank Communications Ltd (2005). Battery management system (bms). https://www.mpoweruk.com/bms.htm.

A Logbook

Table A.1: Work contribution of every member to the report

Section	Authors
Symbols	AB, SM
Summary	YB
1	CM
2	HI
3.1	AK
3.2	AK, RP
3.3	SM, AK, RP
3.4	AK, RP
3.5	SM
3.6	WV
3.7	WV
3.8	WV
3.9	WV
4.1	CM
4.2	CM
4.3	CM
4.4	CM
4.5	AB, RP
4.6	WV, CM
4.7	CM

Section	Authors
4.8	SM
4.9	WV
4.10	WV
4.11	WV
4.12	WV
4.13	WV
5	YB
6.1	AK
6.2	HI
6.3	AK, HI
6.4	AK, HI
6.5	AK
6.6	AK
6.7	AK
6.8	AK
6.9	AK
6.10	AK
7.1	HI
7.2	HI
7.3	HI

Section	Authors
8.1	IB
8.2	NG
8.3	NG
8.4	AB
8.5	IB, RP, YB
8.6	YB
8.7	IB
8.8	IB, NG
8.9	IB
8.10	NG
8.11	IB
8.12	NG
9.1	IB, RP
9.2	NG
9.3	SM, CM
9.4	SM
9.5	AB, NG
9.6	AB, RP
9.7	RP
10	SM
11	CM

Authors: AB - Angka Bayu, AK - Antonio Kung, CM - Cedric Meire, HI - Hussein Ibrahim, IB - Itamar Bukai, NG - Nico Gartland, P - Robbert Proost, SM - Skip de Metz, WV - Willem Völker and YB - Yunus Bak.